Université d'Ottawa · University of Ottawa

PATTERN FORMATION IN GEOCHEMICAL SYSTEMS

by

Sergei Katsev

Thesis submitted to
the Faculty of Graduate and Postdoctoral Studies
in partial fulfillment of the requirements for the degree of
Doctor of Philosophy

Ottawa Carleton Institute for Physics
University of Ottawa
Ottawa, Canada

October 2, 2002

Abstract

Compositional patterns are extremely common in natural minerals. While, in many cases, variations in the solid mineral composition reflect the external changes in the environment at the time of the mineral formation, the role of self-organization is increasingly acknowledged. For example, in reaction-transport systems, the patterns may form spontaneously from an unpatterned state at the time of crystal growth and then become preserved by being "frozen" in the solid mineral. In this work, the pattern formation by self-organization is investigated by means of model construction and computer simulations in several minerals from different geologic environments.

The impact of environmental noise is investigated on a model of oscillatory zoning in plagioclase feldspar. It is shown that environmental noise can lead to pattern formation such as oscillatory zoning, even when no deterministic periodic solutions exist. Coherence resonance close to the Hopf bifurcation is observed.

Oscillatory zoning in barite-celestite system is simulated to quantitatively describe the results of the previously reported nucleation and growth experiments. The zoning is thought to be formed by autocatalytic growth from an aqueous solution. In addition to the description of the reaction-diffusion system in terms of partial and ordinary differential equations, a cellular automata model is proposed for the first time for this oscillatory crystallization type of problems.

A quantitative model of banding in Mississippi Valley-type sphalerite is presented. Banded ring-like patterns are shown to arise due to a self-propagating sequence of growth and dissolution (coarsening wave). A two-dimensional model is presented for the first time and the conditions for the pattern generation and preservation are discussed.

A number of time series analysis techniques are applied to characterize the compositional patterns observed in natural minerals as well as in the colored rythmites found in the marine clay sediments of the Ottawa Valley. Several caveats in interpreting the results of such analyses are outlined.

Sommaire

Les motifs compositionnels sont extrêmement courants dans les minéraux naturels. Tandis que, dans beaucoup de cas, les variations de la composition d'un minéral solide reflètent les changements externes dans l'environnement au moment de la formation du minéral, le rôle des mécanismes d'auto-organisation est de plus en plus reconnu. Par exemple, dans les systèmes avec réaction chimique et transport diffusif, les motifs peuvent se former spontanément à partir d'un état non organisé au moment de la croissance cristalline et deviennent préservés par la suite dans le minéral solide. Dans ce travail, nous étudions la formation des motifs par auto-organisation en construisant des modèles théoriques et en analysant des simulations sur ordinateur pour plusieurs minéraux dans des environnements géologiques différents.

L'impact du bruit environnemental est étudié dans un modèle de zonation oscillatoire dans un plagioclase magmatique. On montre que le bruit environnemental peut induire la formation de motifs comme la zonation oscillatoire, même lorsque les solutions périodiques déterministes n'existent pas. On observe un phénomène de résonance cohérente près de la bifurcation de Hopf.

La zonation oscillatoire dans le système de barytine-célestine est simulée pour décrire quantitativement les résultats des expériences précédemment publiées sur le nucléation et la croissance de ces cristaux. Nous supposons que le zonation est le résultat d'une croissance autocatalytique du soluté. En plus de la description du système de réaction-diffusion en termes d'équations différentielles partielles et ordinaires, un modèle d'automate cellulaire est proposé pour la première fois dans ce type de problèmes de cristallisation oscillatoire.

Nous présentons un modèle quantitatif de la formation de bandes colorées typiquement observées dans la sphalérite du type de la vallée du Mississippi. Les motifs des bandes circulaires et colorées apparaissent en raison d'une onde de propagation de croissance et de dissolution. Nous présentons pour la première fois un modèle bidimensionnel et nous discutons les conditions pour la génération de ces motifs et leur préservation.

Un certain nombre de techniques d'analyse de séries chronologiques sont appliquées pour caractériser les motifs compositionnels observés dans des minéraux naturels commes les couches colorées observées dans les sédiments d'argile marine de la vallée de la rivière des Outaouais. Nous décrivons plusieurs difficultés d'interprétation de telles analyses.

Acknowledgments

There are a number of people that I am indebted to for this work. I would like to thank my supervisor, Ivan L'Heureux, for introducing me to the field of nonlinear dynamics and for his guidance throughout the entire project. I am grateful to Tony Fowler for many fruitful discussions and for patiently answering my questions about the geological aspects of this work. I would like to thank André Longtin, John Bechhoefer, and Steve Godfrey for their helpful comments and Jeanne Percival and Jan Aylworth for providing the Leda clay data. I would like to recognize the help and moral support of my colleagues and friends that are too numerous to mention. I also thankfully acknowledge the financial support of the University of Ottawa and the Ministry of Training, Colleges and Universities of Ontario.

Above all, I am most grateful to Sanya for inspiring, supporting by all means and tolerating me during all these years.

Publications and Conferences.

Publications:

1. S. Katsev and I. L'Heureux, Impact of environmental noise on oscillatory pattern formation in crystal growth: Plagioclase feldspar, *Phys. Rev. E* **61**, 5, 4972-4979, 2000.

2. S. Katsev, I. L'Heureux, and A. D. Fowler, Mechanism and duration of banding in Mississippi Valley-type sphalerite, *Geophys. Res. Lett.* **28**, 24, 4643-4646, 2001.

3. S. Katsev and I. L'Heureux, Two-dimensional model of banding pattern formation in minerals by means of coarsening waves: Mississippi Valley-type sphalerite, *Phys. Lett. A* **292**, 66-74, 2001.

The following manuscripts are currently in press:

4. S. Katsev and I. L'Heureux, Caveats in interpreting the results of short time series analysis, submitted to *Computers & Geosciences*.

5. S. Katsev and I. L'Heureux, Autocatalytic model of oscillatory zoning in experimentally grown (Ba,Sr)SO_4 solid solution, accepted to *Phys. Rev. E*.

Conference presentations

1. S. Katsev, I. L'Heureux, and A. D. Fowler, Banding pattern formation in natural sphalerite by means of coarsening waves, STATPHYS 21 - IUPAP International Conference on Statistical Physics, Cancún, Mexico, 15-20 July, 2001.

2. S. Katsev, I. L'Heureux, and A. D. Fowler, Banding pattern formation in natural sphalerite by means of coarsening waves, Canadian Association of Physicists (CAP) Congress, Québec City, 2-5 June, 2002.

Content

Chapter 1

Introduction

Patterns in natural minerals have long since attracted the attention of researchers. Multicolored concentric rings in agates, alternating dark and light layers in zebra stone, and many other orderly structures are the readily observed examples of compositional mineral patterns. Similar structures caused by variations of the mineral composition are found in a multitude of mineral species. It has been traditionally believed that these variations reflect the corresponding changes in the geological environment and therefore contain a record of these changes. The incentive was therefore to read those records as one would read tree rings to extract information about the past geological settings that existed at the time of the rock formation.

After it was shown by Turing [1] and Prigogine [2] that patterns may form spontaneously from an unpatterned state in conditions far from thermodynamic equilibrium, there has been rising awareness in the geophysical community that many of the compositional patterns may be due to self-organization. In particular, reaction-transport systems were shown to give rise to a variety of patterns. Most pattern formation processes involve growth of a crystalline phase from a liquid in the form of either melt or solution. In nature, this transition from a liquid state to solid mineral often occurs under conditions that are far from thermodynamic equilibrium. The diffusion in the liquid in the vicinity of the crystal surface coupled to the reaction at the crystal-liquid interface and to the fluctuations in the bulk liquid reservoir provide possibilities for the complex dynamics that may lead to pattern formation.

In this work, the potential for self-organized behavior is investigated for several systems. The models are proposed to explain the patterning in several minerals that form in magmatic and sedimentary environments; also, a theoretical ground is presented for an experiment, in which patterning was obtained under laboratory conditions.

This thesis is organized as follows. Chapters 2 to 4 are introductory and present the theoretical framework of the current study while Chapters 5 to 8 contain the research findings.

Chapter 2 presents a general overview of the pattern formation problem in minerals. It gives several examples of the most studied naturally observed compositional patterns and describes the geological environments in which the patterned minerals are formed. It also describes the currently existing hypotheses about the origin of these patterns and discusses the necessary conditions for emergence of these orderly structures by self-organization.

Chapter 3 presents the microscopic theory of crystal growth.

Chapter 4 introduces the basics of the stochastic processes. It describes the difference in Ito and Stratonovich calculus and introduces the description of a stochastic system in terms of the Fokker-Planck equation for the probability distribution of the stochastic variable.

Chapter 5 presents a model of oscillatory zoning in magmatic plagioclase and investigates the non-trivial effects of environmental noise on that model.

Chapter 6 presents a model of the autocatalytic growth of a barite-celestite solid solution from an aqueous solution. The description of the diffusion-interface reaction system in terms of partial and ordinary differential equations is complemented by a cellular automata approach, which, to the best of the author's knowledge, is applied to this sort of oscillatory crystallization problem for the first time.

Chapter 7 describes the model of compositional trace element banding in sphalerite (ZnS) found in Mississippi Valley-type ore deposits. Both one-dimensional and two-dimensional models are presented

Chapter 8 discusses the application of the time series analysis methods to characterize compositional patterns in minerals. The deficiencies of several methods are discussed and the results of the analysis of several patterns are presented. The analysed patterns include oscillatory zoning profiles in plagioclase and hydrothermal garnets as well as colored rythmites in the marine clay deposits of the Ottawa Valley.

Finally, **Chapter 9** contains some concluding remarks and suggestions for future research. Three **appendices** complete the presentation of the thesis.

Chapter 2

Overview of geochemical pattern formation

This chapter presents an overview of pattern formation in geochemical systems. A phenomenological description of the patterns observed in natural minerals is first provided followed by a brief review of the experimental techniques employed to observe and characterize those patterns. Then the hypotheses about their origins and the models proposed to date are presented. Typical geological environments in which patterned minerals are formed are also reviewed. The final section of this chapter provides the connection between the mineral pattern formation studies and related areas of geology.

2.1 Examples of patterns

Pattern formation in minerals is a widespread phenomenon observed in a variety of mineral species that are formed under extremely diverse geological conditions. Although the term "pattern" has been extensively used to describe all sorts of orderly structures found in natural systems, in this work its use will be restricted to structures formed by spatial variations of the mineral composition. The description below concentrates on two types of such compositional patterns. The first type of patterns (intra-crystalline compositional patterns) is characterized by mineral composition variations within a single crystal (zoning). This study particularly focuses on the cases of *oscillatory zoning* (OZ) whereby the mineral composition varies in a non-monotonic fashion, often exhibiting almost regular oscillations. The second type of patterns includes compositional structures formed by agglomerates of particles. The patterns are typically characterized by a succession of concentric bands or flat layers of different chemical composition, which alternate within the mineral bodies.

Compositional patterns of both types have been observed in more than 75 rock-forming and accessory minerals comprising most major mineral classes: silicates (hydrous and anhydrous), sulfides, oxides, halides, carbonates, phosphates, and sulfates

[3]. Patterned samples have been found in magmatic rocks, hydrothermally altered rocks, mineralized rocks, and carbonate sequences. The spatial scales of the patterns of interest extend from micrometer and sub-micrometer scales for intra-crystalline zoning to millimeters or centimeters in the case of bands formed by ensembles of individual crystallites.

2.1.1 Oscillatory compositional zoning in single crystals

Many single crystals in naturally formed minerals exhibit growth-shells of varying chemical composition that are usually seen as alternating layers when viewed in cross-section. Such oscillatory zoning patterns are found in a great variety of minerals formed under very different conditions. Oscillatory zoning is observed in crystals in igneous, sedimentary and metamorphic environments as well as in hydrothermal deposits. It is very common in intermediate composition volcanic rocks [4,5]. Although the term "oscillatory" is used to characterize the mineral zoning, the fluctuations in the crystal composition are not necessarily periodic or regular.

Oscillatory zoning in single crystals is interpreted as a primary growth texture. In the oscillatory-zoned samples, growth layers are typically parallel to crystallographic planes of low Miller indices. Planar layers oriented along the main crystallographic directions indicate that faced morphology has been preserved throughout the crystal growth history. The zoning may reflect concentration variations in the mineral trace elements or in its major components. In the latter case, zoning is often produced by variations in the concentration ratio of the two end-members of a binary solid solution.

In this section, we give a phenomenological description of some typical oscillatory zoning patterns and characterize the geophysical environments in which they are formed.

Magmatic plagioclase

The compositional pattern found in plagioclase feldspar is probably the oldest known [6] and the most studied example of oscillatory zoning in minerals. Plagioclase is a major component of many igneous and metamorphic rocks and is essentially a binary solid solution with the two end-members: anorthite $CaAl_2Si_2O_8$ (An) and albite $NaAlSi_3O_8$ (Ab). The oscillatory zoned crystals are believed to have crystallized from saturated silicate liquids within magma chambers. The patterns are typically found frozen into crystals that were erupted from these chambers with the lava flows.

Oscillatory zoned samples show patterns that are clearly visible, for example, in a polarizing microscope. In these patterns, the An concentration varies from the core of the crystal to its rim, exhibiting multiple oscillations (Fig.1). Microprobe analysis shows that the An molar composition in such crystals varies between the zones by approximately 5-15 %. Typical oscillatory zoned samples have tens of zones whose thickness ranges from about 10 to 100μm. Superimposed on these more or less regular variations, abrupt changes in the mineral composition and irregular non-oscillatory patterns are often found [5]. The An-composition profile in oscillatory zoned crystals is often found to follow a saw-tooth pattern, i. e. it contains multiple spikes within which the An concentration steeply increases and then gradually decreases in the direction away from the crystal core. These spikes are typically superimposed on an overall decreasing baseline, thus defining a so-called normal zoning. Reverse zoning, whereby the An concentration baseline generally increases towards the edge of the crystal, is also occasionally observed.

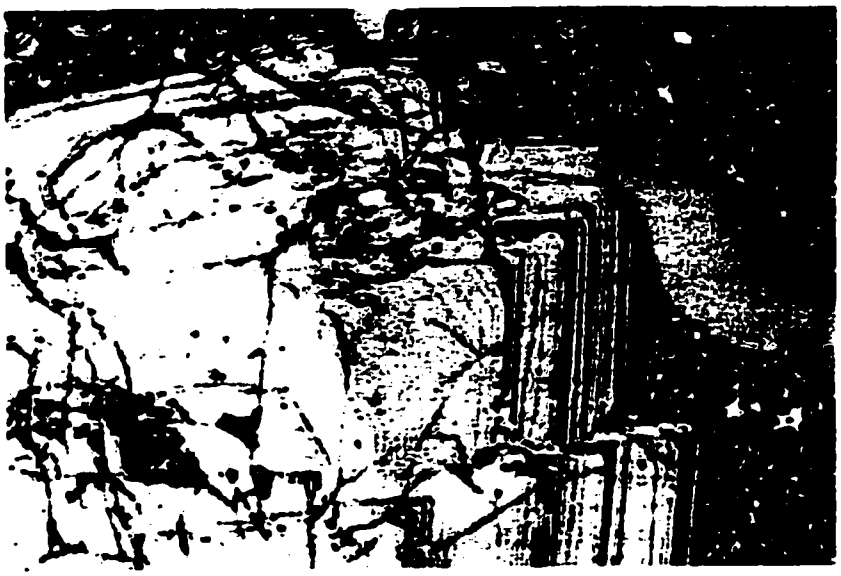

Fig. 1 Nomarski image of oscillatory zoning in plagioclase (from [7]). The field of view is 500 μm wide. The sample is from an andesite, Montserrat, Lesser Antilles.

Metamorphic and hydrothermal garnet

Intracrystalline zonation of metamorphic minerals is frequently observed in minerals formed in hydrothermal systems [8]. In particular, the phenomenon of oscillatory zoning is often described [9] in garnet single crystals. For example, it has been

extensively studied in grossular-andradite (grandite) garnets formed in the hydrothermal environment of the Oslo rift region (Southern Norway) [10,11].

Garnets are a group of silicate minerals with the general formula $A_3B_2(SiO_4)_3$. The A here represents divalent elements such as calcium, iron, magnesium and manganese and the B represents a trivalent metal such as aluminum, chromium, iron, and, in some cases, other elements. Grandite garnets are formed by a binary solid solutions of grossular ($Ca_3Al_2Si_3O_{12}$) and andradite ($Ca_3Fe_2Si_3O_{12}$). Oscillatory intracrystalline chemical zonation patterns found in these crystals (Fig.2) are chiefly perpendicular to the dodecahedral crystal faces {110} and involve changes of the Fe^{3+}/Al ratio as well as variations in the trace element concentrations [12]. The thickness of the zones varies from 10 to 100 μm and the size of the zoned crystals ranges from 0.1 to 1mm. The zoning profiles are often characterized by occasional sharp transitions between two (or three) relatively well defined composition ranges, which is consistent with the existence of a miscibility gap [13].

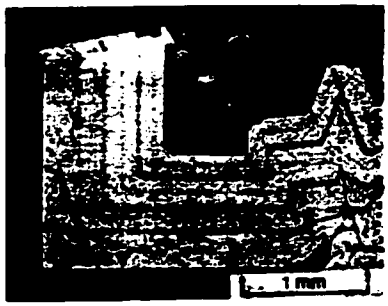

Fig. 2 Zoning in garnet (from [14]). The image was obtained by backscattered electron microscopy. The darker regions are grossular-rich and the lighter regions are andradite-rich. The sample is from the Oslo rift region, Norway.

The correlations that are commonly found to exist among the patterns observed in garnet crystallites located short distances from each other [11] suggest that the crystal growth conditions that lead to the pattern formation were controlled by external changes in the environment. However, there also exists some evidence [15] for a fast partially locally-controlled crystal growth process under possibly far-from-equilibrium conditions.

Experimentally grown barite-celestite

Oscillatory zoning in $BaSO_4$-$SrSO_4$ solid solution is one of the few examples of oscillatory zoning that was produced experimentally [16] (to the best of the author's knowledge, zoning in calcite [17] was the only other case of oscillatory zoning produced

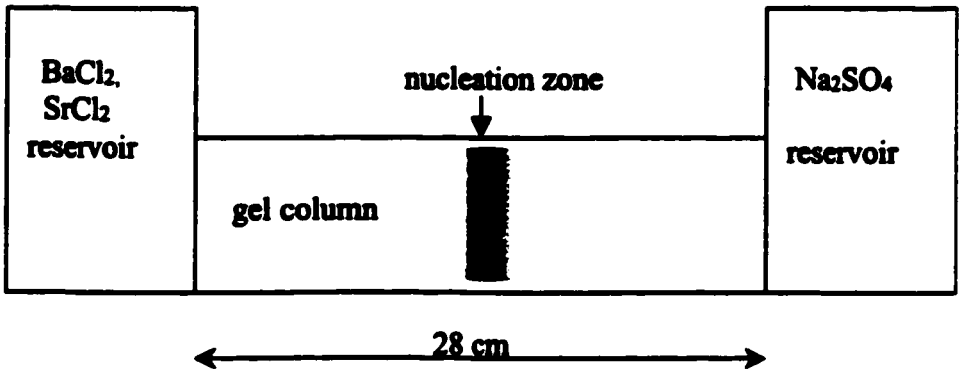

Fig. 3 Experimental setup, in which oscillatory zoned crystals of $(Ba,Sr)SO_4$ were synthesized in [16]. The reservoirs containing the mother solutions are connected by a gel column 28 cm in length. The reactants counterdiffuse in the column and $(Ba,Sr)SO_4$ crystals nucleate and grow in some region (shown as grey) inside the column. After one month of growth, the crystals were extracted and their morphology was studied by scanning electron microscopy.

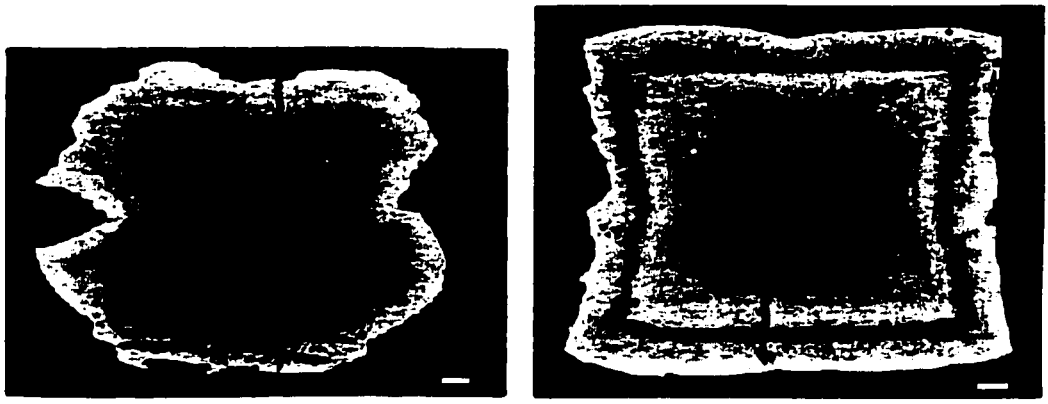

Fig. 4 Oscillatory zoned crystals of experimentally grown $(Ba,Sr)SO_4$ (from [16]). Darker areas correspond to Sr-rich parts of the crystals. The image was obtained as a backscattered scanning electron micrograph. The scale bar corresponds to 10μm.

experimentally). In the experiments by A. Putnis's group, barite-celestite solid solution crystals were grown from aqueous solutions that were counterdiffused in a gel column connecting the reservoirs that contained the initial reactants (Fig. 3). The barite-celestite crystallites were formed in the middle of the gel column as a result of the reactions $BaCl_2+Na_2SO_4 \rightarrow BaSO_4 + 2NaCl$, $SrCl_2+Na_2SO_4 \rightarrow SrSO_4 + 2NaCl$. When the concentrations of reactants in the reservoirs were higher than about 0.3*M*, the crystals developed oscillatory zoning (Fig. 4). The oscillatory patterns within the crystals were characterized by abrupt changes in the crystal composition from about 25 to 90 percent Ba between the zones, which were about 10μm wide.

Calcite

Calcite ($CaCO_3$) is a mineral typically found in sedimentary rocks and is the predominant mineral of limestone. Due to its high solubility in water at low temperatures it often fills the pores in other minerals in sedimentary, igneous and metamorphic rocks and in hydrothermal ore deposits. Oscillatory zoning in calcite is relatively common and characterized by μm-scale fluctuations in the concentration of trace elements, such as Mn or Sr. Such zoning has been traditionally attributed to large scale fluctuations in the composition of fluids, from which the calcite grows, and underlies the so-called cement stratigraphy concept, although recently an approach suggesting self-organisation has been developed [18].

Zircon

Zircon ($ZrSiO_4$) is a widespread mineral accessory of many igneous rocks (e.g. granite and syenite). Substitution of U for Zr underlies the use of zircon as a geochronometer. Oscillatory zoning in zircon [19,20,21] is characterized by changes in rare earth element (U and Th) concentrations on spatial scales from less than a micron to several hundreds of microns. The zoning is believed to be due to a substitution of U, Th, and P for Zr during the crystal growth and is believed to be self-organized [19].

2.1.2 Banding formed by crystalline agglomerates

Mississippi Valley-type sphalerite in hydrothermal ore deposits

One of the most notable examples of pattern formation in hydrothermal minerals is banding observed in Mississippi Valley-type (MVT) sphalerite (ZnS). The patterns are typically characterised by clusters of sub-mm nested, sequentially coloured, bands of ZnS crystals. Sphalerite can have a limited substitution of Fe for Zn within its structure and

the banding patterns are defined by the variations in the Zn/Fe ratio. The banded sphalerites of the MVT deposits typically have light colored ZnS rich cores that are surrounded by a sequence of dark and light bands, which reflect the variations in the iron content (Fig. 5) [22]. The bands are arranged in the cm-sized clusters and in general become more Fe-rich toward the exterior of the cluster. Individual bands are composed of a myriad of platy crystals oriented normal to the bands. The sphalerite is often intergrown with arborescent crystals of galena and other minerals (e.g. calcite, pyrite, fluorite, barite) all of which have filled cavities within the host carbonate rocks.

Fig. 5 Banding in MVT sphalerite. One dollar coin is shown to indicate the scale. The concentric colored ring structures reflect variations in the trace iron content.

Agates

Agates are rounded bodies up to several decimeters across and are commonly found in cavities within volcanic rocks [23]. From the outside inward, they typically consist of concentric, regularly spaced layers of microcrystalline chalcedony fibers, a layer of micro- and/or macrocrystalline equant quartz, and a central void. Agates are thought to form as the result of successive precipitation out of hydrothermal solutions in the cavity or due to crystallization of a silica-rich lump accumulated in the cavity.

Champlain Sea clay sediments

In marine and lacustrine environments, horizontal layers of varying mineral composition are commonly formed, usually due to the seasonal variations in the mineral and organic matter deposition rates. As an example of such structures, sequences of about 400 colored clay bands are found in the marine sediments of the ancient Champlain Sea,

which occupied the Ottawa Valley and low lands along the St. Lawrence River about 11,000 years ago. The widths of these bands are within the range 0.5 to 20 cm and the variations in the band colors correlate with the differences in the clay and silt content between the bands [24]. In most deposition systems of this type, the changes in the amount of deposited material usually correlate with the local and global changes in the environment. Therefore, identifying the trends in the banding sequence may provide clues to reading the paleo-climatic record.

2.2 *Experimental techniques used to observe patterning in minerals*

A number of observational techniques are used to detect and quantify the oscillatory zoning in minerals. The most commonly used methods [7] are described below.

The petrographic microscope (in transmitted light mode) is commonly used for the semi-quantitative characterization of mineral zoning. A ~30μm thick wafer of a translucent mineral sample is viewed between two cross-polarizing filters, so-called crossed Nicols illumination. Since the index of refraction varies with the mineral composition and the transmission of light through most minerals is anisotropic, interference allows the identification of the mineral type.

Nomarski differential interference phase contrast microscopy (NIC) is based on using the microscope in the reflected light mode. A light beam is transmitted through the objective lens and then split by a Nomarski prism. One of the resulting beams is reflected off a polished and etched surface of the sample and is then recombined through the prism with the second beam. Their interference produces the image of the surface which allows to distinguish relief features as small as 2-10 nm in height. However, the horizontal resolution is limited to about 0.5μm because the interference pattern is observed in an optical microscope and the method does not allow to obtain quantitative information about the sample.

The scanning electron microscope (SEM) can be used in back-scattered mode to collect quantitative data that are converted into concentration profiles. However, this technique has a number of limitations, such as the difficulty to resolve subtle zoning and the typical 256 gray scale of the digital equipment, which restrict its use for oscillatory zoning observations. The horizontal resolution of this technique is about 0.2-0.3 μm.

The electron microprobe (EMP) collects precise quantitative data through the spectral analysis of radiation emitted from the sample. The spatial resolution is usually limited by the size of the electron beam and the activation volume of the sample. In spite of this, it is possible to probe oscillatory zoning of major elements down to the ~10μm scale.

The laser interferometry technique is based on the fact that the refraction index may depend on the local chemical composition. A laser beam is split in two and then recombined after one of the resulting beams is transmitted through the sample. The interference picture allows to extract information about the variations of refraction index with a spatial resolution of 1-2μm. After refraction index measurements are calibrated to chemical composition by means of a microprobe analysis, a chemical resolution of 1-2 mol% may be achieved.

Other techniques that are used for the observations of the oscillatory zoning include transmission electron microscopy (TEM) [25], atomic force microscopy (AFM) [26], and X-ray reflection topography [27].

2.3 *Hypotheses for the formation of patterns in minerals*

Traditionally, pattern formation in minerals has been attributed to the effects of systematic large-scale changes in the environment. Changes in the temperature, the pressure, the pH, the influx of new components, and other large-scale processes may alter the composition of the growing crystals. Mineral zoning that results from such external changes can be regarded as their record and is termed *extrinsic*.

In recent years, it has been proposed that some cases of zoning may be due to self-organization. In far-from-equilibrium conditions, in nonlinear systems, patterns have been shown to arise spontaneously [2], without external template, due to complex nonlinear coupling between the variables controlling the system's dynamics. Such patterning, which results from the system's internal processes, is called *intrinsic*.

Physical mechanisms of intrinsic patterning may include autocatalytic reactions, instabilities in reaction-diffusion systems [28,29] or nonlinear coupling between, say, diffusive transport and the processes at the crystal-liquid interface.

For example, several self-organization models have been proposed to explain the oscillatory zoning in plagioclase. Sibley *et al* [30] presented a metallurgically-based qualitative model based on the constitutional undercooling mechanism. Composition of the melt near the growing crystal was proposed to be different from its bulk value due to slow diffusion transport. Therefore, the local chemical potential difference between the crystal and the melt (effective undercooling) is different from its bulk value for the same temperature. In the model, the isothermal growth, which is initiated when the system reaches a certain degree of undercooling, is considered to stop at equilibrium. As the diffusion of components from the bulk liquid through the boundary layer increases the constitutional undercooling, the growth does not start immediately but only after some time due to the nucleation barrier (see e.g. Section 3.1). The model predicted the commonly observed saw-tooth shape of the concentration profiles in the crytal but, as with all qualitative models, it could not be verified by comparing it to the experimental observations. Also, the model predicted strictly repetitive zoning, which is not commonly observed. Wang and Merino [31] proposed a dynamical model describing a diffusion-controlled growth of plagioclase crystals. In that model, limit cycle solutions were obtained for the crystal composition as a result of feedback between the crystal growth velocity and the species concentrations in the melt. Wang and Wu [32] considered another diffusion-controlled model in which the partition coefficient that relates the An concentration in the melt near the crystal surface to the concentration in the solid phase was shown to be a multi-valued function for a certain range of parameters. Oscillatory behavior was then obtained as the system switched between the two stable solution branches. L'Heureux and Fowler [33,34] have developed a simple model in which nonlinearities stemmed from the coupling between the melt composition and the growth rate and the boundary condition imposed by using a nonlinear partitioning at the interface, as reviewed in Sections 5.1.3 and 5.2.1. In that model, the system was shown to exhibit a Hopf bifurcation whereby the unique steady state loses its stability to a limit cycle thus generating oscillatory zoning. More models of plagioclase zoning can be found in section 5.1.3.

Since many observed composition profiles appear contaminated with noise, the effects of random changes in the environment have been investigated in several works. Jamtveit [13] suggested that external noise may be responsible for zoning in hydrothermal garnets as the system is stochastically kicked between two stable states. The physical nature of those states, however, was not specified. Holten *et al* [35] investigated the effects of large-amplitude noise on various plagioclase zoning models,

including the model of L'Heureux and Fowler [33]. They found that environmental fluctuations are reflected in the crystal zonation smoothed by the diffusion transport. Katsev and L'Heureux [36] found that external noise of small amplitude can qualitatively change the diffusive system's dynamics near the Hopf bifurcation point. In that work, coherence resonance was detected and the system exhibited oscillatory behavior in a regime where no oscillations existed in the absence of noise.

2.4 Overview of geological environments

This section gives a brief overview of the various geological environments in which patterned minerals are commonly found.

2.4.1 Hydrothermal ore deposits

Hydrothermal mineral deposits [37] are formed when a hot aqueous solution – a hydrothermal solution – flows through a channel in the crust, or over a restricted portion of the surface of the crust, and the minerals dissolved in the solution precipitate locally. The size of the deposits is typically much less than a cubic kilometer in volume, which is small compared with most geologic features. While hydrothermal fluids are widespread, hydrothermal deposits are relatively scarce. The interest in these deposits is high mainly due to the seemingly similar mechanisms of their formation and their importance in the mining industry.

From the analysis of fluid inclusions in the mineral deposits, it is known that hydrothermal solutions are saline. The solvent water typically comes from seawater, groundwater, metamorphic water, or magmatic water. In spite of this variety, studies of hydrogen and oxygen isotopes of the water lead to the conclusion that the actual source of water is not the main controlling factor in the formation of the hydrothermal mineral deposits.

The flow of hydrothermal fluids is due to eight major causes [37]: 1) a difference in hydrostatic pressure between the source and the outlet of an aquifier, 2) a build-up of lithostatic pressure in compacting rock which reduces the porosity and extrudes fluids upward, 3) osmotic pressures developing across natural membranes, such as shales, 4) convection due to density differences induced by local heat sources, 5) upward displacement of lighter fluids by very saline, heavier fluids, 6) fluid releases from cooling

magmas, 7) generation of liquid and gaseous hydrocarbons beneath an impervious shale cap in a sedimentary basin, and 8) release of solutions in dehydration reactions in metamorphic environments.

The typical major components of hydrothermal fluids are sodium, potassium, calcium, and chlorine. In ore-forming solutions, concentrations of these elements range from 20,000 to 150,000 ppm [38,39]. Other elements may also be present, such as magnesium, bromine, sulfur (as sulfate or sulfide), strontium, iron, zinc, carbon (as HCO_3^- and CO_2), and nitrogen (as NH_4^+). Concentrations of these elements are typically in the range from 200 to 3000 ppm.

Many ore minerals are sulfides, which have low solubilities in water. The solubilities required to transport the necessary amounts of metals to their place of deposition are achieved by the formation of complex ions that serve as carriers for metals and inhibit the precipitation of sulfide minerals. In sulfur-rich solutions, complex ions $Zn(HS)_3^-$ may be formed, which are capable of carrying large amounts of metal. However, the metal/sulfur ratio required for such complexing is rarely achieved in natural brines. Fluid inclusions studies [37] support the idea that the more common metal carriers are chlorine complexes such as $ZnCl_2$ and $CuCl_3^{2-}$. These complexes can form in chlorine-rich solutions and transport metals in the presence of a low concentration of dissolved sulfide ions. In order to be transported, the total number of metal atoms in the solution must exceed the number of reduced sulfur atoms (as distinct from oxidized sulfur atoms). Because of this requirement, when precipitation occurs, more reduced sulfur needs to be added to the solution in order to precipitate most of the metal in the solution. There is also evidence, that contribution from organic complexes may play an important role in hydrothermal ore-forming processes, especially below 250°C [40]. For example, there are hypotheses that zinc and lead may have been carried into the Mississippi Valley-type deposits by organic complexes rather than inorganic ones, which provide much lower solubilities (~0.1 ppm for each metal) [41].

Precipitation of minerals from hydrothermal solutions may be caused by several factors [37]. A decrease in temperature may reduce solubility and lead to precipitation when the solution reaches saturation. Temperature changes may affect the solubility products of sulfide and oxide minerals, the stability of the complex ions transporting the metals, or the hydrolysis constants of ligands, such as Cl^-, involved in the formation of complexes. In order to remove most of the material from the solution, a temperature drop of 20°C or more is usually needed. Such temperature decrease is relatively rare because

of the large amount of heat that needs to be dissipated. It may be achieved when a hot rising solution mixes with a cold water near the surface, when the pressure in rising fluid is adiabatically decreased, or when heat is dissipated to the wallrocks along the flow channel. Precipitation may also occur when changes in pressure alter the solubility. However, large pressure changes, of the order of 1000 bars, are needed to cause significant precipitation, which implies very deep fluid circulation. Pressure-controlled boiling may also lead to precipitation. Many hydrothermal deposits precipitate as a result of chemical reactions between the hydrothermal solution and the rocks in their flow channels [37]. Sulfide minerals are precipitated when the stability of chloride complexes is decreased by hydrogen ion-removing reactions, such as dissolution of carbonates or hydrolysis of feldspars. Another possible mechanism for sulfide minerals precipitation involves adding reduced sulfur species, such as H_2S, to the solution from wallrocks. Mixing of the hydrothermal fluids with solutions of different compositions (for example, with a H_2S-rich solution) can also bring about chemical changes and thus cause mineral precipitation.

Although the chemistry of the solutions and the processes that lead to the formation of hydrothermal mineral deposits are understood relatively well, certain important aspects of ore formation remain enigmatic. In particular, the geological time and duration of the mineralization events are largely unknown.

Ore minerals rarely contain sufficient concentrations of radioactive atoms to allow reliable determination of mineral ages by radiometric means. Dating of associated minerals in the hydrothermal alteration assemblage has revealed that, for the mineral deposits formed in association with a magmatic event, mineralization and magmatism are essentially coincident. In most other cases, however, the age of mineralization is uncertain. A recently applied Rb-Sr dating [42,43,44,45] of sphalerite holds great promise for dating nonmagmatic ores, especially Mississippi Valley-type deposits, although the validity of this method is still under investigation as it is complicated by inclusions of Rb- and Sr-bearing minerals in sphalerite [43].

While the time of mineralization may be determined by the above mentioned methods, the question of duration of a hydrothermal ore-forming process remains unanswered for practically all classes of deposits. The answer to this question has considerable practical importance as it would tell for how long lasted an ore-forming process leading to the formation of the few industrially important ore bodies. It was shown [46] that, given sufficient fluid flow, times of a few thousand years are sufficient

for the formation of most ores of magmatic-hydrothermal origin. In sediment-hosted deposits, such as MVT, determining the duration of mineralization remains a difficult question. It is further complicated by the possibility that mineralization events may have recurred many times over several millions of years [47]. Estimates based on measurements of thermally induced irreversible processes in organic matters associated with the ores and on fluid inclusion studies [48] suggested that the thermal event that formed the Shullsburg ores in the Upper Mississippi Valley district lasted about 300,000 years. However, the thermal alteration of organic materials is a progressive process and the duration of each mineralization episode could not be determined by that technique.

2.4.2 Igneous and metamorphic rocks

Igneous rocks are crystallized from a hot rock melt or magma. Crystallization of magma may be imposed by heat loss, a rise toward the surface with a small degree of adiabatic cooling (typically about 0.4°C/km), or an assimilation of materials which increase the crystallization temperature [49].

In magma crystallization, the effective undercooling inside the melt depends on the melt composition, which changes with time. Thus, the relationship between the undercooling and the temperature becomes complex. To obtain information about the evolution of the undercooling during magma cooling and crystallization, the growth rates are typically estimated based on the rock textures studies. The dynamics of the undercooling inside the bulk magma is then reconstructed using the experimentally established relationship between these approximate growth rates and the undercoolings [50].

By relating the crystallization rate data to cooling rate experiments in which the crystallization temperature interval (T_L- T_S) was known, typical volcanic cooling rates 100°C/hr were estimated to provide a minimum time-averaged growth rate for plagioclase 10^{-7} cm/s [50]. In general, typical natural plagioclase growth rates were estimated to be in the wide range 10^{-10} to 10^{-5} cm/s [50,51].

Metamorphic rocks are those that largely remain in the solid state while being changed by heat and/or pressure, with or without overall chemical change. Most metamorphic rocks crystallize under stress, which results in a characteristic foliation or parallelism of the constituent grains. Metamorphic rocks are commonly found in the proximity of heat sources, such as adjacent igneous intrusions (contact metamorphism),

or in the regions of higher pressure and shearing stress that are, for example, due to continental collisions (regional metamorphism).

2.4.3 Non-equilibrium conditions in geological systems

Self-organized pattern formation can only occur under non-equilibrium conditions, which means that the geological system must be undergoing some kind of change. These changes may be brought about by several general types of processes [52]. The system may be maintained out of equilibrium by externally imposed temperature gradients, pressure, or ongoing chemical reactions. Some of these processes may be considered, for example, in analogy with the stir-tank and batch chemical reactors [52].

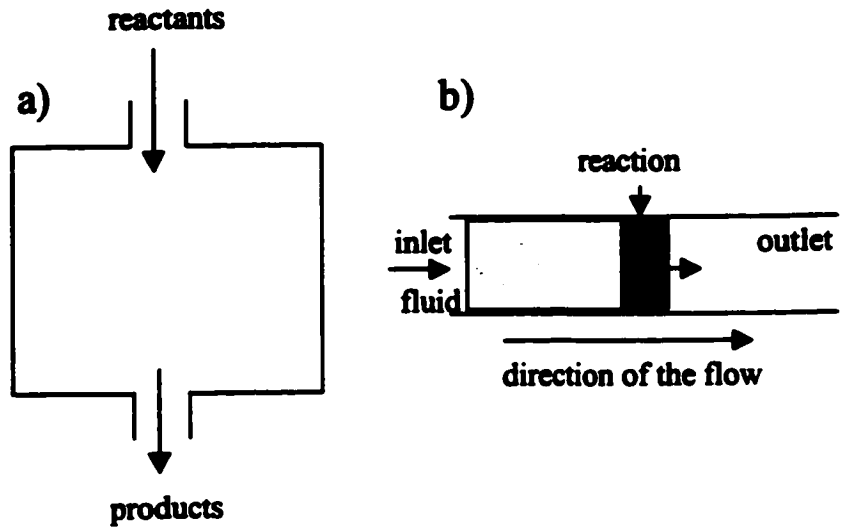

Fig. 6 Types of systems, in which non-equilibrium conditions can be produced and maintained. (a) Stir-tank reactor. **(b)** Flow-tank reactor.

In a "stir-tank" type of system (Fig.6a), reactants are introduced to a reaction chamber through an inlet and the products of reaction are removed from an outlet. The reaction chamber then can be maintained out of equilibrium. Water-rock reaction fronts may be regarded in analogy with a flow-tank reactor (Fig. 6b). An inlet fluid is constantly injected into an aquifer. If the fluid is out of equilibrium with one or more minerals in the aquifer, the reaction zone advances in the direction of the flow and is constantly maintained out of equilibrium. Consequently, self organized patterns may be expected to form in such fluid-rock interaction systems.

Alternatively, in a "batch reactor" type of system, reactants are thrust into the reaction chamber. This type of situation occurs when magma is injected into country rock

or into the ocean or above land. Non-equilibrium conditions exist when minerals are formed while the magma adjusts to the new temperature and pressure. In general, changing temperature and pressure lead to energy flows and ensure out-of-equilibrium conditions. For example, self-organized processes may occur during subsidence and upheaval in sedimentary and metamorphic rocks.

Rocks may also be maintained out of equilibrium by mechanical stresses or temperature gradients. The free energy of a mineral grain increases with the applied stress. Since this dependence on stress is different for different minerals in the system, the free energy may be lowered by the mineral grain segregation. Also, thermal gradients can create gradients of reaction affinity and therefore induce reaction and transport processes.

In magma chambers, far-from-equilibrium conditions can arise as a result of magma mixing, releases of gases, changes in pressure and/or temperature in magma prior to eruption, and eruption events themselves. The time during which these far-from-equilibrium conditions exist and the degree of effective undercooling are largely unknown and very little information is currently available on this subject [53,54].

2.5 *Geological implications of mineral patterning*

Oscillatory and banded patterns in minerals have been traditionally viewed as records of the mineral formation history. The distribution of both major and trace elements in the patterned crystals is believed to contain information about different aspects of growth. The incentive is therefore to read the zoning record similar to the way one would read tree rings to reconstruct the evolution of the geological system. Although zoning in minerals may not necessarily reflect some kind of periodic changes in the environment, it is believed to be closely connected to or controlled by the external conditions. Thus, understanding the mechanisms of the pattern formation in minerals should yield information about the evolution of their environments and the conditions of their genesis [55]. Such information would help to solve geological problems arising in petroleum and mineral exploration, in the studies of the magma chamber dynamics and the processes leading to volcanic eruptions [7].

Growth of crystals from magma is one of the fundamental processes of geology. Many authors have studied compositional zoning in volcanic rocks to obtain information about the processes taking place inside the magma chambers. For example, changes in

the oscillatory zoning regimes were interpreted as corresponding to various stages of the magma chamber evolution, such as slow cooling, magma mixing, and melting [53].

Correlations in Fe and Mn trace element zoning in calcite over large distances lead to carbonate cement stratigraphy used by the petroleum industry for chronostratigraphic purposes. The interest in understanding the zoning mechanism comes from the fact that calcite zoning has been related to changes in the redox conditions at the scale of the calcite-forming fluid reservoir during rock cementation.

Similar large-scale correlations (over the distances of many 10's of km) were interpreted to occur in banding of MVT sphalerites in the Tri-state mining area (Missouri, Arkansas, and Tennessee). Such correlations were thought to reflect basin-scale changes in the hydrothermal fluids chemistry and therefore to be important in the genesis of the Zn-Pb ore deposits [56]. However, the hypothesis of the self-organized origin of the sphalerite banding pattern suggests that banding may also be caused by local processes on the scale of centimeters, and therefore some of the large-scale correlations may be accidental.

Chapter 3

Crystal growth mechanisms

In the vast majority of cases, compositional patterns are believed to form during the process of solid mineral growth from a liquid phase. In the framework of self-organization models, patterns result from the complex interplay of a number of processes taking place during crystal growth. This chapter describes the microscopic processes that lead to the formation of the solid crystalline phase and define its subsequent evolution. Since the crystals in naturally formed minerals grow predominantly from the liquid phase in the form of aqueous solution or melt, only those two growth environments will be considered. Similar results may be obtained for the formation of crystals from vapor, although this case is of minor significance in natural environments.

The formation of a crystal proceeds through two main stages: nucleation and growth [57]. Nucleation involves the formation of an atomic cluster large enough to be thermodynamically stable while crystal growth involves further enlargement of this cluster. The subsequent evolution of the ensemble of the resulting crystallites often involves ripening whereby large crystallites grow at the expense of the smaller ones. The transformations in the solid phase, such as solid diffusion, recrystallization, aging, or spinodal decomposition, will be ignored here. While possibly important for the subsequent preservation of the patterns, these phenomena are believed to be insignificant for the self-organized pattern formation processes in the natural minerals considered in this work, mainly because of the much larger time scales associated with the transformations in the solid mineral.

3.1 Nucleation

The nucleation phase involves the formation of clusters of atoms in a supersaturated solution or undercooled melt. As a necessary condition for the formation of such clusters to be thermodynamically favored, the bulk contribution, ΔG_r, to the

molecular Gibbs free energy change needed to attach one atom to an existing molecular cluster should be negative. In the case of crystallization from a melt,

$$\Delta G_r = -\Delta s_m \Delta T = \Delta h_m \Delta T / T_m = -\Delta\mu, \qquad (1)$$

where Δs_m is the molecular entropy of melting, Δh_m is the molecular enthalpy of melting, T_m is the melting temperature, $\Delta T = T_m - T$ is the undercooling, and $\Delta\mu$ is the chemical potential difference (per molecule) between the crystal and the melt. For crystallization from an aqueous media,

$$\Delta G_r = -kT \ln\Omega = -\Delta\mu, \qquad (2)$$

where k is the Boltzman constant and Ω is the supersaturation ratio, which is usually defined as

$$\Omega = \frac{\prod_j a_j}{K_{eq}}, \qquad (3)$$

where a_j are the activities of the various species in the solution and $K_{eq} = \Pi\, a_j^{eq}$ is the solubility product. In the case of a single element dissolved in an ideal solution, eq. (3) reduces to the simple ratio of the solute concentration in the solution to its equilibrium concentration.

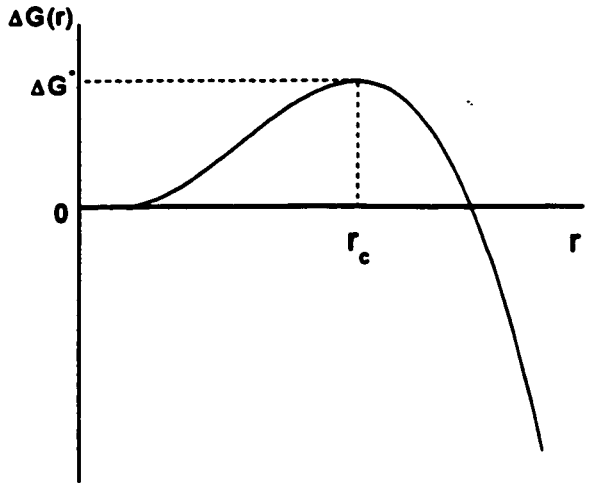

Fig. 7 Free energy change in the formation of a spherical cluster of radius r. The curve exhibits a maximum at some critical value r_c. For $r < r_c$, the cluster is unstable and will dissolve while for $r > r_c$ the cluster is thermodynamically favored to grow.

The shape of the emerging clusters is often assumed spherical. This approximation is usually taken because of a lack of detailed information about the geometry of the cluster [58]. To form a cluster, work must be done against the surface tension. Then the total free energy change for the formation of a spherical cluster of radius r containing n atoms or molecules is

$$\Delta G_n = n\Delta G_r + 4\pi r^2 \sigma, \tag{4}$$

where σ is the surface tension, which, in general, depends on the cluster size but is considered here as a constant. By setting $4/3\pi r^3 = nv_c$, where v_c is the volume of a molecular unit in the solid phase, it is easy to see that, for small clusters, the free energy increases with r because the surface energy term dominates while for large clusters the first negative term is more important (Fig. 7). The free energy curve thus exhibits a maximum at ΔG^* at a critical value r_c. Below this value, clusters are too small to be stable while clusters with $r > r_c$ are stable and their growth is thermodynamically favored. By finding the maximum of the curve $\Delta G(r)$, the critical nucleus size n_c , the critical radius, and the critical energy for spherical clusters are easily derived:

$$n_c = \frac{32\pi v_c^2 \sigma^3}{-3\Delta G_r^3} \tag{5}$$

$$r_c = \frac{2v_c\sigma}{-\Delta G_r} \tag{6}$$

$$\Delta G^* = \frac{16\pi\sigma^3 v_c^2}{3\Delta G_r^2}, \tag{7}$$

The critical size of a cluster drops quickly as the supersaturation (undercooling) increases so, in far-from-equilibrium conditions, nuclei consist of a very small number of atoms. Because of the discrete nature of the molecular building units that make up the cluster, the same critical nucleus size may be appropriate for a range of supersaturations. For small nuclei, the expressions above must be considered as only an approximation because the surface energy depends strongly on the shape of the cluster, which, in that case, constantly changes in time. Calculating nucleation rates for such clusters requires special considerations [59].

Homogeneous nucleation

Homogeneous nucleation occurs in the bulk of a solution or a melt. This type of nucleation usually dominates at high supersaturations (undercoolings) or in the absence of pre-existing crystallization centers such as impurities.

In the case of solidification from melts, the energy barrier ΔU (of the order of few kcal/mol) associated with viscous transport must be overcome in order to attach a molecular unit to the cluster. The steady state nucleation rate (a number of stable clusters formed per unit volume per unit time) is proportional to the total flux of molecular units towards the critical nucleus. It is therefore proportional to the surface area of the cluster and the frequency of the molecular unit attachment events. The frequency of the elementary attachment acts is proportional to the concentration of units near the surface of the cluster. Since the nucleation rate is proportional to the number of clusters in the melt, which is, in turn, also proportional to the molecular units concentration, the nucleation rate becomes proportional to the square of the concentration (expressed as a number of molecules per unit volume). In melts, this concentration can be taken as the inverse of the molecular volume in the melt v_1. Since the probability of a fluctuation large enough to create a cluster with more than n_c atoms is proportional to $\exp(-\Delta G^* / kT)$, and likewise for the probability of overcoming the viscous flow barrier ΔU, the steady state rate of nucleation can be written [57] as

$$J_{melt} = 4\pi r_c^2 \frac{f\lambda}{v_1^2} \exp\left(-\frac{\Delta U}{kT}\right) \Gamma \exp\left(-\frac{\Delta G^*}{kT}\right), \tag{8}$$

where f is a frequency factor, λ is the mean free path of particles in the liquid (of the order of the atomic diameter), and the dimensionless factor Γ is the so-called Zeldovich correction factor, which characterizes the width of the region around r_c (Fig. 7) for which the free energy change ΔG is within the interval kT of the critical value ΔG^*. The processes taking place in this region are most important in determining the overall rate of nucleation. Assuming spherical symmetry and isotropic interfacial tension [57],

$$\Gamma = \frac{(\Delta h_m \Delta T)^2}{8\pi v_c (\sigma^3 kT)^{1/2} T_m^2}, \tag{9}$$

and the critical values of ΔG and r are obtained from eqs. (1), (6), and (7) as

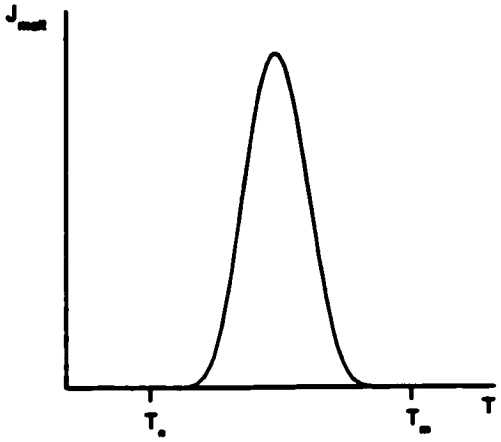

Fig. 8 Nucleation rate from melt J_{melt} as a function of temperature. As the temperature decreases, nucleation does not start immediately below the melting temperature T_m, which corresponds to a finite nucleation barrier. The curve exhibits a maximum as, at low temperatures, the viscosity of the melt prevents nucleation. Below the glass transition temperature T_g, the melt glassifies before nucleation takes place.

$$r_c = \frac{2\sigma v_c T_m}{\Delta h_m \Delta T}, \tag{10}$$

$$\Delta G^* = \frac{16\pi\sigma^3 v_c^2 T_m^2}{3\Delta h_m^2 (\Delta T)^2}. \tag{11}$$

As seen from eq. (8), the rate of nucleation from a melt depends not only on the undercooling ΔT but also on the absolute value of the temperature. Hence its temperature dependence exhibits a maximum (Fig. 8) as the temperature decreases from the melting point but, at low temperatures, the increased viscosity $\eta \sim \exp(\Delta U/kT)$ inhibits the transport processes in the melt and prevents nucleation. Below the glass transition temperature T_g, the melt solidifies into an amorphous glass before orderly crystallization can takes place.

In the case of the nucleation from **solutions**, a desolvation energy barrier ΔU must be overcome in order to attach a molecule to the nucleus. The value of this energy barrier (~20 kcal/mol) is greater than ΔU for melts. The steady state rate of nucleation from a solution [60] is given by

$$J_{eq} = 4\pi r_c^2 C^2 f\lambda \exp\left(-\frac{\Delta U}{kT}\right)\Gamma \exp\left(-\frac{\Delta G^*}{kT}\right) \tag{12}$$

where C is the solute concentration in the solution in number of molecules per unit volume, which plays the role of $1/v_1^2$ in eq. (8), and

$$\Gamma = \left(\frac{\Delta G^*}{3\pi k T n_c^2} \right)^{1/2} . \qquad (13)$$

From Eqs. (2), (7) and (12), it is easy to see that the steady state nucleation rate in a solution is proportional to $\exp(-(\ln \Omega)^{-2})$, which results in its sensitive dependence on the degree of supersaturation (Fig. 9). The nucleation does not start until some critical supersaturation Ω_c is reached, after which the nucleation rate increases sharply. The negligible rate of the homogeneous nucleation at small supersaturations facilitates alternative nucleation mechanisms. For example, in the experiments for $BaSO_4$ nucleation

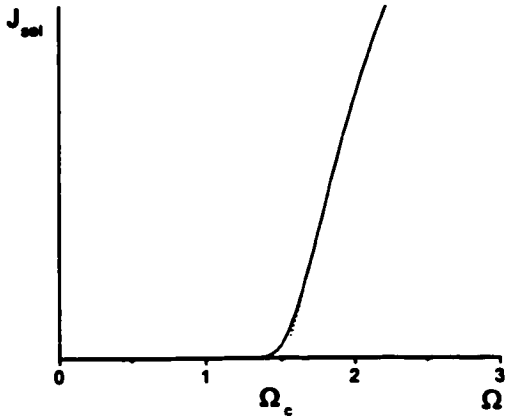

Fig. 9 Nucleation rate from solution J_{sol} as a function of supersaturation. A critical value of the supersaturation Ω_c needs to be achieved in order for the nucleation to start. For $\Omega > \Omega_c$, the nucleation typically proceeds at a very fast rate.

at room temperature, a switch from homogeneous to heterogeneous nucleation was observed as the concentration of the salt in the solution dropped below $0.01M$ [61].

Heterogeneous nucleation

Nucleation of a new phase on the surface of an existing solid phase is called heterogeneous nucleation. At low enough supersaturation (undercooling), and in a system containing impurities and inhomogeneities, nucleation first occurs on these defects and proceeds at a much faster rate than homogeneous nucleation.

When nucleation takes place on a pre-existing solid surface, the free energy change ΔG depends on the configuration of the particular nucleation site, e.g. it depends on whether the nucleus is being formed on a plane surface or in a crack, as well as on the wetting properties between the substrate and the nucleating phase. For the simple case of a cluster of phase β in a shape of spherical segment nucleating from phase α on a flat substrate surface, the critical free energy change is calculated as [58]

$$\Delta G^* = \frac{4\pi}{3}\frac{(\sigma^{\alpha\beta})^3 v^2 (2-3\cos\theta+\cos^3\theta)}{\Delta G_r^2}. \qquad (14)$$

Here, $\sigma^{\alpha\beta}$ is the surface tension between the phases α and β and θ is the wetting angle. By comparing Eqs. (7) and (14), it is seen that for any $\theta < 180°$ heterogeneous nucleation is energetically more favorable than the homogeneous one. In the case of complete wetting ($\theta = 0$) there is no energy barrier to nucleation. An expression for the steady state heterogeneous nucleation rate is easily obtained by substituting eq. (14) into eq. (12) or (8) and replacing the surface area of the critical nucleus $4\pi r_c^2$ by the area of the segment $4\pi r_c^2(1-\cos\theta)$.

A more typical case is the formation of a flat 2D 'island' on the planar surface of a substrate. If the nucleus is assumed to have the shape of a "pancake" with radius r, then the critical free energy change and critical radius are calculated [57] as

$$\Delta G^* = \frac{\pi\chi^2 A}{-\Delta G_r}, \qquad (15)$$

$$r_c = \frac{\chi A}{-\Delta G_r}, \qquad (16)$$

where χ is the specific energy of the edge of the "pancake" and A is the area that each molecular unit occupies on the surface. Then the rate of the 2D-nucleation from a solution may be written [57] as

$$J_{eq} = fCv_1\left(\frac{\Delta\mu}{kT}\right)^{1/2}\exp\left(-\frac{\Delta U}{kT}\right)N_0\exp\left(-\frac{\pi\chi^2 A}{kT\Delta\mu}\right). \qquad (17)$$

Here N_0 is the density of the adsorption sites at the surface of the solid phase (in number of sites per unit area). Similarly, for the case of nucleation from a melt,

$$J_{melt} = f\left(\frac{\Delta\mu}{kT}\right)^{1/2}\exp\left(-\frac{\Delta s_m}{k}\right)\exp\left(-\frac{\Delta U}{kT}\right)N_0\exp\left(-\frac{\pi\chi^2 A}{kT\Delta\mu}\right), \qquad (18)$$

where the term $\exp(-\Delta s_{\infty}/k)$ comes from the consideration of the total flux of molecular units to the surface of the nucleus, which is calculated as the difference between the incoming and the outgoing molecular unit fluxes.

3.2 *Growth and Dissolution*

After a nucleus larger than the critical size is formed, its further growth requires a sequence of processes that involve diffusive transport of molecular units through the bulk liquid to the crystal, attachment of those units to the crystal surface, their diffusion along the surface, and their attachment to the places with higher bond energy, such as the edges of molecular layers or kink sites. The rates of crystal growth and dissolution are determined by the interplay of the diffusive transport processes in the bulk media and the processes at the solid/liquid interface, the overall growth (dissolution) rate being defined by the slowest of these processes.

When crystal growth is controlled by diffusion, it usually leads to the formation of spherical structures with no clear distinction between crystal orientations [58]. On the contrary, interface-controlled growth typically results in anisotropic crystals [62]. It usually occurs when concentration gradients around the growing crystal are small over the typical crystal interface length scales. However, pure diffusion or interface-controlled processes are the extreme cases and it is often hard to specify the dominating growth-controlling mechanism. Also, as the temperature rises, the rates of surface reactions increase much faster than those of diffusion [58] so the same mineral may grow by different mechanisms as the conditions change.

Since both diffusion and surface processes act at the same time and are interdependent, after some very small transition period the actual rates of both processes become equal. However, if the process is surface-controlled, the aqueous concentration near the crystal surface is close to its bulk value while for the diffusion-controlled processes the liquid near the interface is in equilibrium with the crystal and its concentration near the interface is different from the bulk concentration.

3.2.1 Surface-controlled growth

The mechanism of crystal growth is largely defined by the morphology of the crystal surface. Therefore, knowing the surface structure is crucial in determining the crystal growth rate. Rough crystal faces offer an abundance of kink sites and grow by the 'normal' growth mechanism whereby continuously arriving building units attach

themselves at many available sites at the interface and the overall direction of growth is normal to the surface. Normal growth mechanism is typical for crystals growing at fast rates under high supersaturations. Atomically smooth surfaces grow orderly, by sequential spreading of atomic layers (surface nucleation and lateral layer spreading mechanism). The nucleation of the one-layer-thick 2D-nuclei leads to creation of the atomic steps at the crystal surface and the crystal increases its size due to tangential propagation of these steps, layer by layer. Finally, spiral growth occurs at the sites where screw dislocations emerge at the crystal surface, as the dislocations offer non-vanishing sources of atomic steps at which the attachment of molecular units occurs.

As the supersaturation (undercooling) increases, a roughening transition occurs when the surface structure changes from atomically smooth to rough. This transition causes a corresponding switch in the growth mechanisms.

Normal growth

Rough crystal surfaces offer an abundance of kink sites and can grow by **normal** mechanism at any supersaturation. To attach a unit to the crystal, a dissolvation or viscous transport energy barrier ΔU has to be overcome. The crystal growth rate can be obtained as a difference between the rate of attachment of the molecular units to the crystal surface and the rate of their detachment. In the case of growth from **melts**, the growth rate (length per time) can be expressed [57] as

$$R_{melt} = af\left(\frac{a}{\delta}\right)^2 \exp\left(-\frac{\Delta s_m}{k}\right)\exp\left(-\frac{\Delta U}{kT}\right)\left[1-\exp\left(-\frac{\Delta \mu}{kT}\right)\right] \qquad (19)$$

where f is frequency of thermal vibrations of the atoms at the interface (considered the same in crystal and melt), a is the size of the building unit, and δ is the distance between suitable attachment sites. The term $(a/\delta)^2$ characterizes the geometric probability of finding a suitable kink site and the term $\exp(-\Delta s_m/k)$ characterizes the probability for a liquid atom to form an appropriate activation complex with an attachment site. At small undercoolings $\Delta\mu = \Delta s_m \Delta T << kT$, eq. (19) reduces to the form

$$R_{melt} = \beta_m \Delta T, \qquad (20)$$

$$\beta_m = af\left(\frac{a}{\delta}\right)^2\left(\frac{\Delta s_m}{kT}\right)\exp\left(-\frac{\Delta s_m}{k}\right)\exp\left(-\frac{\Delta U}{kT}\right), \qquad (21)$$

where β_m is a temperature-dependent quantity called the kinetic coefficient for crystallization in melts. The approximate linear dependence of growth rate on undercooling is a consequence of the statistical independence of the individual attachment acts and is characteristic of normal growth. While Eq. (19) describes the growth of large flat crystal faces, an approximation [57]

$$R_{melt}(r) = R_{melt}(1-r_c/r) \tag{22}$$

is often used to describe growth of small rounded crystallites. Here, r_c is the critical nucleus size, r is the crystallite radius, and R_{melt} is given by Eq. (19).

The dependence of growth rate from **solutions** on $\Delta\mu$ for systems with only one element dissolved in the solution is of the form [58,63]

$$R \sim (1-e^{-|\Delta\mu|/kT}) \tag{23}$$

The case of dissolution is described by $\Delta G > 0$. From eqs. (2) and (3) one obtains

$$C_{eq} - C = C_{eq}(1 - e^{\Delta\mu/kT}) \tag{24}$$

(with $\Delta\mu < 0$) so the growth rate (23) is a linear function of the concentration difference ($C_{eq} - C$). Similarly to eq. (20), the rate of normal growth from a solution is thus given by [59]

$$R = \beta_s v_c(C - C_{eq}), \tag{25}$$

where v_c is the volume of the building unit in the crystal phase, C is the concentration (in molecules per volume) at the interface, and the kinetic coefficient β_s is given by

$$\beta_s = \frac{af}{C_{eq}v_c}\left(\frac{a}{\delta}\right)^2 \exp\left(-\frac{\Delta h_d}{kT}\right)\exp\left(-\frac{\Delta U}{kT}\right), \tag{26}$$

where Δh_d is the molecular enthalpy of dissolution. From (24) it follows that near equilibrium, i.e. for small $\Delta\mu$, the concentration at the crystal-liquid interface and, consequently, the growth rate vary linearly with $\Delta\mu$.

Surface nucleation growth

Consider a surface nucleation growth mechanism for which two-dimensional nuclei are created on a flat crystal surface and then grow laterally until they cover the surface completely (Fig.10). The macroscopic crystal growth rate depends on the nucleation rate and on the speed v_{step} of lateral propagation of new layers along the crystal

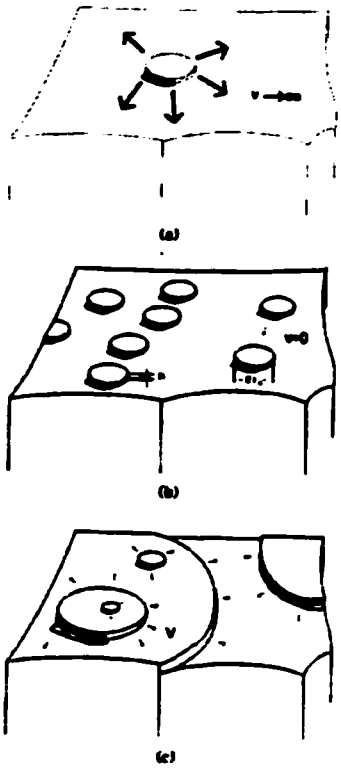

Fig. 10 Surface nucleation growth mechanisms (the figure is reproduced from [58]). a) A nucleus, which appears on a flat crystal surface grows fast to completely cover the entire crystal face. b) The speed of growth is very slow and the crystal grows by nucleation only. c) 2D clusters nucleate on several existing molecular layers and grow laterally.

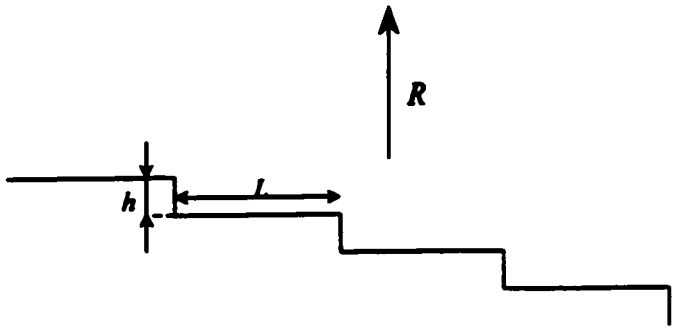

Fig. 11 Growth by lateral spreading of atomic steps. The surface grows with the rate R by lateral advancing of the steps. L denotes the average distance between the steps and h is the step height.

surface. If the surface is formed by a set of steps propagating with the speed v_{step} then the rate of the surface advance in the normal direction is

$$R = hv_{step}/L, \tag{27}$$

where h is the step height and L is the spacing between steps (Fig.11). A simple mononuclear model (Fig.10a), which assumes a fast growth of nuclei so that each new 2D-nucleus immediately grows to cover the entire crystal face, gives the growth rate

$$R = JhA, \tag{28}$$

where J is the nucleation rate given, for example, by eqs. (17) and (18) and A is the area of the crystal face. The opposite case of a very slow lateral growth is considered in a model where each layer is formed as a result of the nucleation of many nuclei (Fig.10b). The growth rate is then given by

$$R = J\pi r_c^2 h, \tag{29}$$

where r_c is the radius of the critical 2D nucleus. In the more complex birth and spread model (Fig.10c) (also called multilayer or polynuclear), which considers both simultaneous nucleation of 2D nuclei and their growth at large supersaturations, the growth rate is predicted to be [59]

$$R = h J^{1/3} v^{2/3}_{step}. \tag{30}$$

To estimate v_{step}, additional approximations are taken. Impurities can significantly affect the growth rate by altering the speed of step propagation. Typically, impurities break the steps thus inhibiting growth or dissolution. However, in some cases, they were found to catalyze these processes as the impurity atoms adsorbed at the surface may decrease the nucleation energy ΔG^*.

Surface nucleation growth mechanism is common for growth from solutions [59]. In spite of convective fluxes in liquids, there exists a relatively undisturbed boundary layer of width δ near the crystal surface through which components are transported by diffusion. Propagating steps serve as linear sinks for the diffusion field in the boundary layer. By calculating the diffusive flux toward the steps, the step propagation speed is obtained [59,64] as

$$v_{step} = \beta_{st} v_c (C - C_{eq}) = \frac{\beta_{st} v_c (C^{\infty} - C^{\infty}_{eq})}{1 + \frac{\beta_{st} h}{\pi D} \log\left(\frac{L}{h}\right) \sinh\frac{\pi\delta}{L}}, \tag{31}$$

where C^{∞} and C_{eq}^{∞} are the concentration and the equilibrium concentration in the bulk liquid, D is the diffusion coefficient, and β_{st} is the step kinetic coefficient, which has a form similar to eq. (26). As seen from eq. (31), v_{step} decreases with the distance between the steps. By substituting (31) into (27), the growth rate is obtained in the form

$$R = b(p)v_c(C^{\infty} - C_{eq}^{\infty}), \tag{32}$$

where the kinetic coefficient $b(p)$ depends on the orientation of the crystal face described by the parameter $p = h/L$, i.e. the growth is anisotropic (Fig. 12). For small p, $b(p) = \beta_{st}|p|$.

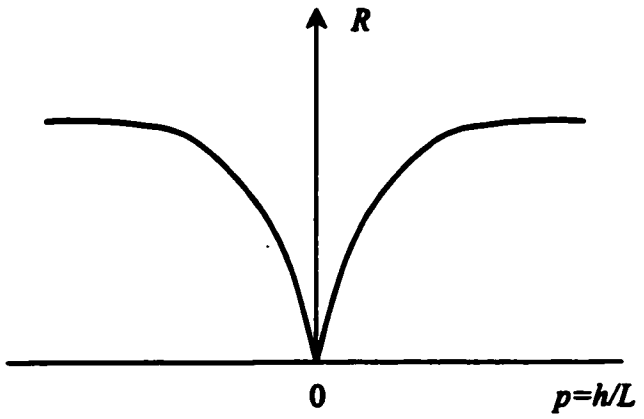

Fig. 12 Dependence of the growth rate on the crystal face orientation p

In melts, the propagation of steps is limited by the rate at which heat is transferred away from the steps. The step propagation speed is

$$v_{step} = \beta_{st}^{T}(T_{eq} - T). \tag{33}$$

Since thermal conductivity is typically much faster than diffusion (by about three orders of magnitude), the growth rate in melts is much faster than the growth rate in solutions for the same value of the thermodynamic driving force $\Delta\mu/kT$.

Spiral growth

The growth of crystals facilitated by screw dislocations is best described by the Burton-Cabrera-Frank (BCF) theory [65]. It is predicted and often observed to be the dominant growth mechanism near equilibrium, as screw dislocations offer a non-vanishing source of kink sites. The growth rate is derived through the speed of spiral step

propagation as $R = v_{step}h / L$, where L is the spacing between the steps. v_{step} is determined by surface diffusion and the rate law is found to be of the form

$$R_{BCF} = \frac{A}{T}\Delta\mu^2 \tanh\left(\frac{B}{\Delta\mu}\right), \tag{34}$$

where A and B are constants. For small $\Delta\mu$, i.e. near equilibrium, eq. (34) predicts a quadratic dependence of growth rate on $\Delta\mu$. In solutions, as it follows from eq. (24), the growth rate is therefore a quadratic function of the concentration difference (C-C_{eq}). Far from equilibrium, when $\Delta\mu$ is large, the rate law (34) becomes linear in concentrations.

3.2.2 Diffusion-controlled growth

When the growth is controlled by diffusion in the bulk liquid, its rate is determined by the influx of building units from the liquid, which, in turn, is defined by the concentration near the interface. The concentration evolution is described by the diffusion equation

$$\frac{\partial C}{\partial t} = D\nabla^2 C \tag{35}$$

with appropriate boundary conditions. Far away from the crystal,

$$C(l\to\infty) = C_\infty, \tag{36}$$

where l denotes the distance from the center of the crystal. At the interface ($l = r$), the mass conservation principle leads to

$$D(\vec{\nabla}C)\cdot\vec{n} = (\rho_c - C)V(\vec{n},\Delta\mu), \tag{37}$$

where ρ_c is the molecular density in the crystal (in number of particles per unit volume), V is the speed of the interface movement due to growth, and the normal vector $\vec{n}$ describes the orientation of the interface. To complete the description of the diffusive process, an initial condition at t=0 is also required.

In most cases, when the crystal continuously grows or dissolves, a diffusion steady state is never reached and the growth rate varies with time (e.g. as $\sqrt{t}$, see later). Nevertheless, finding a steady state solution by setting the left hand side of eq. (35) equal to zero proved to be useful in deriving the growth rate laws, which depend on the crystal geometry and the boundary conditions.

For a spherical crystal of radius r, the characteristic time for a change in the concentration field is r/V. The time scale of diffusion is r^2/D. So, if $V<<D/r$, then the diffusion field adjusts itself quickly to the changes imposed by the growing crystal and eq. (35) can be reduced to the Laplace equation $\nabla^2 C=0$. The smaller the crystal, the less restrictive is this condition on V.

For a spherical crystal growing from a solution where $v_c C<<1$ with the growth rate given by (25), the steady state concentration profile in the solution, which satisfies the boundary conditions (36) and (37), and the steady state growth rate are given [59] by

$$C(l) = C_\infty - (C_\infty - C_{eq})\frac{\beta_s r/D}{1+\beta_s r/D}\frac{r}{l} \tag{38}$$

$$V = \frac{v_c \beta_s (C_\infty - C_{eq})}{1+\beta_s r/D}, \tag{39}$$

where β_s is the kinetic coefficient. It follows that for $\beta_s r/D<<1$, the concentration at the interface is close to the bulk concentration and the growth rate is defined by the kinetics of the processes at the crystal surface (kinetic regime). It does not depend on the crystal size, which itself grows linearly with time as $r \approx \beta_s v_c (C_\infty - C_{eq})t$. When $\beta_s r/D>>1$, the concentration in the solution is given by $C \approx C_\infty - (C_\infty - C_{eq})r/l$ and the growth rate is $V \approx Dv_c(C_\infty - C_{eq})/r$. Integration of the last expression gives a parabolic dependence of crystal size on time $r \approx \sqrt{2Dv_c(C_\infty - C_{eq})t}$, which does not depend on the processes at the crystal surface (diffusive regime).

In melts, the growth rate is most frequently limited by thermal diffusion, i.e. the rate at which heat is carried away from the interface. The kinetic and conduction regimes can be defined for this case similarly to the kinetic and diffusive regimes in the case of growth limited by chemical diffusion. The balance of heat fluxes at the interface can be written as

$$a_c(\vec{\nabla}T_c)\cdot(-\vec{n}) - a_m(\vec{\nabla}T_{melt})\cdot\vec{n} = T_Q V,$$

where a_c and a_m are thermal diffusivities (cm^2/s) in the crystal and the melt, respectively, and $T_Q=\Delta H/\lambda$, where ΔH is the heat of melting and λ is the heat capacity. If the undercooling in the bulk melt with respect to the melting temperature T_m is $T_m - T_\infty > T_Q$ then crystallization is possible even in the absence of thermal diffusion. If $T_m - T_\infty < T_Q$ then the undercooling at the crystal surface drops to zero following a thermal diffusion law as $t^{-1/2}$ and so does the growth rate $V \sim t^{-1/2}$. In analogy to Eqs. (38) and (39),

$$T_m - T_{iface} \approx \frac{T_m - T_\infty}{1-(\beta^T T_Q r / a_m)}$$

$$V = \beta^T (T_m - T_{iface}) \approx \frac{\beta^T (T_m - T_\infty)}{1-(\beta^T T_Q r / a_m)},$$

where T_{iface} is the temperature at the interface and β^T is the kinetic coefficient. The parameter $\beta^T T_Q r/a_m$ defines the kinetic (<<1) and conduction (>>1) regimes. For large crystals, the growth rate is controlled by the thermal conductivity while the surface processes are important for small, typically sub-micron, crystallites. Similarly to the growth from solutions, the crystal size increases linearly with time in the kinetic regime $r \approx \beta^T (T_m - T_\infty) t$ and follows a parabolic law in the conduction regime $r \approx \sqrt{2a_m (T_m - T_\infty) t / T_Q}$.

3.2.3 Dissolution

As in the case of the crystal growth, the main processes governing crystal dissolution are the interface reaction and the diffusion. In some cases, these processes may be complicated by some others, such as convection or uphill diffusion in electrolytes whereby ions diffuse against their concentration gradients to maintain the overall electrostatic neutrality in the solution.

For small undersaturations, dissolution can be considered as negative growth. The same considerations that were mentioned for the crystal growth apply also for the dissolution: detachment of units from the crystal surface, their transport into the bulk liquid, etc. Expressions for the surface-controlled dissolution rate may be obtained from the corresponding growth rate expressions by taking $\Delta\mu < 0$. Near equilibrium, the dissolution rate increases linearly with the undersaturation (overheating). However, as the undersaturation $|\Delta\mu|$ becomes large, the dissolution rate approaches a limiting value and exhibits a so called dissolution plateau (Fig. 13). A trivial example of this effect is given by the fact that the dissolution rate for a crystal in a water-based solution cannot exceed the value for a crystal placed in distilled water.

For aqueous solutions, it is often assumed [66] that minerals with low solubilities dissolve by surface control mechanisms while dissolution of those with high solubilities is controlled by diffusion. For example, $BaSO_4$ (solubility $1 \cdot 10^{-5}$ mole/l) and $SrSO_4$ (solubility $90 \cdot 10^{-5}$ mole/l) both dissolve by surface-controlled mechanism [66]. The actual dissolution rate is determined by the slowest of the diffusion transport processes

and the surface processes. Thus, the surface morphology, which determines the surface dissolution rate, defines only the upper limit for the total dissolution rate.

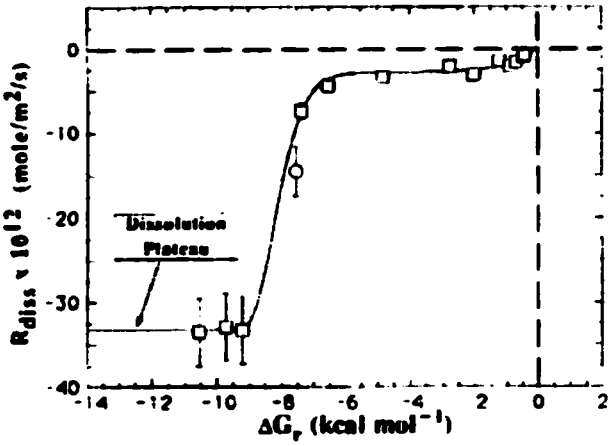

Fig. 13 Dissolution plateau. The dissolution rate exhibits a plateau for large undersaturations. The example shown is the albite dissolution rate as a function of undersaturation (from [67]). The temperature is 80°C and pH 8.8.

In melts, due to their viscosity, crystal dissolution is usually diffusion-controlled [68]. In presence of convection, dissolution is controlled by diffusion through the boundary layer. Crystal dissolution experiments in which convection is suppressed indicate that the dissolution rate is inversely proportional to the square root of time. The propagation of the concentration profiles into the melt is directly proportional to the square root of time.

3.3 Ripening

Ripening involves the gradual increase of the average crystal size in the system due to the recrystallization processes in which solid material is transferred from smaller crystallites to the larger ones. Coalescence of crystallites is energetically favored as it decreases the area term in Eq. (4) for the same amount of solid material n. When two crystals are placed near each other in the solution, the concentrations of solutes near the surfaces of the crystals are different because of the Gibbs free energy dependence on the surface curvature. Concentration in the solution in equilibrium with a curved surface of crystallite of radius r is given by the Gibbs-Thomson relation:

$$C(r) = C^{\infty} \exp\left(\frac{2\sigma v_c}{kTr}\right), \tag{40}$$

where C^{∞} is the equilibrium concentration for a flat surface. Equilibrium aqueous concentration close to smaller crystals is higher than near larger crystals. A concentration gradient directed from the smaller crystallites to the larger ones then appears, which promotes the flux of solute away from the smaller crystals. This flux causes precipitation of the solute at the surface of the larger crystals and dissolution of the smaller ones. Thus, the larger crystals grow while the smaller ones dissolve.

When crystallites are relatively far apart from each other, the average size of the crystallites in a system not far from equilibrium is estimated [59] to increase with time as

$$\langle r \rangle^3 = \frac{8Dv_c^2 C^{\infty} \sigma t}{9kT}, \qquad (41)$$

where D is the diffusion coefficient. This formula allows to estimate the time required for the formation of particles of macroscopic size. For an average crystallite size $\langle r \rangle \sim 10^{-3}$ cm, when $C^{\infty} = 10^{20}$ cm^{-1}, $v_c = 4 \cdot 10^{-23}$ cm^3, $D = 10^{-6}$ cm^2/s, $\sigma = 200$ erg/cm^2, $T = 370$K, the ripening time is of the order of 10^6 s $\approx$ 12 days.

Chapter 4

Stochastic dynamics

In the past 20 years, studies of stochastic processes and the impact of noise on dynamical systems have evolved into a broad field of nonlinear dynamics. It is widely recognized that the presence of noise in a nonlinear dynamical system may lead to non-trivial effects that qualitatively change the system's dynamics [69]. Noise can cause what are called noise-induced transitions, such as the creation of new stable states, which would not otherwise exist, switching between co-existing stable states, or resonance effects.

This chapter gives an overview of the basic concepts and methods used in the studies of stochastic nonlinear systems. First, the most commonly used noise processes and their statistical and geometrical characteristics will be reviewed. Then the link between stochastic differential equations and the evolution of the probability distribution for the stochastic variable [70] will be explained. Finally, the phenomena of coherent and stochastic resonances will be briefly discussed. In the next chapters, these concepts will be applied to investigate the effects of the stochastic environmental fluctuations on pattern formation in minerals and to characterize the statistical properties of the observed noisy compositional profiles in patterned minerals.

4.1.1 Characteristics of noise processes

Let $x(t)$ be a stochastic variable which varies aperiodically and randomly with time t according to some law. Such a variable is said to represent a stochastic (noise) process. When sampled, the stochastic variable takes on a different set of values for each noise realization. One of the characteristics of the stochastic process is its probability distribution, i.e. the probability of finding the stochastic variable in any particular range of values. If the probability distribution remains constant in time then the process is called stationary. The stochastic process can also be characterized by its mean value,

variance, and higher moments, its two-point autocorrelation function, and other characteristics. For a stationary process $x(t)$, the mean value $\langle x \rangle$, variance σ^2 and autocorrelation function $G(\tau)$ are defined in the limit of an infinitely long process as

$$\langle x \rangle = \lim_{T\to\infty} \frac{1}{T} \int_0^T x(t)dt . \tag{42}$$

$$\sigma^2 = \langle (x - \langle x \rangle)^2 \rangle = \lim_{T\to\infty} \frac{1}{T} \int_0^T (x(t) - \langle x \rangle)^2 dt \tag{43}$$

$$G(\tau) = \lim_{T\to\infty} \frac{1}{T} \int_0^T x(t)x(t+\tau)dt . \tag{44}$$

The autocorrelation function characterizes how the value of the process $x(t)$ at some time t affects its value at time $t+\tau$. It is closely related to the Fourier power spectrum of the process $S(\omega)$

$$S(\omega) = \lim_{T\to\infty} \frac{1}{2\pi T} \left| \int_0^T e^{-i\omega t} x(t)dt \right|^2 . \tag{45}$$

The relation between the correlation function of the process and its power spectrum is given by the Wiener-Khinchin theorem:

$$S(\omega) = \frac{1}{2\pi} \int_{-\infty}^{\infty} e^{-i\omega\tau} G(\tau)d\tau \tag{46}$$

$$G(\tau) = \int_{-\infty}^{\infty} e^{i\omega\tau} S(\omega)d\omega . \tag{47}$$

A completely uncorrelated stochastic process, i. e. whose value at any given time does not depend on its value at any other time, is called **white noise** and will be denoted here as $\xi(t)$. This process $\xi(t)$ is a discontinuous, irregular function and is nowhere differentiable. In modeling, a Gaussian white noise is most commonly used, for which the values $\xi(t)$ are drawn from a Gaussian distribution (see e.g. Appendix A). For most applications, the noise value distribution is chosen to have zero mean:

$$\langle \xi(t) \rangle = 0. \tag{48}$$

Since the values of the noise process at different moments of time are completely independent, the autocorrelation function is described by a delta function

$$\langle \xi(t_1)\xi(t_2)\rangle = 2D\delta(t_1-t_2), \tag{49}$$

where D characterizes the intensity of the process. Accordingly, the Fourier power spectrum of the white noise process is flat, i. e. the power is distributed equally among all frequencies. A paradoxical consequence of this is that the total power dissipated in all frequencies is infinite. The variance of the white noise, as seen from eqs. (43), (48), and (49), is also infinite. White noise is an idealization and does not exist in nature. However, it has proved to be an extremely useful approximation for many real noise processes because analytical results that are obtained in the white noise approximation may be relatively easily applied to systems in which the typical correlation time of the noise

$$\tau_{cor} = \frac{1}{\sigma^2}\int_0^\infty G(\tau)d\tau \tag{50}$$

is much smaller than the characteristic time scale of interest.

If a stochastic process is constructed in such a way that at any moment of time the value of $x(t)$, instead of being chosen randomly, is changed by a random increment then the standard **Brownian noise** process is obtained, also called a random walk process. If the increments of the stochastic variable x are drawn from a Gaussian distribution then the noise process is called a Gaussian Brownian noise. Unlike white noise, Brownian noise has a continuous sample paths. It can be regarded as an integral of the white noise over time.

Brownian noise is a non-stationary process. Its standard deviation changes with time as

$$\sigma = \sqrt{2Dt},$$

where the parameter D characterizes the intensity of the parent white noise process according to eq. (49). Brownian noise is commonly used to describe, for example, the diffusion of a particle in liquid, in which case D is equivalent to a diffusion coefficient.

Another widely used noise process is the **Ornstein-Uhlenbeck process**. It is a continuous Gaussian-distributed process defined as a random walk with a drift term; at every moment of time the process variable is incremented by

$$dx = -xdt/\tau + \sqrt{D}dW(t), \tag{51}$$

where $dW(t)=\xi(t)dt$ is the increment of a Brownian noise process produced by a white noise of unit intensity and the parameter τ is the so-called noise correlation time. The presence of the drift term makes the process stationary, i. e. its variance is independent of time and the probability distribution of the stochastic variable $x(t)$ is constant in time. The correlation function, in the stationary limit, is

$$< x(t)x(s) >= D\tau \exp(-|t-s|/\tau) \qquad (52)$$

and the 2-time correlations decay exponentially with time. The Ornstein-Uhlenbeck noise is widely used to simulate natural noise processes because it has a finite correlation time, it is stationary and has continuous sample path. White noise may be taken as a good approximation of an Ornstein-Uhlenbeck noise when the characteristic time scales of the studied deterministic system are much larger then the noise correlation time.

4.1.2 Fractal properties of stochastic processes

The Brownian walk is a self-affine fractal. A formal definition of a self-affine fractal is that $x(bt)$ is statistically equivalent to $b^H x(t)$ where H is the so-called Hurst exponent. The Hurst exponent is related to the fractal dimension of the process. If d is the box-counting fractal [71] dimension then $H = 2\text{-}d$.

For a time series that is a self-affine fractal, the Fourier power spectral density $S(\omega)$ exhibits a power law dependence on frequency: $S(\omega) \sim \omega^{-\beta}$. The exponent β is related to the fractal dimension and Hurst exponent as $\beta = 2H+1 = 5 - 2d$. For example, standard Brownian process exhibits fractal scaling with a Hurst exponent $H = 0.5$ and a power spectrum exponent $\beta = 2$ [71].

4.1.3 Stochastic differential equation

Let the motion of a stochastic system be described by the *Langevin equation*

$$\frac{dx}{dt} = a(x,t) + b(x,t)\zeta(t), \qquad (53)$$

where x represents the set of state variables, the coefficients a and b are, in general, functions of x and time t, and $\zeta(t)$ is a rapidly varying stochastic process. When modeling, one does not usually have direct information about the noise variable. Instead, the assumptions on the nature of the noise and its coupling to the dynamical system variables are made based on the observed effects of the noise on the state variables. Due to the properties of the white noise which facilitate an analytical treatment of the stochastic

differential equations, here the noise process $\zeta(t)$ is taken to be the white noise $\xi(t)$ with unit intensity $D=1$. The effective noise strength is then defined by $b(x,t)$.

The noise process can be classified according to the way the dynamical variables x appear in the term $b(x,t)$. If the coefficient in front of $\zeta(t)$ is independent of x then the noise is called additive. It is simply added to the deterministic dynamics of the system. If, however, the coefficient b depends on one or more state variables then the noise is termed multiplicative. Its intensity depends on the position of the system in its phase space and changes as the system evolves.

The equation (53) is poorly defined from the physical point of view because the derivative of a physical quantity x changes discontinuously. However, due to the fact that the integral of $\xi(t)$ over time

$$W(t) = \int_0^t \xi(t')dt' \tag{54}$$

is a continuous process, the corresponding *integral equation* can be interpreted consistently:

$$\begin{aligned} x(t) - x(0) &= \int_0^t a[x(s),s]ds + \int_0^t b[x(s),s]\xi(s)ds = \\ &= \int_0^t a[x(s),s]ds + \int_0^t b[x(s),s]dW(s). \end{aligned} \tag{55}$$

The integral over the stochastic term needs to be defined as it is different from the conventional (Rieman) integral. The *stochastic integral*

$$\int_0^t b(s)dW(s) \tag{56}$$

can be defined as the limit of the partial sums

$$S_n = \sum_{i=1}^{n} b(\sigma_i)[W(s_i) - W(s_{i-1})] \tag{57}$$

where the intermediate points σ_i are chosen such that $s_{i-1} \le \sigma_i \le s_i$. It then turns out that the limit of these sums depends on the particular choice of the intermediate points σ_i. In the Ito interpretation, the points σ_i are chosen to coincide with s_{i-1} and the stochastic integral (56) is defined as

$$\int_0^t b(s')dW(s') = \text{ms-lim}\left\{\sum_{i=1}^{n} b(s_{i-1})[W(s_i) - W(s_{i-1})]\right\}. \qquad (58)$$

where ms-lim indicates that the limit is taken in the mean square sense. In the **Stratonovich** interpretation, the stochastic function is evaluated in the middle of the interval $[s_{i-1}, s_i]$ and the integral (56) is defined as

$$\int_0^t b(s')dW(s') = \text{ms-lim}\left\{\sum_{i=1}^{n} b(\frac{s_i + s_{i-1}}{2})[W(s_i) - W(s_{i-1})]\right\}. \qquad (59)$$

The stochastic integration of the Langevin equation (53) using these two definitions results in two different types of *stochastic differential equations* (SDE):

Ito SDE: $$dx = a\,dt + b\,dW(t) \qquad (60)$$

Stratonovich SDE: $$dx = [a - \frac{1}{2} b \frac{\partial b}{\partial x}]dt + b dW(t) \qquad (61)$$

This difference in the SDE formulation leads to qualitatively different results in the treatment of physical problems. Nevertheless, both approaches are widely used in the analysis of the noise effects in dynamical systems.

4.1.4 Fokker-Planck equation and probability distribution

Solving numerically the SDE (see e.g. Appendix A) produces different solutions for each realization of the noise process. Given the Langevin-type equation (53), one can obtain the corresponding equation that would describe the evolution of the system in terms of the probability density of finding it in a certain region of its parameter space [69]. The probability density distribution allows to investigate the possibilities of noise-induced states and incurring shifts in the deterministic bifurcation points as the system parameters change. Using the probability density approach, one can study how an ensemble of initial conditions propagates with time. In the case of white noise, this equation (the Fokker-Planck equation (FPE)) is easily derived and can be solved exactly for univariate systems [72]. In most multivariate systems, the FPE must be solved numerically.

Let the phase space of the system be defined by a set of coordinates $\{x_i\}$, and the motion of the particle described by the stochastic differential equation (in Ito form)

$$dx_i(t) = A_i[x(t), t]dt + \sum_j B_{ij}(x(t), t)dW_j(t) \ . \qquad (62)$$

The evolution of the probability density $p(\{x_i\},t)$ is then described by the Fokker-Planck equation

$$\frac{\partial p}{\partial t} = -\sum_i \frac{\partial}{\partial x_i}\{A_i p\} + \frac{1}{2}\sum_{ij}\frac{\partial}{\partial x_i}\frac{\partial}{\partial x_j}\{B_{ij}B_{jl}p\}. \qquad (63)$$

In Stratonovich form, this equation is written as

$$\frac{\partial p}{\partial t} = -\sum_i \frac{\partial}{\partial x_i}\{A_i p\} + \frac{1}{2}\sum_{jk}\frac{\partial}{\partial x_i}\left\{B_{ik}\frac{\partial}{\partial x_j}[B_{jk}p]\right\}. \qquad (64)$$

Solving this equation allows to predict the behavior of the system subjected to white noise.

4.1.5 Coherence and stochastic resonances

Resonance noise-induced phenomena include stochastic and coherence resonances. The intensively studied [73,74] stochastic resonance (SR) occurs in systems whose deterministic dynamics exhibits several steady states and in presence of an external, usually weak, deterministic forcing. In the absence of noise, this forcing is too weak to induce switching between the steady states. As the noise intensity increases, such transitions are facilitated as fluctuations become large enough to move the system from one state to another. A resonance-like synchronization of the transitions occurs when the characteristic frequency of stochastic hopping (Kramers rate) matches the frequency of the external forcing [74].

Coherence resonance (CR), also often called autonomous or internal stochastic resonance, is in many ways similar to SR. It occurs in nonlinear oscillating systems when the noise stimulates a coherent motion in an autonomous system (i. e. without external signal). Suppose the system is in a deterministic fixed point state close to a Hopf bifurcation where the stability of that state changes to a limit cycle. It was shown [75] that the power spectrum characteristic of the system in the limit cycle regime, can, nevertheless, be visible in the presence of noise even before the bifurcation occurs, i.e. when deterministically the system is still in the fixed point state (so called noisy precursor of the bifurcation). The noise 'probes' the region beyond the bifurcation thus exciting the characteristic frequency of the limit cycle. As a result, a peak appears in the power spectrum $S(\omega)$ at the limit cycle frequency. Increasing the noise intensity kicks the system farther away from the stable state and thus increases the height of the peak. On the other hand, because of the system's nonlinearity, the relative width of the peak also

increases. This kind of system's response to noise can be characterized by a signal-to-noise ratio (SNR) R. While several definitions of SNR are used in characterizing the behavior of a noisy system near the bifurcation [76,77], we choose the one that is best suited to describe the system's response around a frequency of interest relative to the broad-spectrum response around this frequency. Thus, we define the SNR at some particular frequency Ω as the ratio of the area of the peak to the characteristic value of the background spectral response at this frequency [74]:

$$R = \left[\int_{\Omega-\Delta\omega_1}^{\Omega+\Delta\omega_2} S(\omega) d\omega \right] / S_b(\Omega). \tag{65}$$

Here, $\Delta\omega_1+\Delta\omega_2$ defines the width of the integration window around Ω and $S_b(\Omega)$ is the value of the background floor line at the frequency of interest. The floor line is drawn to join the boundaries of the peak defined by the integration window.

As the noise intensity increases, the SNR passes through a maximum and then steadily decreases, i.e. the system's response is optimized for some specific noise intensity range. This behavior is characteristic of both coherence and stochastic resonances.

Chapter 5

Effect of noise on oscillatory zoning in plagioclase

The compositional pattern observed in many plagioclase crystals has been an archetypal example of oscillatory zoning for more than a century. Despite a large number of models proposed to explain the formation of the oscillatory pattern, its origin remains conjectural. Experimental work performed so far on plagioclase has been unable to support any of the proposed theories over others and no oscillatory zoned plagioclase crystals were obtained under controlled laboratory conditions.

In this chapter, the impact of the environmental noise on the pattern formation in plagioclase is investigated in the framework of a constitutional undercooling model [36], which suggests that the oscillatory compositional pattern is due to self-organization. First, several previously proposed models for the oscillatory zoning in plagioclase are reviewed along with available experimental data. Then the constitutional undercooling model is presented and the effects of the environmental noise on plagioclase crystal growth are described. Then the effects of dissolution are considered and, finally, the results are discussed.

5.1 Plagioclase zoning

5.1.1 Physico-chemical characteristics of plagioclase

Plagioclase is a member of the feldspar family of minerals. It is found in many rocks and is essentially a binary solid solution of anorthite $CaAl_2Si_2O_8$ (An) and albite $NaAlSi_3O_8$ (Ab).

The crystal structure of plagioclase is complicated by the varying ratio of Al/Si from albite to anorthite and by the charge linkage of Ca to Al and of Na to Si [78]. Although the crystal lattices of both solid solution members have triclinic symmetry, ordering of $AlSi_3$ units in albite is topologically incompatible with crystal structures

formed by Al_2Si_2 units in anorthite, which leads to complex superstructures in intermediate composition plagioclase. The unit cell volume increases by only about 0.3% as the solid solution composition changes from Ab-rich to An-rich, reaching its maximum at about $Ab_{20}An_{80}$ composition. Substitution of NaSi for CaAl in the solid solution leads to the formation of domains with a fine and complex texture within the crystal. Generally, because of the high degree of local order in plagioclase, there is little driving force for segregation of albite and anorthite from the solid solution.

The equilibrium phase diagram of plagioclase is shown in Fig. 14. For typical pressures found in natural environments, plagioclase crystals grow from dry melt in a temperature range from approximately 1200 to 1800K. Increasing pressure generally shifts the liquidus and solidus lines towards higher temperatures while increase in the water content decreases the corresponding transition temperatures.

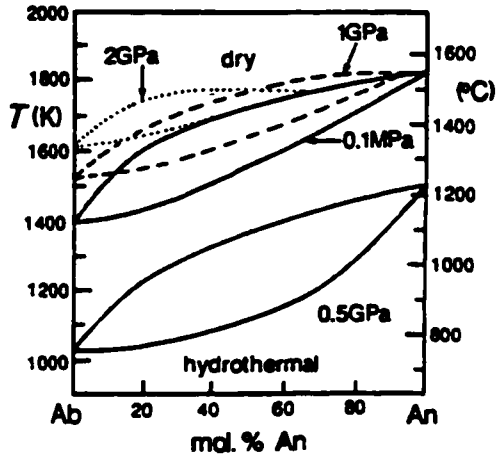

Fig. 14 Plagioclase phase diagram (after [78]). Melting relations are shown in dry plagioclase at low and high pressure and in hydrothermal at $P(H_2O)$=0.5GPa.

Experimental data obtained using quench methods for the case of plagioclase growth from dry melts [79,80,81] indicate that the plagioclase growth rates vary with undercooling and crystal/melt composition in the range 10^{-4} to 10^{-8} m/s for undercoolings ranging from about 50 to 600 K (Fig.15). Measurements of the growth rates in the system Ab-An in the presence of water yielded values of the growth rate at the pressure 0.5GPa and temperature 1073-1323 K in the range $(0.8\text{-}6)10^{-10}$ m/s with no strong compositional dependence [82]. Other estimates [83,84] produced growth rates for

plagioclase from melts in presence of water to be from 10^{-12} to 10^{-8} m/s for undercoolings ranging from 20 to 250 K.

The diffusion coefficient in Ab-An melt strongly depends on temperature, in accordance with the Arrhenius equation $D = D_0 \exp(-Q/RT)$, where Q is the molar diffusion activation energy and R is the gas constant. Interdiffusion in plagioclase is generally complicated by coupling between the diffusion of NaSi and CaAl, which is necessary to maintain the electrostatic neutrality. The activation energy and the diffusion

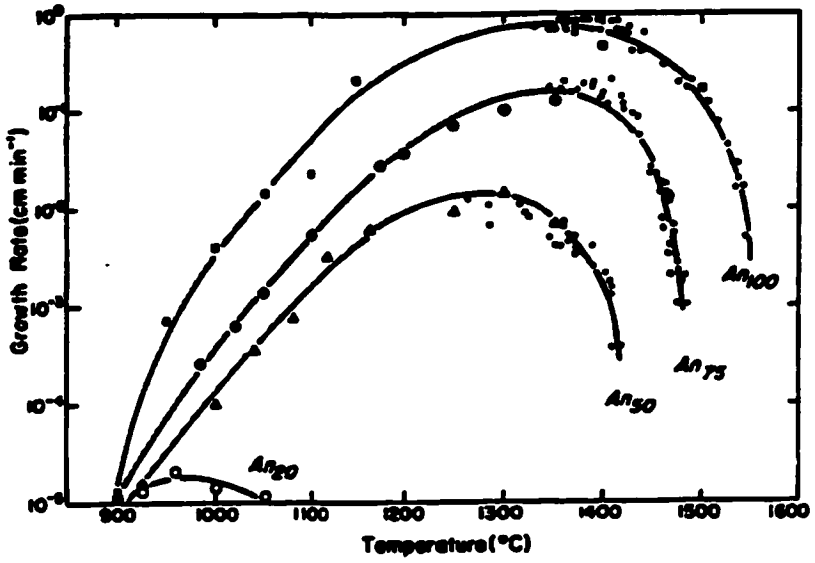

Fig. 15 Plagioclase growth rates from melt (from [81]). The growth rates were measured in a microscope heating stage experiment as well as using a quenching technique. The liquidus temperatures for An_{75}, An_{50}, and An_{20} are 1500°C, 1450°C, and 1100°C, respectively. Small dots represent the data obtained during the heating stage experiment while larger symbols correspond to the data from quenched samples.

pre-factor D_0 were estimated for plagioclase to be about $D_0=2\cdot10^{-7}$ m^2/s and Q=120 kJ/mol [85]. Viscosity of the melt also depends on the temperature approximately as $\eta = A \exp(U/RT)$, where A is a constant and U is a viscous flow activation energy. Viscosity measurements in the plagioclase melt yielded viscosity values about 10^5 P at temperatures around 1450 K [86].

5.1.2 Zoning description

Oscillatory zoned plagioclase samples show clearly visible patterns, whereby the An concentration varies from the core of the crystal to its rim (Fig.1). Layers of similar composition are frequently traceable completely around the crystal. Microprobe analysis

shows that the An molar composition typically varies by 5 to 15 %. The zoned samples typically have tens of zones ranging in thickness from 10 to 100μm. Superimposed to these more-or-less regular variations, abrupt changes and irregular patterns are often found [5]. Dissolution surfaces are also very common. The An-composition profile often exhibits a saw-tooth pattern consisting of multiple spikes within which the An concentration steeply increases and then gradually decreases (in the direction from core to rim). This oscillatory pattern is often superimposed on an overall decreasing An concentration profile thus defining so-called normal (non-oscillatory) zoning.

Pearce and Kolisnik [5], based on observations of plagioclase crystals using laser interference microscopy and Nomarski interference techniques, recognized two types of zoning: small zones less than 10 microns thick with compositional variations having the magnitude up to 10 An% and larger zones (often more than 50 microns thick), in which the An content varies by up to 35%. They also reported the saw-tooth shape of the concentration profile and noted that the individual zones are characteristically bounded by discontinuities in the composition profile, in which the crystal composition changes abruptly on length scales less than 0.3 μm.

5.1.3 Oscillatory zoning models and experimental data

It has been long known that steady periodic patterns may spontaneously form in the reaction-diffusion systems from an unpatterned state, e.g. through Turing instability [1]. Given this potential for self-organizing behavior, several models have been proposed to explain the oscillatory zoning in plagioclase by intrinsic mechanisms acting on a small spatial scale of the crystal-melt system. Reviews of the proposed models are presented in [4] and [7]. Some of these models have already been mentioned in section 2.3.

The first self-organization quantitative model of oscillatory zoning in plagioclase was proposed by Haase *et al.* [87]. The oscillatory pattern was suggested to form because of an autocatalytic geochemical reaction coupled with an isothermal, diffusion-controlled crystal growth. A positive feedback between the growth rate and the crystal composition was suggested. Periodic solutions were generated in that model through a limit cycle for large times. However, the expressions used for the crystal growth rates were based on several assumptions and their exact physical basis, as well as the nature of the autocatalytic feedback, was unspecified. Allègre et al [88] suggested a model of diffusion-controlled plagioclase growth from a melt. In their model, a time delay between the actual growth rate and its kinetic value was introduced. The model exhibited damped

oscillatory solutions but no stable oscillatory regime was found. Pearce [4,89] offered a simple one-dimensional discretized model, which could be viewed as an extension of the previously described qualitative model by Sibley *et al* [30]. The model used a finite-element technique, in which the liquid was divided into cells covering the so-called zeroth layer immediately adjacent to the crystal and a certain volume of the local liquid. The model produced regular oscillations when the crystal growth rate substantially exceeded the diffusion rate. Lasaga [90] proposed a model of diffusion-controlled growth with realistic growth rate expressions. A partition coefficient K was introduced to relate the An concentration in the melt in the vicinity of the crystal-melt interface c to the An concentration in the solid c_s. The partition coefficient $K=c_s/c$ was chosen to be larger than 1, as prescribed by the shape of the equilibrium phase diagram of plagioclase (Fig. 14). No oscillatory solutions were found in that model. L'Heureux and Fowler [33,34,91] proposed a model, in which the isothermal diffusion-controlled plagioclase growth was considered for $K<1$. The latter condition is possible locally near the interface in far-from-equilibrium conditions, as demonstrated by Wang and Wu [32] who derived a disequilibrium partitioning relation in a silicate melt from kinetic arguments, by defining the partition coefficient as a fraction of a selected end-member in the total molecular attachment flux from the melt towards the crystal surface. In the models [33,34,91], the growth rates were approximated using the experimental data of [81]. Oscillatory solutions were then shown to arise through a Hopf bifurcation for a certain range of $K<1$. For $K>1$, no oscillatory solutions could exist, in agreement with the model of Lasaga. The effects of temperature variations on that model were investigated in [92], where the latent heat of crystallization and the temperature dependence of the diffusion coefficient were taken into account. The thermal corrections were found to be small, mainly due to the fact that thermal diffusion is much faster than chemical diffusion. The decrease in the ambient temperature due to an overall magma cooling was also considered. It was found that oscillatory zoning was suppressed for large cooling rates (larger than 0.01K/s) and high initial temperatures, which may provide a reason why no oscillatory-zoned plagioclase have been synthesized in the laboratory.

Holten *et al.* [35,93] suggested that external noise (such as rapid variations of the fluid composition due to magma mixing, gas releases or temperature changes) may play an important role in the formation of the oscillatory patterns in plagioclase crystals. By studying the effects of environmental noise on a generic crystal-melt system, they showed that fluctuations that occur on scales much larger than the size of the growing crystal produce realistic zoning patterns. In their first work [35], they used bounded

Brownian noise fluctuations superimposed on the bulk composition with rather long correlation time and large amplitude (about 30% of the average bulk composition). As a consequence, the concentration pattern recorded in the crystal follows the fluctuations of the bulk concentration and the diffusive system acts as a filter that reduces the influence of the environmental fluctuations on the growing crystal. In a second paper [93], a model of plagioclase growth in magmatic systems [91] was analyzed among four other crystal growth models for possible sensitivity to noise. In other models, growth of carbonates in sedimentary systems [18], garnets in hydrothermal systems [13], and silicates from a silicate melt [32] was investigated. In the absence of noise, all these models produced oscillatory or chaotic solutions. The solutions were shown to be sensitive to noise applied at the boundary of the diffusion layer, the plagioclase model being the most sensitive of all. In all simulations, a Brownian noise with rather long correlation time and restricted value range was used.

In contrast, as will be seen in this chapter, our simulations [94] indicate that oscillatory zoning can be caused by uncorrelated noise of small amplitude. In presence of noise, our model produces oscillatory patterns even when no deterministic oscillations exist. The patterns are then formed as a result of the complex interplay between the stochastic external processes and the internal nonlinear dynamics of the system. The external noise thus triggers, rather than drives, the system's dynamics and noise-induced phenomena, such as coherence resonance and advancement of bifurcation points, are possible.

Efforts to characterize the observed zoning have been primarily concentrated on obtaining spatial concentration profiles and measuring their properties. Higman and Pearce [95] obtained the first-return map of the plagioclase zoning by plotting the thickness of the $(n+1)$st zone against the thickness of the nth zone. Based on the shape of the return map, they concluded that the zoning-producing dynamics is at least partly determined by a deterministic system with low phase space dimension (the results of this analysis are further mentioned in section 8.2). In observations by Pearce and Kolisnik [5], the plagioclase zoning was found to consist of both small-scale (~10μm) and large-scale (50+μm) zones. The finer zones were suggested to result from local diffusion processes in the boundary layer around the growing crystal while the wider zoning was proposed to be due to some large-scale external changes in the growth conditions, for example, resulting from a turbulent convection in magma.

In spite of a large number of observations of plagioclase zoning, many important characteristics of the crystal-forming process remain unknown or speculated about. For example, the duration of the oscillatory-zoned crystal formation cannot be measured experimentally and is usually estimated based on the assumed crystal growth rate, which, in turn, is approximated from crystal growth experiments conducted in similar conditions.

The role of dissolution in the process of the oscillatory pattern formation remains unclear. It is believed to remove part of the zoning sequence from the crystal and some suggestions were made [4] about the qualitative mechanism by which the dissolution may contribute to the sharp increases in the An concentration, which are frequently observed as discontinuities in the composition profiles. However, it is not clear if the dissolution is an integral part of the zone growth cycle and no published model currently includes both growth and dissolution.

5.2 Impact of noise on oscillatory zoning in plagioclase

5.2.1 Deterministic growth model

The model is based on the isothermal nonlinear plagioclase growth model proposed by L'Heureux and Fowler [33,34]. Crystal growth is considered in one dimension perpendicular to the crystal face and the frame of reference is chosen to be moving with the interface, so that x=0 corresponds to the crystallization front and the distance from the interface x is related to the space coordinate in the laboratory frame of reference x' through the transformation

$$x(t) = x'(t) - \int_0^t V(t')dt', \tag{66}$$

where $V(t)$ is the crystal growth rate. The dynamical evolution of the concentration of An (mole per unit volume) in the melt $c(x,t)$ is then described by the diffusion equation

$$\frac{\partial c}{\partial t} = \frac{\partial}{\partial x}(D\frac{\partial c}{\partial x}) + V(c(0,t))\frac{\partial c}{\partial x} \tag{67}$$

where $c(0,t)$ is the An concentration in the melt near the interface and D is an effective diffusion coefficient. The concentration dependence of this coefficient is neglected. The growth velocity V is determined only by the local concentration at the interface $c(0,t)$. Since the molar volumes of An and Ab are nearly equal, the molar concentration c can be

non-dimensionalized by the molar volume of An [33]. This way, it becomes equivalent to the molar composition of An in the solution and is bounded $0<c<1$.

A realistic expression for $V(c(0,t))$ for a given temperature T has been approximated [33] by fitting the empirical data obtained for synthetic plagioclase [81] to the Calvert-Uhlmann growth model [96]. In that model, the growth is interpreted as a geometric average of two mechanisms, a longitudinal growth R_s by surface nucleation and a continuous growth R_c along the surface. The growth rate is then given by

$$V = U(R_s R_c^2)^{1/3}, \tag{68}$$

where U denotes a velocity scale. The rate of the continuous growth is approximated according to eq. (19) and the rate of the surface nucleation growth is determined by the nucleation rate (18) through eq. (30). Expressions for R_s and R_c that describe the characteristic temperature dependence of the growth rate are given by

$$R_s = \exp\left(-\frac{3a}{T\Delta T}\right)\exp\left(-\frac{b}{T-T_g}\right) \tag{69}$$

$$R_c = \left[1-\exp\left(-\frac{\Delta G}{RT}\right)\right]\exp\left(-\frac{b}{T-T_g}\right). \tag{70}$$

Here, the parameter a is related to the surface tension of the critical nucleus, b to the viscosity of the melt, and $\Delta T=T_L-T$ is the undercooling, with T_L being the liquidus temperature, and T_g is the glass-transition temperature. ΔG is the difference in molar Gibbs free energy between the crystal and the melt. The concentration dependence of the growth velocity comes mainly from the liquidus line $T_L(c(0,t))$ and the velocity scale $U(c(0,t))$, which are approximated to fit the experimental data in Fig.15 [33]. The expression $T-T_g$ in the denominator of the exponent in (69) and (70) comes from an empirical Vogel-Tammann-Fulcher relation [97], which provides better fit to the experimental data than the standard $1/T$ expression used in Section 3.2.

The boundary condition far from the crystal-melt interface is such that the concentration is equal to the bulk concentration of An in the melt:

$$c(\infty,t) = \tilde{c} \tag{71}$$

The boundary condition at the growing front is derived from the continuity of the mass flux at the crystal interface:

$$D\frac{\partial c}{\partial x}\bigg|_{x=0} + [c(0,t) - c_s(t)]V = 0 \qquad (72)$$

Here, $c_s(t)$ is the An concentration in the crystal at the interface. We have neglected the diffusion in the solid phase. A nonlinear phenomenological partition relation between $c_s(t)$ and $c(0,t)$ was proposed by Lasaga [90]:

$$c_s(t) = \frac{K_D B c(0,t)}{A + (K_D - 1)c(0,t)} \qquad (73)$$

If c' refers to the concentration of another major component (i.e. Ab) in the solution, then $K_D = c_s(t)c'(0,t) / [c(0,t)c_s'(t)]$ is an effective exchange-equilibrium constant whereas $A = c(0,t) + c'(0,t)$ and $B = c_s(t) + c_s'(t)$ are approximately constant [90]. When c refers to the concentration of a trace element, a simple relation can also be used that employs a constant partition coefficient K:

$$c_s(t) = Kc(0,t) \qquad (74)$$

For major elements, the nonlinear relation (73) reduces to (74) if we assume $c \approx$ const in the denominator of eq. (73) in the spirit of a mean field theory approach [90]. As verified numerically, both partition relations (73) and (74) lead to similar results but, for simplicity, the expression (74) is used in the reduced model described below. The nonlinear coupling necessary to generate self-oscillatory solutions stems from the nonlinear concentration dependence of the growth velocity V.

In conditions close to equilibrium, the partition coefficients K_D or K can be derived from the equilibrium phase diagram and are larger than unity. However, in situations where far-from-equilibrium conditions prevail, K_D or K must be derived from kinetic arguments [32] and can take values smaller than one.

In the model described by eqs. (67)-(73), a steady-state solution for c_s exists. For $K_D > 1$, this steady state solution is stable and the system relaxes to this fixed point without oscillations. This corresponds to the situation where the crystal has a constant, well-defined An composition, as is observed in crystals formed in close-to-equilibrium conditions. For $K_D < 1$ there is a regime where underdamped oscillations to the steady state exist. For smaller values of K_D, the system undergoes a Hopf bifurcation, beyond which the attractor is a limit cycle. For a typical value of $\hat{c} = 0.3$ at $T = 1400$ K, the Hopf bifurcation occurs at $K_D = 0.2434$. A transition to chaotic behavior through a period doubling sequence is also observed for still smaller values of K_D. The simpler form (74)

of the partitioning relation (73) produces similar sequences of dynamical behaviors: as K decreases, there is a transition from a steady state to a limit cycle through a Hopf bifurcation (at K_H) and then to chaos [33].

5.2.2 Reduction to two nodes

The description of the diffusion process can be simplified by rewriting the model in terms of ordinary differential equations. Wang and Merino [18] proposed a dynamical model of zoning in calcite and plagioclase, which is based on the evolution of the concentration of two species at one point near the interface. This results in two coupled ordinary differential equations, which can generate oscillatory solutions. We adopt here the spirit of their approximations and take the idea one step further by suggesting a reduction of the crystallization dynamics to the concentration evolution at two distances L_1 and L_1+L_2 from the growth front (Fig. 16). L_1+L_2 corresponds to the thickness of the boundary layer. This enables us to describe the essentially continuous process by two coupled ordinary differential equations that mimic the general dynamics of the parent model and allow for the possibility of a limit cycle. Stability analysis can be easily performed as well. We will refer to this approximation as the 2-node model, from the nomenclature conventionally used in finite-element techniques.

We integrate the diffusion equation (67) with respect to the space coordinate and take the following approximations [18] (see Fig. 16):

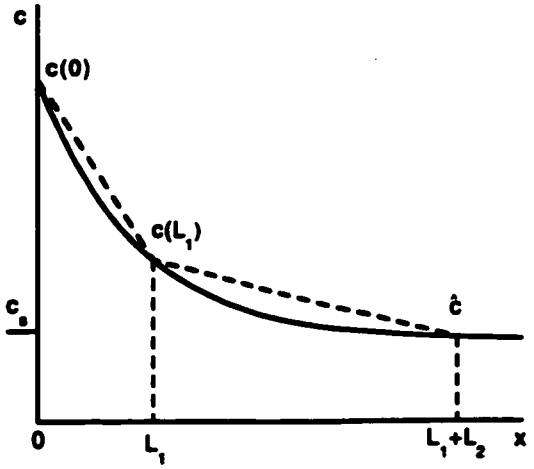

Fig. 16 Reduction of the plagioclase model to two nodes. Anorthite concentration is evaluated at 2 nodes: at the interface and at the distance L_1 from it. The smooth concentration profile is approximated by linear segments. The concentration at the distance L_1+L_2 is taken to be equal to the bulk concentration of An, $\hat{c}$. The An concentration in the crystal c_s is related to the concentration in the melt at the interface $c(0)$ through the partitioning relation (74).

$$\int_0^{L_1} c\,dx \approx [c(L_1)+c(0)]L_1/2 \tag{75}$$

$$\left.\frac{\partial c}{\partial x}\right|_{0<x\le L_1} \approx [c(L_1)-c(0)]/L_1 \tag{76}$$

Similarly,

$$\int_{L_1}^{L_1+L_2} c\,dx \approx [c(L_1+L_2)+c(L_1)]L_2/2 \tag{77}$$

$$\left.\frac{\partial c}{\partial x}\right|_{L_1<x\le L_1+L_2} \approx [c(L_1+L_2)-c(L_1)]/L_2 \tag{78}$$

The boundary condition (71) becomes $c(L_1+L_2)=\hat{c}$. After imposing the condition (72) and taking into account the partition relation (74) we obtain the following system of two ordinary differential equations:

$$\begin{aligned}\dot{\alpha} \equiv f_1(\alpha,\beta) &= d\beta(1+l+l^2)-d\alpha(1+l)-dl^2 \\ &-\nu(\alpha)K\alpha+\nu(\alpha)\beta(1+l)-\nu(\alpha)l,\end{aligned} \tag{79}$$

$$\dot{\beta} \equiv f_2(\alpha,\beta) = dl^2-d\beta l(1+l)-dl\alpha+\nu(\alpha)l-\nu(\alpha)l\beta. \tag{80}$$

Here, the dimensionless variables are $\alpha=c(0)/\hat{c}$, $\beta=c(L_1)/\hat{c}$, $l=L_1/L_2$, $\nu(\alpha)=V/V_0$, $d=D/(V_0\,L_1)$, and the dimensionless time is $\tau=2\,t\,V_0/L_1$. We have introduced V_0 as a typical growth velocity scale, for instance, the value corresponding to the steady growth regime. We approximate the crystal growth velocity as

$$V(\alpha) = V_0 \exp[m(\alpha-\alpha_{st})], \tag{81}$$

where α_{st} is the concentration in the melt in the steady growth regime and m is a constant. Equation (81) is a fairly good approximation of the experimental data [81] for a wide range of temperatures if $\hat{c}$ is large enough (e. g. $\hat{c}>0.2$ and for a typical growth temperature T=1400 K [33]). For T=1400 K the corresponding value of the factor m is 2.96.

5.2.3 Stability analysis

For all values of the parameters in the 2-node model (Eqs. (79) and (80)), there exists at least one fixed point, which will be referred to as 'global'. By definition, we chose the velocity scale such that $V=V_0$ at this point for all parameter values. A stability diagram for this fixed point is shown in Fig.17. Similarly to the full plagioclase growth model (67-73), for $K>1$ the fixed point is always a stable node. As K decreases, the fixed point changes to a stable focus and then to an unstable focus through a Hopf bifurcation. For reasonable values of the parameters m=2.96, l=0.25, and d=0.5 the Hopf bifurcation generates a stable limit cycle at K_H=0.439. For K<0.426, two new fixed points are created through a tangent bifurcation: a saddle point and a stable node. The limit-cycle solution then loses its stability. Since the Hopf bifurcation occurs at a value of K higher than in the PDE model, we do not expect quantitative agreement between the two models. However, the dynamics are analogous in the neighborhood of the Hopf bifurcation.

For our purpose of investigating how external noise can influence the generation of periodic solutions, the most interesting region is the one near the Hopf bifurcation where the global fixed point is a stable focus.

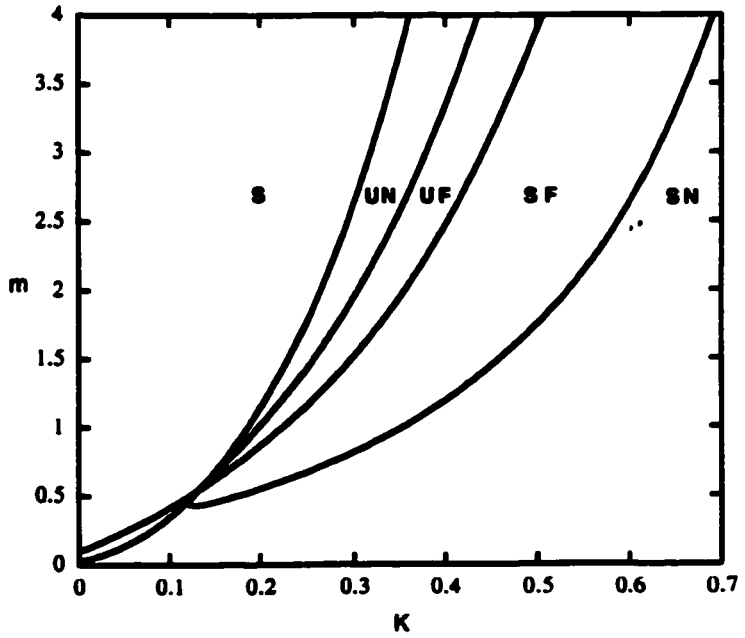

Fig. 17 Stability diagram for the global fixed point in the two-node model. The stability regions are as follows: S - saddle, UN - unstable node, UF - unstable focus, SF - stable focus, SN - stable node. The parameters are l=0.25 and d=0.5.

5.2.4 Stochastic environmental fluctuations

Suppose the system is subjected to some environmental noise such as fluctuations of temperature or concentrations of elements. Since changes in the system's parameters can be caused by a variety of different factors (e.g. gas releases, magma mixing-induced fluctuations, turbulence, growth of other crystals, acoustic noise, etc.), it is reasonable to assume that the amplitude of the fluctuations follow a Gaussian distribution. We also postulate that these changes occur over a time scale which is much faster than the crystal growth time, and can be considered uncorrelated. Therefore, we choose white Gaussian noise as an approximation for the environmental fluctuations. Plagioclase crystals grow in an environment where thermal diffusivity is much greater than component diffusion. Consequently, the process is mostly isothermal [92]. We will investigate the effects of fluctuations in the bulk concentration $\hat{c}$ of the element in a fashion similar to Holten et al [35].

In the full growth model described by the PDE (67), the noise would appear in the modified boundary condition (71):

$$c(\infty,t) = \bar{c}[1+\sigma\xi(t)], \tag{82}$$

where σ denotes the amplitude of the noise relative to $\hat{c}$ and $\xi(t)$ is a Gaussian white process with zero mean and unit intensity:

$$<\xi(t)>=0 \tag{83}$$

$$<\xi(t)\ \xi(t')>=2\delta(t-t'). \tag{84}$$

In the reduced 2-node model (79),(80), fluctuations of the form $c(L_1+L_2,t)=\bar{c}[1+\sigma\xi(t)]$ lead to a multiplicative noise term:

$$\dot{\alpha} = f_1(\alpha,\beta) - (dl^2 + vl)\sigma\xi(t), \tag{85}$$

$$\dot{\beta} = f_2(\alpha,\beta) + (dl^2 + vl)\sigma\xi(t), \tag{86}$$

where f_1 and f_2 are the right hand sides of Eqs.(79),(80). We have disregarded the terms that contain the time derivative of the noise. These terms become important when the correlation time of the noise approaches zero. However, preliminary simulations, in which the algorithm of [98] for an Ornstein-Uhlenbeck colored noise was used, indicate that there is a wide range of noise correlation times for which the approximation (85)-(86) is valid. In this range, the correlation time of the noise is large enough so that the terms containing the time derivative of the noise are negligible and at the same time it is

much smaller than the dynamical time scale of the deterministic system so that the white noise approximation is still useful. It should be noted that, although the terms that contain the time derivative of the noise have no physical meaning in the case of white noise, they may play a significant role in the dynamics of the system in the case of colored noise (e. g. it may shift the bifurcation point from its deterministic value [99]).

5.2.5 Simulated profiles and evidence for coherence resonance

Concentration profiles were generated in two ways. The partial differential equation (67) was solved using a Crank-Nicholson finite-difference scheme with iteration of the nonlinear terms. The ordinary stochastic differential equations (85), (86) were integrated using the first-order method adapted from [98], which turned out to be sufficiently precise for our purposes. The Stratonovich interpretation of this algorithm was employed (Appendix A). Other algorithms such as Heun's [100] yield similar results. To obtain results analogous to direct observations, we need to produce the spatial profile of the concentration in the crystal. In order to do so, the space coordinate was obtained by integration [33, 34]:

$$x(t) = \int_0^t v(\alpha(t'))dt'. \qquad (87)$$

Transformation of the time series into spatial profiles generally biases the shape of the concentration spikes towards the crystallization front.

We investigated the system's response to external noise in the region of the parameter space that corresponds to the deterministically stable fixed point close to the Hopf bifurcation where its stability changes to a limit cycle. Typical crystal concentration profiles simulated according to the PDE and the 2-node models, respectively, are shown in Fig.18 and Fig.19. The simulation results show that the generated patterns exhibit an oscillatory behavior. Thus, oscillatory concentration patterns are possible in presence of noise even when no oscillation exists deterministically.

The amplitude of the stochastic oscillations of the crystal An concentration derived from the PDE model is about 2% for a noise amplitude of 0.5% of the bulk concentration. This is of the same order of magnitude as the lower limit of observed concentration variations. In Fig.18, the average zone width is 27μm.

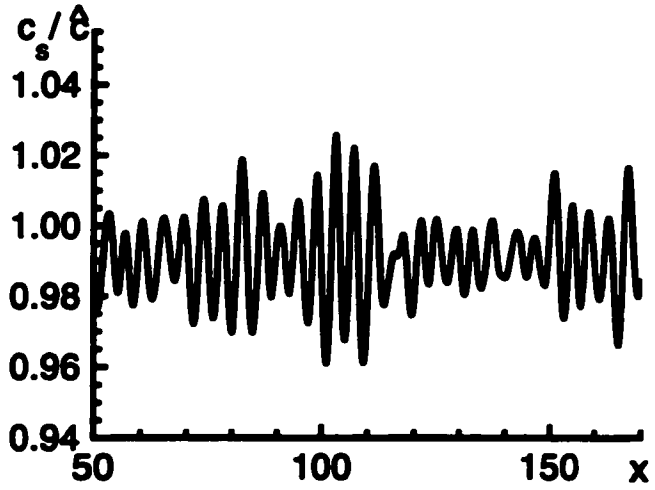

Fig. 18 Spatial concentration profile generated by the full PDE model. The parameters are T=1400 K, $\hat{c}$ =0.3, K=0.25, and σ=5·10^{-3}. The deterministic attractor for these parameter values is a stable focus. The transient solution is not shown. One space unit corresponds to 6.62 μm.

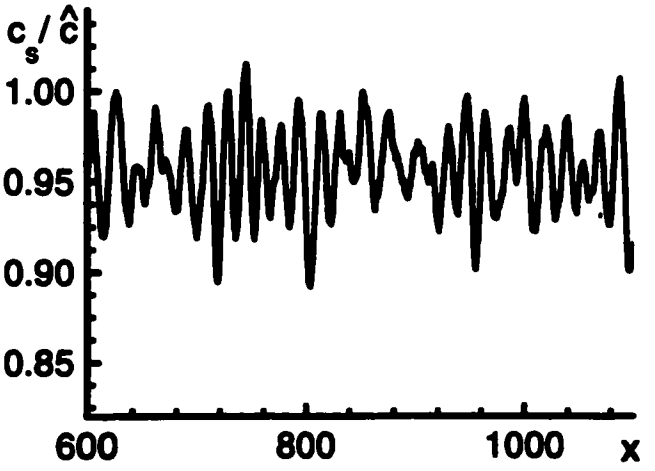

Fig. 19 Spatial concentration profile generated by the two-node model. The parameters are K=0.445, m=2.96, l=0.25, d=0.5, $\hat{c}$ =0.3, and σ=10^{-4}. The deterministic attractor for these parameter values is a stable focus. The transient solution is not shown. One space unit corresponds to 21.79 μm.

Replacing the smooth concentration profile by linear segments (Fig. 16) makes the interface composition more susceptible to the fluctuations of the bulk concentration. The 2-node model thus possesses greater sensitivity to the external noise. Changes in crystal An concentration of the same magnitude (2%) are generated by a noise amplitude of only 0.01% of the bulk concentration. In Fig.19, the average zone width is 416μm, which is large compared to actual zone widths. However, as mentioned earlier, quantitative agreement is not expected from this simplified model. Nevertheless, both the full and the reduced model exhibit similar qualitative dynamics in terms of the shape of the concentration profiles.

A spectral analysis was performed on the time series. Close to the Hopf bifurcation, the frequency of the motion around the stable focus manifests itself in the dynamics of the noise-perturbed system. While the spectrum of the external noise is flat, the characteristic peak of the system's natural frequency is clearly visible in the power spectrum (Figs. 20 and 21). The amplitude of the oscillations increases as the noise amplitude increases. As the parameter K increases, thus taking the system away from the Hopf bifurcation in the stable focus region, the oscillations become smaller in amplitude, and additional frequencies become more noticeable.

In general, before the onset of the limit cycle at the Hopf bifurcation point, an increase in the noise amplitude may have two effects on the power spectrum of the response [76]. First, because of the nonlinearity of the system, the spectral peak around the dominant frequency may become broader. This effect was found to be insignificant in the present case. The width of the peak remained approximately constant over a wide range of noise intensities. Second, as the noise kicks the system's trajectory farther from its stable point, the amplitude of the damped oscillation becomes larger, thus increasing the height of the peak in the power spectrum. The exact dependence of the peak height on the intensity of external perturbations is determined by the system's nonlinearity and may be partly controlled by noise. The strength of the response increases with the amplitude of the noise but is limited by the system's nonlinearity. As a result, the system's response is maximized for a certain noise amplitude.

The strength of the system's response to the external noise can be quantified by R, the signal-to-noise ratio (SNR), as defined by eq. (65), with the integration window $\Delta\omega_1+\Delta\omega_2$ chosen to be symmetrical about the peak. The function $S(\omega)$ in this case can be computed as a Fourier transform of the correlation function:

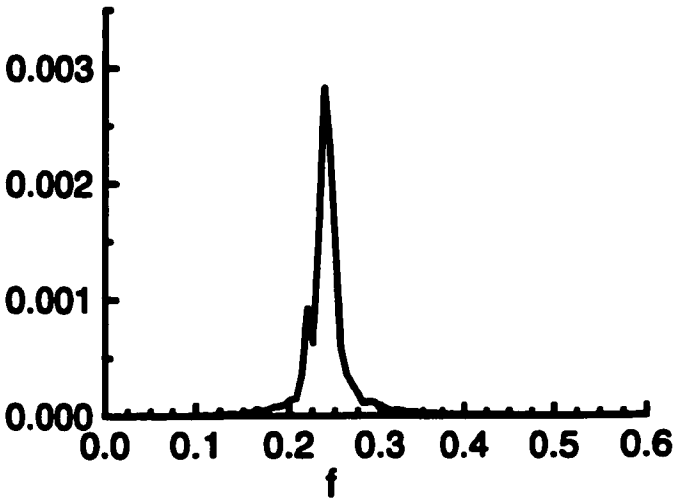

Fig. 20 Power spectrum for the PDE model. The power spectrum was computed from the time series corresponding to the space concentration profile shown in Fig. 18. One frequency unit corresponds to 0.228 Hz.

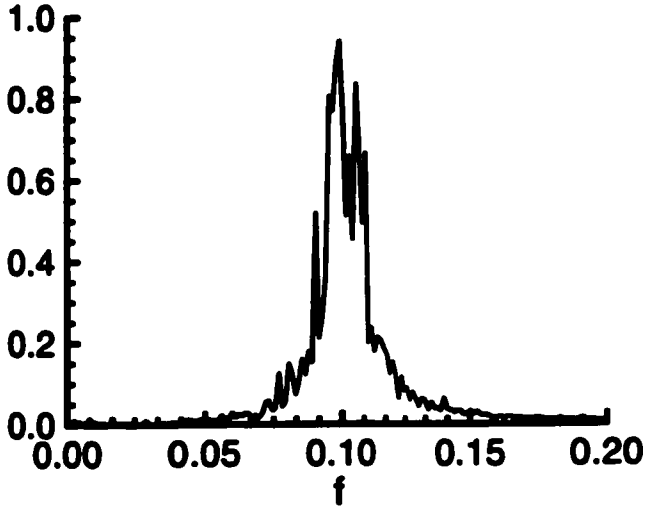

Fig. 21 Power spectrum for the two-node model. The power spectrum was computed from the time series corresponding to the space concentration profile shown in Fig. 19. One frequency unit corresponds to 0.019 Hz.

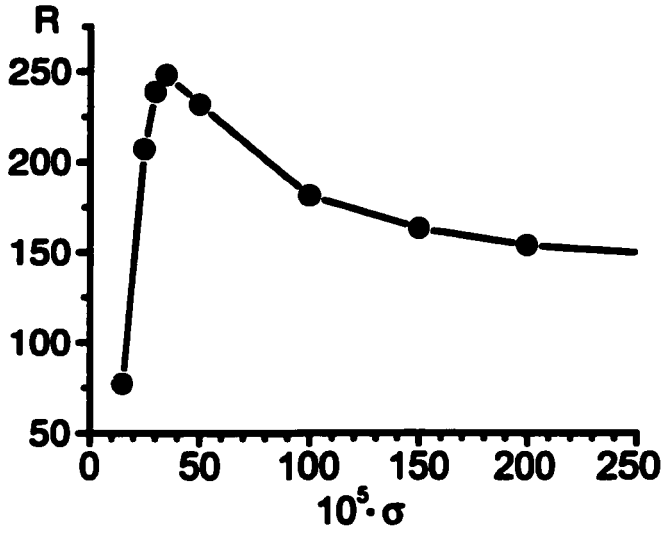

Fig. 22 Signal-to-noise ratio computed from the PDE model. The parameters are T=1400 K, $\bar{c}$ =0.3, and K=0.25. The deterministic attractor for these parameter values is a stable focus. The spectral response is averaged over 400 noise realizations as well as over the phase of the deterministic damped oscillations. The window of integration in eq. (65) contained 14 bins.

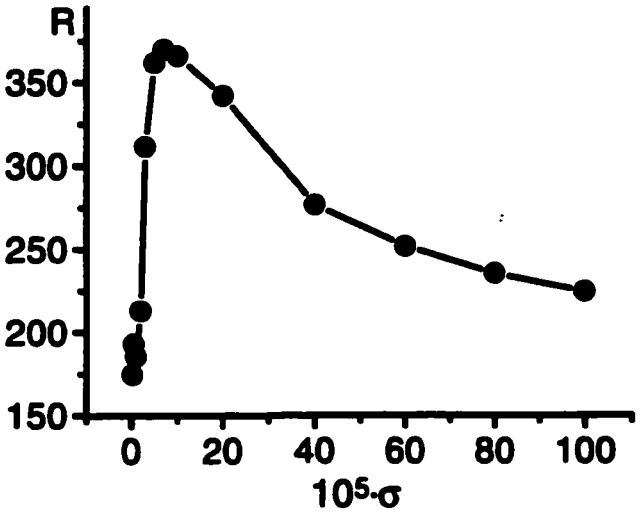

Fig. 23 Signal-to-noise ratio computed from the two-node model. The parameters are K=0.445, m=2.96, l=0.25, and d=0.5. The deterministic attractor for these parameter values is a stable focus. The spectral response is averaged over 1000 noise realizations as well as over the phase of the deterministic damped oscillations. The window of integration in eq. (65) contained 32 bins.

$$S(\omega) = \hat{c}^{-2} \int_{-\infty}^{\infty} e^{-i\omega\tau} \langle\langle c_s(t+\tau) c_s(t) \rangle\rangle d\tau. \qquad (88)$$

The double bracket indicates that the correlation function is averaged over the realizations of the noise as well as over the phase of the deterministic damped oscillations that exist in the region where the fixed point is a stable focus.

The SNRs obtained from both models have a distinct peak (Figs. 22 and 23). The system's response to the external noise shows a steep increase in the range of small noise intensities. As the noise increases, the SNR slowly decreases.

The response of the system to noise indicates that a so-called noisy precursor of the bifurcation [75] is observed in the vicinity of the Hopf bifurcation. In general, before the Hopf bifurcation, the power spectrum will have a strong response at a frequency close to that of the limit cycle created at the bifurcation point. The fact that the SNR curve passes through a maximum suggests that there is a so called coherence resonance (CR) [76], i. e. the response of a nonlinear system to noise is optimized for certain noise amplitude.

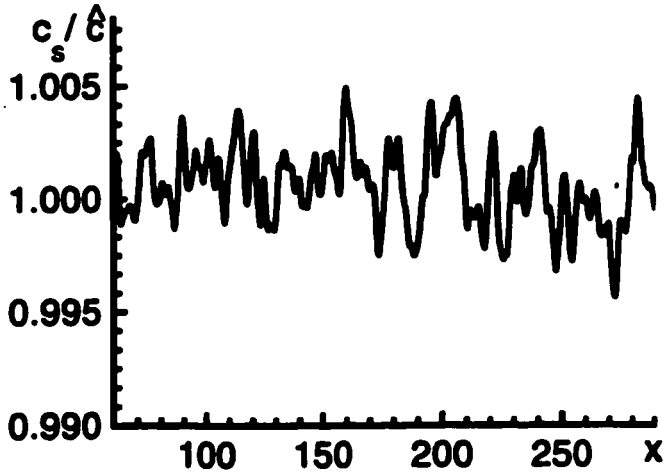

Fig. 24 Spatial concentration profile for K>1 generated by the full PDE model. The parameters are T=1400 K, $\hat{c}$ =0.3, K=1.20, and σ=5·10^{-3}. The deterministic solution for these parameter values is a stable node. The transient solution is not shown. One space unit corresponds to 210μm. Variations occur on a much larger horizontal scale than in the case of smaller K because of the strong dependence of the steady state velocity scale on the value of K.

Along with the main frequency, several lower frequencies consistently appear near the main peak and become more apparent as the system moves farther from the bifurcation in the stable focus region. One of them, located close to the main frequency, causes a beat-like pattern in the concentration profiles (Fig.18).

It is interesting to note that even for values of $K>1$, when no damped deterministic oscillation exists, the external noise has some organizing influence on the crystallization process (Fig. 24). Here, small variations of concentration form a correlated pattern that is very different from the input uncorrelated noise (in contrast to the case studied by Holten *et al* [35]).

Fig.25 shows a return map for the PDE model, i.e. the width W_{n+1} of the $(n+1)$-th zone plotted versus the width W_n of the n-th zone in Fig.18. This type of analysis is common in nonlinear dynamics to identify what might be a low-dimensional chaotic attractor. Since random noise is a key part of our models, there should be no particular pattern for small noise intensities. Indeed, in the low noise range the points seem to fill up the space evenly, which is a signature of randomness. When the noise takes the system far enough from its steady state, the deterministic dynamics of the system prevails over the stochastic motion. For large excursions the return map seems to exhibit a triangular pattern similar to the one observed for natural plagioclase [95]. The emergence of such a pattern may indicate a possibility of noise-induced chaos. The return maps obtained from the reduced 2-nodes model show no sign of such a pattern (Fig.26). This can be expected because the triangular non-repeating pattern may be a signature of chaotic attractor while the dimension of the model (79), (80) does not allow for chaotic solutions. The idea that zoning in plagioclase could be a result of a complex interplay between the deterministic nearly oscillatory internal dynamics and the external stochastic fluctuations is supported by the fact that in many cases the return maps for plagioclase appear random and no specific fractal dimension can be found [35].

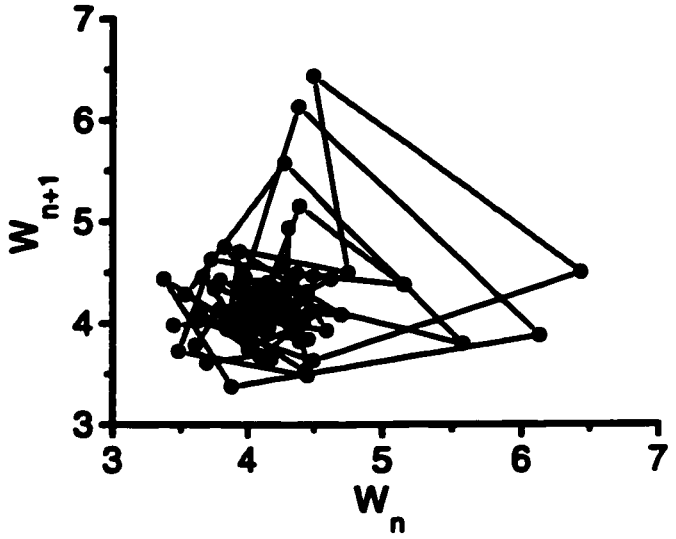

Fig. 25 Return map for the PDE model. The return map corresponds to the space concentration profile in Fig. 18 generated by the full PDE model. One space unit corresponds to 6.62μm.

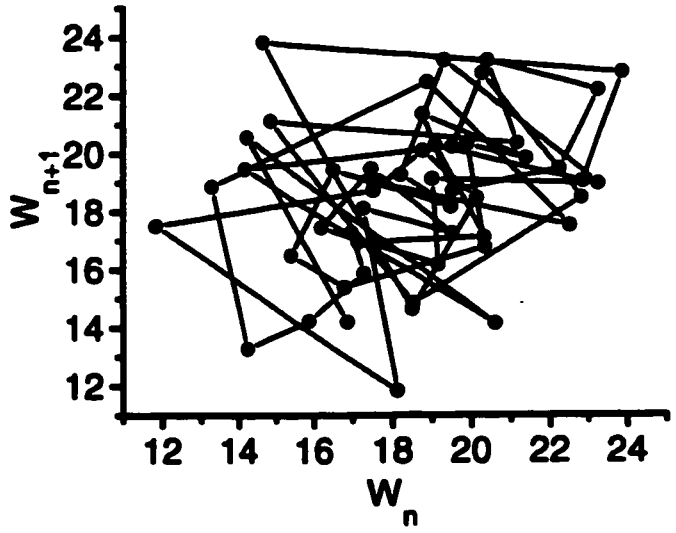

Fig. 26 Return map for the two-node model. The return map corresponds to to the space concentration profile in Fig. 19 generated by the 2-nodes model. One space unit corresponds to 21.79μm.

5.2.6 Fokker-Planck Equation

The Fokker-Planck equation for the 2-node model (85),(86) can be written in the Stratonovich interpretation (see section 4.1.4) as

$$\frac{\partial p}{\partial \tau} = -p\left(\frac{\partial f_1}{\partial \alpha} + \frac{\partial f_2}{\partial \beta}\right) - f_1 \frac{\partial p}{\partial \alpha} - f_2 \frac{\partial p}{\partial \beta}$$
$$+ \frac{\sigma^2}{2}\left[g^2\left(\frac{\partial^2 p}{\partial \alpha^2} + \frac{\partial^2 p}{\partial \beta^2} - 2\frac{\partial^2 p}{\partial \alpha \partial \beta}\right) + 3gg'\left(\frac{\partial p}{\partial \alpha} - \frac{\partial p}{\partial \beta}\right) + p(g'^2 + gg'')\right] \qquad (89)$$

where $p=p(\alpha,\beta,\tau)$ is the probability density for the system to be in a state around (α,β) at time τ, $f_1=f_1(\alpha,\beta)$ and $f_2=f_2(\alpha,\beta)$ are the deterministic terms defined in (79,80), $g=g(\alpha)=-[dl^2+v(\alpha)l]$ is the multiplicative part of the stochastic term in (85,86), and σ is the amplitude of the noise. In the stationary regime ($\partial p/\partial\tau=0$), the boundary conditions are naturally defined as the absence of probability flux across the borders of the region $0<\{\alpha,\beta\}<1/c$.

The stationary version of eq. (89) was solved numerically using the successive overrelaxation method (see Appendix B). Fig. 27 shows the stationary probability distribution corresponding to the regime for which the stable focus exists before the Hopf bifurcation (K=0.445, σ=0.02). The coordinates are the dimensionless An concentrations α and β in the melt near the interface and at the distance L_1 from it, respectively. The maximum of the probability density is shifted from the deterministic fixed point. A small crater is formed, which suggests the presence of a stochastic limit cycle and consequently a noise-induced shift in the bifurcation point (advancement). A distinct feature is the presence of a tail-shaped slow manifold adjacent to the area around the deterministic fixed point. The maximum of the probability density is located on this manifold. In terms of the system's dynamics, any relatively large fluctuation in the concentration makes the system converge to this manifold very quickly. After that, it takes a long time to come back to the vicinity of the stable focus. This results in a saw-tooth shape of the concentration time series and space profiles at high noise amplitude.

The question arises whether the noise truly advances the Hopf bifurcation point. In a 'naive' generic case, based on the normal form for the Hopf bifurcation, postponement of the bifurcation is expected. However, it was shown [99] for the Brusselator system (an important example exhibiting a Hopf bifurcation) that multiplicative noise coupled to a fast variable may cause an advancement of the bifurcation point. Although, for the Brusselator system, analogue simulations [101] found

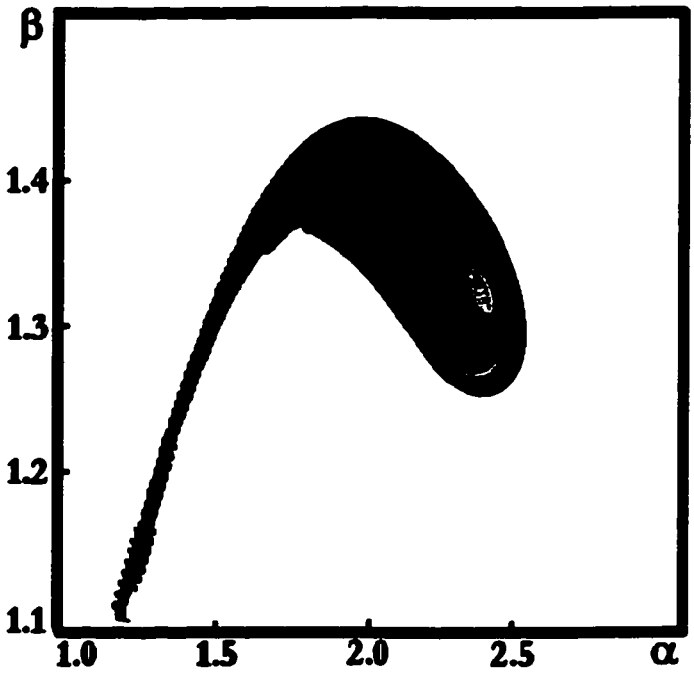

Fig. 27 Stationary probability density obtained from the two-node model. The figure shows the logarithm of the stationary probability density obtained as a solution of the Fokker-Planck equation (89) corresponding to the 2-nodes model. The parameters are K=0.445, d=0.5, m=2.96, σ=0.02, and $\hat{c}$=0.3. The deterministic attractor for these parameter values is a stable focus located at α=2.15, β=1.35. Darker areas correspond to higher probability densities. The spacing between level curves is 0.2 and the value of $\ln p$ corresponding to the light level curve in the crater is -0.3. The presence of a crater suggests the existence of a limit cycle and, consequently, a shift in the Hopf bifurcation point (advancement). The 'tail' represents a slow manifold, which is responsible for the appearance of saw-tooth patterns in the spatial concentration profiles at higher noise intensities.

only postponements, some qualitative agreement with the prediction of [99] in terms of shifts in the probability density was observed. In our model, the system's motion is faster in a direction approximately perpendicular to the tail-shaped slow manifold of Fig. 27. From eqs. (85),(86), it is seen that the variable $\alpha+\beta$ is deterministic. Therefore, the noise effectively drives the system in the direction $\beta=-\alpha$, which approximately corresponds to the direction of the fast motion. This provides a coupling mechanism between the noise and a fast variable in analogy with the Brusselator case [99].

5.3 Consideration of dissolution effects

Many oscillatory-zoned plagioclase samples show signs of dissolution events in their history [53]. It is therefore interesting to investigate the effects of dissolution in the framework of the current model. The model considers isothermal crystal growth when the local temperature-concentration conditions at the interface fall in the range that roughly

corresponds to the region between the solidus and liquidus lines in the equilibrium phase diagram. However, the model imposes no restrictions on the dissolution of the crystal when the melt concentration crosses the liquidus line.

Diffusion in the plagioclase crystal-melt system is described by the diffusion equation (67) with the boundary conditions (71) and (72). Dissolution can generally be regarded as negative growth (section 3.2.3) and the velocity of the interface V should, in this case, be considered as the dissolution rate. The dependence of the dissolution rate on the melt composition at the interface is assumed to have the same functional form as the rate of the crystal growth. The steady state concentration profile in the melt obtained by setting the left side of eq. (67) to zero and applying the boundary conditions (71) and (72) is given by

$$c_{st}(x) = \hat{c} + c_{st}(0)(1-K)\exp\left(-\frac{V_0}{D}x\right), \tag{90}$$

where K is the partition coefficient and V_0 is the steady state dissolution (or growth) rate. To simplify the analysis, a simple partition relation (73) is assumed here and in the following. By setting x=0 in this equation and solving for the steady-state concentration at the interface $c_{st}(0)$, one obtains

$$c_{st}(0) = \hat{c}/K \tag{91}$$

and the steady-state concentration profile is

$$c_{st}(x) = \hat{c}\left(1+\frac{1-K}{K}\exp\left(-\frac{V_0 x}{D}\right)\right). \tag{92}$$

From eq. (92) it follows that, for the equilibrium case V_0=0, a steady-state solution is only possible for K=1. The concentration $c_{st}(x)$ is then constant: $c_{st}(x)=\hat{c}$ everywhere in the melt. For all other values of K, it is impossible to satisfy the boundary condition (71) for the equilibrium case.

For the case of dissolution (V_0<0), the steady-state concentration profile given by eq. (92) does not exist (unless K=1) because the solution diverges for $x \to \infty$ and the boundary condition (71) cannot be satisfied. As pointed out in section 3.2.3, in theory, the dissolution rate for a diffusion-controlled process changes with time, generally as $V \propto t^{-1/2}$. This type of temporal behavior is indeed observed in some dissolution experiments [102]. Interpretation of this result for the case of a crystal dissolution in a natural environment

poses certain problems. It implies that a crystal submerged in a melt cannot dissolve at a constant rate. The speed of dissolution must decrease, asymptotically approaching zero. However, from general considerations, it is clear that, once the crystal started to dissolve, it would continue doing so because the process is favored thermodynamically. Convection and fluctuations in the environment would affect the diffusion boundary layer around the crystal and eventually the crystal dissolution rate would reach a certain finite steady state value. This type of behavior, which is more likely to occur in natural systems than the time-dependent case mentioned above, is reported in many dissolution experiments [68] and constant dissolution rate values are quoted in the literature [103]. For example, for plagioclase of intermediate composition, the dissolution rate was found to be about $30 \cdot 10^{-7}$ cm/s for a temperature of about 1500K [104]. One way to account for the constant dissolution rate is, for example, to consider advection flows [68]. The effective velocity V_0, which enters eq. (92) then includes two terms, describing both advection and diffusion, which counteract each other and therefore V_0 can be made positive. The steady dissolution regime then exists but the velocity V_0 can no longer be measured experimentally.

Besides being caused by rising temperature or some other changes in the external conditions, dissolution events, in principle, may occur at certain stages of the system's evolution as part of its internal dynamics. For example, the dissolution may be caused by a constitutional overheating effect whereby the changes in the local melt composition near the crystal-melt interface induce the dissolution of the crystal by shifting the melt concentration across the liquidus line. It is therefore interesting to investigate if the dissolution events may occur in the dynamics of the system described by the present model. It was shown previously for the case of a positive rate V (growth) that dynamical states, in which concentration varies in an oscillatory fashion, are possible when $K<K_H<1$. Stability analysis indicates that for all values of $\tilde{c}$ in the entire range of temperatures there exists a certain range of K values for which the deterministic solution of the model is oscillatory. We would like to investigate the possibility of a dissolution event in the course of such oscillations.

The existence of a macroscopic plagioclase crystal requires the bulk melt concentration $\tilde{c}$ to be greater than the concentration at which dissolution occurs for a given temperature. Close to the equilibrium, the value of the melt concentration at which dissolution occurs is given by the concentration at the liquidus line. In non-equilibrium conditions, melting may occur at different concentration values. In our case, we will define the melting concentration c_m as the characteristic concentration in the melt near the

crystal surface, for which the crystal starts to dissolve. The overall growth of the crystal is thermodynamically favored only if the bulk concentration is $\hat{c} > c_m$. In the opposite case ($\hat{c} < c_m$), dissolution events cannot occur in the process of the oscillatory crystal growth because the crystal dissolves completely once the concentration at the interface $c(0)$ drops below c_m.

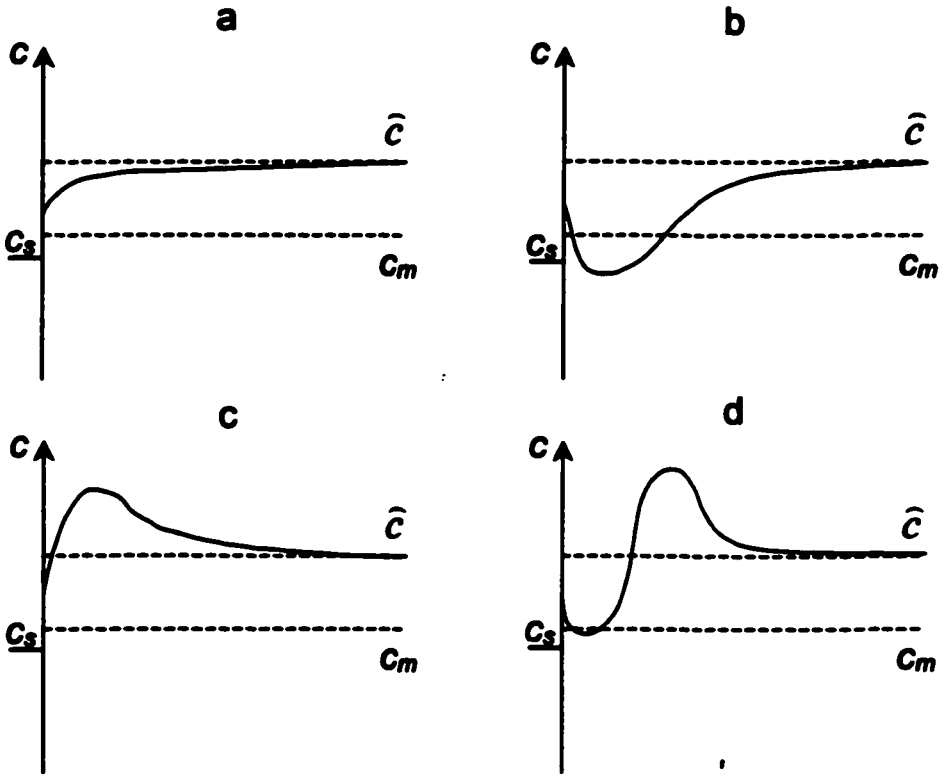

Fig. 28 Impossibility of dissolution in the present constitutional undercooling model. a,c) $\partial c(0,t)/\partial x > 0$; b,d) $\partial c(0,t)/\partial x < 0$.

Since, in the oscillatory regime, the partition coefficient is $K<1$, the melt concentration at the interface c_0 is always greater than the concentration in the solid ($c_s = Kc_0$). From this relation and eq. (92) for $x=0$, it immediately follows that $c_s = \hat{c}$ in the steady state. Thus, in the steady state, $c_0 > c_s = \hat{c} > c_m$.

Since the melt concentration at the interface evolves in time in a continuous fashion, in order for its value to achieve the region where dissolution can occur ($c_0 < c_m$), the system must, at some point in its evolution around the steady state, pass a state where $c_m < c_0 < \hat{c}$. Several types of the melt concentration profiles may correspond to this

situation (Fig. 28). If the melt concentration increases away from the interface into the melt (Fig. 28a,c) then

$$\left.\frac{\partial c}{\partial x}\right|_{x=0} > 0. \qquad (93)$$

However, the growth rate in the region $c_\infty < c_0 < \hat{c}$ is $V>0$ and the boundary condition (72) for $K<1$ ($c_s<c(0)$) necessarily requires that

$$\left.\frac{\partial c}{\partial x}\right|_{x=0} < 0. \qquad (94)$$

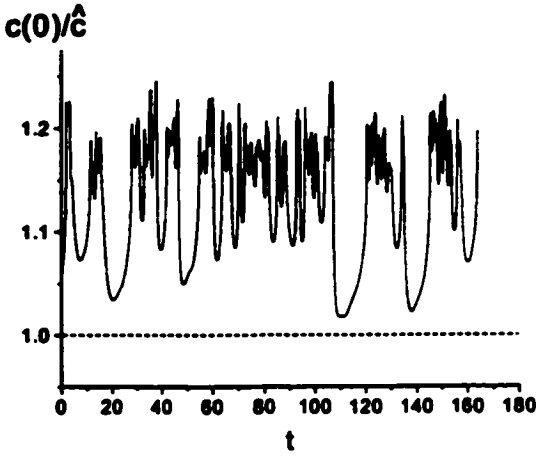

Fig. 29 Time evolution of the interface melt composition in presence of noise. The melt composition at the interface generated by the full PDE model is shown as a function of time. T=1563K, $\hat{c}$ =0.19 (marked on the graph by a dotted line), K=0.883, and σ=0.04. For the given temperature, the concentration at the liquidus line is $c_\infty/\hat{c}$ =0.74.

Dissolution is thus impossible to achieve in the course of concentration oscillations about the steady state for the type of the concentration profiles in the melt shown in Fig. 28a,c. The condition of negative space derivative at the interface can be fulfilled if the melt concentration is not a monotonous function of the distance in the vicinity of the interface (Fig. 28b,d). Such situations may, in principle, occur in the presence of noise. Numerical results (Fig. 29), however, demonstrate that adding a reasonable amount of noise to the boundary condition far from the crystal according to eq. (82) does not allow for the possibility of such dissolution events. The melt concentration at the interface $c(0,t)$ never becomes smaller than $\hat{c}$. The system's dynamics becomes extremely slow for $c(0,t)$ close to $\hat{c}$ and dissolution is not possible for the noise amplitudes within any reasonable limits.

5.4 Discussion

We have shown that fluctuations of environmental parameters such as magma composition may lead to pattern formation exhibiting an oscillatory character in plagioclase. Variations in the crystal growth environment may be caused by magma mixing, changes in H_2O content, releases of gases or temperature variations. The exact physical nature of these environmental fluctuations as well as their magnitude is an interesting question but outside the scope of the present work.

In our model of plagioclase growth from melt, relatively small random fluctuations of the bulk concentration of An stimulate the internal dynamical processes, which result in a more or less regular compositional zoning. Close to a Hopf bifurcation, in the region where the deterministic steady state of the system is stable focus, the noise excites oscillations with a frequency close to the frequency that deterministically the system exhibits after the bifurcation. As a side effect, some lower frequencies are also generated. The signal-to-noise ratio exhibits a distinct peak typical of coherence resonance phenomena. The presence of noise thus extends the available parameter space for which oscillatory zoning may be observed.

The return maps generated according to the full stochastic PDE model for large excursions in the concentration profile show triangular patterns similar to the ones observed in natural plagioclase.

The reduced 2-node model, in which the spatial dependence of the concentration is approximated by straight lines, has a dynamical behavior which is similar to the full PDE model around the Hopf bifurcation point. The solution of the Fokker-Planck equation for this case suggests the possibility of advancement of the bifurcation due to noise. The presence of a slow manifold in the region of phase space adjacent to the area around the deterministic fixed point results in the oscillations taking the form of spikes. Since the model is described by two variables, it is unable to produce chaotic deterministic solutions. As a next step, one could suggest a three-node reduction that would then allow one to simulate the chaotic behavior.

It was shown that dissolution events are impossible in the deterministic dynamics of the current model, as well as in the presence of noise with a reasonably small intensity introduced to the boundary condition. While other plagioclase zoning models that are based on intrinsic mechanisms were also unsuccessful in reproducing the dissolution

events, the dissolution surfaces observed in natural plagioclase crystals are likely to be caused by sudden external heating events (extrinsic mechanisms).

Chapter 6

Banding in $(Ba,Sr)SO_4$

6.1 Autocatalytic model of banding in $(Ba,Sr)SO_4$

Oscillatory patterns in $(Ba,Sr)SO_4$ single crystals constitute one of the very few examples of mineral oscillatory zoning phenomena that have been reproduced in a laboratory environment [16]. Oscillatory zoned crystals of barite-celestite solid solution synthesized by A. Putnis's group contained up to 10 zones where Ba crystal composition switched abruptly between roughly 25 and 90 percent. The typical zone width was about 7-10 μm and the typical zoned crystallites were about 150 μm in size.

The experiment was conducted in a controlled environment and therefore most of the microscopic crystal growth parameters, such as supersaturation or the diffusion coefficient, are known or can be estimated with sufficient precision. Since this kind of information is almost never available for minerals growing in a natural environment, constructing a model that can simulate the experimentally observed oscillatory zoning is an important step towards understanding natural oscillatory zoning.

In this section, we suggest an autocatalytic model of oscillatory banding in $(Ba,Sr)SO_4$ crystals. The numerical solutions are obtained for the two limit cases: the one-dimensional growth of a flat crystal face and the growth of a small spherical crystallite. Also, a reduced model for the growth of a spherical crystallite is considered, which allows to perform a more complete analysis. Finally, the impact of fluctuations in the crystal growth environment on the oscillatory pattern formation is considered.

Table I. Experimentally obtained textures in $(Ba,Sr)SO_4$.

Concentrations at the reservoirs M_i, M Ba-Sr-SO_4	Type of zoning	Nucleation location[#] y, cm	Core[@] X	Nucl. time τ, h	Concentration at nucleation[**], $\hat{m}$, mM Ba / Sr / SO_4
0.5-0.5-0.5	OZ	13-16	0.90	288	7.7-1.4 / 6.8-1.2 / 1.4-8.7
0.5-0.5-0.3	OZ	15-18	0.90	312	3.6 -0.6/ 3.1-0.5 / 4.0-17.1
0.3-0.3-0.5	OZ	16[*]	0.91	336	1.7 / 1.6 / 13[*]
0.3-0.3-0.3	Z1	13-15		360	9.0-3.7 / 8.2-3.2 / 2.4-6.4
0.5-0.5-0.1	Z1	17-20	0.88	384	3.0-0.6 / 2.6-0.5 / 5.9-17.0
0.3-0.3-0.1	Z1	18[*]	0.89	408	1.6 / 1.4 / 24[*]
0.3-0.1-0.1	BA	21[*]	0.94	576	1.7 / 0.8 / 30[*]
0.1-0.3-0.1	Z1 & Z2	21[*]	0.79	624	0.9 / 1.6 / 31[*]

The crystal zoning experimental data is taken from [105]. The nucleation time is counted from the moment the solutions enter the gel column.

Notation: OZ – oscillatory zoning, Z1 = Ba rich-Sr rich-Ba rich, BA = barite, Z2 = Sr rich – Ba rich – Sr rich.

[#] Location of the nuclei in the gel column is taken from [106] were it was reported for the pure barite case.

[@] The composition of the crystal core is assumed equivalent to the composition of the newly nucleated crystallites. The corresponding data is taken from [107].

[*] The concentrations of Ba^{2+} and Sr^{2+} at the nucleation site at the nucleation time were taken from [105]. The corresponding nucleation location and the concentration of SO_4^{2-} were calculated using Eq. (110).

[**] The concentrations at the nucleation site were calculated from Eq. (110). The range of the values given corresponds to the range in the nucleation location y.

6.1.1 Crystal growth conditions.

In a series of experiments by A. Putnis's group [16,105,106,107], barite and barite-celestite solid solution crystals were grown from an aqueous solution during counterdiffusion in a gel column connecting the reservoirs with the initial reactants (Fig.3). The pore diameter in the gel varied from less than 0.1 μm up to 0.5 μm and the 'effective water' content in the gel was about 95.6%. The morphology of the obtained crystals was studied by scanning electron microscopy. Various zoning textures [105] corresponding to different initial reservoir concentrations are reproduced here in Table I. Nucleation and growth of the Ba-Sr crystals from the solution have been extensively studied [26,106,107,108] and data are available for many of the important parameters.

The available experimental data allows us to make some estimates about the process of crystal growth. Let r be the characteristic distance from the core of the crystal to its edge. The barite-celestite crystals grew by r=70 μm in about a month, which gives an average growth rate $V_{av} \sim 3 \cdot 10^{-9}$ cm/s. For a typical diffusion coefficient D of the order of 10^{-5} cm^2/s, a characteristic time scale for the adjustment of the diffusion field around the crystal is $r^2/D \approx 5$ s. This is much smaller than the crystal growth time $r/V_{av} \approx 1$ month and therefore the diffusion field adjusts quickly to changes in concentration caused by the crystal growth.

In the approximation of a spherical crystal, the considerations of section 3.2.2 can be generalized for the case of multicomponent growth from a solution. If c is the solid molar concentration of some species and m is the corresponding concentration in the solution, then crystal growth occurs in a kinetic regime if the factor $cV_{av}r/(Dm) \ll 1$. For typical aqueous concentrations at the nucleation site of about 2mM and a characteristic solid molar volume of 52 cm^3/ mole, it follows that $cV_{av}r/(Dm) \approx 0.02$. A straightforward evaluation of the factor $\beta r/D$ in eq. (38) yields a similar result: $\beta r/D \approx 0.07$, where β was evaluated from eq. (39). It follows that for small crystallites, the growth is defined by the processes at the crystallite-solution interface and the solution concentration in the vicinity of the interface is close to its bulk value. As the crystallites grow larger, diffusion starts to play a role. These estimates are consistent with experimental observations reported in several works [109,110]. Switching from an interface-controlled growth by polynuclear mechanism to a diffusion-controlled growth was observed in those experiments in $BaSO_4$ growth from solution when the size of the crystals exceeded a certain value. In those nucleation-and-growth experiments, the change in growth mechanisms was observed when the crystallite size exceeded about 1μm. The Ba concentration in the solution at the

time of the mechanism change exceeded 0.4mM and the growth rate was about $3 \cdot 10^{-7}$ cm/s.

6.1.2 Model

Our model is based on a previously suggested model of the $(Ba,Sr)SO_4$ growth from a strongly supersaturated solution [111]. In that work, growth of a flat crystallite face was considered and the partial differential equations describing the dynamics of the reaction-diffusion system were reduced to a system of ordinary differential equations. Linear stability analysis of that system and its direct numerical solution demonstrated the existence of oscillatory solutions. Here, the set of PDEs is directly solved in order to obtain a more accurate description of the diffusion and the crystal growth. The model is further improved by an extension to the case of the radial growth of a spherical crystal and the consideration of noise effects.

We consider the growth of $(Ba,Sr)SO_4$ crystals from a solution in the setup shown in Fig.3. We are not interested in the nucleation phase [26] and therefore consider only the growth of a previously nucleated crystallite. The growth proceeds according to the precipitation reactions

$$SO_4^{--} + Ba^{++} \rightarrow BaSO_4,$$

$$SO_4^{--} + Sr^{++} \rightarrow SrSO_4,$$

where both $BaSO_4$ and $SrSO_4$ are incorporated in the same crystal to form a solid solution. The following symbolic notation is used in the description of the model below: A= SO_4^{--}, B=Ba^{++}, C=Sr^{++}, BA= $BaSO_4$, and CA= $SrSO_4$. Since the growth layers of similar chemical composition in the observed zoned crystals are parallel to the crystal faces, we first consider growth only in one dimension, in the direction perpendicular to the crystal face. We choose a frame of reference moving with the growing crystal in such a way that x=0 always corresponds to the crystal-solution interface.

If $m_i(x,t)$ are the concentrations (moles per volume) of the ions of species i (i=A,B or C) and V is the rate of the crystal surface advance (length/time) then the evolution of the species concentration fields in the diffusion boundary layer surrounding the crystal is given by the diffusion equations:

$$\frac{\partial m_i}{\partial t} = D_i \frac{\partial^2 m_i}{\partial x^2} + V \frac{\partial m_i}{\partial x} \qquad (95)$$

where D_i are the diffusion coefficients in the solution (assumed independent of the concentration) and the second term is due to the choice of the coordinate system. The boundary condition far from the growing crystal is naturally given by

$$m_i(\infty,t)=\bar{m}_i(t), \tag{96}$$

where $\bar{m}_i(t)$ are the bulk values of the concentrations at the crystallization site that may depend on time because of the influx of species from the reservoirs. The continuity of the mass current at the crystal-solution interface (x=0) gives the second boundary condition:

$$D_i\frac{\partial m_i}{\partial x}\bigg|_{x=0}+[m_i(0,t)-c_i(t)]V=0, \tag{97}$$

where $c_i(t)$ denotes the molar concentration in the solid at the growing front. It is clear from the stoichiometry that $c_A=c_B+c_C$. Also, for the case of crystal growth from a solution, $c_i>>m_i$ (in contrast to the case described by Eq. (72) for plagioclase growth from a melt).

Since the above estimates suggest that a change in a growth mechanism may occur as the crystal becomes larger, an extension of the model to the case of a spherical crystal is useful. By writing the diffusion equations for the solution species in spherical coordinates and assuming the growth in the radial direction only, one finds that equations (95), (96), and (97) can be transformed into

$$\frac{\partial m_i}{\partial t}=D\frac{\partial^2 m_i}{\partial \rho^2}+\frac{2D}{\rho'}\frac{\partial m_i}{\partial \rho}+V\frac{\partial m_i}{\partial \rho} \tag{98}$$

$$m_i(\rho\to\infty,\,t)=\bar{m}_i(t), \tag{99}$$

$$D\frac{\partial m_i}{\partial \rho}\bigg|_{\rho=0}+[m_i(0,t)-c_i(t)]V=0 \tag{100}$$

where ρ is the distance from the interface measured in the radial direction and ρ' is the distance from the center of the crystal. If the initial nucleus has the size r_0 then

$$\rho'(t)=\rho(t)+r_0+\int_0^t V(t')dt'. \tag{101}$$

It is convenient to describe the composition of the solid phase by the mole fraction of $BaSO_4$ in the crystal X ($0\le X\le 1$). The relationship between X and c_i is then given by

$$c_B = \frac{X}{v_{BA}X + v_{CA}(1-X)}; \qquad c_C = \frac{1-X}{v_{BA}X + v_{CA}(1-X)}, \tag{102}$$

where v_{BA} and v_{CA} are the molar volumes of the solid $BaSO_4$ and $SrSO_4$, respectively.

Evolution of the crystal composition X at the interface is determined kinetically by the rates V_{BA} and V_{CA} at which the units of BA and CA are attached (or detached) to the crystal surface. They can be defined as the growth rate for a flat crystal face consisting of pure $BaSO_4$ and $SrSO_4$, respectively, in m/s. The total growth velocity is then [111]

$$V = V_{BA} + V_{CA}. \tag{103}$$

Using mass balance across the crystal-liquid interface (see Appendix C),

$$L\alpha \frac{dX}{dt} = [V_{BA} - X(V_{BA} + V_{CA}/\alpha)][X + (1-X)\alpha]^2, \tag{104}$$

where $\alpha = v_{CA}/v_{BA} = 0.89$ and L is the effective crystal-solution interface width which characterizes the roughness of the interface. If the difference in molar volume is neglected, this equation reduces to

$$L\frac{dX}{dt} = V_{BA} - XV. \tag{105}$$

In the steady state, the crystal composition is thus kinetically defined [112] as $X = V_{BA}/V$.

The three equations (95) or (98) are coupled among themselves as well as with eq. (104) through the term containing the growth velocity V.

In general, the crystal growth rate V depends nonlinearly on the concentrations in the solution m_A, m_B, and m_C near the interface. Generalizing eqs. (23)-(25) for the case of a continuous two-component growth of the crystal surface in contact with a dilute solution, the growth rate can be approximated by

$$V_{BA} = \beta'_{BA}(m_B m_A - m_B^0 m_A^0) \tag{106}$$

where m_i^0 are the equilibrium concentrations in the solution and β'_{BA} is the kinetic coefficient [57]

$$\beta'_{BA} = a_{BA} f v_{BA}^2 (a_{BA}/\delta_{BA})^2 \exp[-\Delta U_{BA}/kT]. \tag{107}$$

Here, a_{BA} is the size of a molecular building unit, f is a frequency factor, v_{BA} is the molar volume in the solid, δ_{BA} is the average distance between the kink sites, and ΔU_{BA} is the energy barrier for the incorporation of the building unit into the crystal. The factor $(a_{BA}/\delta_{BA})^2$ characterizes the probability of finding a suitable kink site on a two dimensional surface of the crystal. The growth rate V_{CA} can be defined in a similar way.

Attachment of the $BaSO_4$ units to the $BaSO_4$ kink sites is energetically favoured over their attachment to the $SrSO_4$ kink sites because of the lattice misfit and because chemical bonding is generally stronger between units of the same species. Thus, the average distance between the favorable kink sites for the attachment of $BaSO_4$ is expected to decrease with increasing $BaSO_4$ molar fraction in the crystal surface. The simplest relation that mimics this dependence on the crystal composition is [111]

$$(a_{BA}/\delta_{BA}) \propto X + p_1; \quad (a_{CA}/\delta_{CA}) \propto 1-X+p_2, \tag{108}$$

where the constants $p_{1,2}$ characterize the residual probabilities of finding a favourable kink site for the growth of $BaSO_4$ on a pure $SrSO_4$ surface, and vice-versa. The growth rates then take the form

$$V_{BA} = \beta_{BA}(m_B m_A - m_B^0 m_A^0)(X + p_1)^2;$$
$$V_{CA} = \beta_{CA}(m_C m_A - m_C^0 m_A^0)(1 - X + p_2)^2, \tag{109}$$

where $\beta_{BA,CA}$ are new kinetic coefficients. For highly supersaturated solutions, the product of the equilibrium concentrations in eqs. (109) can be neglected [111]. This expression for the growth rates thus describes the autocatalytic growth of a two-component crystal.

The autocatalytic dependence of the growth rates on the crystal composition provides for the possibility of generating oscillatory patterns in the crystal composition by the following qualitative mechanism: When the surface of a growing crystallite is rich in, say, B, the attachment of B units to the crystal surface from the solution is energetically favored over the attachment of C. Thus, a B-rich crystal zone is formed while the solution in the vicinity of the crystal is being depleted of B and becomes enriched in C. Eventually, a C-rich layer will nucleate on the surface of the B-rich crystal, which causes further autocatalytic attachment of the C units from the solution and therefore a growth of a C-rich crystal zone. This, in turn, depletes the solution of C while diffusion gradually increases the concentration of B until nucleation of B occurs and the cycle is thus repeated.

To correctly simulate the crystal growth experiment in the setup shown in Fig.3, one needs to know the time dependence of the bulk concentrations $\hat{m}_i$ in the solution at the crystallization site. The evolution of the concentration profiles in the gel can be found analytically [111] by solving the corresponding diffusion equations. Considering the reservoirs to be inexhaustable (which is a good approximation for experiment duration times less than one month and for large reservoir concentrations [106]) and neglecting the depletion of the solution due to crystallization, the time evolution of the aqueous concentrations at the crystallization site is given by

$$\hat{m}_{B,C}(t) = M_{B,C}\,\mathrm{erfc}\left(\frac{y}{2\sqrt{D_{B,C}(t+\tau)}}\right),$$
$$\hat{m}_{A}(t) = M_{A}\,\mathrm{erfc}\left(\frac{H-y}{2\sqrt{D_{A}(t+\tau)}}\right), \qquad (110)$$

where M_i are the known concentrations of the components i in the reservoir, y is the distance from the $BaCl_2$-$SrCl_2$ reservoir to the nucleation site, H=28 cm is the total column length, and τ is the nucleation time measured from the moment the solutions enter the gel column. The location of the crystallization site y can be determined from the $BaSO_4$- $SrSO_4$ nucleation experiments in the same experimental setup [106,107].

6.1.3 Steady state solutions of PDEs

Eqs. (95) with boundary conditions (96) and (97) do not have a steady-state solution. This is easily shown by tentatively setting the left-hand side of the equation to zero and integrating twice over the space coordinate x to obtain what would be the steady-state concentration distribution in the solution:

$$m_{st,i}(x) = C_{1i} + \frac{D_i}{V}\exp\left(-\frac{x}{D_i/V}\right)C_{2i}\,. \qquad (111)$$

The integration constant C_{1i} can be obtained from the boundary condition (96):

$$C_{1i} = \hat{m}_i; \qquad (112)$$

The boundary condition (97) does not allow one to determine the second integration constant C_{2i} but leads to $\hat{m}_i = c_{st,i}$, where $c_{st,i}$ are the steady state molar concentrations in the crystal. The latter relation is impossible because the concentration in the solid phase c_{st} is always greater than the concentration in the solution.

A steady state may be achieved, however, if a diffusion boundary layer of finite width is considered. If the boundary condition (96) is taken not at the infinity but at some finite distance from the interface l, then the integration constant C_{2i} can be obtained as

$$C_{2i} = \frac{V}{D_i}(\hat{m}_i - c_{st_i})e^{\frac{V}{D_i}l} \tag{113}$$

and the equation (111) becomes

$$m_{st_i}(x) = c_{st_i} - (c_{st_i} - \hat{m}_i)e^{\frac{V}{D_i}(l-x)}. \tag{114}$$

By taking this relation at x=0 and expanding the exponent, the boundary layer width can be obtained

$$l = \frac{D_i}{V}\frac{\hat{m}_i - m_i(0)}{c_{st_i} - \hat{m}} \approx \frac{D_i}{V}\frac{\hat{m}_i - m_i(0)}{c_{st_i}}. \tag{115}$$

In this case, the concentration profiles in the solution near the crystal interface have an approximately linear form

$$m_i(x) \approx m_i(0) + c_{st_i}\frac{V}{D_i}x. \tag{116}$$

While the current work does not rely on the above simplifications, the approximations (115) and (116) were taken in [111].

If instead of linear growth in one dimension, a radial growth of a spherical crystallite is considered, then a pseudo-steady-state solution similar to eq. (38) can be obtained by solving equation (35) with boundary conditions (36) and (37) and the growth rates given by (109). If the diffusion field in the solution adjusts itself adiabatically to the changes caused by the increase in the crystal size and the difference in solid molar volume is neglected so that $X_{st}=V_{BA}/V$ in eq. (105), the steady-state concentration profile in the solution can be obtained in the form

$$m_i(\rho') \approx \hat{m}_i - \frac{V_i}{\nu D_i}\frac{r^2}{\rho'}, \tag{117}$$

where the steady-state growth rate V_i is either $V_B=V_{BA}$, or $V_C=V_{CA}$, or $V_A=V_{BA}+V_{CA}$, r is the slowly increasing crystal radius, $\rho' \geq r$ is the distance from the center of the crystal, and ν is the molar volume. When the second term is small, the concentration near the

crystal-solution interface is close to the bulk concentration value, and the crystal growth occurs in the kinetic regime. However, as the crystal becomes larger, diffusion starts to play a role.

The pseudo-steady-state concentrations at the interface $m_i(r)$ are obtained as the solutions of the system of equations (117) taken at $\rho'=r$ where the growth rates V_i depend on $m_i(r)$ through (109). If the solution concentration at the interface is not very different from its bulk value and the equilibrium concentrations in eqs. (109) are neglected then the steady state concentrations at the interface are

$$\begin{aligned} m_A &\approx \hat{m}_A[1-\hat{m}_B\alpha_B^{'}-\hat{m}_C\alpha_C^{'}] \\ m_B &\approx \hat{m}_B[1-\hat{m}_A\alpha_B] \\ m_C &\approx \hat{m}_C[1-\hat{m}_A\alpha_C], \end{aligned} \tag{118}$$

where

$$\alpha_B = r\frac{1}{\nu}\beta_{BA}(X+p_1)^2/D_B \;;\; \alpha_C = r\frac{1}{\nu}\beta_{CA}(1-X+p_2)^2/D_C$$

$$\alpha_B^{'} = r\frac{1}{\nu}\beta_{BA}(X+p_1)^2/D_A \;;\; \alpha_C^{'} = r\frac{1}{\nu}\beta_{CA}(1-X+p_2)^2/D_A$$

In the general case of arbitrary interface concentrations, the pseudo-steady-state solution also exists and is continuous both in r and X, as verified numerically for a wide range of parameter values. This indicates that, under the current approximations, the steady-state solution is always stable. Therefore, oscillatory solutions or switching between steady states are only possible when those approximations cease to be valid, i.e. when the distortion of the diffusion field in the solution due to the changes in the crystal size r is considered.

The steady-state value of the composition X is obtained by setting the left-hand side of the Eq. (105) equal to zero. Using the approximation (109), one obtains

$$X_{ss} = \frac{V_{BA}}{V} = \frac{\beta_{BA}m_B(X_{ss}+p_1)^2}{\beta_{BA}m_B(X_{ss}+p_1)^2+\beta_{CA}m_C(1-X_{ss}+p_2)^2}. \tag{119}$$

If the concentrations m_B and m_C are similar, $\beta_{BA}\approx\beta_{CA}$, and the small parameters p_1 and p_2 are approximately equal, then the steady-state composition is close to one of the values in the set

$$X^s = \{0, 0.5, \text{or } 1\}, \tag{120}$$

These values correspond to pure $SrSO_4$, a crystal composition with equal proportions of Ba and Sr sulphate, or pure $BaSO_4$, respectively.

The diffusion of Ba^{++}, Sr^{++}, and SO_4^{--} from the reservoirs (Fig.3) is coupled to the diffusion of Cl^- and Na^+ to maintain the overall electrical neutrality of the solution. The effective diffusion coefficients for the salts can be estimated from the Nernst-Hartley relation [58]:

$$D_{salt} = \frac{(z_+ + |z_-|)D_+D_-}{z_+D_+ + |z_-|D_-}, \tag{121}$$

where D_+ and D_- are the tracer diffusion coefficients for the cations and anions and z_+ and z_- are the respective charges. Thus, using ionic diffusion data for individual elements [58], the binary diffusion coefficients can be obtained as $D(BaCl_2) = 1.39 \cdot 10^{-5}$ cm^2/s, $D(SrCl_2) = 1.34 \cdot 10^{-5}$ cm^2/s, and $D(Na_2SO_4) = 1.23 \cdot 10^{-5}$ cm^2/s. The diffusion coefficients for multicomponent ionic diffusion when more than two ionic species are considered, in general, depend on the concentration of the species in the solution [58] and therefore their values change as the concentration profiles evolve in time. However, they should not be very different from the binary coefficients calculated above.

6.1.4 Numerical results

The equations were non-dimensionalized in the following way: The concentrations m_i were scaled by a typical value $\bar{m} \sim 5$ mM $= 5 \cdot 10^{-6}$ mole/cm^3. The solid-phase concentrations were scaled by the inverse molar volume of $BaSO_4$ $\bar{c} = 1/v_{BA} = 0.019$ mole/cm^3. The growth velocity was scaled by a typical value $\bar{V} \sim 10^{-8}$ cm/s. The space coordinate x was scaled by the width of the diffusion boundary layer defined in eq.(115): $\bar{l} = \bar{m} D_A / \bar{V} \bar{c} \approx 3$ mm where D_A is the effective diffusion coefficient for SO_4^{--}, $D_A = 1.23 \cdot 10^{-5}$ cm^2/s. This value of the diffusion boundary layer width is consistent with the value obtained in [18] where the diffusion profile was similarly approximated by a linear segment in modeling calcite zoning. The time variable was scaled by $\bar{t} = \bar{l}^2 / D_A \approx 8.3 \cdot 10^3$s $= 2.3$h and the effective crystal-solution interface width L was scaled by $\bar{L} = \bar{V} \bar{t} \approx 0.8$ μm. In addition, several other dimensionless parameters were introduced: $\alpha = \nu_{CA} / \nu_{BA}$, $\beta = \beta'_{CA} / \beta'_{BA}$, $d_B = D_B / D_A$, and $d_C = D_C / D_A$. The equations (95)-(97), and (104) then transform into

$$\frac{\partial m_i}{\partial t} = d_i \frac{\partial^2 m_i}{\partial x^2} + \gamma V \frac{\partial m_i}{\partial x} \tag{122}$$

$$m_i(l,t) = \hat{m}_i(t) \tag{123}$$

$$d_i \left.\frac{\partial m_i}{\partial x}\right|_{x=0} + [m_i(0,t)\gamma - c_i(t)]V = 0 \tag{124}$$

$$L\alpha \frac{dX}{dt} = [V_{BA} - X(V_{BA} + V_{CA}/\alpha)][X + (1-X)\alpha]^2 \tag{125}$$

where all the variables are in their dimensionless form and d_A=1. The ratio of the concentration scales in the aqueous and solid phases is $\gamma = \bar{m}/\bar{c} = 0.25 \cdot 10^{-3}$. Due to the finite grid size, the boundary condition (123) is taken at the distance l from the interface, which is of the order of $\bar{l}$.

The nondimensionalized system of three partial differential equations (122) alone with the boundary conditions (123) and (124) and the ordinary differential equation (125) were solved using a Crank-Nicholson algorithm with adaptive step size and iteration over the nonlinear term containing the growth velocity V.

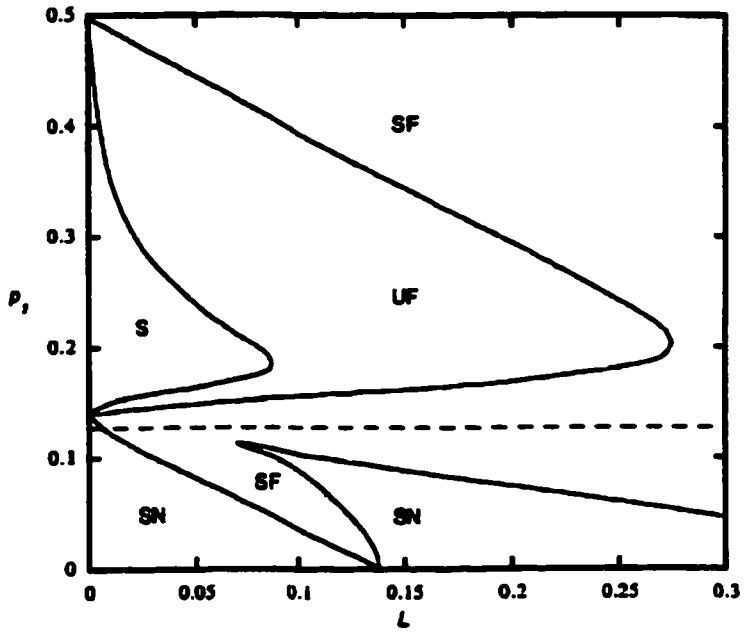

Fig. 30 Linear stability diagram for the reduced model of [111]. The corresponding parameter values are $\hat{m}_i$=2, α=0.89, β=1, d_B=0.79, d_C=0.74, and p_1=p_2. The stability regions are denoted as follows: SF - stable focus, UF - unstable focus, S - saddle, and SN - stable node. The bistability region extends below the dashed line in the diagram.

First, crystal growth was considered for constant bulk species concentrations $\bar{m}_i$=const. For a one-dimensional system, due to the finite grid size, a steady crystal growth regime is eventually achieved if the system is let to evolve for a sufficiently long time. The stability of these steady state solutions can be investigated in analogy with the types of solutions found for the reduced version of the system [111]. There, the linear stability analysis indicated the presence of a stable focus, an unstable focus, a stable node, and a saddle (Fig. 30). A bistable regime for which two different stable steady states coexist was observed for small values of the parameters p_1 and p_2.

Here, the stability of the steady state was determined numerically by observing the dynamical solution behavior in the vicinity of the steady state. Due to the difficulties in determining the exact linear stability type for the numerical solutions, only the stability property (stable or unstable) for the steady state was recorded. The regions of stability found in the present case are illustrated in Fig. 31 for a simplified version of the system with d_B=d_C=1, p_1=p_2=p, γ=0, α=1, and β=1. The bulk concentrations in the solution were taken as $\bar{m}_i$=2. For the range of the parameters L and p considered, two stable steady states coexist for small values of p (Fig. 32). For large values of p, the steady state is unstable and the numerical solution exhibits oscillatory character (Fig. 32). The exact value of p for which the steady state loses its stability depends on the value of l. The line that separates the regions of stability in Fig. 31 corresponds to the line that separates the regions of unstable focus and stable focus in Fig. 30. In the general case of arbitrary values of d_B, d_C, γ, α, and β, the region of bistability in Fig. 31 is separated from the region where the steady state becomes unstable by a region where there exists only one stable steady state. This is also consistent with the stability properties of the reduced system. Increasing the values of the bulk concentrations shifts the curve in Fig. 31 down, thus enlarging the region where the steady state is unstable. In the general case of arbitrary d_B, d_C, γ, α, and β, the curve, which separates the region where a single stable steady state exists from the unstable region, is also shifted downward.

Similar results are obtained for the case of a spherical crystallite growth in the limit of large crystallite radius. For r~1, the concentration in the solution varies on a spatial scale of the order $\tilde{l}$ and the approximation of a flat crystal surface is sufficiently accurate. For smaller crystallites, however, the concentration variations occur on a much smaller scale and the system's dynamics is different (Fig. 33). For small initial crystallite radius, the stable steady state does not lose its stability even for large values of the parameter p.

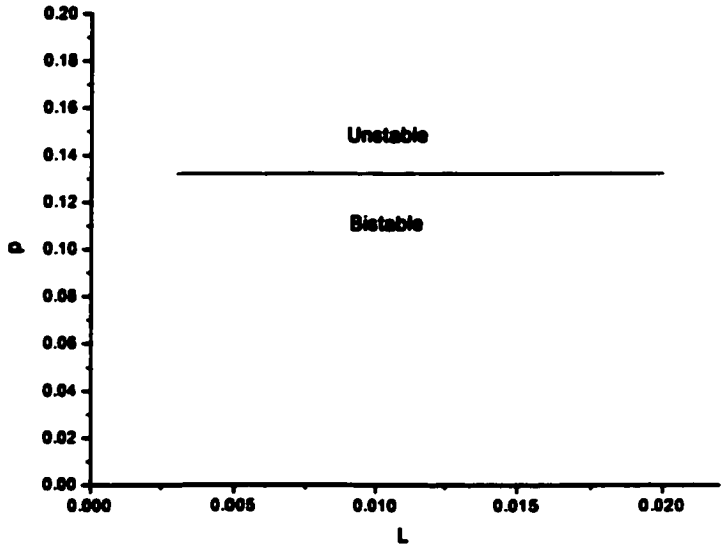

Fig. 31 Stability diagram for the full PDE model in 1D. The stability of the steady state was determined numerically. For simplicity, here $d_B=d_C=1$, $p_1=p_2=p$, $\gamma=0$, $\alpha=1$, and $\beta=1$. The horizontal boundary between the stable and unstable regions corresponds to the horizontal line between the SF and UF regions in Fig. 30. The stability of the system for small values of L could not be determined because of the strong dependence on the width of the boundary layer l, which appears in numerical simulations when the concentration profile in the solution evolves on a spatial scale comparable with the size of the simulation grid.

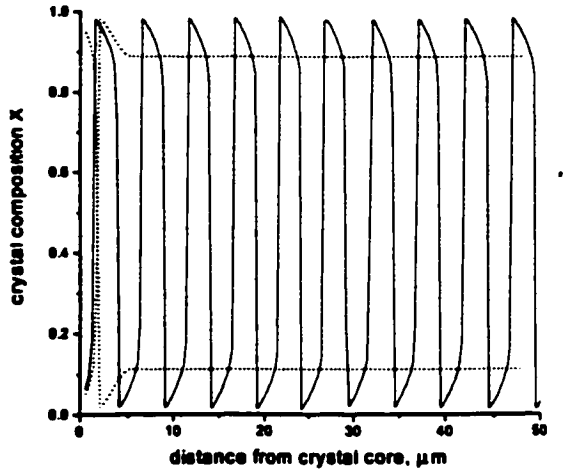

Fig. 32 Numerical solutions of the full PDE system for the growth of a flat crystallite face. The parameters are $d_B=d_C=1$, $p_1=p_2=p$, $L=0.01$, $\gamma=0$, $\alpha=1$, and $\beta=1$. The dashed lines are the solutions in the region of bistability in Fig. 31, $p=0.13$. The solid line is the oscillatory solution for $p=0.14$. The bulk concentrations are considered constant $\hat{m}_i=2$.

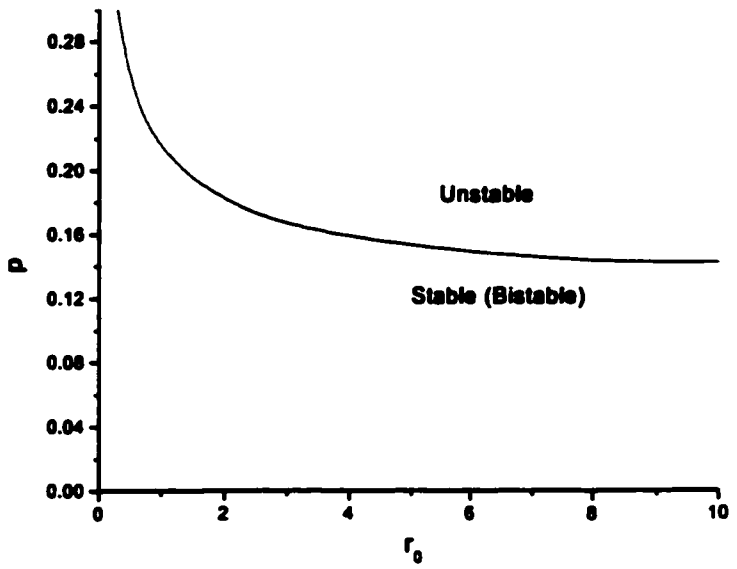

Fig. 33 Stability diagram for the full PDE model for a spherical crystallite. The stability of the system is indicated as a function of the initial crystallite radius r_0. The dimensionless interface roughness is L=0.01, other parameter values are the same as in Fig.31.

To compare the simulated crystal composition profiles with the ones observed in the experiment, changes in the bulk solution concentrations need to be taken into account. Calculations based on eqs. (110) indicate that concentrations $\hat{m}_i$ may change by as much as 10 times during the crystal growth time.

The spatial concentration profiles calculated according to eqs. (110) were verified to fit the experimental concentration data. The fit is satisfactory when the diffusion coefficient is chosen as D_B=1.39·10^{-5} cm^2/s and the concentrations $M_{A,B,C}$ are taken in the gel adjacent to the reservoirs.

The calculated aqueous concentrations values at the crystallization site at the time of nucleation are shown in Table I. The initial (core) composition of the observed crystallites [107] is also listed in Table I.

Fig. 34 shows the types of numerical solutions obtained for the case of growth of a spherical crystallite when the time dependence of the bulk concentrations in the solution is taken into account. The crystal composition X is shown as a function of the distance r-r_0. For sufficiently large size of the initial crystallite r_0, a transition from a

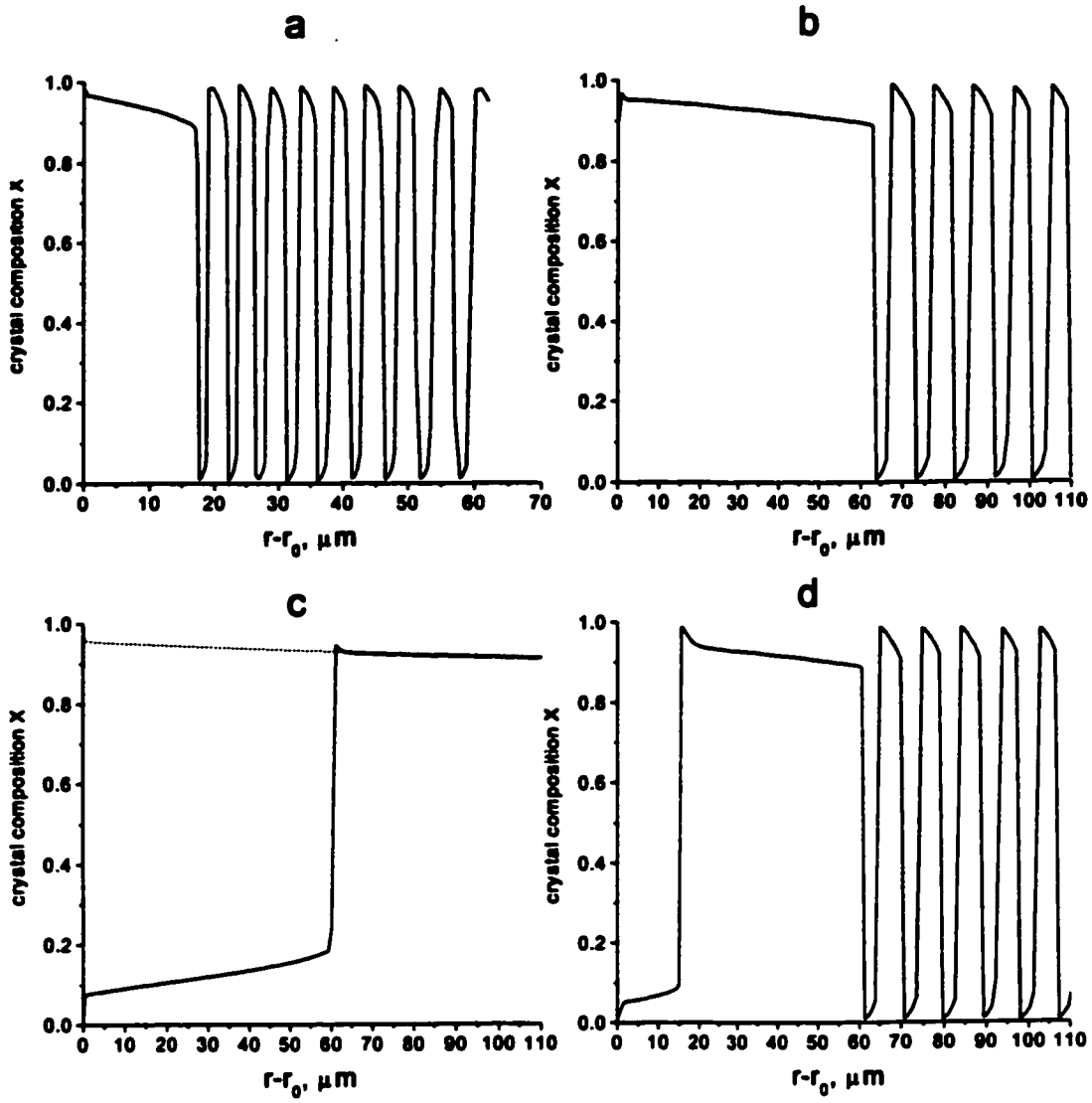

Fig. 34 Numerical solutions of the full PDE system for a spherical crystallite.

The crystal composition X is shown against the radial distance r-r_0, which characterizes the amount of the crystal grown on top of the initial crystalite of the size r_0. The time dependence of the bulk solution concentrations is considered according to eq. (110), the values of the reservoir concentrations M_i are given below along with the time t counted from the moment the solutions enter the gel column to the moment the crystal radius is r_0. Other parameter values are d_B=1.127, d_C=1.087, p_1=0.08, p_2=0.10, α=0.89, β=0.9, γ=2.5 $\cdot 10^{-4}$, and L=0.01. The growing crystallite was considered to be located at y=15cm from the reservoir containing $BaCl_2$ and $SrCl_2$.

a) r_0=10, M_i =0.5M, t=300h; For larger r_0, the result is about the same, which corresponds to the approximation of a flat crystallite surface. b) r_0=3.0, M_i =0.5M, t=400h; c) r_0=0.5, M_i =0.3M, t=360h; d) r_0=3.0, M_i =0.5M, t=400h.

stable steady state (either Ba-rich or Sr-rich) to an oscillatory solution occurs as the supersaturation in the solution increases due to the solute diffusion from the reservoirs (Fig. 34a). The same type of dynamic behavior is obtained when the growth of a flat infinitely large crystal face is considered. For smaller crystallites, however, this transition occurs for higher values of the local solution concentrations (greater time t counted from the start of the experiment) (Fig. 34b).

Due to the difference in the diffusion coefficients, molar volumes, and kinetic coefficient of the two solid solution end members, one of the two stable steady states may lose its stability while another remains stable as the solution concentrations increase with time. In this case, the crystal composition may jump rapidly from one composition range to another (Fig. 34c,d). Further increase in the local supersaturation may cause a subsequent transition to an oscillatory type of solution (Fig. 34d).

6.2 Reduction to ODEs and the effects of noise

As was shown in the previous section, the species concentrations in solution vary almost linearly with the distance from the crystal-solution interface. This diffusion profile can be approximated by a single straight line, in which case the model can be reduced to a system of coupled ordinary differential equations for the concentrations at the crystal face $m_i(0,t)$ [111] (similarly to the reduction of the plagioclase model in section 5.2.2). Such a reduction allows one to perform a linear stability analysis and thus analytically obtain the qualitative characteristics of the system's dynamics.

The eqs. (122) are integrated over x and the boundary conditions (123)-(124) are taken into account in a way similar to sec. 5.2.2. Using dimensionless variables and omitting the argument $(0,t)$ from m_i, eqs. (122)-(124) then become [111]

$$\begin{aligned}
\frac{dm_A}{dt} &= 2(\tilde{m}_A(t) - m_A) + 2V(\gamma\tilde{m}_A(t) - c_A) - \frac{d\tilde{m}_A(t)}{dt}, \\
\frac{dm_B}{dt} &= 2d_B(\tilde{m}_B(t) - m_B) + 2V(\gamma\tilde{m}_B(t) - c_B) - \frac{d\tilde{m}_B(t)}{dt}, \qquad (126) \\
\frac{dm_C}{dt} &= 2d_C(\tilde{m}_C(t) - m_C) + 2V(\gamma\tilde{m}_C(t) - c_C) - \frac{d\tilde{m}_C(t)}{dt},
\end{aligned}$$

where $c_A = c_B + c_C$ and c_B and c_C are defined in (102). The equation (125) completes the reduced model.

In the case of a spherical crystal, a similar reduction of eqs. (98)-(100) to a system of ODEs involves integration of the equation (98) over the volume and approximating the diffusion profile by a linear segment of length l. The resulting system of equations in a nondimensionalized form is

$$\frac{dm_i}{dt}\left(\frac{l^3}{12}+\frac{rl^2}{3}+\frac{r^2l}{2}\right)=d_i(\tilde{m}_i(t)-m_i)\frac{(l+r)^2}{l}-r^2V(c_i-\gamma m_i(t))-\gamma m_iV\left(\frac{l^2}{3}+rl\right)$$
$$-\gamma\tilde{m}_iV\left(\frac{2l^2}{3}+rl\right)+\gamma V(\tilde{m}_i(t)-m_i)\frac{(l+r)^3-r^3}{3l}-\frac{d\tilde{m}_i(t)}{dt}\left(\frac{l^3}{4}+\frac{2rl^2}{3}+\frac{r^2l}{2}\right) \quad (127)$$

where r is the radius of the crystal, which slowly increases as

$$r(t)=r(0)+\gamma\int_0^t V(t')dt' \quad (128)$$

The width of the diffusion boundary layer l, in general, varies with r. This dependence may be approximated, for example, by choosing the value of l to correspond to the distance from the crystal surface where the solution concentration (117) for SO_4^- is equal to $(1-\varepsilon)\tilde{m}_A$, where ε is a small parameter, which gives

$$l=r\left(\frac{Vr}{\nu_{BA}d_A\varepsilon\tilde{m}_A}-1\right). \quad (129)$$

This reduced model (125),(127) reproduces the general features of the dynamics of the original PDE model. It is therefore useful in investigating the system's behavior for small crystal radius r where the equations become stiff. Also, it allows the investigation of the system's dynamic properties by means of a straightforward linear stability analysis.

6.2.1 Linear stability analysis

The linear stability analysis for the system of equations (125) and (126) describing the growth of a flat crystallite surface was performed in [111] and its main results are summarized in the stability diagram of Fig. 30. Eqs. (127) reduce to (126) in the limit of large r (and l=1) and therefore their stability properties are the same in that limit. However, as was shown earlier (e.g. eq. (117)), the crystal-growth mechanism

depends on the crystallite size. Therefore, it is important to investigate how the stability of the system changes with crystallite radius r and width of the diffusion boundary layer l.

A steady state for the autonomous ($\hat{m}_i$=const) version of the equations can be obtained by setting the left-hand side of eqs. (127) to zero. If the terms proportional to γ are neglected for simplicity, the steady state is easily shown to have the form

$$m_{i,st} = \hat{m}_i - \frac{V_{st} c_{i,st} / d_i}{l/r^2 + 2/r + 1/l}, \tag{130}$$

where V_{st} is the steady state growth rate. In the limit of large r ($r>>l$), it reduces to

$$m_{i,st} \approx \hat{m}_i - c_{i,st} \frac{V_{st}}{d_i} l, \tag{131}$$

which is consistent with eq. (116) evaluated at $x=l$.

The solution of the system of nonlinear equations (130) and (125) was found numerically to obtain the steady-state values of $m_{i,st}$ and X_{st}. A linear stability analysis was then performed. The stability of the steady states was investigated by finding the eigenvalues of the Jacobian matrix of the system (127), (125) for each steady state.

For a wide range of parameters, there exist three steady states for which the crystal composition is close to the values in the set (120). In the calculations, the terms proportional to γ were neglected, and the following simplifications were made: $p_1=p_2$, $\beta=1$, and $d_A=d_B=d_C=1$. With this choice, the steady states for which the crystal is Ba-rich or Sr-rich are symmetric in crystal composition and have exactly the same stability properties while the crystal composition in the third steady state is exactly $X^s=0.5$.

The steady state $X^s=0.5$ was unstable for all values of the parameters considered. A typical stability diagram for the steady state for which the crystal is Ba-rich (or Sr-rich) is shown in Fig. 35. The stability diagram indicates that the steady state may become unstable via a Hopf bifurcation as the crystallite radius and the width of the diffusion boundary layer increase. This result suggests that an autocatalytic oscillatory crystal growth may occur for given bulk solution concentrations when the size of the crystallite exceeds a certain critical value.

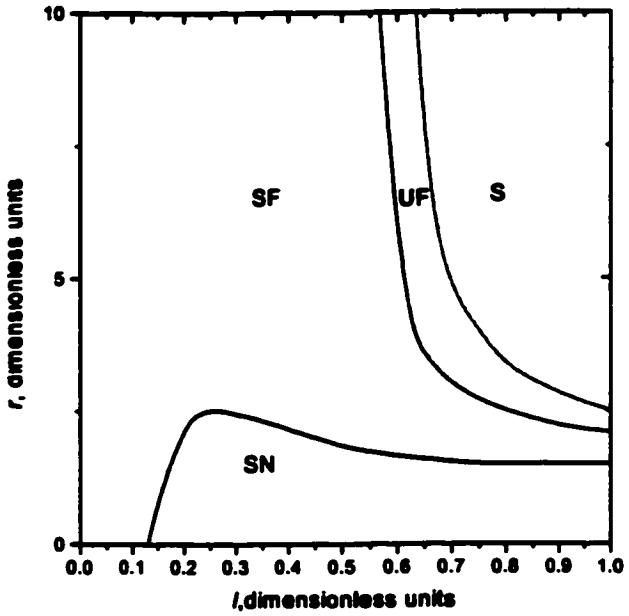

Fig. 35 Linear stability diagram for the reduced model for a spherical crystal. The stability properties are shown for either one of the two steady states where X is close to 0 or 1. The dimensionless parameter values are $\tilde{m}_i$=3, d_B=d_C=1, p_1=p_2=0.20, L=0.01, α=β=1, and γ=0. The notation of the stability regions is the same as in Fig. 30.

Increasing the bulk solution concentrations $\tilde{m}_i$ generally shifts the curves in Fig. 35 towards smaller values of the crystallite radius, thus decreasing the critical value of the crystallite radius for which the steady state loses its stability.

6.2.2 Numerical results

The numerical solutions of the reduced model for the growth of a spherical crystallite are illustrated in Fig. 36. Eqs. (125),(127) were solved using a stiff ODE solver [113] and the integral (128) was calculated using the trapezoid rule.

First, the dynamics of the system was studied for constant bulk concentrations. For small crystallite radius, the system quickly settles into one of the stable steady states (either Ba-rich or Sr-rich). Switching from one steady state to another is possible as the crystal size r and, correspondingly, the width of the diffusion boundary layer l increase slowly in time (Fig. 36a). For large crystallite size, oscillatory solutions similar to the solutions generated by the full PDE model are found (Fig. 36b,c).

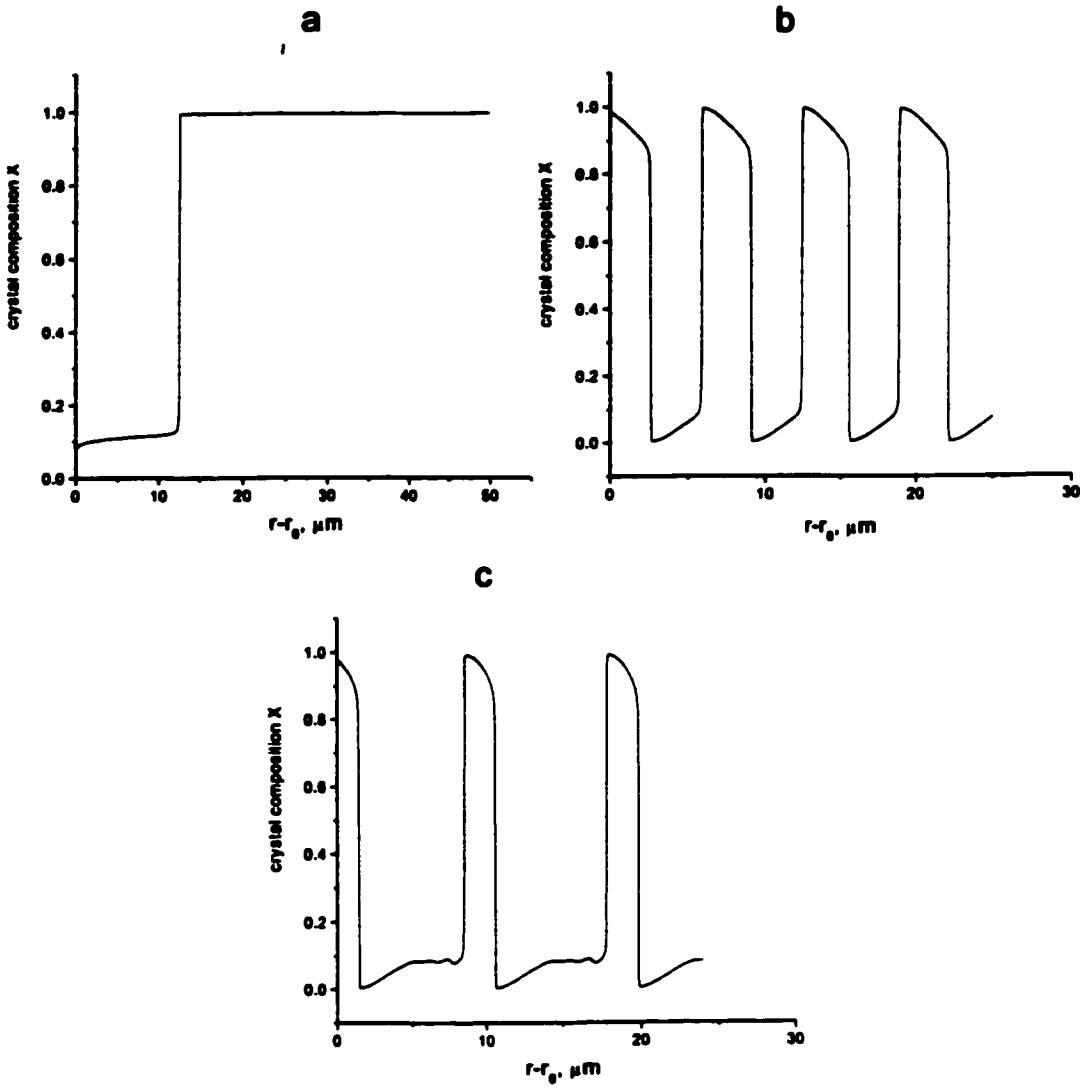

Fig. 36 Compositional profile generated by the reduced model for a spherical crystal

The bulk solution concentrations were kept constant, the parameter values are d_B=1.127, d_C=1.087, L=0.01, α=1.0 β=0.9, and γ=2.5·10^{-4}.

a) A change in the crystal composition occurs as the crystal growth larger as a result of the $l(r)$ dependence. $\bar{m}_A$=2.7, $\bar{m}_B$=3.6, $\bar{m}_C$=2.7, p_1=0.15, p_2=0.11, ε=0.01, and r_0=0.25. b) Oscillatory solution corresponding to the saddle region in Fig. 35 for very large crystal size. $\bar{m}_A$=5.0, $\bar{m}_B$=3.1, $\bar{m}_C$=2.9, p_1=0.09, p_2=0.13, l=1.0, and r_0=10. c) Solution, which roughly corresponds to the border region between the unstable focus and the saddle region in Fig. 35. The parameter values are the same as in b), with the exception of p_2=0.15.

When the time dependence of the bulk concentrations (110) is considered, transitions between the steady states can be observed similarly to the ones observed for the PDE model as the concentrations in the solution around the growing crystallite evolve in time. The steady-state solution of the system, in many cases, sensitively depends on the bulk solution concentrations and therefore on the location of the growing crystallites in the gel column. Relatively small variations in the concentration values lead to qualitative changes in the type of solution, such as a transition from a steady state characterized by a Sr-rich crystal composition to a steady state where the crystal is Ba-rich. Typically, only one such transition can be observed in the course of the crystal growth with the bulk concentrations time dependence described by eqs. (110).

The value of the crystallite radius for which the steady state loses its stability for the bulk solution concentrations and the parameter values used here is greater than the typical crystallite size observed in the experiments by about an order of magnitude. However, switching between the stable steady states, which results in an oscillatory zoning pattern, can be observed in the framework of the current model when small random fluctuations of the bulk concentrations of species at the crystal nucleation site are considered.

6.2.3 The effects of noise

The effect of small fluctuations in the solution concentrations can be considered in the full PDE model by adding a stochastic term to the deterministic bulk concentrations (110):

$$\hat{m}_i(t) = \hat{m}_{i0}(t) + \sigma_i \eta_i(t), \tag{132}$$

where $\hat{m}_{i0}(t)$ are the bulk concentrations of the salts in the solution, $\eta_i(t)$ are the respective noise processes, and the parameters σ_i describe the noise amplitudes. The fluctuations in the solution concentrations around the crystallite may result, for example, from disturbances caused by the growth of other crystallites. From physical considerations, the noise processes $\eta_i(t)$ are expected to be approximately stationary. An Ornstein-Uhlenbeck noise with zero mean and unit variance is therefore used to simulate the aqueous concentration fluctuations for all species. The correlation time τ for the noise processes is chosen significantly larger than the time step in the numerical calculations but much smaller than the total crystal growth time. Since the electroneutrality of the solution can be maintained by the corresponding fluctuations in the Na^+ and Cl^- aqueous

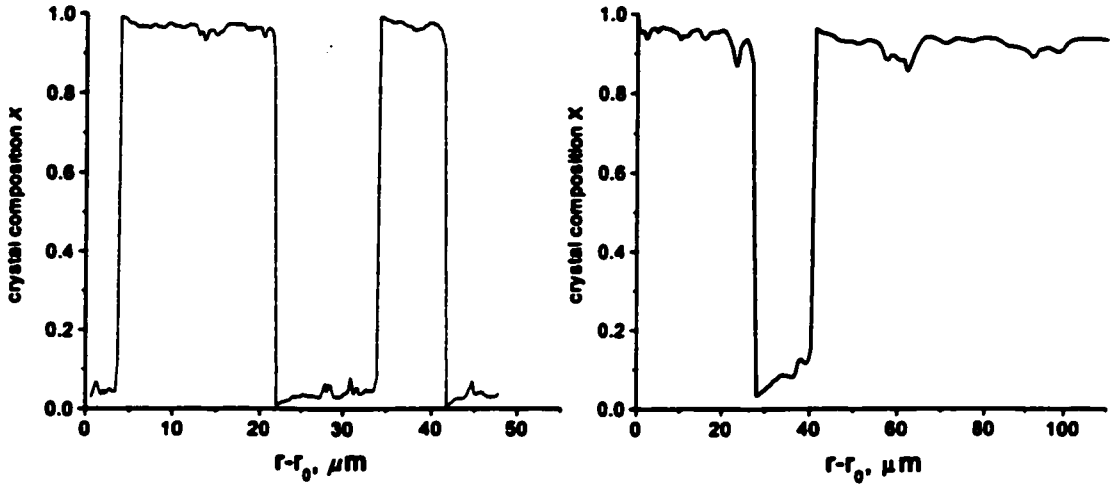

Fig. 37 The effect of noise on the full PDE model. For the parameter values chosen, two stable deterministic steady state co-exist. a) Oscillatory zoning compositional profile generated by the model for the case of a flat crystallite surface. $\widehat{m}_i$=2, d_B=1.127, d_C=1.087, p_1=p_2=0.10, α=0.89, β=0.9, γ=2.5·10^{-4}, L=0.007, and i=2. Independent Ornstein-Uhlenbeck noise processes with amplitudes σ_i=0.3 and correlation time τ=0.1 are used to simulate fluctuations in the bulk concentrations. b) Ba-Sr-Ba type of zoning generated by the model for the case of a spherical crystallite. M_i =0.3M, d_B=1.127, d_C=1.087, p_1=p_2=0.17, α=0.89, β=0.9, γ=2.5 ·10^{-4}, L=0.01, t=360h, y=15cm, and r_0=0.5. Ornstein-Uhlenbeck noise parameters are σ_i=0.3 and τ=2.0. Relatively large τ may describe fluctuations caused, for example, by the growth of other crystallites in the gel.

concentrations, the noise processes for all three species of interest can be considered relatively independent of each other.

When the bulk concentrations (132) are considered in the full PDE model (122)-(125) for the growth of a flat crystal face, an interesting noise-induced effect can be observed when the parameters are chosen to correspond to the bistable region in the stability diagram in Fig. 31 but close to the instability line. Hence, deterministically, two stable steady states coexist for the given choice of parameters. In presence of noise, however, fluctuations in the bulk concentrations may cause the system to make a temporary transition from the bistable region of its phase space to the unstable one (Fig. 31 or 33). This results in stochastically-induced oscillatory compositional patterns (Fig. 37a) characterized by variations of the crystal composition over a wide range.

The same type of noise-induced oscillations is also observed for the PDE model for the growth of a spherical crystallite (Fig. 37b). The frequency of these noise-induced events depends on the noise amplitude and correlation time as well as on how far the system is from the unstable region in its parameter space. Thus, for small supersaturations, in the presence of relatively small noise, only one or two rapid crystal

composition changes may occur during the crystal growth time. This results in the Ba-Sr, Sr-Ba, Ba-Sr-Ba, or Sr-Ba-Sr types of zoning (see Table I). For higher supersaturations (higher reservoir concentrations), the noise-induced concentration changes are more frequent, which results in noisy oscillatory zoning.

6.3 Conclusion

The present model of oscillatory zoning in $(Ba,Sr)SO_4$ solid solution by an autocatalytic mechanism generates solutions which are consistent with the observations of the experimentally grown crystals. Consideration of the physical parameters that determine the crystal growth mechanism as well as the linear stability analysis of the reduced model for the growth of a spherical crystallite indicate that oscillatory zoning arises due to the distortion of the diffusion concentration profiles in the solution caused by the increase in the crystallite size. The oscillatory zoning occurs when the concentrations of the salts in the solution are large and the crystal growth proceeds at a fast enough rate to impact the diffusion profiles in the solution around the crystallite. Fluctuations in the crystallite growth environment may be a significant factor contributing to the oscillatory zoning formation as they facilitate transitions between the steady states of the dynamical reaction-diffusion system.

6.4 Autocatalytic crystal growth: A cellular automata approach

The description of the crystal-liquid interface dynamics in terms of the molecular units attachment probabilities (108) presented above offers a generalized macroscopic view of the many microscopic processes leading to the crystal formation from a solution. The crystal surface composition X that is used in the model is assumed to reflect the average composition in the solid at the crystal-solution interface. Therefore, the molecular processes that take place at the localized sections of the interface are not taken into account although their consideration may be important in modeling the formation of a continuous three-dimensional compositional pattern in a crystal.

In this section, a cellular automata-type method [114,115,116] is used to simulate the process of the crystal growth from an aqueous phase. The general problem of reproducing the macroscopic phenomena by modeling the microscopic behavior of the system is a central problem in many areas of statistical physics and is, in many cases, extremely complex. Computer models of crystal growth processes so far concentrated

mostly on the problems of the interface surface morphologies, simulating the roughening transitions, the growth rate dependence on the supersaturation, and determining the average composition of alloys grown in disequilibrium conditions [117]. Careful search in the literature did not reveal any previous works on the autocatalytic growth of a binary mixture from an aqueous solution.

While not trying to reproduce all the details of the crystal growth from a solution, the simple simulations in this section are an attempt to describe autocatalytic crystal growth from a molecular dynamics point of view.

6.4.1 Attachment kinetics simulations

Consider the surface of a crystal, which is a binary mixture or a solid solution of two species A and B, in contact with an aqueous solution of A and B. The process of crystal growth involves transport of the molecular units from the liquid phase through a diffusion boundary layer to the crystal surface and their subsequent attachment at the surface. The dynamics of the surface attachment processes are determined by many factors including the local crystal structure in the solid phase, the concentrations of the elements in both phases, the curvature of the crystal surface, the presence of impurities or crystal defects, the energy of the chemical bonding between the molecular units of both species, and the lattice strain.

Let us consider the growth of a two-dimensional crystal. The crystal will be assumed large enough so that its surface may be considered flat over the characteristic distances of the interface dynamics (this approximation simplifies the simulations although similar considerations apply for a curved crystallite surface as well). The simulation may be thus limited to simulating the growth of a single crystal face.

The cellular automata simulation process is described as follows. The units of A and B are located on a rectangular grid and are used to represent both the liquid and the solid phases (Fig. 38). The crystal is represented by immobile A and B units located in the grid nodes and forming a closely packed lattice while, in the liquid phase, the units are allowed to move and some of the grid nodes are not occupied (or considered occupied by the solvent units). Initially, in the liquid phase, the units of A and B are located randomly with a density proportional to their respective aqueous concentrations m_A and m_B. The proportion of the number of A and B units in the crystal determines the solid composition similar to eq. (102): $X = c_A / (c_B + c_A)$, where c_A and c_B are the molecular

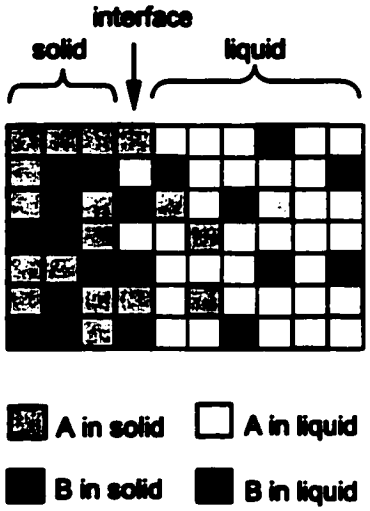

Fig. 38 Cellular automata simulations. In the liquid, the units are free to move while in the crystal they form a closely packed lattice on a rectangular grid. In the liquid, several units may be located in the same grid node, i. e. there is no excluded volume. This approximation should be valid as the solutions are considered dilute.

concentrations of A and B in the solid, respectively, and the molecular volumes of the two species are assumed equal for simplicity. The crystal and the solution are separated by an interface region of width L, which contains units belonging to both phases. In the simulations, the parameter L is used to define the region in space where the units of A or B in the liquid phase in contact with the solid phase may be attached to the crystal (according to the rules defined below).

Diffusion in the solid is neglected and diffusion in the liquid is simulated by the Brownian motion of the individual units in two dimensions. At every time step, the units may change their positions by advancing with equal probabilities to any of the four neighboring grid nodes in the liquid (up, down, left, right). For simplicity, the diffusion coefficient is considered identical for both species, independent of their concentrations and isotropically constant everywhere in the liquid. Far from the interface, the bulk liquid concentration is assumed unchanged and the distribution of the A and B units at some distance l from the interface is restored at every simulation step to reflect the constant bulk solution concentration. In the direction parallel to the crystal-solution interface, a periodic boundary condition is used.

A unit of A or B in the liquid phase, which is in contact with the crystal surface, may be attached to the crystal and become a part of it. The possibility of attachment is considered in the simulation when the unit to be attached is the only one present at the

given grid node next to the crystal. The probabilities of attachment depend, in general, on the local crystal composition, availability of suitable kink sites, the local concentration of the species in the liquid, the energy of the phase transition and the dissolvation energy barrier [57]. Here, we develop two approaches to calculating the attachment probabilities and compare them.

6.4.2 Mean-field approach

In the first approach, the dependence of the attachment probability on the crystal composition is simulated similarly to the model of Ba-Sr oscillatory zoning above. The probabilities of attaching a molecular unit to the crystal surface are proportional to the crystal composition X averaged over the entire crystal surface. In sec. 6.1.2, these probabilities were derived to reflect the compositional dependence of the likelihood to find a kink site suitable for an attachment of the unit of A or B to the crystal surface. In the case of growth of a three dimensional crystal, these probabilities are

$$P_A = \beta_1(X+p_1)^2 \qquad (133)$$

$$P_B = \beta_2(1-X+p_2)^2$$

for the units of A and B, respectively. Here, $\beta_{1,2}$ are constants proportional to the kinetic coefficients for A and B, respectively, X is the normalized crystal composition ($0 \le X \le 1$), and $p_{1,2}$ are the small parameters (assumed constant) characterizing the residual probabilities of attaching an A unit onto the surface containing only B units, and vice versa. For the case of growth of a two-dimensional crystal, the probability of finding a suitable kink site at the crystal surface is described by the expressions in eq. (108) and the probabilities of attachment become

$$P_A = \beta_1(X+p_1) \qquad (134)$$

$$P_B = \beta_2(1-X+p_2).$$

The dynamics of this cellular automata system may be approximately described by a set of ODEs. In the boundary layer approximation (similar to sec. 6.2), these equations are

$$\frac{dX}{dt} = AP_A - X(AP_A + BP_B) \qquad (135)$$

$$\frac{dA}{dt} = \frac{1}{l^2}(\tilde{A} - A) + \frac{2(AP_A + BP_B)}{l}(\tilde{A} - X) \qquad (136)$$

$$\frac{dB}{dt} = \frac{1}{l^2}(\tilde{B} - B) + \frac{2(AP_A + BP_B)}{l}(\tilde{B} - (1 - X)). \qquad (137)$$

Here, A and B are the ratios of the numbers of A and B units near the interface to the total number of the grid nodes in the direction parallel to the interface, $\tilde{A}$ and $\tilde{B}$ are the respective bulk values, and l is the width of the diffusion boundary layer (measured in the sizes of the A and B units). For simplicity, the width of the interface L is taken here equal to 1 and the diffusion coefficients are D_A=D_B=0.5, which corresponds to the situation where the units are allowed to perform one random jump to a neighboring grid node at each time step.

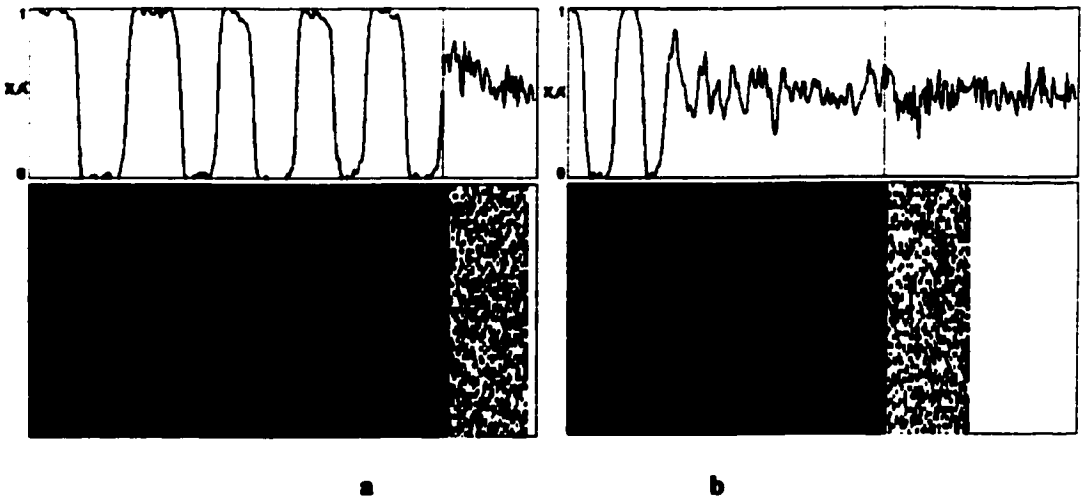

a b

Fig. 39 Attachment kinetics simulation (mean-field). The graphs at the show the composition in the solid X and the ratio of A units to the total number of units in the liquid, A', as a function of distance from the crystal core. The figure at the bottom is a simulation screenshot. The darker squares are the A units and the lighter ones are the B units. The white spaces in the liquid (to the right of the interface line) represent the solvent units. The parameters are p_1= p_2=0.03, l=50, and $\tilde{A} = \tilde{B}$ =0.4. a) β=0.5. b) β=1.

The system of equations (135)-(137) has one steady state X=0.5, which is always unstable in the appropriate parameter range, and the numerical solution of these equations exhibits regular oscillations from very small values of X to values close to 1. Some cellular automata simulation results are shown in Fig. 39. Fig. 39a corresponds to the oscillations about the unstable steady state and Fig. 39b illustrates the case when the approximations that were used to derive eqs. (135)-(137) break down, which results in a discrepancy between the numerical simulations and the linear stability analysis as the bands become too narrow. To compare with the experimentally observed quantities, the volume-averaged concentration is plotted as a function of the distance in the direction

perpendicular to the interface. In Fig. 39a, a series of continuous compositional bands develops due to the coupling between the autocatalytic interface kinetics and the diffusion transport, in accordance with the mechanism qualitatively described in sec. 6.1.2. In the present molecular dynamics simulations, formation of bands was observed when the probabilities of attachment were described by eq. (133) but could not be obtained when the expressions (134) were used. This can be regarded as a manifestation of the general fact that a certain degree of nonlinearity is required for pattern formation.

6.4.3 Microscopic approach

In the second approach, the probability of attachment is defined by the gain in the surface energy which occurs when the molecular unit is attached to the crystal surface. Suppose an energy U_{AA} is released when an A unit from the liquid phase becomes part of the crystal by attaching itself to another A unit in the crystal phase and an energy U_{AB} is released when it is attached to a B unit. The corresponding energies $U_{BB} = U_{AA}$ and $U_{BA} = U_{AB}$ for the attachment of a B unit are defined in the same way. The total energy gain from attaching a molecular unit to the crystal surface at the site with an arbitrary geometrical configuration may be then defined as

$$U = \sum_i \alpha_i U_i , \qquad (138)$$

where the sum includes energy contributions from the neighboring units in the crystal surface and the coefficients α_i depend on the distance between the unit being attached and its i-th neighbour. The autocatalytic character of the attachment process is simulated by choosing $U_{AB} < U_{AA}$. This approximation allows one to account for a surface tension effect. The energy gain for the attachment of a unit to the kink site is greater than for its attachment to a flat crystal surface, which, in the simulations, effectively reduces the roughness of the crystal surface. In the simulations, the sum in eq. (138) is taken over the 8 grid nodes immediately adjacent to the node at which the unit is being attached. In crystallographic terms, this corresponds to the consideration of energy contributions within the first two coordination spheres.

The probability of the attachment of a molecular unit may be defined as

$$P = N_0 \exp (U / kT), \qquad (139)$$

where $N_0 = [\exp(U_{max} / kT)]^{-1}$ is the normalization constant and U_{max} is the maximum possible energy gain for attaching a unit to the crystal. The probability of attachment, in

this approach, is thus defined by the *local* crystal composition at the molecular unit attachment site and by the geometrical configuration of the site.

Fig. 40 shows typical simulation results obtained in following the second approach. The compositional pattern, in this case, is qualitatively different from the one shown in Fig. 39. The autocatalytic growth produces a system of domain-like regions of similar composition that are generally elongated in the direction of the crystal growth. This qualitative difference from the patterns obtained in the first approach is due to the locality of the autocatalytic attachment condition. The units of A from the liquid phase, for example, are readily attached to the sites on the crystal surface where the crystal composition is close to pure A. This, however, does not cause oversaturation of the liquid with the units of B because those units can be attached to the crystal in the neighboring surface regions where the crystal is locally rich in B.

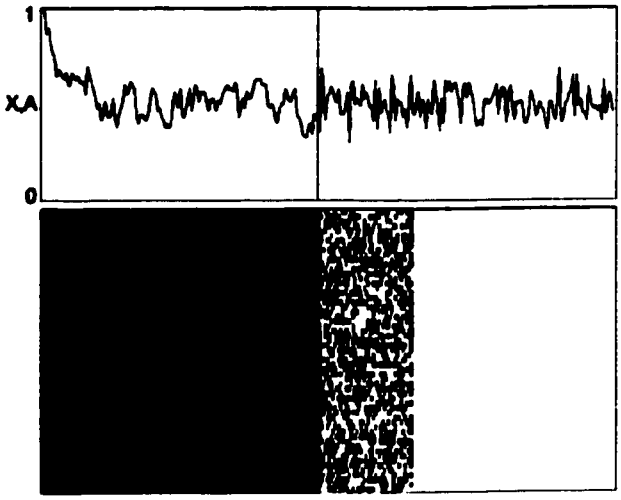

Fig. 40 Attachment kinetics simulations (local attachment conditions). The parameters are l=50, $\tilde{A}=\tilde{B}$=0.4, U_{BA}/U_{AA}=0.025, and U_{max}/kT=7. Due to the local nature of the autocatalytic processes at the interface, a number of domains is formed. The vertical line in the graph indicates the position of the interface.

When the initial crystal composition is homogeneous (e.g. A-rich) along the crystal surface, oscillatory zoning starts to form by the autocatalytic mechanism similar the one that leads to the pattern formation in Fig. 39. However, since, in this case, the autocatalytic attachment mechanism depends on the *local* crystal composition, the coherence of the oscillatory zoning processes at different locations along the interface is rapidly destroyed by the fluctuations in the growth environment. Consequently, no

continuous zoning is observed. After some rather short time (farther to the right in the crystal in Fig. 40), the variations in the crystal composition reflect only the statistical fluctuations in the number and the size of the domains. These fluctuations decrease as the size of the system in the direction parallel to the interface increases.

It is clear that the autocatalytic crystal growth processes at different sites at the crystal surface need to be synchronized in some way in order for a continuous two- (or three-) dimensional banded compositional pattern to form. Such synchronization may be due to factors that act on a spatial scale comparable with the size of the crystal. They may include the contributions from the elastic strain energy due to dislocations which may appear when the units of one species are incorporated into the lattice formed by another, the effects of the lateral diffusion of the adsorbed molecular units along the crystal surface, or other factors.

The strain energy contribution may be considered in the framework of the second approach of the current model, for example, by defining a compositional dependence of the free energy associated with the strain. For small strains, the elastic energy in the lattice increases proportionally to the square of the average distance between the atoms, which, according to the Vegard's rule, is linearly dependent on the solid solution composition. Accordingly, a simple function of the form

$$E = -E_0 [(X-0.5)^2-0.25] \qquad (140)$$

was considered, where the parameter E_0 defines the energy scale. This function exhibits a maximum at X=0.5 and is symmetric about this value. The composition X, in this case, has to be defined as a volume average over the part of the crystal adjacent to the attachment site. The size of the crystal part, over which the averaging is performed, is defined by the characteristic distance between the dislocations in the crystal. In the simulations, however, it was chosen to correspond to the grid size in the direction parallel to the interface. The thus defined strain energy E was added to the energy gain term U in eq. (134). The numerical simulations, however, did not indicate that a continuous zoning pattern is possible in this approximation.

While it is not clear what factor may play a decisive role in synchronizing the molecular attachment processes along the interface, such factors need to be taken into account and their effects need to be properly addressed in quantitative models of the crystal compositional pattern formation by autocatalytic mechanisms.

A number of one-dimensional models have been proposed to explain the oscillatory variations in the solid composition of single crystals by autocatalytic kinetics at the crystal-solution interface (e.g. the current work on $(Ba,Sr)SO_4$ and Ortoleva's model of OZ in [52]). Generally, oscillatory dynamical solutions are obtained in such models for the crystal growth in one dimension and it is then postulated that all the crystal faces exhibit the same oscillatory dynamics simultaneously and coherently during the crystal growth. However, since the autocatalytic processes are typically controlled by local parameters, such as local crystal composition or concentration in the liquid, a continuous zoning pattern that is formed around the entire crystal should be a relatively rare phenomenon. One may expect to find more frequently zoning of a single crystal face. Breaks in zoning and relatively independent zoning on the different sides of the crystal also should be expected. Instead, zoning patterns that are continuous around the entire crystal are more commonly observed. Thus, in future models of banding by the autocatalytic mechanism, it is important to specify the factors that may synchronize the zoning dynamics at different locations along the crystal surface.

Chapter 7

Banding in Mississippi Valley-type sphalerite

This chapter describes the formation of a compositional pattern formed by variations of trace iron content in the mineral sphalerite (ZnS), which is the major component of the Mississippi Valley-type zinc-lead ore deposits. Contrary to the intracrystalline patterns discussed in the previous chapters, this pattern is formed by an agglomerate of crystallites.

7.1 Banding in sphalerite

Mississippi Valley-type (MVT) Pb-Zn deposits are found the world over [118,119,120] and constitute an industrially important source of zinc and lead. A conspicuous feature of many of these deposits is the striking sub-mm pattern formed by clusters of bands within the ZnS mineral sphalerite (Fig. 41).

The patterned sphalerites of MVT deposits often have light colored ZnS-rich cores surrounded by nested, sequentially colored, bands of ZnS crystals (Fig. 41) arranged in cm-size clusters. In many cases, patterned sphalerites are found to form cylindrical pipes of a few cm in length and with a diameter of about 1 cm exhibiting concentric bands that are roughly symmetric about the cylinder axis.

Sphalerite can have a limited substitution of Fe for Zn to form a solid solution [121]. In the sphalerite crystal structure, Fe^{2+} is substituted for Zn^{2+} in a wide range of concentrations. Such substitution changes the cell size only insignificantly, by 0.18% as the Fe content changes from 0 to 30%. Equilibrium mole fraction of FeS in sphalerite does not change with temperature in the range below 500°C but is rather sensitive to pressure. The latter property has warranted the sphalerite's use as a geobarometer.

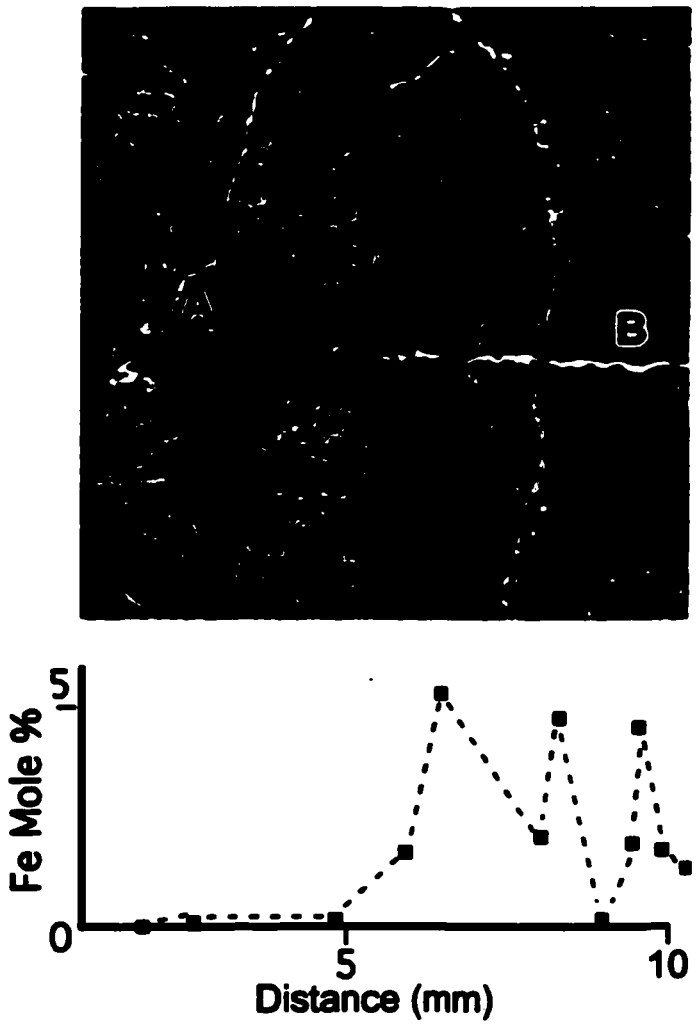

Fig. 41 Sphalerite banding

Image of banding within ZnS cluster from the Pine Point deposit, North West Territories, Canada. The photograph was taken using plane-polarised light that was transmitted through a ~30μm thick polished section of the rock (field of view ~ 1cm). In general, the sphalerite varies in colour with increasing iron content from colourless, through progressively darker shades of grey, to a dark brown to black. In general, clusters have relatively clear ZnS-rich cores and are surrounded by more Fe-rich bands. The black fan-shaped masses are crystals of PbS, and the white fractures are un-filled. The plot shows Fe content (mole %) vs. distance for selected points (squares) analysed along a traverse line roughly extending from A to B as indicated on the photo. Individual data points represent an analysis area of approximately 5μm in diameter and on the plot are connected by a dashed line. The data were collected by means of wavelength dispersive electron microprobe analysis. The image is courtesy of Anthony D. Fowler.

Electron microprobe analysis show [22] that band colors reflect variations in Fe/Zn ratio. The bands are often observed to become more Fe-rich toward the exterior of the cluster. Individual bands are composed of a myriad of platy crystals oriented in the direction away from the center of the cluster and normal to the bands. The sphalerite is often intergrown with arborescent crystals of galena (PbS) and other minerals (e.g. calcite, pyrite, fluorite, barite) all of which have filled cavities within host carbonate rocks. At an empirical level the patterns resemble those produced in the classic experiments of Liesegang [122].

MVT deposits are thought to be formed at shallow depths (~1km) in pre-existing porous host rocks near the edges of sedimentary basins [118]. They originate, in the absence of igneous intrusions, from hydrothermal fluids (~100 °C) that were generally several 10's of °C hotter than the carbonate host rocks. Accordingly, the hot fluids are thought to have formed deeper within the basin [123,124,125,126]. These fluids are also considered to consist of acidic brines [127] transporting Fe^{++} and Zn chloride complexes to the shallow carbonate host rocks where they reacted with H_2S-rich pore fluids to form sulphide minerals. This conceptual model belongs to the class of the so-called "mixing models" [128].

The origin of the ZnS patterns and the length of time required for their formation remain enigmatic. However, time-series analysis [22] of the banded ZnS clusters and empirical observations of their intergrown branching galena crystals strongly suggest that the patterns result from a process of self-organization. Far-from-equilibrium crystal growth arose as a result of the introduction of Zn-Fe-bearing solutions into carbonate aquifers containing H_2S-rich fluids [128].

Accordingly, we propose here a model that considers the co-precipitation of ZnS and FeS, crystallite growth, dissolution, and ripening. The model belongs to a class of competitive particle growth (CPG) models. The preliminary version of the model [129] is here generalized to relate the crystallite composition to the growth and dissolution rates and extended to two dimensions. A realistic banded pattern in quantitative agreement with the observations is simulated both in one and two dimensions. The pattern is predicted to form on a time scale typical of Liesegang band formation [130]. Also, some general issues about modeling pattern formation by precipitation and ripening processes in two dimensions are discussed.

7.2 Model

In the context of mixing models, we consider that an iron-zinc-rich brine flows into a reservoir (the porous rock) filled with a H_2S-rich fluid. Thus, new sphalerite crystals are formed as a result of the reactions

$$Fe^{++}+H_2S \xrightarrow{k_1} FeS_{aq}+2H^+,$$

$$ZnCl_2+H_2S \xrightarrow{k_2} ZnS_{aq}+2H^++2Cl^-,$$

$$mZnS_{aq}+nFeS_{aq} \longleftrightarrow (Zn_mFe_n,S_{m+n}),$$

where $k_{1,2}$ are the reaction rate constants. At the low temperatures considered, complexing of iron with chloride is unlikely [41]. ZnS and FeS reversibly precipitate to form a solid solution. We consider that FeS and ZnS are incorporated in the same crystallite.

Let $F(\vec{x},t)$ and $Z(\vec{x},t)$ be the Fe^{++} and $ZnCl_2$ concentrations in the solution (number of moles per unit pore volume), respectively, where the vector $\vec{x}$ describes the spatial coordinate, and let $\vec{V}$ be the velocity of the advecting fluid. The origin of the coordinate system will be chosen here at the point where the brines are injected. If $D_{F,Z}$ are the diffusion coefficients of Fe^{++} and $ZnCl_2$, respectively, then $F(\vec{x},t)$ and $Z(\vec{x},t)$ are obtained as solutions of the reaction-diffusion equations

$$\frac{\partial F}{\partial t} = D_F \nabla^2 F - \vec{V}\cdot\vec{\nabla}F - k_1 F \qquad (141)$$

$$\frac{\partial Z}{\partial t} = D_Z \nabla^2 Z - \vec{V}\cdot\vec{\nabla}Z - k_2 Z \qquad (142)$$

with the appropriate boundary and initial conditions (defined below in sections 7.3 and 7.4).

Now, let $B(\vec{x},t)$ and $C(\vec{x},t)$ be the concentrations of FeS and ZnS, respectively, in the solution (number of moles per unit pore volume). The precipitation dynamics is described by

$$\frac{\partial B}{\partial t} = D_B \nabla^2 B - \vec{V}\cdot\vec{\nabla}B + k_1 F(\vec{x},t) - U_B/\phi \qquad (143)$$

$$\frac{\partial C}{\partial t} = D_C \nabla^2 C - \vec{V}\cdot\vec{\nabla}C + k_2 Z(\vec{x},t) - U_C/\phi \qquad (144)$$

where $D_{B,C}$ are the diffusion coefficients of FeS and ZnS, respectively, $U_{B,C}$ are the precipitation rates of FeS and ZnS, and ϕ is the local host rock porosity. The boundary conditions (see sections 7.3 and 7.4) are chosen to correspond to the absence of the mass flux at the origin and the absence of diffusive flux far from the reaction front. The advection velocity $\vec{V}$ describes the macroscopic flow of liquid through the system and for simplicity can be assumed constant.

We consider sphalerite crystallites as spheres of radius $r(\vec{x},t)$ whose surface composition is characterized by the FeS mole fraction in the solid phase $p(\vec{x};t)$. The latter correlates with the observed band color and is therefore the main variable of interest. For simplicity, we consider in the following that there exists a number of previously nucleated sphalerite crystallites and that only growth and ripening take place (postnucleation regime [131,132]). Under these conditions, conservation of mass leads to instantaneous precipitation rates given by

$$U_B = \frac{\partial}{\partial t}\left(\frac{4\pi}{3}\theta N r^3 p\right) \tag{145}$$

$$U_C = \frac{\partial}{\partial t}\left(\frac{4\pi}{3}\theta N r^3 (1-p)\right) \tag{146}$$

where θ is the average solid molar density and N (assumed constant [133]) is the number of crystallization centers per unit rock volume. The crystallites are assumed to grow through a normal growth mechanism at the rate which is determined by the growth rates $V_{B,C}$ of FeS and ZnS, respectively [33]:

$$\frac{\partial r}{\partial t} = V_B + V_C. \tag{147}$$

For a dilute solution, the growth rates may be written as

$$V_B=\beta_B(B-B_{eq}(r)) \; ; \; V_C=\beta_C(C-C_{eq}(r)), \tag{148}$$

where $\beta_{B,C}$ are the microscopic kinetic coefficients of growth (see 3.2.1) and $B_{eq}(r)$, $C_{eq}(r)$ are the equilibrium concentrations of FeS and ZnS. Computation of the B_{eq} and C_{eq} values [33] is based on the Gibbs-Thomson relation with a radius-dependent surface tension:

$$B_{eq}(r) = B^{\infty} \exp\left(\frac{2\sigma(r)v}{k_B T N_A r}\right) \tag{149}$$

and similarly for $C_{eq}(r)$. Here, B^{∞} is the equilibrium concentration of the element B in the solution in contact with a flat crystallite surface, v is the molar volume of the element in the precipitate, T is temperature, k_B is the Boltzmann constant, N_A is the Avogadro number, and $\sigma(r)$ is the effective surface tension between the crystallite and the solution.

In principle, the surface tension depends on the crystallite composition. This dependence can be described by the following approximate expression, which is obtained by applying Butler's equation [134] to the binary Zn-Fe solid solution:

$$\exp\left(\frac{\sigma a}{k_B T}\right) = p\exp\left(\frac{\sigma_1 a}{k_B T}\right) + (1-p)\exp\left(\frac{\sigma_2 a}{k_B T}\right), \tag{150}$$

where a is the area of a molecular unit at the crystallite surface and $\sigma_{1,2}$ are the surface tensions of pure FeS and ZnS crystallites, respectively. Since the value of p is small (of the order of few percent), the effective surface tension σ can be taken as approximately equal to the surface tension of pure ZnS.

The dependence of the surface tension on the crystallite radius was derived from thermodynamic arguments by Koenig [135] as

$$\sigma(r) = \sigma^{\infty}\exp\left(-\int_0^{\delta/r} 2\frac{1+z+z^2/3}{1+2z(1+z+z^2/3)}dz\right), \tag{151}$$

where σ^{∞} is the surface tension of a flat crystal and δ is a small microscopic size characterizing the thickness of the Gibbs surface. The surface tension decreases with crystallite radius as the increase in the crystal surface curvature reduces the number of bonds between a molecule at the surface and molecules in the bulk crystal. The integral (151) can be simplified using Padé approximants and to a good approximation [133]

$$\sigma(r) = \sigma^{\infty}\frac{r^2 + r\delta}{r^2 + 3r\delta + \delta^2/\alpha} \tag{152}$$

where α=0.3043. This expression ensures the convergence of the exponents in eq. (149) for small r and will be used in the numerical calculations.

The evolution of the crystallite surface composition p is defined kinetically, through the growth rates of the individual elements, as

$$L\frac{\partial p}{\partial t} = V_B - p(V_B + V_C) \tag{153}$$

The roughness parameter L characterizes the length scale of the crystallites surface fluctuations [52] and is small compared to the crystallite radius r (see Appendix C). The value of r cannot become very small since only the crystallites whose size is larger than the critical nucleus size are considered here.

In summary, the model consists of a set of nonlinear partial differential equations (143),(144),(147), and (153) for the variables B, C, r, and p with the corresponding boundary conditions and the chemical forcing terms defined by (141),(142). The two latter equations are decoupled from the rest and can be solved independently.

7.3 Banding in 1D

We assume first that the essential dynamics of the system occurs in one dimension, along an axis with an origin coinciding with the point where the fluids mix. The system of equations (143), (144), (147), and (153) then becomes

$$\frac{\partial B}{\partial t} = D_B \frac{\partial^2 B}{\partial x^2} - V\frac{\partial B}{\partial x} + k_1 F(x,t) - \frac{\partial}{\partial t}(ar^3 p) \tag{154}$$

$$\frac{\partial C}{\partial t} = D_C \frac{\partial^2 C}{\partial x^2} - V\frac{\partial C}{\partial x} + k_2 Z(x,t) - \frac{\partial}{\partial t}(ar^3(1-p)) \tag{155}$$

$$\frac{\partial r}{\partial t} = V_B + V_C \tag{156}$$

$$L\frac{\partial p}{\partial t} = V_B - p(V_B + V_C), \tag{157}$$

where the constant $a \equiv 4/3\pi\theta N$ from eqs. (145) and (146).

The boundary conditions that correspond to the absence of mass flux at the origin and the absence of diffusive flux far from the reaction front are

$$D_B \left.\frac{\partial B}{\partial x}\right|_{x=0} - VB(0,t) = 0; \quad D_C \left.\frac{\partial C}{\partial x}\right|_{x=0} - VC(0,t) = 0 \tag{158}$$

$$D_B \left.\frac{\partial B}{\partial x}\right|_{x=\infty} = 0; \qquad D_C \left.\frac{\partial C}{\partial x}\right|_{x=\infty} = 0 \tag{159}$$

The boundary conditions for the diffusion equations (141) and (142) describing the evolution of the Fe^{++} and $ZnCl_2$ concentrations in the solution are given by

$$F(x=0;\, t) = F_0,\ \ Z(x=0;\, t) = Z_0, \tag{160}$$

$$F(x=\infty;\, t) = 0,\ \ Z(x=\infty;\, t) = 0.$$

The initial conditions for $F(x,t)$ and $Z(x,t)$ are

$$F(x,\, 0) = 0, \qquad Z(x,\, 0) = 0, \quad x \neq 0 \tag{161}$$

and the initial conditions for $B(x,\, t)$ and $C(x,t)$ where chosen as

$$B(x,\, 0) = B_{eq}(r_{av}), \qquad C(x,\, 0) = C_{eq}(r_{av}), \tag{162}$$

where r_{av} is the average crystallite radius in the system.

The initial crystallite radius $r(x,t)$ was chosen either as constant $r(x,0) = r_0$ (homogeneous initial condition) or as a function of the distance, in which case the sizes of the crystallites were taken as fluctuating randomly about some average value (inhomogeneous initial condition). In cases where chemical forcing was not considered, the following initial crystallite radius distribution was considered: $r(x,0)=r_0$ except at $x=0$.

7.3.1 Linear stability analysis

Solutions to the steady states of the homogeneous autonomous ($F=Z=0$) version of the system (154)-(157) are readily obtained. For a spatially homogeneous steady state, equations (154) and (155) become identities, and the steady-state solution to the equations (156) and (157) with the expressions (148) indicates that the concentrations B and C are equal to their equilibrium values $B_{eq}(r)$ and $C_{eq}(r)$ for the given value of the crystallite radius. The steady-state values of B, C, and r do not depend on the value of the crystallite surface composition p, which can be chosen arbitrarily. The latter fact reflects the approximation that, for reasonably small values of p, the effective surface tension between crystallite and solution only weakly depends on the crystallite surface composition.

A linear stability analysis using a Fourier expansion of perturbations about the steady state was performed. Assuming the perturbations to have the form $e^{\omega t+ikx}$, the modes ω were obtained numerically as functions of the wave vector k (Fig. 42). The analysis demonstrates that for all values of $k>0$ there always exists a solution $\mathrm{Re}\,\omega(k)>0$

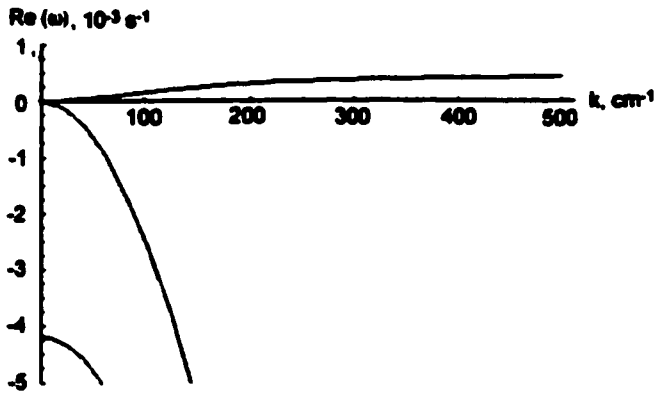

Fig. 42 Typical dispersion curves in 1D. There exist four solution branches for $k>0$. One unstable branch $\mathrm{Re}\,\omega(k)>0$, one Re $\omega(k)=0$ and two stable branches Re $\omega(k)<0$. The time (frequency) and space (wave vector) ranges reflect the characteristic time and spatial scales of Liesegang-type banding.

and therefore all steady states are unstable to inhomogeneous ($k\neq 0$) perturbations. The dispersion curve $\mathrm{Re}\,\omega(k)$ approaches a positive constant for large values of k. In general, no specific spatial scale of the pattern is selected. For some parameter values, the dispersion curve exhibits a positive maximum for a finite wave vector, but it is too weak to be seen in our numerical results. However, the numerical results suggest that there exists a nonlinear selection process that defines a specific pattern length scale.

7.3.2 Numerical results

Using characteristic parameter values [129], the system of equations (154)-(157) was solved numerically using a Crank-Nicholson algorithm with forward-projection of the nonlinear terms [136]. Typical results are illustrated in Figs. 43, 44, and 45. Volume-averaged crystallite FeS molar fraction $\bar{p}$ is shown instead of the surface molar fraction p, to compare with the experimentally observed quantity.

When an (unstable) steady state of the system exists, patterning both in terms of crystallite radius r and composition $\bar{p}$ develops. Fig. 43 illustrates a pattern developing from an initially homogeneous state. The numerical results suggest a 1mm core at the origin whose composition corresponds to almost pure ZnS. Further from the origin, we obtain a series of regularly spaced crystallite aggregates, in which the size of the crystallites become larger with time because of ripening. The composition $\bar{p}$ indicates that the molar fraction of FeS in the crystallites varies from about 1 to 10 molar percent. In mineral sphalerite, this would correspond to a series of light Zn-rich and dark Fe-rich

bands. Depending on the parameter values, the distance between the neighbouring bands varies from 0.8 to 3.0 mm and formation of these bands takes a few days to several months.

Growth patterns, such as those shown in Fig. 43, develop by means of coarsening waves, similar to the ones described in previous works for other systems [131,137]. Because the system is unstable to the changes in crystallite radius, a perturbation induced by the hydrothermal fluid injection creates a self-propagating wave of growth and dissolution. The wavelength and therefore the size of the pattern are defined by the nonlinear properties of the system. If the system is left to evolve from an initial state

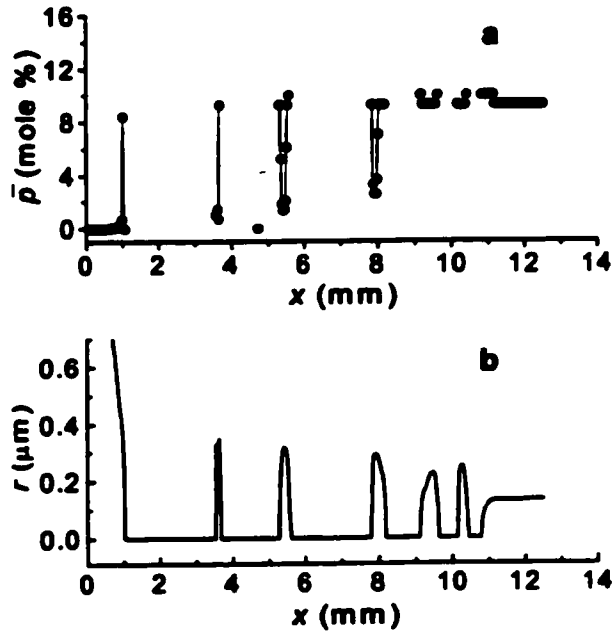

Fig. 43 Band formation in sphalerite from a homogeneous initial state. a) Average crystallite FeS molar fraction $\bar{p}$ vs. distance from the origin x. b) Crystallite radius r vs. distance x from the origin. Bands are generated by a "coarsening wave" [138], i. e. a reaction front which propagates in time leaving behind it a succession of crystal growth and dissolution zones of a specific spatial size. $D_B=D_C=8\cdot10^{-7}$ cm^2/s (appropriate for 100°C), $v=1.6\cdot10^{-6}$cm/s, $k_1=k_2=6.4\cdot10^{-3}$ s^{-1}, $a=3.5\cdot10^{4}$ mole/cm^6, $\beta_C/\beta_B=1.5$, $L=1.3\cdot10^{-6}$cm, $F(0,t)=0.5\cdot10^{-9}$ mole/cm^3, and $Z(0,t)=7\cdot10^{-9}$ mole/cm^3. Initially, $B=34.30\cdot10^{-9}$ mole/cm^3, $C=3\cdot10^{-11}$ mole/cm^3, and all crystallites have FeS molar fraction $p=10\%$ and radius $r=1.3\cdot10^{-5}$ cm. Time $t=105$ hours.

characterized by a random crystallite radius distribution, the coarsening process leads to the formation of a series of large crystals separated by more or less regular intervals (Fig. 44a,b). The frequency of the resulting bands increases farther away from the origin. Slower coarsening (e. g. for smaller F and Z terms) results in a more regular banding (Fig. 44c,d). The average concentration of Fe increases towards the edge of the system, in general agreement with the observation that bands of natural sphalerite clusters become more iron-rich away from their ZnS-rich cores.

The mechanism of pattern formation by coarsening waves appears to be very general. Coarsening waves are also observed when no external hydrothermal fluids are considered and the initial perturbation is induced by a change in crystallite size at the

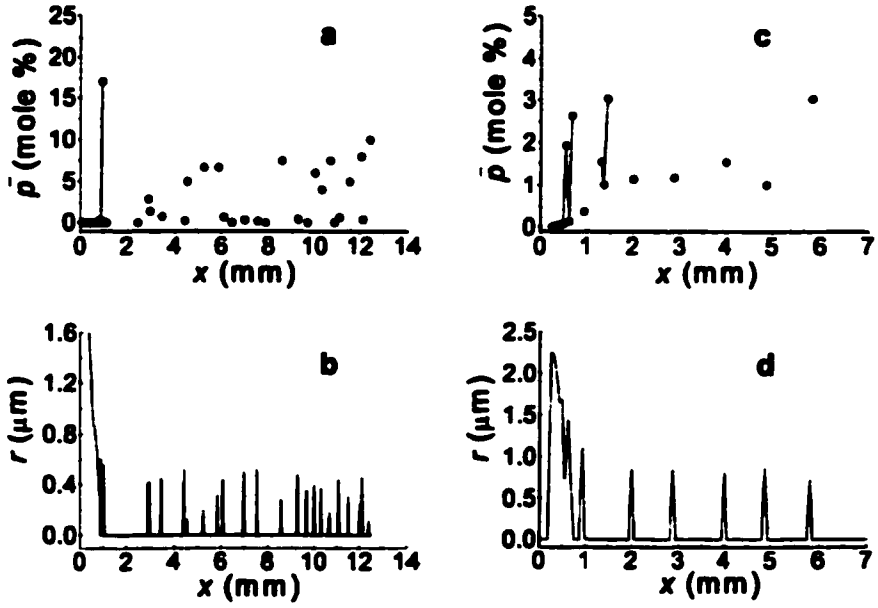

Fig. 44 Bands formation when initial crystallites have random sizes. a),b) Parameter values are the same as in Fig. 43. Time t=92 hours. c),d) Slower coarsening results in more regular banding. β_C/β_B=1.5, v=7.2·10^{-6}cm/s, $F(0,t)$=0.3·10^{-9} mole/cm^3, and $Z(0,t)$=3·10^{-9} mole/cm^3. Initial crystallite sizes were in the range of 10% around r=3.25·10^{-5} cm, B=33.33·10^{-9} mole/cm^3, C=3·10^{-11} mole/cm^3. Time t=610 hours. Other parameters are as in Fig. 43.

origin. Advection is also not required for the existence of the coarsening patterns, although its presence appears to reduce the time of the pattern formation.

For a wide range of parameters, the composition $\bar{p}$ of the crystallites evolves on a time scale which is much faster than that of the change in radius r. Figure 45 shows an example of a rapidly formed compositional pattern that develops without significant ripening.

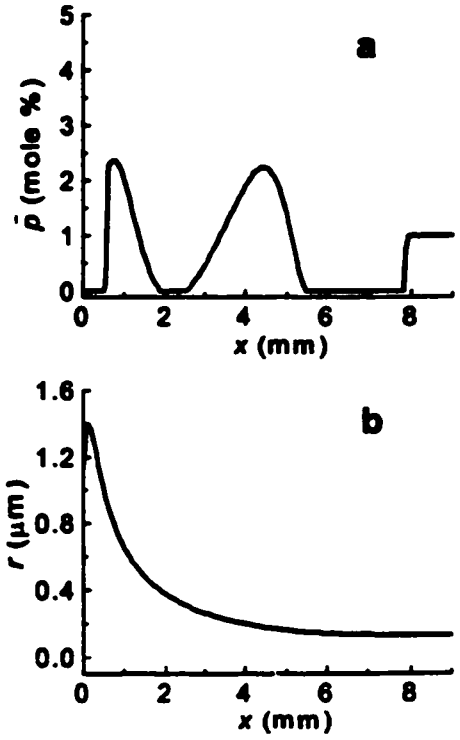

Fig. 45 Rapidly formed compositional pattern without ripening. a),b) For higher concentration of elements in the injected brines, a pattern is formed without ripening by changes in the crystallite composition. D_B=1.0·10^{-7} cm^2/s, D_C=1.2·10^{-7} cm^2/s, β_C/β_B=0.1, v=1.6·10^{-6}cm/s, $F(0,t)$=3·10^{-9} mole/cm^3, and $Z(0,t)$=30·10^{-9} mole/cm^3. Other parameters are as in Fig. 43. Time t=6.5 hours.

7.4 Banding in 2D

To simulate the banded pattern formation for more realistic conditions, we now consider the system's dynamics in two dimensions, in a plane with an origin coinciding with the center of a small region where the (Fe,Zn)-rich brine is initially injected. In assuming planar dynamics, we are led by observations of banded sphalerites which are

sometimes found in a shape of cylindrical tubes with banding occuring in a radial direction, away from the tube axis (Fig. 46). We therefore choose the cylindrical system of coordinates characterized by the distance from the origin ρ and the angle φ.

Fig. 46 Sphalerite sample with patterned clusters in a form of cylindrical pipes. A one dollar coin is shown to indicate the scale. The cylindrical patterned clusters extend through the sample and their axes are approximately parallel.

The diffusion of the Fe^{++} and $ZnCl_2$ in the solution is then described by eqs. (141) and (142) with the following boundary and initial conditions:

$$F(\rho_0(\varphi),\varphi;\, t) = F_0,\ Z(\rho_0(\varphi),\varphi;\, t) = Z_0, \tag{163}$$

$$F(\rho=\infty,\varphi;\, t) = 0,\ Z(\rho=\infty,\varphi;\, t) = 0,$$

$$F(\rho,\varphi;\, 0) = 0,\ Z(\rho,\varphi;0) = 0,\ \text{for } \rho > \rho_0.$$

Here, $\rho_0(\varphi)$ defines the size and the shape of the channel through which the brine is injected. For simplicity, we assume a circular shape ρ_0=const.

The boundary conditions for the diffusion equations (143), (144) and (147) become

$$\text{at } \rho=\rho_0:\ D_B\vec{\nabla}B - \vec{V}\cdot B = 0;\ \ D_C\vec{\nabla}C - \vec{V}\cdot C = 0 \tag{164}$$

$$\text{at } \rho=\infty:\qquad \vec{\nabla}B = 0;\qquad \vec{\nabla}C = 0 \tag{165}$$

$$B(\varphi+2\pi)=B(\varphi);\qquad C(\varphi+2\pi)=C(\varphi) \tag{166}$$

where the last two conditions correspond to the periodic character of the angle coordinate φ. The initial conditions for $B(\rho, t)$ and $C(\rho, t)$ are defined similarly to the one-dimensional case in section 7.3.

Given the observed cylindrical symmetry of the banded sphalerite clusters, we may assume the principal flow direction to be along the cylinder axis and therefore the projection of the velocity $\vec{V}$ on the plane of interest to have only a radial component, which is for simplicity assumed constant.

7.4.1 Linear stability analysis

The steady state of the homogeneous autonomous (F=Z=0) version of the system (143)-(144),(147),(153) is found similarly to the one-dimensional case. A linear stability analysis using the Fourier expansion of perturbations about a steady state was performed. Assuming the perturbations to have the form $e^{\omega t+ik\rho+im\varphi}$ (m integer), the modes ω were obtained. Typical dispersion curves Re[$\omega(k,m)$] are shown in Fig. 47.

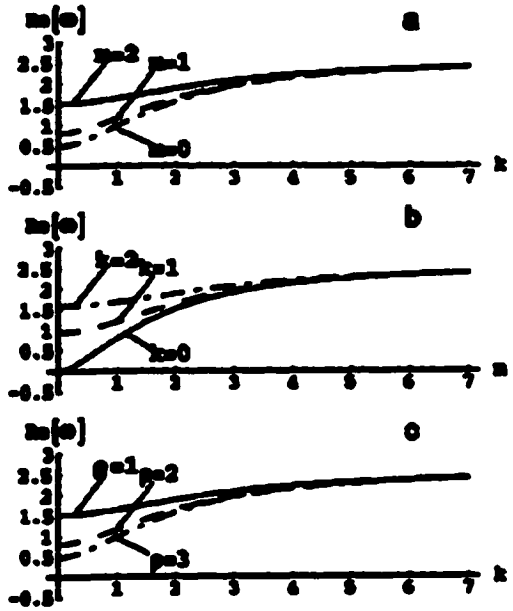

Fig. 47 Typical dispersion curves in 2D case. Only the unstable branch $\omega \geq 0$ is shown. The distance is measured in units of 0.125 cm, which correspond to the typical length scale of the banding pattern and the time unit is $1.6 \cdot 10^4$ s, which reflects the characteristic time of Liesegang-type banding. Parameter values are given in Table II. a) Re$\omega(k)$ for various m; ρ=1. b) Re$\omega(m)$ for various k; ρ=1. As only integer values of m should be considered, the continuous curve is meant as a guide to the eye only. c) Dependence of dispersion curves Re$\omega(k)$ on the distance from the origin ρ for m=2.

There always exist four solution branches: one $\mathrm{Re}\omega \equiv 0$, two stable branches $\mathrm{Re}\omega < 0$ (not shown) and one unstable branch $\mathrm{Re}\omega \geq 0$. The analysis demonstrates that all steady states are unstable to inhomogeneous perturbations in both radial and angular directions for all parameter values, i. e. the system is intrinsically unstable to coarsening. The positive branch of the dispersion curve $\mathrm{Re}[\omega(k,m)]$ approaches a constant for large values of the wave vector k (Fig. 47a), as well as for large values of m (Fig. 47b). In the absence of inhomogeneous perturbations (k=0, m=0), the system is marginally stable ($\mathrm{Re}\omega$=0). In contrast to the one dimensional case, the shape of the dispersion curve $\mathrm{Re}[\omega(k,m)]$ depends on the distance from the origin ρ (Fig. 47c).

No specific spatial scale of the pattern is selected at this linear level of analysis. However, similarly to the one-dimensional case, the numerical results below suggest that there exists a nonlinear selection process that defines a specific pattern length scale.

Table II. Parameter values for sphalerite banding simulations in 2D.

D_B, D_C	1.0×10^{-6} cm^2/s	L	1.3×10^{-6} cm
D_Z	1.0×10^{-6} cm^2/s	F_0	1.0×10^{-9} mole/cm^3
D_F	2.6×10^{-6} cm^2/s	Z_0	10.0×10^{-9} mole/cm^3
k_1, k_2	6×10^{-4} s^{-1}	B_{eq}	34.3×10^{-9} mole/cm^3
β_1 / β_2	1.7	C_{eq}	3.9×10^{-11} mole/cm^3
V	0	r_{init}	1.3×10^{-5} cm
σ^∞	200 erg/cm^2	p_{init}	0.1
T	100 °C	ρ_0	0.06 cm
V	3.98×10^{-23} cm^3	$\frac{4\pi\theta N}{3}$	3.5×10^{4} mole/cm^6
δ	2×10^{-7} cm		

7.4.2 Numerical results

To solve the above model, the differential operators in the diffusion equations were discretized on a two-dimensional grid in polar coordinates. We used the alternate direction implicit method [136] with iterations on the nonlinear terms. Thus, for each time step, the solution was sequentially propagated by first applying an implicit algorithm in one direction and then in the other. Hence, each time step resulted in the straightforward inversion of two tri-diagonal matrices.

Table II presents the typical parameter values. The advection velocity may be chosen V=0 for simplicity, a non-zero value does not qualitatively change the results. p_{init} denotes the initial value of p used in the computations. In all simulations, the values of δ and L specified in Table II were small compared to a typical crystallite radius r.

Fig. 48 shows the pattern which forms in the absence of forcing terms when a cylindrically symmetric perturbation at the distance ρ_0 from the origin is initially present

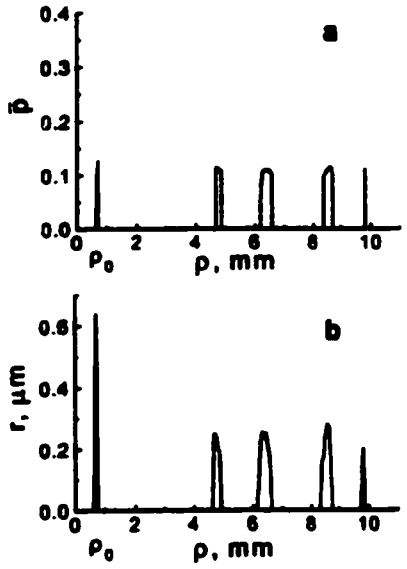

Fig. 48 Pattern obtained in the absence of forcing terms. Small cylindrically symmetric perturbation near the origin in the absence of forcing terms leads to a pattern formation in the otherwise homogeneous system by creating a successive growth and dissolution sequence (coarsening wave). The obtained pattern is cylindrically symmetric and only the radial component is shown. a) Volume averaged crystallite composition $\overline{p}$ vs. distance from the origin ρ. b) Crystallite radius r vs distance from the origin ρ. Parameter values are given in Table II. Time t=65 hours.

in the otherwise homogeneous system. The local crystallite volume-averaged composition $\bar{p}$ is plotted instead of the surface composition p in order to compare with experimental measurements. Because of the system's instability to inhomogeneous fluctuations, a ring of slightly larger crystallites at ρ_0 creates a cylindrically symmetrical growth and dissolution wave which propagates in the radial direction. A series of bands is subsequently formed as the result of ripening, each band consisting of an agglomerate of crystallites. The pattern formation dynamics is typical of this class of crystal-solution systems and has been described qualitatively in several works (e. g. [52]).

When crystallite sizes are initially randomly distributed about the steady-state value, the growth of local fluctuations throughout the system in the absence of forcing terms leads to a random pattern formed by a small number of crystallites, which are larger than the initial ones because of ripening.

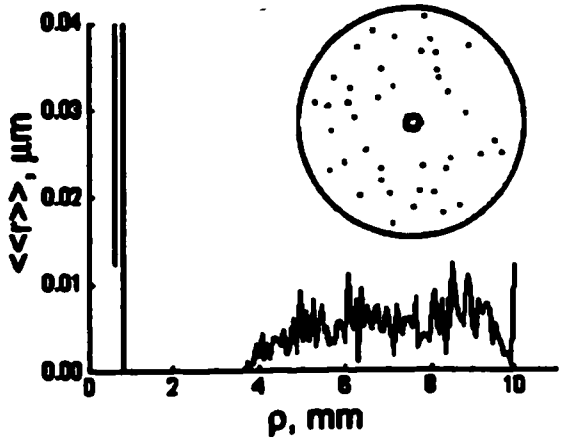

Fig. 49 Pattern obtained in the absence of forcing terms with random initial crystallites and a large crystal at the origin. Pattern obtained in the absence of forcing terms in a system where initial crystallites have random sizes uniformly distributed within 1% of their steady-state value. A large crystal (five times the average crystal size) is initially present at the origin. Crystallite radius averaged over the angular coordinate $<r>$ is shown vs the distance from the origin ρ. Coarsening leads to a small number of crystallites (shown in the insert as dots) located randomly beyond the depletion area surrounding the large central crystal. Parameter values are given in Table II. Time t=215 hours.

Since local fluctuations in the crystallite size grow fast, a strong symmetry-inducing influence is needed for the generation of a ring pattern. Such an effect may arise, for example, due to a very large initial perturbation near the origin. Fig. 49 shows the pattern obtained with such an initial condition in the absence of external forcing when the initial crystallite sizes fluctuated randomly about their steady-state value. A very large crystal (five times greater than the average crystallite size in the system) is initially present at ρ_0. The area around this large central crystal is depleted of solid material (the so called "greedy giant" effect [52]). Further away, the few remaining crystallites are located rather randomly. Concentric rings band structure can hardly be traced beyond the depleted region.

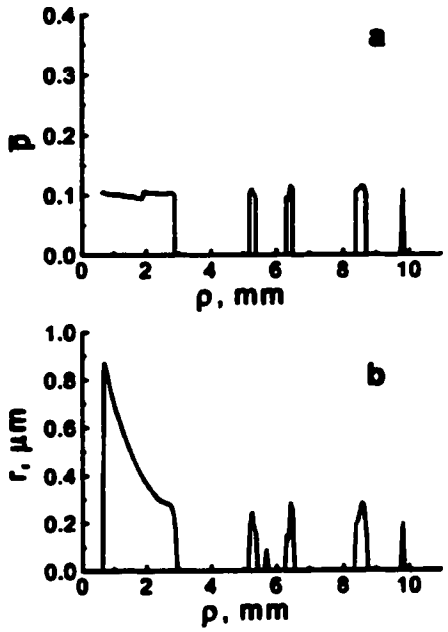

Fig. 50 Pattern obtained in presence of external forcing in an homogeneous system. An externally imposed concentration gradient due to the injection of a (Fe,Zn)-rich brine induces a ring-like banding pattern in the initially homogeneous system similar to the one shown in Fig. 48. A large central core is formed due to the strong disequilibrium conditions near the origin. a) Volume averaged crystallite composition $\bar{p}$ vs distance from the origin ρ. b) Crystallite radius r vs distance from the origin ρ. Parameter values are given in Table II. Time t=215 hours.

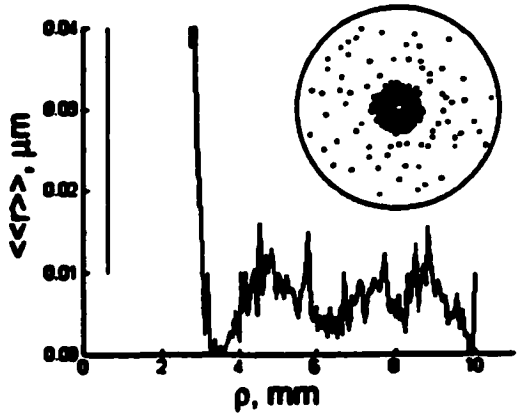

Fig. 51 Pattern obtained in presence of external forcing for random initial crystallites. The pattern is obtained in presence of an externally induced concentration gradient in a system where initial crystallites have random sizes uniformly distributed within 1% of their steady-state value. Crystallite radius averaged over the angular coordinate $<r>$ is shown vs the distance from the origin ρ. Coarsening leads to a pattern similar to the one shown in Fig. 49 for the system without external forcing. However, in this case averaging over several realizations indicates that the remaining crystallites (shown in the insert as dots) are located along the circular bands. Parameter values are given in Table II. Time is t=215 hours.

Another possible way to induce symmetry is to impose a cylindrically symmetrical external concentration gradient. Such a gradient may arise when the (Fe,Zn)-rich brine is introduced in the local reservoir containing initial sphalerite crystallites where it reacts with the local H_2S-rich fluid. Fig. 50 shows the pattern obtained by coarsening and ripening in an initially homogeneous system when such external forcing is present. A steady cylindrically symmetric distribution of Fe^{++} and $ZnCl_2$ in the solution is quickly achieved, which then plays a role of an external forcing for the crystallite-solution system. The influx of reactants at the origin has an effect similar to that of the single perturbation described above. A system of bands similar to the ones shown in Fig. 48 also develops. In addition, a very large central core is formed due to the strong disequilibrium conditions near the origin.

Fig. 51 shows the pattern developing in the presence of external forcing when the radii of initial crystallites randomly fluctuate about their steady-state value. Similar to the case described in Fig. 49, coarsening results in a relatively small number of ripened crystallites surrounding a large central core. Averaging the obtained crystallite size distributions over several realizations shows that these crystallites form several bands separated roughly by the same intervals, as in the homogeneous case (Fig. 50).

In all simulations, the time of pattern formation is of the order of months which is extremely short on a geological time scale. In the framework of the current model, band formation appears to be a very rapid process triggered by a one time sudden event in the geochemical environment such as the injection of a metal-bearing brine.

7.5 Discussion

We have presented a new model, which reproduces the main features of banding patterns observed in natural sphalerite of MVT deposits [94]. Our approach is based on a fluid mixing model [118,127] whereby a metal bearing hydrothermal fluid is introduced into an H_2S-rich carbonate aquifer. This initiates the far-from-equilibrium conditions leading to the self-organized pattern formation by means of the coarsening waves, which appears to be a fairly general pattern formation mechanism [131,137,138]. Post-nucleation macroscopic pattern formation occurs due to the dependence of the equilibrium solution concentration on particle radius.

The patterns generated by both one- and two-dimensional models consist of a Zn-rich core and a series of mm-scale banded aggregates of (Zn,Fe)S crystallites. Consistent with the observations of several MVT deposits, the computed Fe molar fraction within the bands varies from approximately 1 to 10%. The Fe molar fraction in the bands generated by the one-dimensional model gradually increases from a Zn-rich core, which is also consistent with many observations of the natural sphalerite. However, the two-dimensional model does not reproduce this increase in the Fe concentration.

Extending simulations from 1D to 2D brings forward the important aspect of the circular symmetry inducing mechanism. In most one-dimensional simulations (e.g. [52,131,137]) the wave of crystal growth and dissolution is assumed to be triggered by some internal minor fluctuation at the origin, e. g. a slightly bigger crystallite or a local supersaturation change. It then initiates a coarsening wave which leaves behind a series of more-or-less regularly spaced bands. When interpreting the results obtained in one dimension, these bands are usually assumed to be continuous in the direction perpendicular to the line of wave propagation. In two dimensions, however, in the absence of external forcing, ring-like bands due to a small internal initial fluctuation near the origin may only be obtained in the case of an otherwise perfectly homogeneous system (Fig. 48). Since the crystallite-solution system is intrinsically unstable, coarsening in presence of fluctuations of the initial crystallite sizes results in a number of larger crystallites, which may be distributed in some regular fashion but do not constitute

continuous ring-like bands. In other words, a minor internal fluctuation near the origin is not enough to induce a cylindrical symmetry in the system. The initial perturbation at the origin must be either very large compared to the typical size of the fluctuations in the system (Fig. 49) or be induced by a sudden external chemical forcing (Fig. 51).

Several models have been proposed (e.g. [52], our Fig. 48) in which two-dimensional ring-like patterns are obtained by growth, dissolution and coarsening in an idealistic system where only a single initial perturbation exists near the origin of the otherwise homogeneous system. In order to be meaningful, such models should properly address the question of generating and preserving the circular symmetry of the pattern, as local coarsening tends to destroy it. Our results suggest that this local coarsening is a fast process, although the actual susceptibility of the system to coarsening may be overestimated because several microscopic parameters were estimated by their order of magnitude only. The speed with which the fluctuations grow depends on several parameters, most notably on the effective crystal-solution interface width L.

Another distinction between the 2D coarsening system and the 1D system is the absence of a steady wave-propagation regime. In one-dimensional models, the coarsening wave is self-sustained [129,131]. It may propagate at an approximately constant speed for very long distances. In contrast, in 2D, this is not possible because the dynamics of the system depends on the distance from the origin and the speed of the wave changes with time.

The time required for the pattern formation is predicted to be of the order of months, which is surprisingly short compared to the typical times of mineral formation (a simple estimate based on the mass-conservation principle yields for the latter a time scale of tens of thousands of years when the speed of the hydrothermal fluid flows and their concentrations of Fe and Zn [124] are considered). It should be emphasized, however, that the amount of solid sphalerite precipitated during the time span of simulation is very small. The pattern is formed mainly by coarsening of the pre-existing sphalerite crystallites. Therefore, although the formation of the entire cm-scale sphalerite cluster may take thousands of years, the band pattern itself is predicted to form very quickly. Subsequent formation of the crystallite bands involves coarsening of the already recrystallized system and filling up of the interband zones by the newly precipitated sphalerite which is a much slower process. It cannot be adequately described within the limits of this model because nucleation of new sphalerite crystallites starts to play a significant role. Also, the effect of the external concentration gradient is expected to

vanish with time due to the exhaustion of the local brine reservoir. In the natural environment, the gaps between the bands are filled by newly nucleated sphalerite and other minerals. The composition of these new sphalerite crystallites will correspond to the new solution concentrations of the elements. This, along with segregation processes, may constitute an important part of the pattern formation and preservation mechanism in MVT sphalerite.

Our work supports the hypothesis that sphalerite banding is a self-organized process controlled by the local crystal-growth environment. This idea argues against the long-range correlation of mm, or smaller-scale sphalerite bands (e.g. [139]. Indeed, our observations of numerous sections from several ore deposits suggest that in many cases banding is not correlative at the thin section scale (2-3 cm). Clearly, there may be banding which is the result of long-range processes. However, we show that the sphalerite pattern formation process may be local. Therefore, alternation of Zn-rich and poor bands resulting from this process may lead to spurious correlations.

Chapter 8

Time series analysis of oscillatory and banded patterns

When studying pattern formation processes in natural geological environments, in most cases, we are presented only with their final result, i. e. the patterned crystal. The researcher usually has no means of observing, let alone controlling, the conditions and the parameters of those processes. Reproducing the natural pattern formation processes under controlled conditions in the laboratory is in many cases impossible because of the difficulties in creating and maintaining the right conditions and because of the large time scales involved. To obtain information about the physical properties of the system, in which patterned minerals are formed, two approaches are generally followed.

The first approach is to make assumptions about the structure and the physico-chemical parameters of the system and then build a model capable of reproducing the experimental results. The essential parameters typically have to be estimated based on the available indirect geological data. The degree of validity for such a model is, in many cases, established based on the qualitative and/or quantitative similarity of its output to the experimentally obtained data. In particular, one of the possible criteria for a model's validity is its ability to simulate compositional profiles with the same statistical characteristics as the profiles observed in the natural patterned crystals.

The second approach is to phenomenologically analyze the available experimental data in order to extract information that could lead to understanding the internal structure of the system. For example, by analyzing compositional zoning patterns, one may determine whether those patterns represent a record of some stochastic process or they are a result of a deterministic dynamical process contaminated by environmental noise. Combined with the first approach, the statistical properties of the data may provide additional quantitative criteria to be used in establishing the validity of the proposed model.

While in the previous chapters the first approach was followed, here we apply the second approach. In studying the compositional variations in zoned or banded minerals, we consider the measured crystal composition data as a space series. Typically, the data are obtained as sequences whereby the crystal composition is recorded as a function of the distance from the crystal core. For many analysis methods, when the pattern is considered to be produced by some dynamical process, the properties of which are to be determined, the series must be considered as a time series. The spatial compositional profile can be considered as a time series for analysis purposes if the growth rate of the crystal remained approximately constant during the time of the crystal formation and if no dissolution events occurred during that time. In general, though, the transformation from the space variable to the time variable has the form

$$t(x) = \int_0^x \frac{dx'}{V(x')}, \tag{167}$$

where $V(x')$ is the crystal growth rate at the time $t(x')$ in the crystal growth history. In some cases, the growth rate can be estimated by assuming that it depends on the crystal composition X as $V(x')=V[X(x')]$. The values of X are obtained from the measured composition profile.

Besides this non-trivial transformation from the experimentally obtained spatial profile to a time series, the analysis is frequently complicated by the shortness of the measured data sets and the nonstationarity of the series.

Time series analysis methods have been most commonly applied to measure geometric scaling properties of the series, such as the Hurst exponent, to detect the signature of possible deterministic dynamics [140], calculate the dimension of a possible chaotic attractor [141], or to determine other characteristics of the series [142].

8.1 Caveats in interpreting the results of the time series analysis

Time and space series analysis methods have become widespread and valuable tools in studying geological data. However, many of the common methods, while accurate in the theoretical limit of continuous long series, may lead to significant errors when applied to the short discretized sequences of real experimental data [143]. In this section, we outline some caveats that should be avoided in the analysis of such series. We show that the Hurst exponents cannot be calculated with sufficient accuracy from such data sets. We also show that the presence of large inhomogeneities in the series, such as

large abrupt changes in crystal composition, may lead to spurious results in detecting fractal scaling, calculating Hurst exponents, and in interpreting the return maps constructed from such series. To the best of our knowledge, these caveats in interpreting the analysis results have not been reported previously. Our results suggest that many of the published results [144,145] of such series analysis, in order to be meaningful, need to be revised and substantiated by additional evidences.

8.1.1 Measurement error on the Hurst exponent

In many cases, when dealing with geological and geochemical data, Hurst exponent values (see 4.1.2) are calculated in the fashion described below from a single series consisting of a short discrete set of values. To decide to what extent the calculated Hurst exponent value may be taken as characteristic of the series geometrical scaling, the possible error in the calculated value of the exponent needs to be estimated. Thus, we need to determine the range within which a Hurst exponent value calculated from a short series may deviate statistically from its actual value.

For relatively long series, most of the methods cannot reliably reproduce the Hurst exponent values with uncertainties smaller than 0.1, over the full range of their values (e.g. [71] and references therein). Slightly better results (with uncertainty of about 0.05) can be achieved for H close to 0.5 for very large, high quality data sets.

In this work, we illustrate that the uncertainty in the Hurst exponent values measured from short series is typically much larger. We use Brownian noise as an exemplary process with known fractal dimension. In the theoretical limit of an infinitely long series or when a statistical average is taken over a very large number of noise realizations, the Brownian noise is characterized by a Hurst exponent of H=0.5.

To measure the Hurst exponent, we use a simple method that is frequently employed for that purpose in geosciences [35,71]. First, the so-called series width $w(l)$ is calculated as a function of the scale l:

$$w(l) = \langle(\langle(x - \langle x\rangle_l)^2\rangle_l)^{1/2}\rangle, \qquad (168)$$

where $\langle x\rangle_l$ denotes the average over the part of the series of length l. The outer brackets indicate averaging over all possible averaging windows of width l. The function $w(l)$ is then plotted on a log-log plot and, if a power-law dependence is obtained over some range, the slope of the straight-line fit to the $w(l)$ graph is used as a measure of the Hurst exponent.

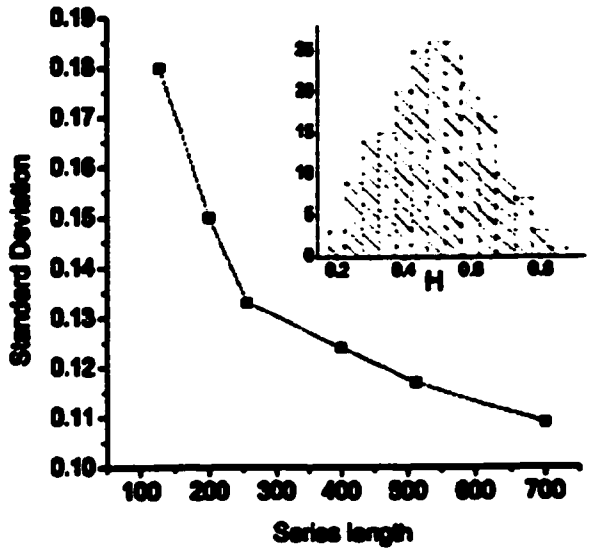

Fig. 52 Distribution of the Hurst exponent values. The inset shows a typical distribution of the Hurst exponent values measured from different realizations of Brownian noise. The graph shows the standard deviation of such a distribution as a function of the series length.

In all tests described below (except for a few explicitly mentioned cases), the series were 256 point long. When the Hurst exponent values were calculated from 200 Brownian noise realizations and binned in a histogram, a rather symmetric bell-shaped distribution was obtained (inset in Fig. 52). The distribution has a maximum around H=0.5 and occupies the range from 0.2 to 0.8. When the series length is increased, the width of the distribution decreases thus improving the accuracy of the Hurst exponent (Fig. 52).

For individual realizations, a fractal scaling exists in a limited region of intermediate scales. For small scales, the $w(l)$ graph typically curves down as a result of averaging over a large number of small-sized data sets while for large l the number of data points is insufficient to obtain an accurate result. For short series, the region of the intermediate scales where fractal scaling exists may not be properly defined for all realizations and the exact shape of the distribution depends on the particular choice of the scaling region that is used to calculate H.

A similar type of distribution for the measured Hurst exponent values is obtained when a so-called bounded Brownian noise is used, whereby a Brownian noise process is confined to a specific range of values. When the process variable reaches the boundary of the range, it is reflected off that boundary. This noise type is frequently used to simulate

fluctuations in the values of physical parameters that are naturally limited to a certain range, e. g. a percentage of an impurity in a crystal [35]. Such restriction of the noise process introduced anti-persistence to the series. Anti-persistent behavior is characterized by $H<0.5$, and our simulations indicate that the restriction of the process variable range indeed decreases the distribution's mean value but does not significantly affect its variance.

Thus, in the cases of a Brownian noise and a bounded Brownian noise, the value of H obtained from geometrical scaling calculated according to Eq. (168) from a single short realization may deviate from the theoretical value for the actual dynamical process by as much as ≈ 0.3 (as illustrated by the total width of the distribution in Fig. 52). Because of such a wide range, special care should be taken when interpreting the scaling parameters obtained from experimental data sets.

8.1.2 Impact of 'jumps' and 'spikes' on measured fractal scaling

Many experimentally measured zoning profiles are substantially inhomogeneous. Quite often, they consist of several regions where the crystal composition fluctuations have relatively small magnitude separated by transition regions where large changes in the crystal composition occur over a very short space interval (e.g. [10]). Such transitions between the different ranges of the series variable will be referred to here as 'jumps'. Another irregularity, which is commonly found in crystal zoning profiles, are 'spikes', i.e. unusually large or small single values of the crystal composition. In spite of these irregularities, the series are frequently hypothesized to be generated by a single stochastic or chaotic process and fractal scaling is often reported in such series. In many cases, when fractal scaling is observed, it is taken as a characteristic of the underlying pattern-forming process and the corresponding conclusions are drawn about the zoning mechanism. Here we show that, in the case of short series, jumps and spikes in the series may lead to spurious detection of a fractal scaling.

We construct our test series by adding jumps (or spikes) to a noise process, which itself does not exhibit fractal scaling. The width of the series is then calculated according to eq. (168) and plotted as a function of the scale size on a log-log plot. In the simplest case, the series is represented by a step function, in which the location of the step is chosen randomly. Although such a series clearly does not possess any fractal scaling, the function width calculated according to Eq. (168) on a log-log plot has the form of a straight line, which is typically a signature of fractal scaling (Fig. 53). The slope of the

line in Fig. 53 is approximately 1.1. Spurious scaling arises because in the process of $w(l)$ calculation the step is 'swept' more times by wider averaging windows than by the narrower ones so the calculated series width increases with the scale.

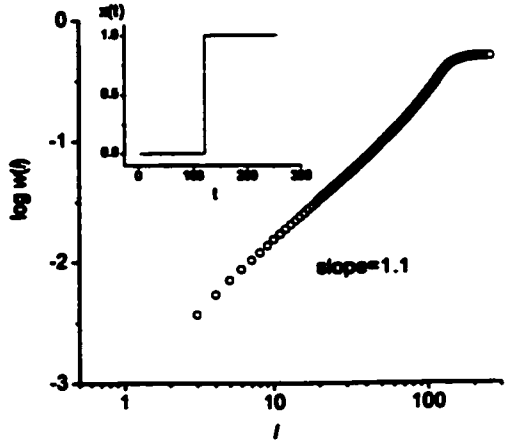

Fig. 53 Spurious scaling due to a jump in the series. The width of the function $w(l)$ was calculated from a series constructed by a step function (shown in the inset).

Analytically, this effect may be illustrated as follows: Suppose the step-function series $x(t)$ starts at $t=0$ and has total length T. Suppose, also, that the step function is chosen such that $x=0$ for $t<a$ and $x=1$ for $t>a$, where a is some value between 0 and T. Let us calculate the series width $w(l)$ according to eq. (168).

If s denotes the position of the starting point of an averaging window of length l then the mean $\langle x \rangle_l$ and the variance $\langle x^2 \rangle_l$ that are taken inside this window are calculated as

$$\langle x \rangle_l = \frac{1}{l}\int_s^{s+l} x\,dt \ , \qquad \langle x^2 \rangle_l = \frac{1}{l}\int_s^{s+l} x^2\,dt \, . \tag{169}$$

Let us assume, for simplicity, that the jump is located far enough from either end of the series and let us consider the spatial scales l such that $l<a$ and $l<T-a$. If the jump in the step function is not covered by the averaging window, i. e. $0<s<a-l$ or $a<s<(T-l)$, then $x(t)$ is constant everywhere within the window and therefore $x-\langle x \rangle_l=0$.

For $a-l< s <a$, integration over the interval from a to $s+l$, in which $x(t)$ is different from zero, gives

$$<x>_l = (s+l-a)/l\,, \tag{170}$$

and thus

$$\begin{aligned} &<(x-<x>_l)^2>_l = \frac{1}{l}\int_s^{s+l}[x(t)-\frac{1}{l}(s+l-a)]^2\,dt = \\ &= \frac{1}{l}\int_s^{a}[0-\frac{1}{l}(s+l-a)]^2\,dt + \frac{1}{l}\int_a^{s+l}[1-\frac{1}{l}(s+l-a)]^2\,dt = \frac{1}{l^2}(s+l-a)(a-s). \end{aligned} \tag{171}$$

Averaging the variance over all averaging windows of width l gives

$$\begin{aligned} w(l) &= \frac{1}{T-l}\int_0^{T-l}\left[<(x-<x>_l)^2>_l\right]^{1/2} ds = \\ &= \frac{1}{T-l}\int_{a-l}^{a}\left[\frac{(s+l-a)(a-s)}{l^2}\right]^{1/2} ds = \frac{\pi}{8}\frac{l}{T-l}. \end{aligned} \tag{172}$$

For $l<<T$, this dependence on l results in an approximately straight line on a log-log plot of $w(l)$ and a spurious Hurst exponent of H=1. Slightly different values of the Hurst exponent may be obtained if the jump is located close to either end of the series.

In simulations, spurious Hurst exponent with smaller values may be obtained, for example, if jumps are added to a series generated by a white noise (Fig. 54). White noise may be regarded to exhibit scaling with H=0 [146]. Adding jumps, which are larger in magnitude than typical noise fluctuations, produces a fractal scaling. As seen in Fig. 54, the jumps produce a false fractal scaling even if their magnitude is not very large compared to the white noise fluctuations. Spurious Hurst exponents may also be obtained when jumps are added to a series produced by a non-scaling Ornstein-Uhlenbeck noise (Fig. 55). The value of the exponent measured from such series generally increases with the correlation time τ of the noise process.

Spikes in the series also lead to spurious scaling regions (Fig. 56). Analytical calculations similar to the ones performed above for the case of a single jump indicate that a single spike in the series leads to the series width $w(l)$ of the form

$$w(l) = \frac{\sqrt{l}}{T-l} \tag{173}$$

and consequently, for $l<<T$, to a spurious Hurst exponent H=0.5.

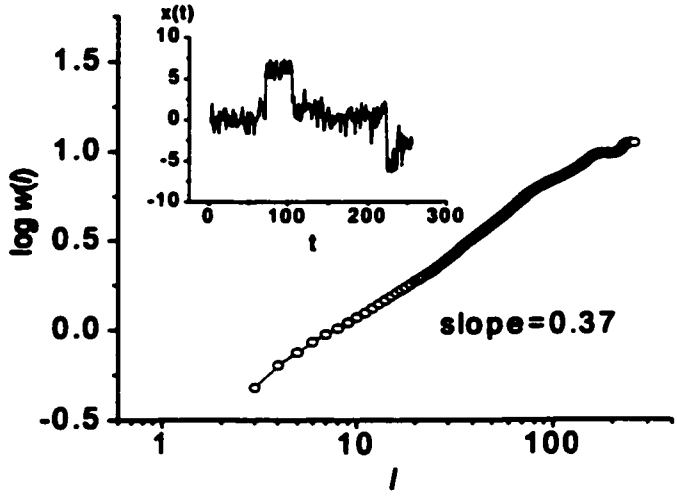

Fig. 54 Spurious scaling is obtained when jumps are added to the series. Four jumps of random magnitude and sign (up or down) were added at random locations in the series generated by white noise. The resulting series is shown in the inset and the graph shows the corresponding width of the function $w(l)$.

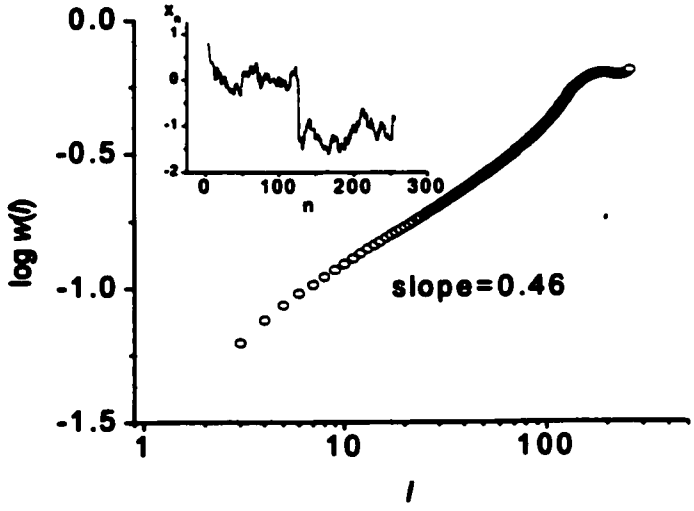

Fig. 55 One jump added to Ornstein-Uhlenbeck noise. The correlation time is τ=10.

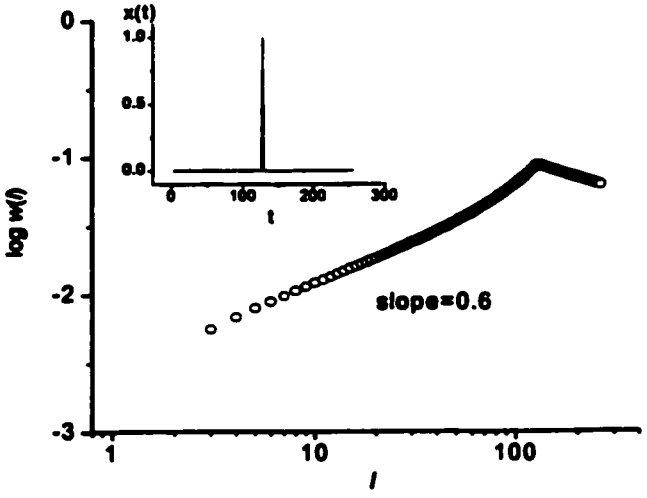

Fig. 56 Series width $w(l)$ computed from a series containing one spike. The slope of the straight line in the "scaling" region is approximately 0.6. The difference from the analytically found value of 0.5 is due to the error of the fit and the approximations taken in deriving eq. (173).

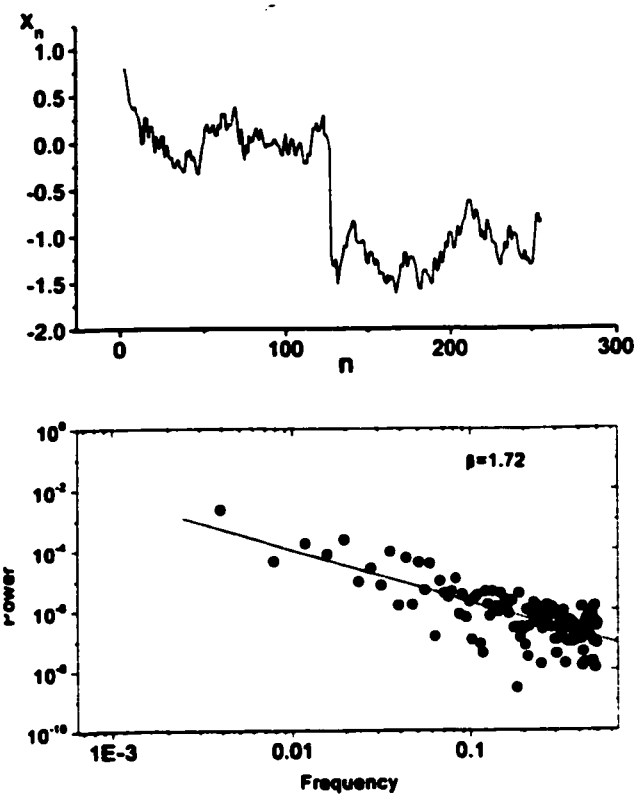

Fig. 57 Spurious power spectrum scaling. The data series containing 256 points was produced by adding one jump to an Ornstein-Uhlenbeck noise process with the correlation time τ=10. The noise realization is the same as in Fig. 55.

Besides measuring the function width (168), a power-spectrum method is often employed to detect fractal scaling in a series and to determine the value of the Hurst exponent (e.g. [20]). For a series that exhibits such scaling, the power spectrum (usually obtained by performing a Fourier transform on the series) follows the power law

$$S \propto \omega^{-\beta}, \tag{174}$$

where ω is the frequency and the exponent β is related to the Hurst exponent H by $H=(\beta-1)/2$ [71]. Thus, for Brownian noise, $\beta=2$.

Consider an infinitely long series, which consists of one jump described by a step function $\Theta(t)$ defined as $\Theta(t)=0$ for $t\leq 0$ and $\Theta(t)=1$ for $t>0$. The Fourier transform of this function yields

$$Y(\omega) = \int_{-\infty}^{+\infty} \Theta(t) e^{-i\omega t}\, dt = \int_{0}^{+\infty} e^{-i\omega t}\, dt = \frac{1}{i\omega} \tag{175}$$

and the power spectrum is $S(\omega) = |Y|^2 \propto \omega^{-2}$. Consequently, the spurious fractal scaling is obtained with the scaling exponent $\beta=2$, which is the same value as for the Brownian noise! Applying this method to a noisy series of finite length with one jump typically produces slightly smaller values of β. In Fig. 57, spurious power spectrum scaling is obtained when one jump is added to an Ornstein-Uhlenbeck noise. Fitting a straight line to the power spectrum in Fig. 57 yields $\beta=1.72$, which corresponds to $H=0.36$.

The power spectrum of a single spike is approximately that of a delta function and is flat. Therefore, the presence of spikes in the series produced by some scaling process may decrease the measured value of β. In general, detecting the scaling exponent by fitting a straight line to the series power spectrum is, in practice, insufficiently accurate for most short experimental series because of the large error in the fit.

8.1.3 Impact of 'spikes' in the series on return map analysis

Return maps are commonly used to detect the presence of the low-dimensional dynamics in the series. They are particularly often used for the analysis of the compositional zoning profiles [95] because they can be used even for short series. The map is constructed by plotting the value of the $(n+1)$-st point in the data set (e.g. the width of the zone) as a function of the n-th point. If the series were made of random uncorrelated data, then the points on the plot would evenly fill the space. The presence of

a consistent pattern in the return map, on the other hand, is a typical indication that some correlations exist in the data.

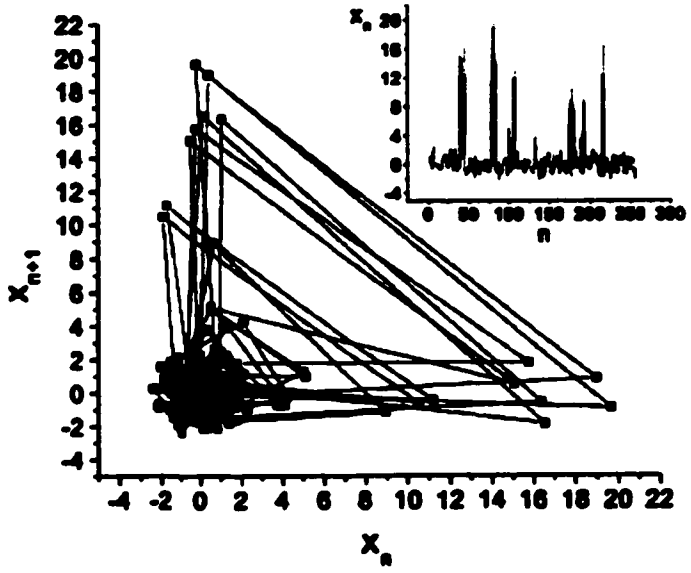

Fig. 58 Return map for a series with spikes. Triangular pattern in the return map is caused by the presence of spikes in the series. The series (shown in the inset) was generated by adding random spikes at random locations to a series generated by white noise.

We show here that spurious patterns may be produced in the return maps if the series contains spikes. Fig. 58 shows a series constructed from a white noise to which several spikes are added at random locations. In the region of large values of the series variable, the corresponding return map shows a clear triangular pattern, which is usually an indication that the series may have been generated by a dynamical system with a low phase dimension. Of course, the pattern in the region of small values is completely random.

8.2 Plagioclase zoning data

Many of the studies of oscillatory zoning in plagioclase concentrate on the modeling approach as opposed to the analysis of the available experimental data series. The plausibility of the proposed models is usually tested by comparing the simulated crystal composition profiles to the zoning observations made by imaging techniques or to the profiles obtained by chemical probing methods. As a criterion of a model's suitability, its ability to produce oscillatory concentration profiles of the right shape is usually taken. Although some requirements for a successful plagioclase model have been formulated

[4], no adequate quantitative measures of the model's 'goodness' have been yet introduced. As a result, several models coexist that are based on very different assumptions. For example, there is a model that explains the oscillatory zoning by the internal crystal growth dynamics near the crystal-melt interface [52] while another model suggests that the external fluctuations in the environment are the most important factor for the zoning formation [147]. No satisfactory criteria have been proposed so far to discriminate between such models.

It is therefore tempting to extract information that may be crucial for discrimination between the proposed models by applying the large arsenal of the time-series analysis tools to the available zoning data. Such information may lead to understanding the nature of the processes that cause the oscillatory zoning in plagioclase.

Phenomenological analysis of the zoning data performed to date has been largely limited to calculating parameters of the fractal scaling in the compositional profiles [35] and to constructing their return maps [95]. Here, we review the results of these two analysis techniques, as well as comment briefly on the application of some other methods.

8.2.1 Analysis of the plagioclase compositional profiles

Geometrical scaling is studied here in the zoning profile of a plagioclase crystal SH-80 from Mount St. Helens (Fig. 59) that was reported by B.Jamtveit's group in [35]. The plagioclase composition data were collected there by means of a particle-induced X-ray emission (PIXE). The length of the series was 172 data points, and plagioclase composition variations were recorded along a straight line extending from the core of the crystal to its rim over an interval of 250μm.

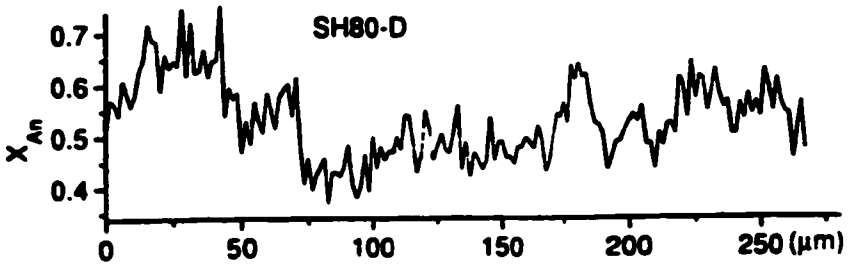

Fig. 59 Plagioclase composition profile (from Holten et al [35]). The crystal composition for the sample SH80-D is recorded as a function of the distance from the core of the crystal to its rim. The data were collected by means of a particle-induced X-ray emission.

In that work, the measured composition profile was transformed into a time series by eq. (167) where the dependence of the plagioclase growth rate on its composition was approximated from previous laboratory experiments on plagioclase crystal growth. Several other assumptions were also made [35]. Approximate power law scaling in the spatial scale range from 10 to about 250μm was reported in that work by plotting the series width as a function of the spatial scale size, as described by eq. (168). A value of the Hurst exponent H=0.22 was thus obtained.

We reproduced the calculations of [35] and obtained the Hurst exponent value of H=0.24 (Fig. 60a). Although in [35] the approximate fractal scaling was reported to exist up to the spatial scale range of 250μm, the calculated series width $w(l)$ can be satisfactory fit by a straight line only in the range from about 15 to 50 μm. The difference between our Hurst exponent and the previously reported value for this composition profile is explained by the error of the fit.

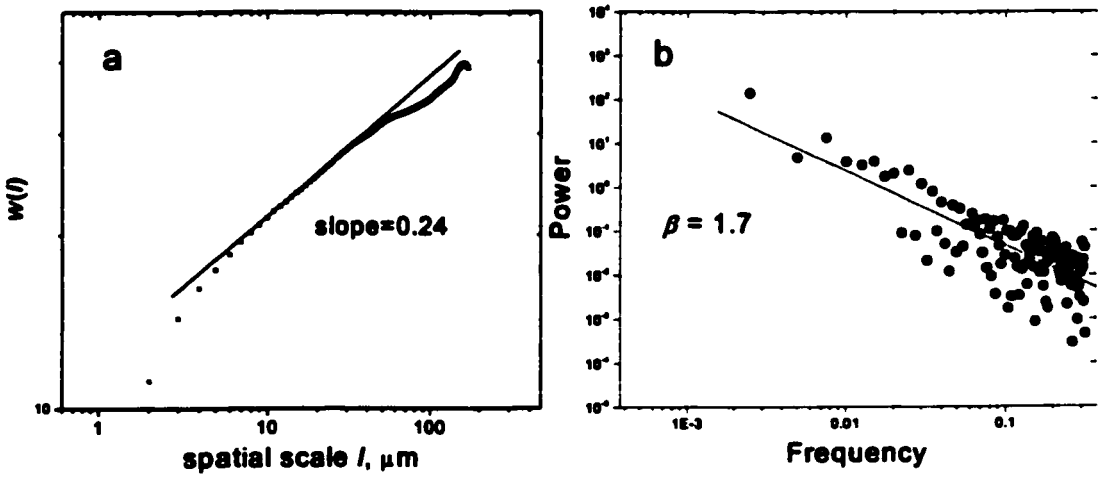

Fig. 60 Fractal scaling measured for the profile in Fig 59. a.) The width of function $w(l)$ b.) The Fourier power spectrum.

The power spectrum scaling parameter that corresponds to H=0.24 is $\beta=2H+1=1.48$, where β is the exponential factor of the power spectrum scaling (see 4.1.2). When the value of β is obtained directly from the series power spectrum by fitting a straight line to the spectrum in the region of low frequencies (corresponding to the spatial scales from about 30 to 200 μm), the value β=1.7 is obtained (Fig. 60b). The corresponding value of the Hurst exponent is H=0.35. Fitting a straight line into the high-frequency region of the power spectrum is too inaccurate to yield a value for the scaling parameter within the acceptable accuracy range but, in that frequency range, the value of

β seems to be smaller than 1.7. In principle, the difference in the scaling parameters for two different spatial scale regions may reflect the presence of two physically different processes in the plagioclase zoning mechanism. As both small scale zoning and large scale zoning are often reported in plagioclase observations [4], different mechanisms may be responsible for the formation of compositional zoning at different scales. However, the inaccuracy of the fractal scaling detection from the power spectrum and the results of the section 8.1 do not allow one to draw any definite conclusions.

A surrogate data analysis is often applied to infer information from the experimental data sets. The method is described in more detail in section 8.5.2, below. Comparison of the observed compositional plagioclase profile with the sets of surrogate data did not reject the hypothesis that the zoning-producing process is linear, such as Brownian noise. The calculated value of H=0.24 is also consistent with the hypothesis that the zoning-controlling process is a fractional Brownian noise.

The correlation dimension for the SH-80 profile was estimated by computing the correlation integrals (described in more detail below in section 8.5.2). No saturation of the slope of the correlation integral was observed for an embedding dimension up to 8. Although the data series is rather short for a reliable analysis, this result indicates that no specific correlation dimension exists for this compositional profile.

Plagioclase profiles are often analyzed by plotting their return maps. Return maps are an important tool in determining whether the data is produced by a stochastic process or a deterministic, possibly chaotic, process. It is hypothesized [95], for example, based on the return maps for plagioclase zoning pattern, that the oscillatory zoning is likely to be produced as a result of the dynamics of a low-dimensional deterministic system. It is then concluded that as few as two or three dynamical variables may be sufficient to adequately describe that system. However, because of the very irregular nature of the plagioclase zoning profiles, which have a lot of 'spikes', the observed triangular patterns in the plagioclase return maps may not be uniquely identified as a signature of a low-dimensional attractor.

This is illustrated in Fig. 61. The data sequence is reproduced after [95]. The data consists of experimentally measured widths of the zones in an oscillatory zoned plagioclase crystal as a function of the zone number (Fig. 61a). The return map, in which the width of the $(n+1)$-th zone is plotted as a function of the n-th zone exhibits a triangular pattern, characteristic of a low-dimensional chaotic system. However, as illustrated in Fig. 61b, such pattern may not necessarily be a consequence of a low-

dimensional nature of a dynamic system. The data sequence in Fig. 61b is obtained by randomly shuffling the data points in the sequence in Fig. 61a. The return map for the thus randomized sequence still exhibits a triangular pattern in the region of large zone widths.

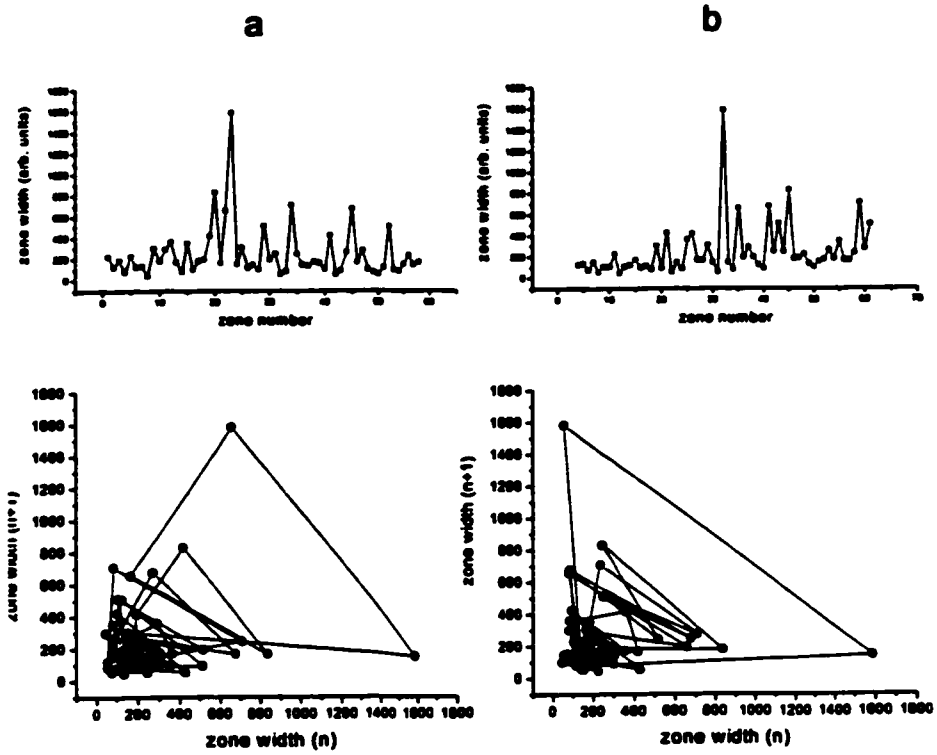

Fig. 61 Return maps. a) The series represents the plagioclase zoning profile (from Higman & Pearce [95]). The corresponding return map exhibits a triangular pattern. b) The original data series is randomized by randomly switching the order of the data points. The triangular pattern in the corresponding return map is caused by the presence of large peaks in the data series. Other structure present in the return map in a), such as the clockwise direction that the points seem to follow, is, of course, lost in the randomized series.

The triangular pattern of the type shown in Fig. 61a is formed in a return map when a narrow zone is followed by a slightly wider zone and then by a very large zone and this pattern is repeated many times in the zoning sequence. While such zone succession is true for almost all large peaks in Fig. 61a, it could not be detected for any other part of the zoning sequence. Thus, while the return map obtained from the original plagioclase zoning data has more structure than the return map of the randomized sequence in Fig. 61b, the triangular pattern in Fig. 61a cannot be uniquely identified as a signature of a low-dimensional dynamic system. It may be a mere consequence of the presence of several extremely wide zones in the sequence.

The pattern in the region of small zone widths in the return map in Fig. 61a is very different from random in a sense that the points in the return map generally can be followed consistently in a clockwise sequence. However, the pattern that those points form is no longer triangular.

In summary, no definite conclusion can be drawn from the plagioclase data analyzed here about either the fractal dimension in the composition profile or the deterministic component in the dynamics of an assumed pattern-generating system. Application of more advanced time series analysis methods [148,149] (e.g. estimation of the correlation dimension of the series [19]) requires better data sets which contain more data points (typically more than 500). For this reason, most studies of plagioclase zoning profiles undertaken so far have been inconclusive [4]. In addition, most time series analysis methods require the series to be stationary. Plotting the running mean for the plagioclase profile SH-80 reveals that the series is substantially nonstationary. This factor limits the applicability of many potentially useful analysis methods.

Due to the high uncertainty in measuring the Hurst exponent value, the values of H obtained for the available experimental profiles [35,145] cannot be accepted as accurate or characteristic of the physical pattern-forming system. The plagioclase composition profile contains several jumps, which, while being potentially important part of the profile, may generate spurious fractal scaling. The observed compositional profiles may, in principle, represent a random noise process with occasional irregularities, such as rapid jumps in the crystal composition, which lead to spurious fractal scaling. Large jumps in composition are a typical feature of plagioclase profiles. They may correspond to large-scale geological events such as sudden decompression of a magmatic system [35].

Application of new analysis methods is needed to reliably extract information from the measured profiles and provide criteria to be used for discrimination between the proposed zoning models. One such method is wavelet analysis [19], which often performs better than standard Fourier analysis in detecting periodicities in data. However, it also requires relatively large data sets. There are reports [150] that neural networks have been successfully used to classify igneous and hydrothermal melanite garnets. The use of the neural networks in classification of the spatial-temporal geochemical data is very promising, although it is still not clear how successful those methods may be in dealing with short and irregular series, such as plagioclase zoning profiles.

8.3 Note on the visual perception of zoning patterns

Justifying the validity of an oscillatory zoning model usually involves comparing the simulated profiles generated by that model with observed composition profiles. The natural zoning patterns are usually observed either by imaging methods, such as laser interference or Nomarski spectroscopy, or by obtaining composition profiles by chemical probing methods. While it is usually implied that the imaging methods and the chemical probing methods are complementary and yield similar descriptions of the zoning patterns [19], a distinction often needs to be made. The oscillatory nature of the zoning is reflected in both characterization techniques but our visual perception of the zoning details may not be the same if the transformation that is used to translate compositional variations into different colors or grey scale levels in the imaging techniques is not linear. For example, sharp transitions seen in the images of the plagioclase zoning may not always correspond to correspondingly large changes in the crystal composition. This difference may lead to confusion in assessing the validity of the zoning models.

The difference in the description of the zoning by imaging techniques and by chemical profiling is illustrated in the following example. The plagioclase compositional profiles in Fig. 59 obtained by PIXE measurements [35] were transformed into a grey-scale image by linearly mapping the crystal composition into grey-scale levels (Fig. 62b). Higher An concentration corresponds to lighter colors in the image. The resulting image of the one-dimensional zoning appears, in many details, different from the image of the same zoning obtained by the backscattered electron photography (BSE) (Fig. 62a). While BSE, when applied to plagioclase, provides rather low image contrast because of the small mean atomic number difference between anorthite and albite, this example, nevertheless, illustrates the point. The "image" obtained by converting the chemical profile data into grey scale contains more 'zones', which correspond to minor fluctuations in the crystal composition and are not seen in the BSE photograph, as well as 'zones' that appear in the profile due to the inclusions in the crystal. On the other hand, the contrast between the An-rich and An-poor zones in the profile is less evident than in the photograph. The relation between the shades of grey in the zoning image and the actual crystal composition is thus non-trivial.

When justifying the validity of the oscillatory zoning models, the images of the crystal zoning and the measured composition profiles should be used with an appropriate degree of caution. On one hand, the models are intended to reproduce the compositional fluctuations in the crystal, and therefore quantitative description of the zoning provided

by chemical probing methods should take precedence over a qualitative description by imaging methods. When a model is evaluated, the simulated composition profiles need to be compared directly to the measured profiles rather than to the patterns observed in the

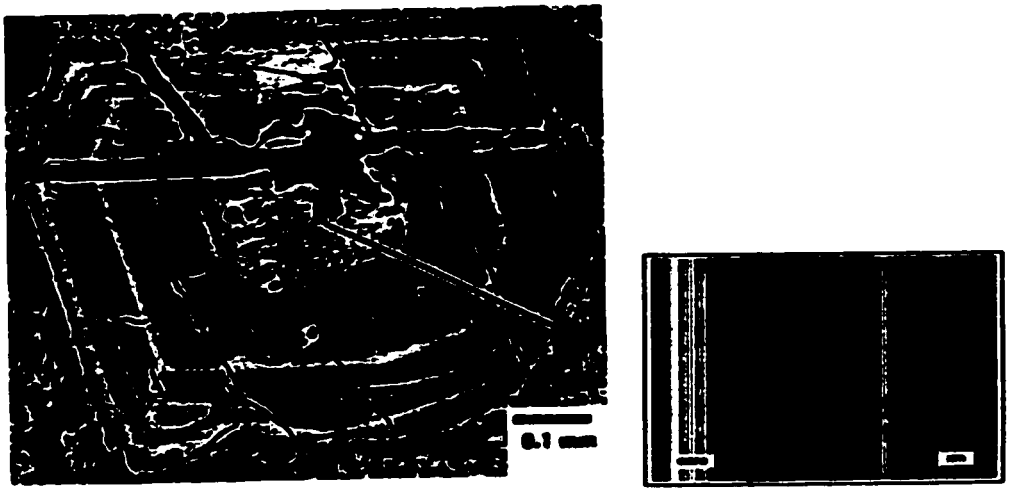

Fig. 62 Visual correspondence between the measured composition profile and the zoning image. a) BSE photograph of a zoned plagioclase crystal SH80-D (from [35]). The line indicates the path along which the composition profile in Fig. 59 was taken. b) The image obtained by linearly mapping the composition data in Fig. 59 into 256 grey scale levels (lighter areas correspond to anorthite-rich parts of the crystal).

zoning images. On the other hand, compositional profiles obtained by probing the chemical composition at a number of points in the crystal may include local fluctuations in the crystal composition that are caused by inclusion of impurities or by composition variations at spatial scales much less than the characteristic zone width. Such composition fluctuations are not important for the zoning formation and therefore should not be tried to be reproduced in a basic model. These fluctuations are typically not seen in the images of the zoned crystals, which better highlight the large-scale features of the zoning.

8.4 Zoning in garnets

Garnets are relatively common in highly metamorphized rocks and in some igneous formations. They typically form under high temperatures and/or pressures. Garnets sometimes contribute to detrital sedimentary rocks although they are not of original sedimentary origin [151]. Oscillatory zoning is a frequently-described phenomenon in garnets [152] and has been intensively studied [10,11] in grandite garnets from the Oslo rift region (southern Norway). These garnets precipitated from hydrothermal solutions associated with contact metamorphism and are found in

hydrothermal veins and skarns, i. e. metamorphic zones where carbonate sedimentary rocks were invaded by large amounts of silicon, aluminum, and iron, typically in the contact area around igneous rock intrusions. The garnet-bearing skarns of the Oslo rift were formed as a result of the infiltration of H_2O-rich fluids at the temperature of 300 to 400 °C through a layered sequence of carbonates and shales.

Widespread intercrystalline correlation [11] among zoning patterns of neighboring crystallites suggests that growth conditions were controlled by external changes in the environment. Garnets are generally believed to form under conditions close to thermodynamic equilibrium and therefore their composition may be regarded as a record of the changes in their growth environment. The fractionation between garnet and the hydrothermal solution is very sensitive to variations in temperature, pH, and salinity [11], which suggests that external noise may have played a significant role in the zoning pattern formation.

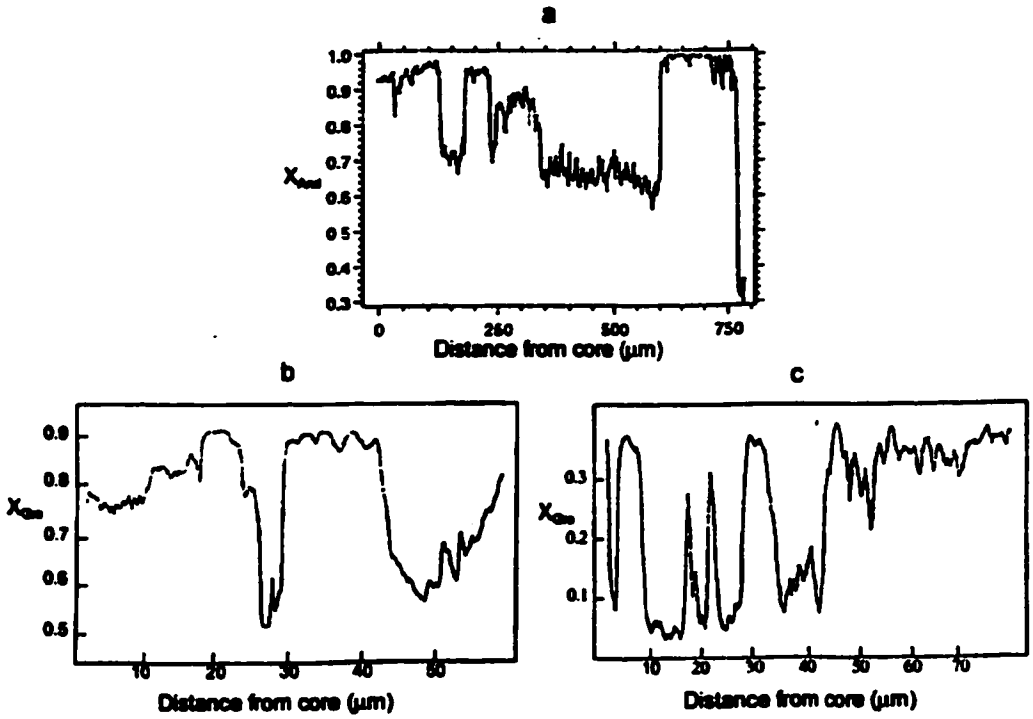

Fig. 63 Oscillatory compositional profiles in garnets. a) Zonation profile (adapted from [10]) obtained by means of an electron microprobe. The zonation is parallel to the {110} crystal face. Andradite fraction in the crystal X_{And} is shown as a function of the distance from the crystal core. b,c) The profiles (reported in [13]) are obtained by taking the ordinate variable (grossular fraction X_{Gro}) as inversely proportional to the darkness of the BSE image. Calibration of composition from color intensity was made from 30 electron microprobe spot analyses.

Hurst exponents have been measured by Holten *et al* for the compositional profiles in several hydrothermal garnet crystals [35]. The profiles consist of the measurements of the grossular concentration in the binary solid solution of grossular ($Ca_3Al_2Si_3O_{12}$) and andradite ($Ca_3Fe_2Si_3O_{12}$) as it varies from the core of the garnet crystal to its rim (Fig. 63). The lengths of the data sets were from 138 to 1528 data points.

Consistent with many observations of both zoned and unzoned garnets [153], crystal composition is typically found to vary roughly within one or more of the three composition ranges: low grossular (<20 molar %), intermediate (about 50 molar %) and high grossular content (>80 molar %).

Hurst exponents values measured from the zoned garnet composition profiles and reported in [35] typically fall in the range from 0.20 to 0.45. The profiles, for which the grossular content is greater than 75%, exhibit wider variations in their Hurst exponents values than other profiles. The two lowest values of the Hurst exponents H=0.14 and H=0.25 were reported for the profiles with very small number of data points (138 and 148 point, respectively). The profiles for the garnets of intermediate composition typically have H values in the range from 0.35 to 0.45.

The reported measured H values for most garnet samples fall into the 0.29-0.45 range and, in principle, this may indicate that the corresponding composition profiles were generated by similar processes, or at least by processes with similar fractal dimensions. The range of the measured H values is consistent with a bounded Brownian noise. This type of noise may be justified physically as the system's parameters may fluctuate according to a continuous noisy process similar to a Brownian walk while external conditions impose limits on the parameters' range.

However, taking into consideration the results of section 8.1.2, the range of possible noise processes may be substantially extended to include processes with higher or lower Hurst exponents, as well as noise processes that do not, in their pure mathematical form, exhibit fractal scaling. For example, if the series is generated by a rapidly varying, uncorrelated noise process similar to white noise, spurious fractal scaling may arise if several one-time abrupt events (jumps) occured in the crystal growth environment that caused switching between the crystal composition ranges across the miscibility gap. In our simulations performed similar to the tests in section 8.1.2, fractal scaling with the Hurst exponents in the range 0.3-0.45 was obtained when transitions between the compositional ranges (e.g. between about 50% and 90% grossular) were added to the series produced by a white noise of small intensity. Thus, the reported Hurst

exponents may not be accepted as a sufficient evidence for the existence of a fractal scaling in the measured compositional profiles.

8.5 Banded patterns of Champlain Sea clay sediments

This section presents the statistical and time series analysis of banded patterns found in the clay sediments of the ancient Champlain Sea.

8.5.1 Description of the data

The Champlain Sea occupied the territory of the present Ottawa Valley about 12,000 years ago. Following the last ice age, ocean water filled the valley, which was depressed by the weight of the ice about 300 meters below the sea level [154]. The Champlain sea then receded as the surface gradually rebounded to its original elevation. The marine sedimental record was preserved in a form of clay and silt deposits, colloquially called Leda clay. Part of these deposits, typically located at the depths 15 to 35m below the surface, consists of colored bands formed by alternating layers of grey and red clay with occasional inclusions of silt layers. Several sample cores of these deposits were extracted by J.Aylsworth's group at the Geological Survey of Canada, and the width of the layers was subsequently measured [24].

The grain-size analysis reported in [24] indicated that the colour of the clay bands correlates with the grain size and silt content within the bands. The grain-size sorting alone, however, was not the cause of the color banding, and the factor that determines the colour of the bands is yet to be determined [24]. The grey bands contain from 0 to about 15 volume percent of fine-grained ($<2\mu m$) clay particles, while the rest of the band volume is filled mostly with coarser-grained silt with occasional inclusions of some minor amounts of sand. In the red bands, the clay content varies from about 15 to 35 volume percent, the rest of the volume within the band being filled with silt. The transition in the band color as the clay content increases is rather smooth, i.e. there is no definite threshold in the clay content that would separate the bands of different colors. As a consequence, several bands of the intermediate 'pinkish grey' color were reported in the banding sequence. Because of the low clay fraction and the high silt content in the grey

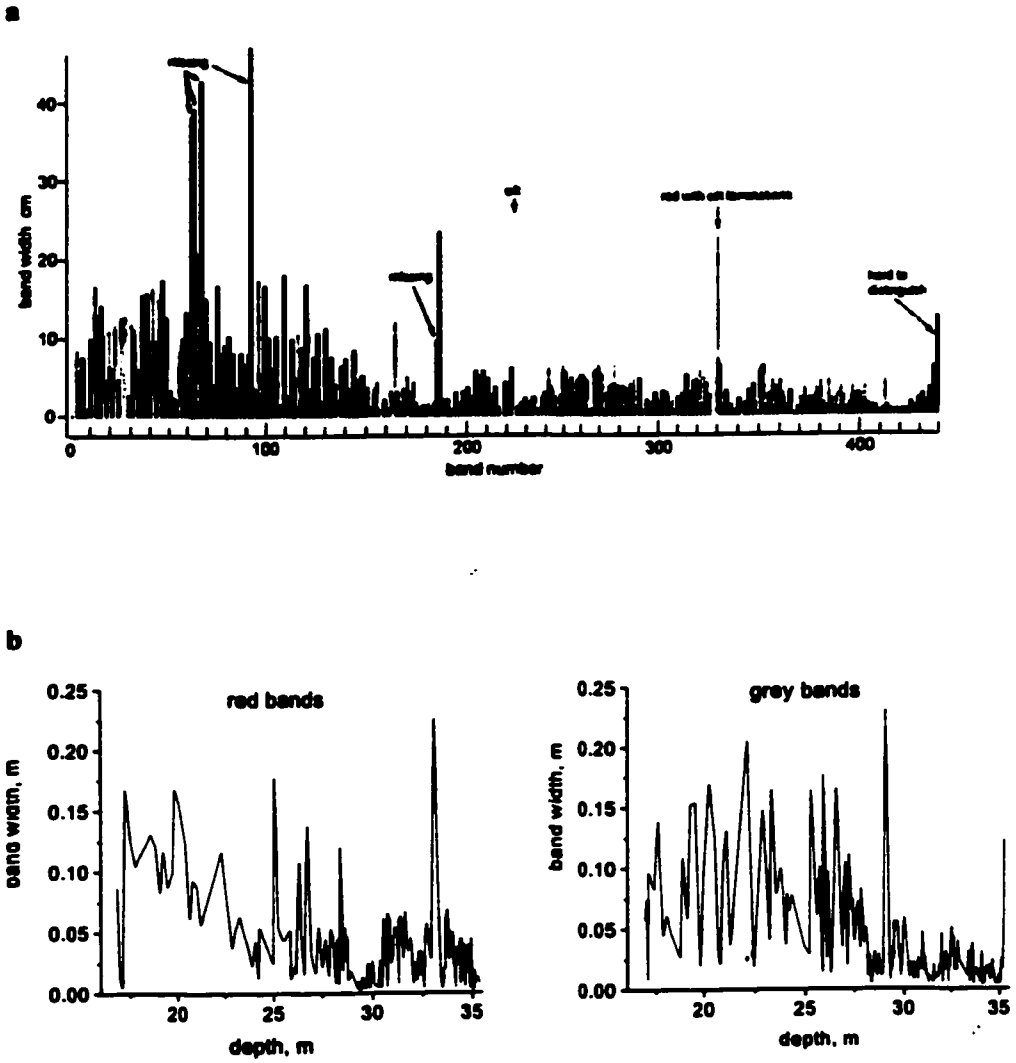

Fig. 64 Champlain Sea clay color bands. a) The band widths are shown as a function of the band number in the series, from the top down. The arrows indicate parts of the banding sequence that were missing from the extracted sample cores and the unusually wide bands whose color could not be clearly distinguished as red or grey. b) Widths of red and grey bands are plotted separately as a function of depth.

bands, the layers of pure silt that were also reported in the banding sequence may probably be regarded as having the same properties as the grey bands that are extremely poor in clay.

Although banding in aqueous sediments typically results from seasonal variations in deposition [155], the origin of the color variations observed in the Leda Clay remains unknown [24]. The duration of time during which the Champlain Sea occupied the Ottawa Valley is estimated to be around 1100-1400 years [156]. While the hypothesis that the banding in the Champlain Sea sediments is caused by seasonal variations is plausible, several aspects of the origin of that banding remain unclear: The number of bands in the observed banding sequence is too small to cover the entire marine phase of the aquatic system evolution. The observed band sequence is composed of about 440 bands, or 220 pairs of red and grey bands, which, if the assumption of a seasonal variation is correct, correspond to only 220 years. To account for the presumably missing bands, additional geological events need to have occurred. For example, some bands may have been eliminated from the sequence as a result of landslides in the more recent geological history. Another difficulty with the seasonal variation hypothesis is the observation that the silt partings typically separate the top of the coarser-grained grey bands from the bottom of the red bands. Normally, the coarsest-grained deposits would occur immediately above the fine-grained winter deposits due to the spring floods [157]. Non-seasonal factors that may contribute to the banding include changes in the beds of the rivers that flowed into the sea and the consequent changes in the content of the deposition materials as well as the oxidation events based on the exposure of the sea bottom and the availability of oxides [154].

For the purposes of the statistical and time-series analysis of the banding data, the measured band widths were recorded both as a function of the band location in the sequence (depth) and as a function of the band number (Fig. 64).

The average width of the bands systematically decreases with depth (Fig. 64). This may be caused either by the increase in an amount of the deposited material at the later stages of sea evolution or by sediment compaction whereby the bands located deeper in the sequence are compressed by the weight of the overlying sediment. At the depths where the banded portion of the sediment is located, only minor compaction of the bands can be expected, i.e. the average band volume can decrease only slightly as the depth increases from about 15 to 35m. However, the observed decrease of the average band width with depth is investigated here in order to determine if it is consistent with the

sediment compaction hypothesis. If the observed trend in the band widths is due to a compaction effect, then the data may be rescaled prior to the analysis in order to get rid of this systematic component in the band width data caused by the mechanical effects of the pressure.

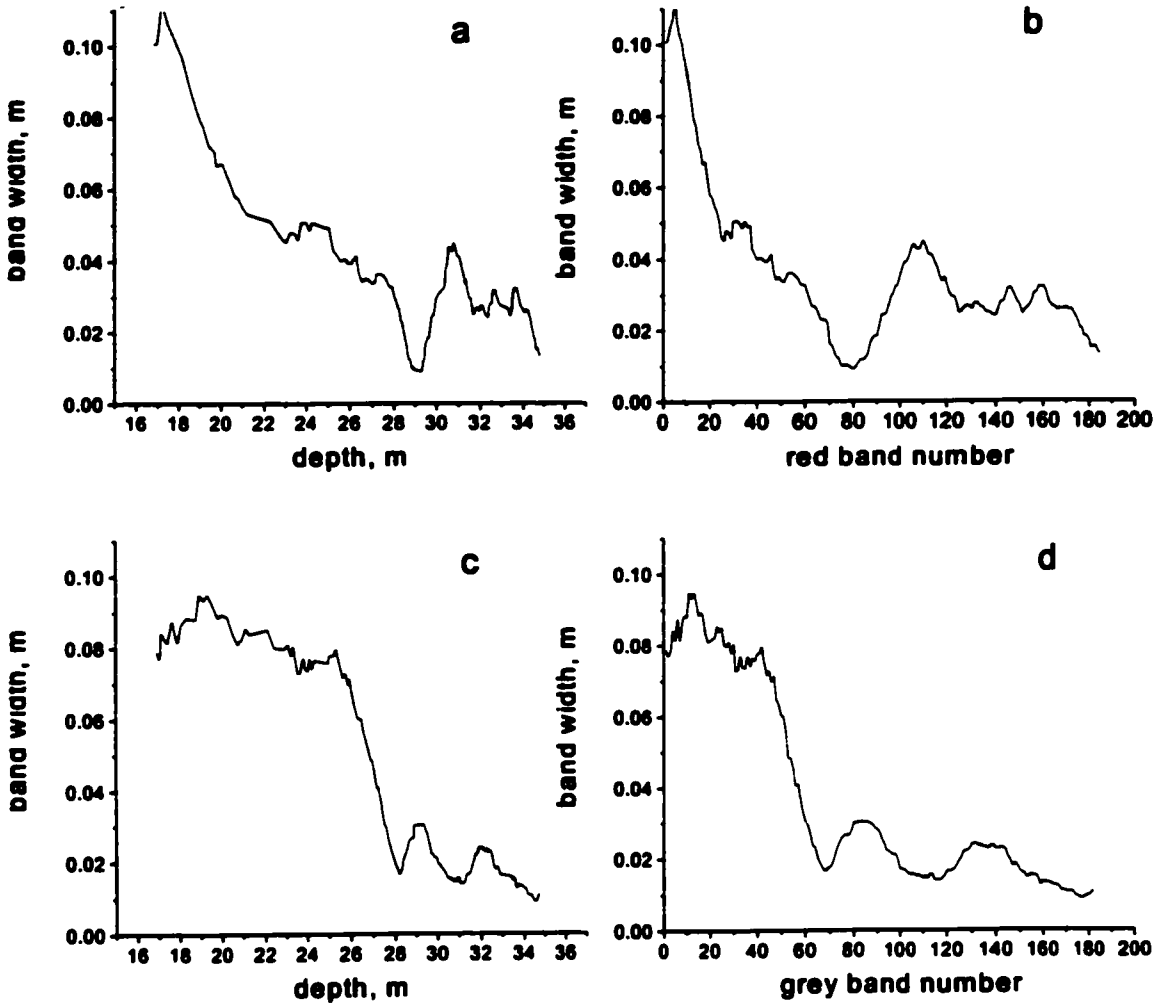

Fig. 65 Average band width. a,b) Running mean for the sequence of red bands in Fig. 64b as a function of band number (a) and depth (b). The width of the averaging window is 20 bands. The widest bands (>17cm) were removed from the series. c,d) Same for the sequence of grey bands in Fig.64b.

The sediment compaction is assumed to be mainly due to the changes in the water content with depth. The corresponding decrease in the sediment porosity φ is then described by [158]

$$\varphi = \varphi_0 e^{-Cz}, \tag{176}$$

where z is the depth, φ_0 is the porosity close to the surface, and C is a constant. If the volume of a band located at some depth z in the banding sequence is $V=WA$, where W is the width of the band and A is the arbitrarily chosen band area, then the amount of solid material per unit volume in that band is $V(1-\varphi)$. Since the compaction does not change the amount of the solid material in the band, one obtains $V_0(1-\varphi_0)= V(1-\varphi)$ and the dependence of the band width W on the depth is given by

$$W = W_0(1-\varphi_0) / (1-\varphi_0 e^{-Cz}), \tag{177}$$

where W_0 is the width of an uncompressed band.

In general, the compaction parameters may be different for the red and grey bands because of the difference in the grain sizes and consequently in the mechanical properties for the bands of different colors. Fig. 65a shows how the average width of the red bands changes with depth. The running mean for the series constructed from the widths of the red bands is shown as a function of depth. The corresponding dependence of the average width of the grey bands on depth is shown in Fig. 65c. The average width of the red bands decreases with depth in general agreement with the law (177). However, the corresponding trend for the grey bands does not conform to the same dependence. An abrupt change in the average band width occurs at a depth of about 26m. Thus, the assumption of a simple hydrostatic compaction described by eq. (177) is insufficient to correctly describe the observed systematic decrease in the band width with depth over the entire banded section of the sediments. Given that normally only minor compaction can be expected at the depth corresponding to the banded section of the deposits, it is likely that the observed trend of increasing band width towards the surface is caused by a significant actual change in the amount of the material being deposited into the sediment during the Champlain Sea evolution, for example as the sea became shallower and the shoreline advanced. The banding data then cannot be adequately rescaled to obtain a more-or-less stationary series and should be treated as is.

The transformation from space to time series required by many time series analysis methods may be achieved if the band width is plotted as a function of the band number instead of the band depth. If the banding is caused by some periodic, e.g.

seasonal, factors then the bands in such series would be recorded as a function of time measured in the periods of these external factors, e.g. years.

The analysis of the clay band series is complicated by several factors. The widths of the bands may have been slightly altered due to the relaxation of the clay following the extraction of the samples. Also, some small portions of the banding record were lost at the time of the sample core recovery. In some cases, the distinction between the grey and the red bands is relatively minor and therefore some small number of bands was characterized as 'slightly reddish', 'grey with red streaks', or 'grey with inclusions of silt'. Consequently, the width of such bands may not be determined accurately.

There are several exceptionally wide bands in the banding sequence. Although there is a possibility that such wide bands have formed as a result of some unusual large-magnitude events in the geological history of the deposits, these bands are more likely to consist of several narrower bands that could not be distinguished properly. This idea is supported by the observation that all of these extremely wide bands either have intermediate "pinkish grey" color or are located in the band sequence near some irregularities such as wide silt layers or a part of the sequence which was lost at the time of the sample extraction (Fig. 64).

8.5.2 Data analysis

The band width data for the red and grey bands was binned in a histogram and the resulting distribution is shown in Fig. 66. The band width distribution for the grey bands occupies the range from 0 to about 17 cm and is bell-shaped with a single peak. The distribution for the red bands, however, suggests that there exist two preferred ranges of band widths. Although most of the red bands have widths in the range from 0 to 6 cm, a few wider bands are clustered around the 12 cm mark. The overall shape of the distribution for the red bands in the region of narrow band widths is also different from the corresponding distribution for the grey bands as it is not bell-shaped. The fact that the widths of the grey and the red bands have different distributions suggests that the fluctuations in climatic conditions that caused the variations in the band widths affected the formation of the grey and the red bands differently.

The magnitude of the width fluctuations for bands at different depths can be visualized by plotting the running variance of the series. For the purposes of this analysis, the band widths were recorded as a function of the band number (starting from the top of the sequence and going down). For each band number, the variance was calculated from

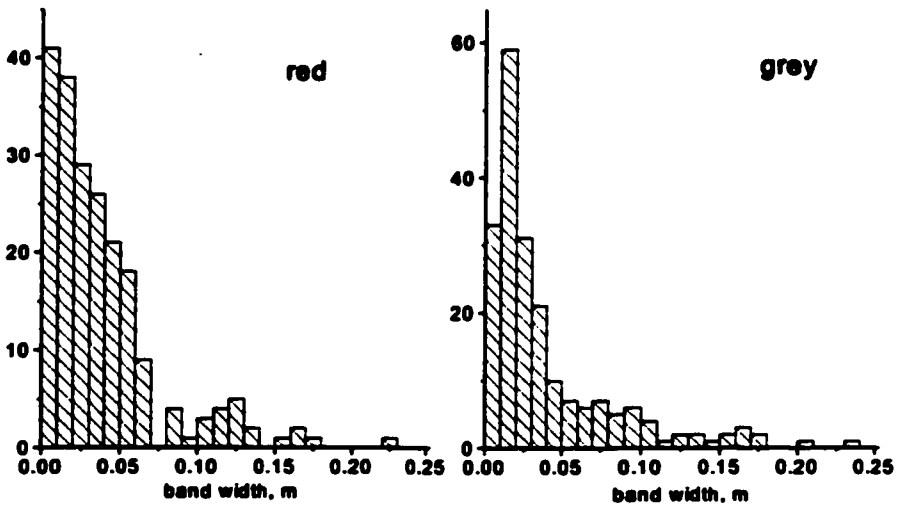

Fig. 66 Distribution of the band widths. The widths of the red and grey bands were binned into a histogram according to the band width ranges.

the part of the series selected by a sliding window of a given width. Fig. 67 shows the running variance of the original series containing both red and grey bands for the case when the averaging window size is equal to 40 bands (or 20 pairs of bands). The result seems to indicate some kind of periodicity in the band data. The shape of the running variance profile as a function of the band number seems to repeat itself with a period of about 110 bands. No specific pattern can be observed when the width of the averaging window is substantially different from 40 bands (larger than 45 or smaller than 35). Plotting the autocorrelation function (Fig. 68) of the series also indicates some correlations in the range of approximately 40 bands and 110 bands. By looking at the series in Fig. 64 one can vaguely perceive what appears to be a cycle with a characteristic period of about 40 bands. A larger cycle of about 110 bands in which the band widths generally increase and then decrease again can also be seen. Since the presence of several extremely wide bands in the series may seriously affect its variance and thus lead to false conclusions about the properties of the entire series, the running variance was recalculated for a series from which the widest bands (over 17cm wide) were removed. In that case, the shape of the curve is substantially different (Fig. 69), and thus the pattern in Fig. 67 is mainly due to the characteristic spacing between the few very wide bands in the banding sequence.

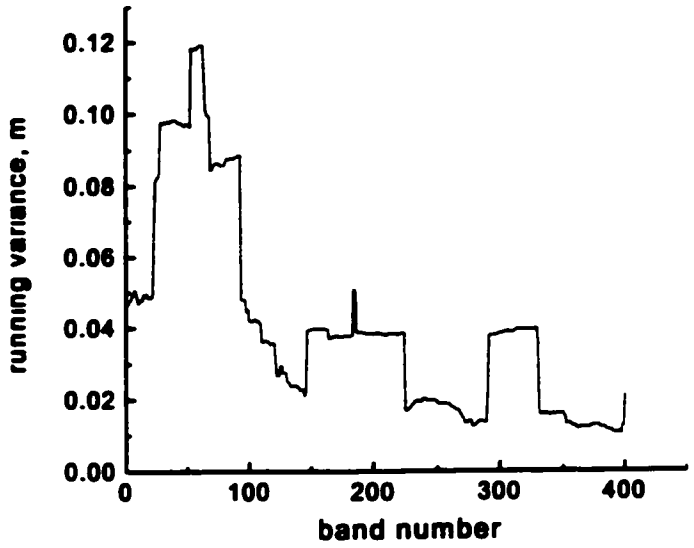

Fig. 67 Running variance. Running variance for the series in Fig.64a. The width of the averaging window is 40 bands.

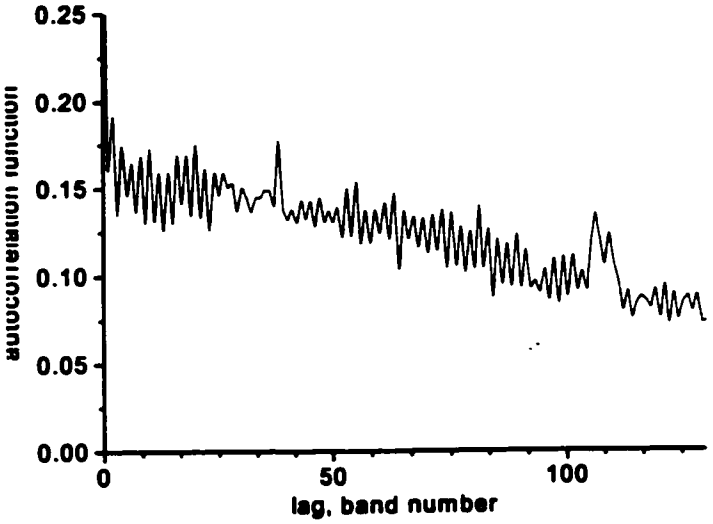

Fig. 68 Autocorrelation function for the series in Fig.64a. Only the lower part of the banding sequence (bands 186 to 440) was used for the analysis because of the apparent nonstationarity in the upper part of the sequence.

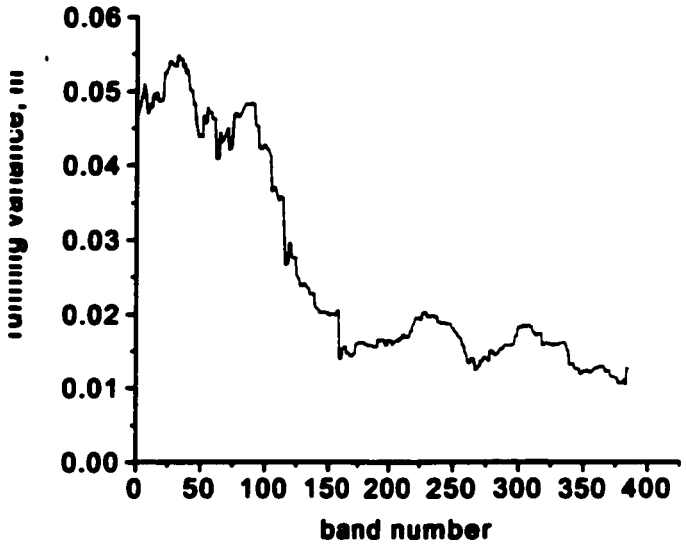

Fig. 69 Running variance. Same as in Fig. 67 but the running variance was calculated for the sequence from which the widest bands (over 17 cm) were removed.

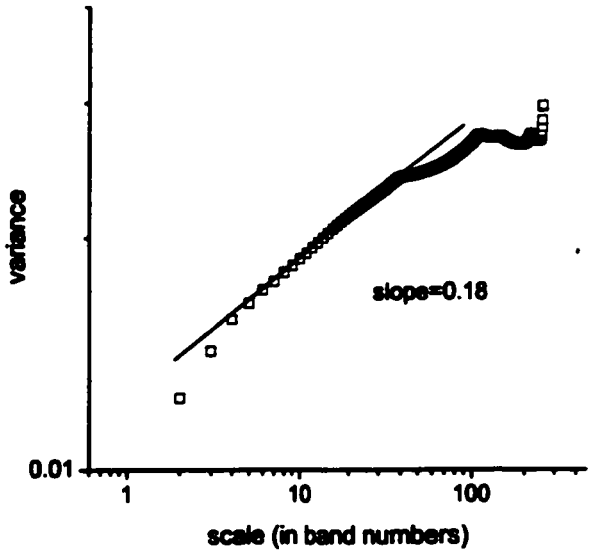

Fig. 70 Fractal scaling. The width of function $w(l)$ is shown as a function of scale measured in band numbers for the lower part of the sequence of red and grey bands (bands 186 to 440).

The variance of the series constructed from the widths of both red and grey bands as a function of the band numbers was plotted against the time scale (eq. (168)) to detect the possible geometrical (fractal) scaling in the series by measuring its Hurst exponent. A scaling in the range from 4 to about 37-40 bands was thus obtained (Fig. 70). The slope of the straight line fitted to the scaling region yields a value of the Hurst exponent H= 0.18. This value is within the range characteristic of Gaussian fractional noise processes, i.e. it is consistent with the hypothesis that the variations in the band widths up to the time scale corresponding to the time of formation of 40 bands may be produced by some stochastic weakly correlated process. However, because of the very irregular nature of the series and the generally low accuracy of the Hurst exponent measurement (see section 8.1.1), no definite conclusions can be drawn.

The correlation dimension [148,159] was evaluated for the banding sequence from the correlation function plot. This method is commonly used to detect a deterministic component in a noisy series by searching for the correlations within the series. First, the time series $x(t_i)$ is transformed into a set of m-dimensional delay vectors $\{X\}_i$ by selecting the components of those vectors as

$$\{X\}_i = \{x(t_i), x(t_i+\tau), ..., x(t_i+(m-1)\tau)\}, \qquad (178)$$

where τ is the lag or time delay and the moments of time t_i are evenly spaced. Then the correlation function $C(r)$ can be calculated as [19]

$$C(r) = \frac{1}{N^2}\sum_{i,j=1}^{N}\Theta\left(r - \left|\{X\}_i - \{X\}_j\right|\right) \qquad (179)$$

where r is the characteristic distance in the m-dimensional phase space, N is the number of the delay vectors and the step function $\Theta(y)$ is $\Theta(y)$ =0 if y<0 and $\Theta(y)$ = 1 if $y \geq 0$. For systems with a deterministic component, the correlation function scales as $C(r)= kr^d$ where d is the correlation dimension. When the correlation functions $C(r)$ are computed for the series for the different values of the embedding dimension m, the deterministic component in the series is detected when the value of d saturates below the size of the embedding dimension m.

Fig. 71 shows the correlation functions computed for the series composed of the widths of the red and grey bands as a function of band number. No saturation in the correlation dimension value occurs for an embedding dimension up to 10. Since no low-dimensional deterministic component is detected, the process that lead to the formation of

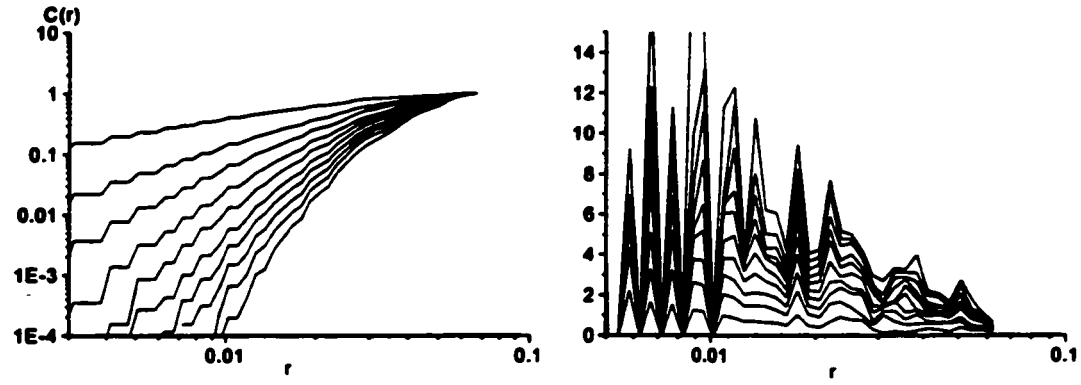

Fig. 71 Correlation dimension. a) Correlation function $C(r)$ is shown as a function of the scale r for the series of red and grey bands starting from the band number 186. The curves (from top down) correspond to embedding dimensions from 1 to 10. b) Slopes of the curves in a).

the banding may be highly stochastic, which is consistent with the previous analysis. However, the series is highly nonstationary and this result should be treated with caution.

Fig. 72a shows the return map constructed for the series of red and grey bands. The width of the nth red band is plotted as the function of the width of the preceding grey band. A similar plot is obtain when the widths of the red bands are plotted against the widths of the grey bands that immediately follow them. The points are mostly grouped in

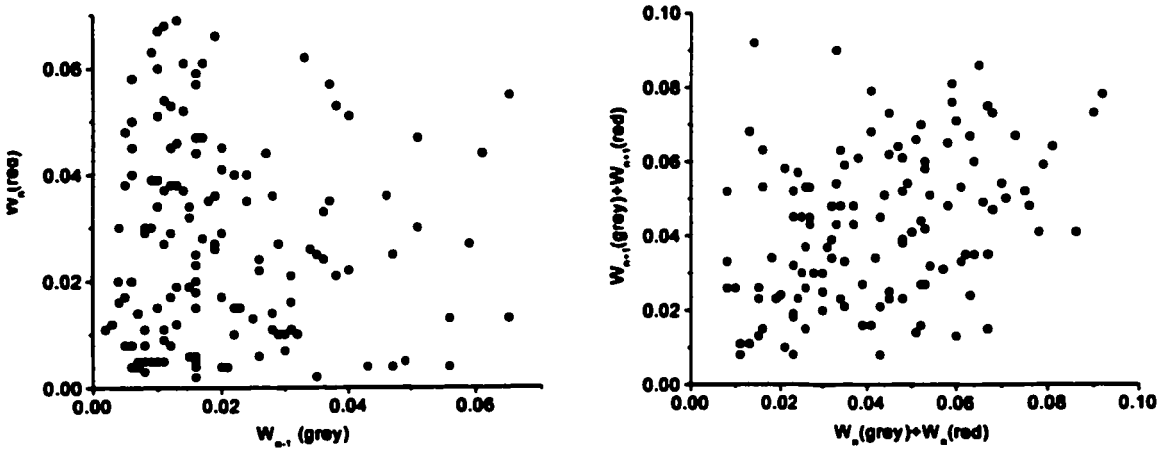

Fig. 72 Return maps for the sequence of red and grey bands. a) The width of the $(n+1)$st red band is plotted against the width of the nth grey band. The region of the return map corresponding to the wide bands is not shown. b) The return map for the series composed of the widths of pairs of adjacent red and grey bands.

the region near the vertical axis, which reflects the fact that the corresponding distributions in Fig. 66 have different widths. No specific correlations between the widths of the red and grey bands can be observed. When the return map for the widths of the pairs of red and grey bands is plotted (Fig. 72b), the points seem to be grouped loosely around the diagonal, which indicates that the total amount of the material deposited in one cycle (in two bands) increases or decreases gradually. A very wide pair of bands does not usually immediately follow a very narrow one, and vice versa.

The banded sequence data was also tested by the surrogate data method [142]. The idea of the method is to first suggest a null hypothesis about the structure within the data and then construct surrogate data series, which preserve the hypothesized property while being different in other respects. A certain quantifier is then calculated both for the original and for the surrogate series. If the value of the quantifier obtained for the original series lies outside of the corresponding quantifier value range obtained for its surrogates then the null hypothesis may be rejected, with the confidence determined by the number of the surrogate data sets.

In our case, the banded sequence was tested against the null hypothesis that the band width values in the sequence may be represented by independent draws from a fixed probability distribution. The surrogate data then could be constructed by randomly shuffling the values of the band widths in the sequence, thus randomizing their order. A third order quantity

$$\varphi(\tau) = \frac{1}{N-\tau}\sum_{n=\tau+1}^{N}(x_n - x_{n-\tau})^3 \qquad (180)$$

may be used as a discriminating quantifier as it measures the asymmetry of a series under

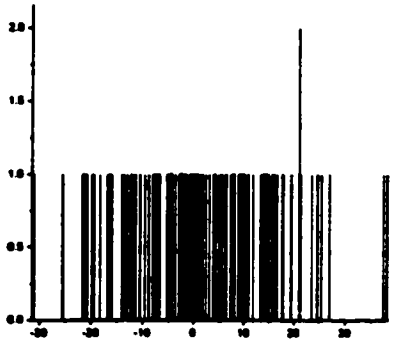

Fig. 73 Surrogate data analysis for the full series of red and grey bands. The horizontal positions of the short bars correspond to the respective quantifier values for the surrogate data set. The quantifier value corresponding to the original dataset is indicated with a longer bar. The vertical scale is arbitrary.

time reversal. Here, x_n is the nth value in the sequence (the width of the nth band), τ is the lag and N is the total number of data points in the sequence [142].

Fig. 73 shows the result of the surrogate data testing for the series of red and grey bands from which the widest bands were removed. The value of the quantifier $\varphi(\tau=1)$ for the original series is marked with a long bar while the corresponding $\varphi(1)$ values for the 99 surrogate series are indicated by the shorter marks. It is seen that the quantifier value for the original series does not stand out from the corresponding values for the surrogates and the null hypothesis cannot be rejected. The same result is obtained when the series $\{x_n\}$ is constructed from the band width values for the bottom 240 bands so that the seemingly nonstationary upper part of the banding sequence is eliminated from the analyzed series.

When the series of only red and only grey bands are tested, the results shown in Fig. 74 are obtained. The widest bands were removed from both sequences as before. For the series constructed from the red or grey band widths, no separation from the surrogates is obtained (Fig. 74). Both for the full series and the separate series of red and grey bands, the null hypothesis also could not be rejected when the value of $\tau>1$ was used.

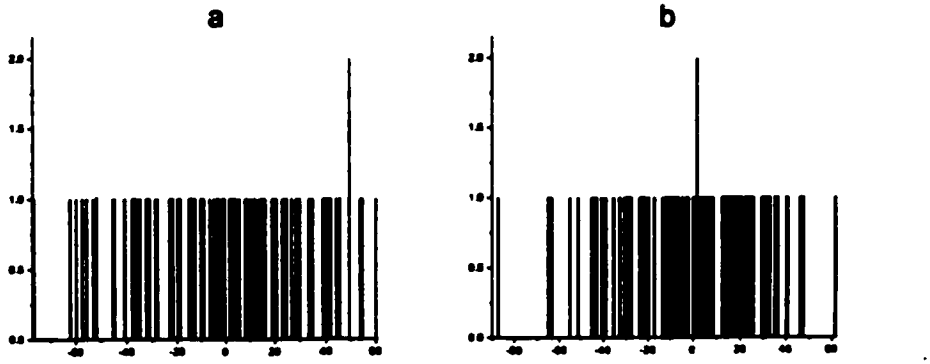

Fig. 74 Surrogate data analysis for the separate series of red and grey bands. a) When the series is constructed from the widths of the red bands. b) When the series is constructed from the width of the grey bands.

Wavelet analysis is a powerful method for series analysis. It allows one to decompose the series in both time and frequency domain using a set of some basis functions (wavelets). The method is, in many cases, superior to Fourier spectrum analysis, as it preserves the time information and also allows one to better detect the periodicities in the data due to the use of non-harmonic localized basis functions. The wavelet transform G of the $x(t)$ series is defined [19] by

$$G(l,t_0)=\frac{1}{l}\int x(t)w\left(\frac{t-t_0}{l}\right)dt, \tag{181}$$

where $l>0$ is a scale parameter, t is the position in the series, t_0 is a translation parameter, and w is a wavelet function. A sinusoidal-shaped Morlet wavelet [160]

$$w^s{}_{t_0,l}(t)=\pi^{-1/4}(ls)^{-1/2}e^{-i2\pi\frac{1}{l}(t-t_0)}e^{-\frac{1}{2}\left(\frac{t-t_0}{ls}\right)^2} \tag{182}$$

is frequently used as the wavelet function. Here, s is the ratio of the width of the analyzing window of the wavelet to the scale l. It is usually set to about 10 to optimize the resolution in periodicity.

The results of the time-frequency decomposition performed on the banded sequence series using Morlet wavelets are shown in Fig. 75. The effect of larger bands is seen in the range of large frequencies at several locations along the time line and its appearance is rather incoherent. However, in low frequences, a continuous signal can be detected for both series of red and grey bands, with a minor shift in frequency for the red band series. The frequency, at which this continuous signal is present, corresponds to the period of about 110 bands, or 55 pairs of bands, which is consistent with our previous findings. The precise determination of the frequency is rather difficult with this method in the region of low frequencies.

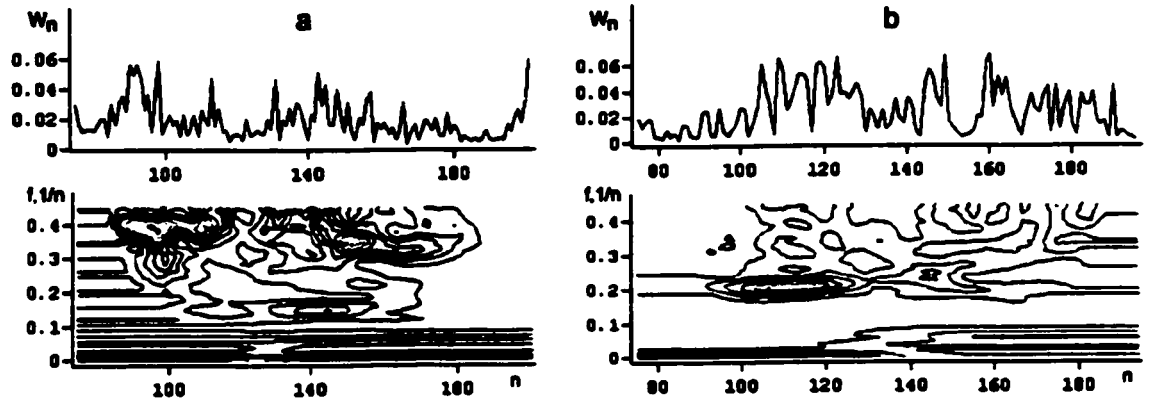

Fig. 75 Time-frequency decomposition using wavelets. a) The series is constructed from the widths of grey bands W_n as a function of grey band number n. b) The series constructed from the widths of red bands W_n as a function of red band number n. Both series include only the bottom part of the banding sequence (starting from the red or grey band number 75). Largest bands were removed from both series.

Conclusion

The analysis indicates that the banding is largely random on a short scale of several tens of bands. At larger scales, periodicities with the characteristic sizes of about 40 and 110 bands seem to be present, although spurious periodicities may have been detected due to the presence of several very large bands in the banding sequence. The wavelet analysis, nevertheless, supports the presence of a weak periodic signal in the series. Although the nature of these variations is very unclear, they probably reflect climatic changes in the Champlain Sea region at the time of the sediment formation. At still larger scales, the general increase of the widths of the red and grey bands for the parts of the sequence that were deposited later in time was probably caused by the overall large time-scale evolution of the Champlain Sea as the ocean water receded from the Ottawa Valley.

Chapter 9

Conclusions

Formation of patterns in minerals, such as oscillatory zoning within single crystals or compositional banding in crystalline aggregates, is an extremely common phenomenon in nature. In most cases, fluctuations in the mineral composition are attributed to the corresponding variations in the geological environment at the time of the mineral formation. However, for several important classes of minerals, self-organization may play an important role in the genesis of those patterns. A spontaneous formation of orderly structures from an initially unpatterned state has been long known to be possible in far-from-equilibrium conditions. In this work, a potential for self-organized behavior during the process of crystal growth has been demonstrated in several reaction-diffusion systems. The pattern formation was simulated using the physical parameters characteristic of the specific geochemical systems and the results obtained agree with the observations in terms of the qualitative similarity and the spatial scales of the patterns. Models of pattern formation in three different environments were presented in Chapters 5 to 7.

In Chapter 5, the impact of environmental noise on the oscillatory zoning formation in plagioclase feldspar was investigated. It was shown that the crystallization process in the albite-anorthite system may be unstable to perturbations when it occurs under far-from-equilibrium conditions, which may lead to oscillatory compositional patterns in the plagioclase crystals. It is suggested that fluctuations in the environment enlarge the range of parameters for which oscillatory zoning is obtained. In the presence of noise, the system exhibited oscillatory dynamics for the parameter range where the deterministic solution was non-oscillatory. A coherence resonance was also observed in the model.

In Chapter 6, an autocatalytic mechanism was proposed for oscillatory zoning formation in a barite-celestite solid solution. Oscillatory zoning within single crystals of

$(Ba,Sr)SO_4$ was observed in the experiments by A.Putnis's group [16] and is one of the very few experimental replications of OZ phenomena. In our simulations, abrupt changes in the crystal composition were shown to arise when the diffusion field around the crystal was sufficiently disturbed by a rapid crystal growth due to the autocatalytic attachment dynamics at the crystal-solution interface.

In Chapter 7, pattern formation by coarsening waves was suggested as a mechanism responsible for the formation of a trace-element compositional banding in the patterned crystallite agglomerates in MVT sphalerite. The non-equilibrium conditions were assumed to be induced and maintained by the continuing influx of a chemically reactive fluid.

Future work on the origin of those patterns should involve improving the models in order to better determine the parameter range in which self-organizing behavior is possible. Also, the underlying assumptions on which the models are based need to be tested. An important aspect of far-from-equilibrium crystal growth that needs to be addressed is the stability of the crystal-liquid interface. At high supersaturations (undercoolings), the interface may become unstable, which may lead to the formation of dendritic structures [161]. In the models of crystal growth presented here, the interface was considered either flat or spherically symmetric. The question of the interface stability at high supersaturations needs to be considered to ensure the validity of this approximation.

The ultimate verification of the models' predictions should rest with the experiment. While several published models generate compositional profiles that agree reasonably well with observations, this fact alone is insufficient to accept them as an adequate description of the processes in natural systems (cf. Karl Popper on falsiability [162]). In order to add scientific value to such models and to be able to choose between several models proposed for the phenomenon in question, one needs to have a discriminating criterion, or at least a possibility that some discriminating test can be set up, to test the model's assumptions and/or predictions. Fortunately, in the case of self-organized pattern formation, such verification procedure is, at least in principle, available. Far-from-equilibrium crystal growth, which is a necessary condition for self-organization, implies fast growth rates. In most cases, the growth of crystals to a macroscopic size should occur on the time scales ranging from several hours to several months. Such relatively short times make it possible, in principle, to reproduce the oscillatory patterns in a laboratory experiment. Although some of the conditions that exist

in the natural environments in which oscillatory zoned crystals are found are hard to reproduce and/or maintain (e.g. high pressure), most of the models, including the ones presented in this work, suggest pattern formation mechanisms that should remain valid under conditions that are relatively easily achievable in a laboratory.

In the case of oscillatory zoning in plagioclase, several models suggest that the patterns are due to the self-organization processes that occur in the crystal-melt reaction-diffusion system at the time of crystal growth. However, oscillatory zoning has never been observed in synthetic plagioclase growth experiments. A multitude of plagioclase textures were observed (e.g. in Lofgren's experiments [82,163]), including dendritic textures that are typical of fast crystal growth, but no oscillatory zoning. It should be noted, however, that, to the best of the author's knowledge, no experiment has been ever set up specifically for the purpose of reproducing the oscillatory zoning. Such an experiment might involve, for example, melting a plagioclase sample, in which oscillatory zoning is observed. This will ensure that the melt has a composition for which oscillatory zoning is possible. The melt should be then crystallized using different cooling regimes and the resulting textures observed. In addition, variations in the crystallization environment parameters should be considered. While the model presented here indicates that fluctuations in the melt composition may be significant in the process of oscillatory pattern formation, variations in other parameters may be important, as well. In particular, pressure changes have never been attempted in plagioclase growth and/or dissolution experiments.

Concerning the oscillatory zoning formation in the barite-celestite solid solution, experimental data are already available, and therefore future efforts should concentrate on a more detailed description of the microscopic processes that are responsible for the zoning formation. While autocatalytic growth seems to be the primary reason for pattern formation, the microscopic description of this process requires some further investigation. As pointed out in section 6.4, where the cellular automata approach is applied to this problem, a mechanism for correlating the composition along the crystal-solution interface is required for the existence of a continuous 3D pattern. This would warrant the use of a mean field-like approximation discussed in Section 6.4.2. In addition, the ability to simulate the oscillatory crystal growth by considering atomic-scale processes at the crystal-liquid interface is interesting by itself and deserves further development.

The idea that the banded pattern formation in MVT sphalerite is due to self-organization is relatively new and, to date, there have been no experimental attempts to

reproduce it. The traditional view of this banding attributes the variations in the Fe content within the banded sphalerite clusters to the large scale (basin-size) variations in the hydrothermal fluid composition. Consequently, the time scale of the pattern formation is assumed to be of the order of thousands of years. Our model suggests that this process is much faster, i.e. that the essential dynamics occurs on a time scale of months. This result enables an experimental verification of the model. The mechanism of banding by coarsening waves appears, in theory, to be very robust, and experiment should answer whether this mechanism could indeed be responsible for the formation of the sphalerite patterns observed in MVT ore deposits. The experiment may involve growth and ripening of sphalerite crystallites in the presence of an ongoing chemical reaction. For example, the growth and ripening of sphalerite crystallites may be studied in a H_2S-containing gel to which the Fe and Zn-rich solutions are being continuously added.

Another approach to verifying the models is to infer information from the available composition profiles obtained from patterned mineral samples. In Chapter 8, some limitations of the commonly used series analysis techniques were outlined that restrict their use for short data sets. As the experimentally obtained compositional profiles often exhibit inhomogeneities, such as jumps and spikes in the mineral composition, spurious interpretation of the analysis results may occur when the fractal scaling of those profiles is analyzed. The reliable analysis of such profiles, therefore, requires the use of more advanced methods as well as the comparison of the results obtained by different analysis techniques.

Appendices

Appendix A. Numerical integration of stochastic differential equations

Given a Langevin type of stochastic differential equation (53) one is usually interested in obtaining the time evolution of the stochastic variable $x(t)$. Here, a numerical integration method is described, which allows to obtain the solution of the Langevin equations in presence of white noise. The equation (53) thus takes the form

$$\frac{dx}{dt} = a(x) + b(x)\xi(t), \tag{183}$$

where $\xi(t)$ is the white noise process with unit intensity and $a(x)$ and $b(x)$ are deterministic functions of x. Obtaining the realization of the stochastic variable $x(t)$ requires the use of stochastic integration described in section 4.1.3.

In the following, the integral of the white noise $\xi(t)$ over an integration time step h will be denoted by

$$W(t) = \int_{t}^{t+h} \xi(t')dt'. \tag{184}$$

Because $W(t)$ is a linear functional of the white noise $\xi(t)$, which is constructed by randomly selecting numbers from a Gaussian distribution, it can also be represented by a set of random Gaussian-distributed numbers. For a white noise with intensity D described by eqs. (48) and (49), the corresponding integral $W(t)$ can be approximated as

$$W(t) = \sqrt{2Dh}\gamma(t), \tag{185}$$

where γ is a Gaussian random number with zero mean and a variance equal to one. It can be generated, for example, according to the Box-Mueller formula

$$\gamma = (-2 \ln \eta_1)^{1/2} \cos(2\pi\eta_2), \tag{186}$$

where η_1 and η_1 are independent random numbers drawn from the interval [0,1] with a constant probability distribution over this interval. From eq. (185), it is seen that $W(t)$ is of the order of $h^{1/2}$.

Modified Euler method

Performing the integration over a small time interval h transforms the Langevin equation (183) into

$$x(t+h) = x(t) + \int_t^{t+h} a(x(t'))dt' + \int_t^{t+h} b(x(t'))\xi(t')dt'. \qquad (187)$$

The functions $a(x)$ and $b(x)$ may be expanded as

$$a(x(t')) = a(x(t)) + \left.\frac{da}{dx}\right|_t \big(x(t') - x(t)\big), \qquad (188)$$

$$b(x(t')) = b(x(t)) + \left.\frac{db}{dx}\right|_t \big(x(t') - x(t)\big). \qquad (189)$$

While the second term in eq. (188), when being substituted in eq. (187), provides a term of order higher than h (and therefore may be discarded in a first order algorithm), the second term in eq. (189) generates a term of order h in eq. (187) and thus needs to be kept. By expressing $(x(t')-x(t))$ in eq. (189) through integrals over time similar to eq. (187) and then substituting eq. (189) back into eq. (187), one obtains the last term in eq. (187) as

$$\int_t^{t+h} b(x(t'))\xi(t')dt' = b(x(t))W(t) + \left.\frac{db}{dx}\right|_t \int_t^{t+h}\left[\int_t^{t'} a(x(t''))dt'' + \int_t^{t'} b(x(t''))\xi(t'')dt''\right]\xi(t')dt' \quad (190)$$

Keeping the terms of the order h gives

$$\int_t^{t+h} b(x(t'))\xi(t')dt' = b(x(t))W(t) + \left.\frac{db}{dx}\right|_t b(x(t)) \int_t^{t+h}\left[\int_t^{t'} \xi(t'')dt''\right]\xi(t')dt' + o(h^{3/2}) \quad (191)$$

and this last expression may be written in Stratonovich calculus [98] as

$$\int_t^{t+h} b(x(t'))\xi(t')dt' = b(x(t))W_1(t) + \left.\frac{db}{dx}\right|_t b(x(t))\frac{1}{2}W_2^2(t) + o(h^{3/2}), \qquad (192)$$

where $W_1(t)$ and $W_2(t)$ are two different Gaussian processes. The first order algorithm can thus be summarized as

$$x(t+h) = x(t) + a(x(t))h + b(x(t))W_1(t) + \left.\frac{db}{dx}\right|_t b(x(t))\frac{1}{2}W_2^2(t). \qquad (193)$$

Heun's method

For additive noise ($b(x)$=const=b), the Heun's first order method can be described [100] as follows. Given the initial value of $x(t=0)$, the value of x at the time h is obtained as

$$x(h) = x(0) + \frac{1}{2}\left[a(x(0)) + a(\mu(h))\right]h + bW(h) \tag{194}$$

where

$$\mu(h) = x(0) + a(x(0))h + bW(h). \tag{195}$$

The values of $x(t)$ at subsequent moments of time $t=2h$, $3h$, ... and so on are obtained by substituting $x(0)$ in the expression (194) for the corresponding values of x at the moments of time t-h. In the multivariate case, when the solution to a set of stochastic variables $\{x^i\}$

$$\frac{dx^i}{dt} = a^i(x) + b^{ij}(x)\xi_j(t) \tag{196}$$

is sought, this formula can be expanded as

$$\begin{aligned} x^i(h) &= x^i(0) + a^i h + b^{ij}W_j(h) + \frac{1}{2}ha^i_k b^{kl}W_l \\ &+ \frac{1}{2}h^2 a^i_k a^k + \frac{1}{4}ha^i_{kl}b^{km}b^{ln}W_m(h)W_n(h) + o(h^{5/2}) \end{aligned} \tag{197}$$

Here $a = a(x(0))$, a^i_j denotes the partial derivative of a^i with respect to x_j, and similarly for a^i_{kl}, and the Einstein convention is used in writing the summation over the repeated indexes.

With Stratonovich calculus, for multiplicative noise, the stochastic differential equation corresponding to eq. (183) can be written as

$$dx = \left[a(x(t)) - \frac{1}{2}b(x(t))\frac{\partial}{\partial x}b(x(t))\right]dt + b(x(t))dW(t) = A(x(t))dt + b(x(t))dW(t) \tag{198}$$

and the expression (194) can be used as before with the new function $A(x)$ used instead of $a(x)$. The algorithm then becomes

$$x(h) = x(0) + \frac{1}{2}\left[A(x(0)) + A(\mu(h))\right]h + \frac{1}{2}\left[b(x(0) + b(\mu(h))\right]W(h), \tag{199}$$

with $\mu(h)=x(0)+A(x(0))h+b(x(0))W(h)$.

Appendix B. Deterministic numerical algorithms

Overrelaxation method

Let us consider an elliptic partial differential equation for a function $u=u(x,y,t)$ in the form

$$\frac{\partial u}{\partial t} = F_1 \frac{\partial^2 u}{\partial x^2} + F_2 \frac{\partial^2 u}{\partial y^2} + F_3 \frac{\partial^2 u}{\partial x \partial y} + F_4 \frac{\partial u}{\partial x} + F_5 \frac{\partial u}{\partial y} + F_6 u + F_7 , \qquad (200)$$

where F_i are some functions of x and y. Suppose a numerical solution for the steady state $u(x,y)$ is sought on a rectangular grid with the horizontal spacing between the nodes Δx and the vertical spacing Δy. Let us describe the position of the nodes in the grid by the indices i and j in the horizontal and vertical directions, respectively. Using the forward-time center-space finite differencing scheme, the derivatives in eq. (200) may be expressed as

$$\frac{\partial u}{\partial t} = \frac{u_{i,j}^{n+1} - u_{i,j}^{n}}{\Delta t}; \qquad (201)$$

$$\frac{\partial u}{\partial x} = \frac{u_{i+1,j}^{n} - u_{i-1,j}^{n}}{2\Delta x}; \quad \frac{\partial u}{\partial y} = \frac{u_{i,j+1}^{n} - u_{i,j-1}^{n}}{2\Delta y} \qquad (202)$$

$$\frac{\partial^2 u}{\partial x^2} = \frac{u_{i+1,j}^{n} - u_{i,j}^{n} + u_{i-1,j}^{n}}{(\Delta x)^2}; \quad \frac{\partial^2 u}{\partial y^2} = \frac{u_{i,j+1}^{n} - u_{i,j}^{n} + u_{i,j-1}^{n}}{(\Delta y)^2} \qquad (203)$$

$$\frac{\partial^2 u}{\partial x \partial y} = \frac{u_{i+1,j+1}^{n} - u_{i+1,j-1}^{n} - u_{i-1,j+1}^{n} + u_{i-1,j-1}^{n}}{4\Delta x \Delta y} \qquad (204)$$

where n is the time iteration step number. When these expressions are substituted into eq. (200), an equation of the following form for the value of $u_{i,j}$ at the time $n+1$ is obtained:

$$u_{i,j}^{n+1} = u_{i,j}^{n} + G(u_{i,j}^{n}, u_{i+1,j}^{n}, u_{i-1,j}^{n}, u_{i,j+1}^{n}, u_{i,j-1}^{n}, u_{i+1,j+1}^{n}, u_{i-1,j+1}^{n}, u_{i+1,j-1}^{n}, u_{i-1,j-1}^{n}) \qquad (205)$$

where the function G is defined by the appropriate combinations of F_i, Δx, Δy, and Δt. The solution, which is obtained by taking successive iterations, then relaxes toward the steady state solution. In the overrelaxation method, this scheme is improved by mixing the thus obtained value at the next time step with the previous value:

$$u_{i,j}^{n+1} = (1-\rho)u_{i,j}^{n} + \rho(u_{i,j}^{n} + G) \qquad (206)$$

where the parameter ρ is chosen arbitrarily to obtimize the convergence rate and G is the same function of u at the time n as in the expression above.

Appendix C. Derivation of crystal-solution interface width approximation

In this appendix, we derive the differential equation for the evolution of the kinetically defined composition at the surface of a spherical crystal (Eq. (104)). We proceed in the spirit of [52], where a similar derivation was performed for the case of a flat interface. We consider an atomically rough surface of a spherical crystallite, which is a binary solid solution with the end-members B and C, in contact with a supersaturated solution. If the number of the atomic units of elements B and C in the crystallite surface are n_B and n_C, respectively, then the surface molar composition X is defined by

$$X = \frac{n_B}{n_B + n_C}. \tag{207}$$

Let us define the interface as a thin spherical shell, whose width is of the order of the length scale of the crystal surface fluctuations. The characteristic radius of this shell r can be used as the average radius of the crystallite. If the accretion rates V_B and V_C are defined as the rates (in cm/s) of crystal surface growth (or dissolution) due to the arrival (departure) of the units of B and C, respectively, then the incoming fluxes of the units of B and C to the interface are given by

$$\frac{\partial n_B^{in}}{\partial t} = G_B 4\pi r^2 = V_B \frac{4\pi r^2}{v_B}; \quad \frac{\partial n_C^{in}}{\partial t} = G_C 4\pi r^2 = V_C \frac{4\pi r^2}{v_C}, \tag{208}$$

where G_B and G_C are the molecular fluxes (number of molecular units per unit area per unit time) towards the crystallite surface and v_B and v_C are the atomic volumes of the species. While units are arriving from the solution to the outer surface of the interface shell, they are leaving the shell at its inner surface due to the motion of the shell associated with the crystallite growth. The corresponding outgoing molecular flux is proportional to the surface composition X and the surface area:

$$\frac{\partial n_B^{out}}{\partial t} = X 4\pi r^2 K, \tag{209}$$

where K is the coefficient of proportionality. In the steady growth regime, when the number of B units in the interface shell does not change, the change in the number of incoming B units per unit time is balanced by the change in the number of outcoming B units. At the same time, the surface composition X corresponding to this steady growth regime may be defined kinetically [112] through the incoming fluxes G_B and G_C as

$$X_{st} = \frac{G_B}{G_B + G_C'}. \tag{210}$$

By comparing eqs. (208), (209), and (210), it follows that $K = G_B + G_C$ and

$$\frac{\partial n_B^{out}}{\partial t} = X 4\pi r^2 \left(\frac{V_B}{v_B} + \frac{V_C}{v_C} \right). \tag{211}$$

Let us now define the molecular density in the solid at the interface as

$$\rho = \frac{1}{X v_B + (1 - X) v_C}. \tag{212}$$

The number of B units in the interface shell may be then obtained as

$$n_B = 4\pi r^2 \rho X L, \tag{213}$$

where the parameter L (assumed constant) is the effective width of the rough crystallite-solution interface defined as

$$L = \frac{1}{4\pi r^2} \int_{shell} \theta(\vec{r}', t) d^3 \vec{r}', \tag{214}$$

where the function θ is equal to 1 if the point $\vec{r}'$ is located in the solid and 0 otherwise. The total change in the number of B units in the interface is then

$$\frac{\partial n_B}{\partial t} = \frac{\partial}{\partial t}\left(4\pi r^2 \rho X L\right) = L \frac{\partial}{\partial t}(\rho X) + 8\pi r L \rho X \frac{\partial r}{\partial t}. \tag{215}$$

By equating this expression to the difference between the incoming flux (208) and the outgoing flux (211) and using the expression (212) for ρ, one obtains

$$\frac{L\alpha}{(X + (1 - X)\alpha)^2} \frac{dX}{dt} + \frac{2L}{r} \frac{X}{X + (1 - X)\alpha} \frac{\partial r}{\partial t} = V_B - X\left(V_B + \frac{V_C}{\alpha} \right), \tag{216}$$

where $\alpha = v_C / v_B$. Taking into account that [129]

$$\frac{\partial r}{\partial t} \approx V_B + V_C \tag{217}$$

and that $L << r$, the term containing $2L/r$ may be neglected with respect to the last term on the right hand side of eq. (216) and we recover equation (104):

$$L\alpha\frac{dX}{dt}=[V_B-X(V_B+V_C/\alpha)][X+(1-X)\alpha]^2. \qquad (218)$$

References

[1] A. M. Turing, The chemical basis of morphogenesis. *Philos. Trans. R. Soc. Lond.* **B237**, 37, 1952.

[2] G. Nicolis and I. Prigogine. *Self-organization in Non-equilibrium Systems*, New-York, Wiley, 1977.

[3] M. Shore and A. D. Fowler, Oscillatory zoning in minerals: a common phenomenon. *Can. Mineral.* **34**, 1111, 1996.

[4] T. Pearce, Recent work on oscillatory zoning in plagioclase, in *Feldspars and their reactions*, edited by I. Parsons, Dordrecht (NATO ASI 313), pp.313--346, 1994.

[5] T. H. Pearce and A. M. Kolisnik, Observations of plagioclase zoning using interference imaging. *Earth-Sci. Rev.* **29**, 9, 1990.

[6] F. Rutley, Notes on some peculiarities in the microscopic structure of feldspars, in *Quart. J. Geol. Soc. London* **31**, 479-488, 1875.

[7] I. L'Heureux and A. D. Fowler. Oscillatory zoning in minerals: Mechanisms and implications, in *Selbstorganisation*, vol. 11: Non-equilibrium Processes and Dissipative Structures in Geoscience, pp. 47-72, Duncker & Humblot, Berlin, 2000.

[8] B. W. D. Yardley, C. A. Rochelle, A. C. Barnicoat, G. E. Lloyd. Oscillatory zoning in metamorphic minerals: an indicator of infiltration metasomatism. *Min. Mag.* **55**, 357-365, 1991.

[9] T. I. Ivanova, A. G. Shtukenberg, Y. O. Punin, O. V. Frank-Kamenetskaya, P. B. Sokolov. On the complex zonality in grandite garnets and implications. *Min. Mag.* **62(6)**, 857-868, 1998.

[10] K. Pollok, B. Jamtveit, and A. Putnis. Analytical transmission electron microscopy of oscillatory zoned grandite garnets., *Contrib. Mineral. Petrol.* **141**, 358-366, 2001.

[11] B. Jamtveit, K. V. Ragnarsdottir, and B. J. Wood. On the origin of zoned grossular-andradite garnets in hydrothermal systems. *Eur. J. Mineral.* 7, 1399-1410, 1995.

[12] B. Jamtveit, R. Wogelius, and D. G. Fraser. Zonation patters of skarn garnets: Stratigraphic records of hydrothermal systems. *Geology* 21, 113-116, 1993.

[13] B. Jamtveit, Oscillatory zonation patterns in hydrothermal grossular-andradite garnets: nonlinear dynamics in regions of miscibility. *Am. Mineral.* 76, 1319-1327, 1991.

[14] B. Jamtveit and R. L. Hervig, Constraints on transport and kinetics in hydrothermal systems from zoned garnet crystals. *Science* 263, 505-508, 1994.

[15] B. Jamtveit and T. B. Anderson. Morphological instabilities during rapid growth of metamorphic garnets. *Phys. Chem. Minerals* 19, 176-184, 1992.

[16] A. Putnis, L. Fernandez-Diaz and M. Prieto, Experimentally produced oscillatory zoning in the (Ba,Sr)SO_4 solid solution. *Nature* 358, 743-745, 1992.

[17] R. J. Reeder, R. O. Fagioli, and W. J. Meyers. Oscillatory zoning of Mn in solution-grown calcite crystals. *Earth-Sci. Rev.* 29, 39-46, 1990.

[18] Y. Wang and E. Merino, Dynamic model of oscillatory zoning of trace elements in calcite: Double layer, inhibition, and self-organization. *Geochim. Cosmochim. Acta.* 56, 587, 1992.

[19] A. Fowler, A. Prokoph, R. Stern, and C. Dupuis, Organization of oscillatory zoning in zircon: Analysis, scaling, geochemistry, and model of a zircon from Kipawa, Quebec, Canada., *Ceochim. et Cosmochim. Acta* 66, 2, 311-328, 2002.

[20] N. M. Halden and F. Hawthorne. The fractal geometry of oscillatory zoning in crystals: Application to zircon. *Am. Mineral.* 78, 1113-1116, 1993.

[21] P. W. O. Hoskin, Patterns of chaos: Fractal statistics and the oscillatory chemistry of zircon. *Ceochim. et Cosmochim. Acta* 64, 11, 1905-1923, 2000.

[22] Fowler, A. D. & L'Heureux, I. Self-organized banded sphalerite and branching galena in the Pine Point ore deposit-Northwest Territories. *Can. Mineral.* 34, 1211-1222, 1996.

[23] Y. Wang and E. Merino. Self-organizational origin of agates: Banding, fiber twisting, composition, and dynamic crystallization model. *Geochim. Cosmochim. Acta* **54**, 1627-1638, 1990.

[24] A. Fritz, Mineralogical, geotechnical and grain size characteristics of the red and grey banded layers in Champlain Sea sediments of the Ottawa Valley, B.Sc. thesis, Dept. of Environmental Science, Carleton University, 1998.

[25] P. J. Heaney and A. M. Davis, Observation and origin of self-organized textures in agates, *Science* **269**, 1562-1565, 1995.

[26] C. M. Pina, M. Enders and A. Putnis. The composition of solid solutions crystallising from aqueous solutions: the influence of supersaturation and growth mechanisms., *Chem. Geol.* **168**, 195-210, 2000.

[27] A. R. Lang, M. Moore, A. M. Makepeace, W. Wierzhowski, and C. M. Welbourne. On the dilation of synthetic type Ib Diamond by substitutional nitrogen impurity. *Phil. Trans. R. Soc. London* **A337**, 497-520, 1991.

[28] H. Haken. *Advanced Synergetics*, New-York, Springer, 1983.

[29] R. Field and M. Berger, eds. *Oscillations and Travelling Waves in Chemical Systems*, New York, Wiley, 1985.

[30] D. F. Sibley, T. A. Vogel, B. M. Walker and G. Byerly, The origin of oscillatory zoning in plagioclase: a diffusion and growth controlled model, in *Am. J. Sci.* **276**, 275-284, 1976.

[31] Y. Wang and E. Merino, Oscillatory magma crystallization by feedback between the concentrations of the reactant species and mineral growth rates, *J. of Petrol.* **34**, 369-382, 1993.

[32] J.-H. Wang and J.-P. Wu, Oscillatory zoning of minerals and self-organisation in silicate solid-solution systems: a new nonlinear dynamical model. *Eur. J. Mineral.* **7**, 1089-1100 , 1995.

[33] I. L'Heureux, Oscillatory zoning in crystal growth: A constitutional undercooling mechanism, *Phys. Rev. E* **48**, 6, 4460-4469, 1993.

[34] I. L'Heureux and A. D. Fowler, Dynamical model of oscillatory zoning in plagioclase with nonlinear partition relation, *Geophys. Res. Lett.* **23**, 1, 17-20, 1996.

[35] T. Holten, B. Jamtveit, P. Meakin, M. Cortini, J. Blundy, and H. Austrheim. Statistical characteristics and origin of oscillatory zoning in crystals. *Am. Mineral.* **82**, 596-606, 1997.

[36] S. Katsev and I. L'Heureux. Impact of environmental noise on oscillatory pattern formation in crystal growth: Plagioclase feldspar. *Phys. Rev.E* **61**, 5, 4972-4979, 2000.

[37] B. J. Skinner, Hydrothermal Mineral Deposits: What we do and don't know, in *Geochemistry of Hydrothermal Ore Deposits*, ed. By H. L. Barnes, 3rd ed., New York, Wiley, 1997.

[38] A. B. Carpenter, M. L. Trout, and E. E. Pickett, Preliminary report on the origin and chemical evolution of lead- and zinc-rich oil field brines in Central Mississippi. *Econ. Geol.* **69**, 1191-1206, 1974.

[39] B. J. Skinner and P. B. Barton, Jr. Genesis of mineral deposits. *Ann. Rev. Earth Planet. Sci.* **1**, 183-211, 1973.

[40] T. H. Giordano. Metal transport in ore fluids by organic ligand complexation, in *The Role of Organic Acids in Geological Processes*, M. D. Lewan and E. D. Pittmann (eds.). New York, Springer-Verlag, 1994.

[41] T. M. Seward and H. L. Barnes. Metal transport by hydrothermal ore fluids, in *Geochemistry of Hydrothermal Ore Deposits*, ed. By H. L. Barnes, 3rd ed., New York, Wiley, 1997.

[42] S. Nakai, A. N. Halliday, S. E. Kesler, and H. D. Jones, Rb-Sr dating of sphalerite and genesis of MVT deposits. *Nature* **134**, 354-357, 1990.

[43] S. Nakai, A. N. Halliday, S. E. Kesler, H. D. Jones, J. R. Lyle, and T. E. Lane. Rb-Sr dating of sphalerites from Mississippi Valley-type (MVT) ore deposits. *Geochim. Cosmochim. Acta* **57**, 417-427, 1993.

[44] J. C. Brannon, F. A. Podosek, and R. K. McLimans. A permian Rb-Sr age for sphalerite from the Upper Mississippi zinc-lead district, Wisconsin. *Nature* **356**, 509-511, 1992.

[45] J. N. Christensen, A. N. Halliday, J. R. Vearncombe, and S. E. Kesler. Testing models of large-scale crustal fluid flow using direct dating of sulfides: Rb-Sr evidence for early dewatering and formation of Mississippi Valley-type deposits, Canning Basin, Ausstralia. *Econ. Geol.* **90**, 877-884, 1995.

[46] E. Roedder. Fluid inclusions as samples of ore-forming fluids. Int. Geol. Cong., XXI Session, Norden, Part XVI, pp.218-229, 1960.

[47] E. Deloule and D. L. Turcotte. The flow of hot brines in cracks and the formation of ore deposits. *Econ. Geol.* **84**, 2217-2225, 1989.

[48] A. P. Gize and H. L. Barnes. The organic geochemistry of the Mississippi Valley-type lead-zinc deposits. *Econ. Geol.* **82**, 457-470, 1987.

[49] D. W. Hyndman. *Petrology of Igneous and Metamorphic Rocks*, 2nd ed., Intl. Series in the Earth and planetary sciences. McGraw-Hill Book Company, New York, 1985.

[50] K. V. Cashman. Textural constraints on the kinetics of crystallization of igneous rocks. In *Modern Methods of Igneous Petrology: Understanding Magmatic Processes*, edited by J. Nicholls and J. K. Russel, pp. 259-309, Reviews in Mineralogy, vol. **24**. Washington, D.C.: Mineralogical Society of America, 1990.

[51] E. Dowty, Crystal growth and nucleation theory and the numerical simulation of igneous crystallization, in *Physics of Magmatic Processes*, Princeton Univ. Press, Princeton, 1980.

[52] P. Ortoleva, *Geochemical Self-Organization*, Vol. 23 (Oxford Monographs on Geology and Geophysics Ser.), Oxford University Press, New York, 1994.

[53] M. L. Stewart and A. D. Fowler. The nature and occurence of descrete zoning in plagioclase from recently erupted andesitic volcanic rocks, Montserrat. *J. Volcan. Geotherm. Res.* **106**, 243-253, 2001.

[54] A. D. Fowler, personal communication, 2001.

[55] T. P. Loomis. Compositional zoning of crystals: A record of growth and reaction history, in *Kinetics and Equilibrium in Mineral Reactions*, edited by S. K. Saxena, New York, Springer-Verlag, 1983.

[56] R. K. McLimans, H. L. Barnes, and H. Ohmoto. Sphalerite stratigraphy of the Upper Mississippi Valley Zinc-Lead District, Southwest Wisconsin. *Bull. Soc. Econom. Geol.* **75**, 351-361, 1980.

[57] I. Markov. *Crystal Growth for Beginners. Fundamentals of Nucleation, Crystal Growth and Epitaxy*. Singapore, World Scienific, 1995.

[58] A. C. Lasaga. *Kinetic Theory in the Earth Sciences*, Princeton University Press, Princeton, 1998.

[59] A. A. Chernov *et al. Modern Crystallography*, Vol 3, Nauka, Moscow, 1980.

[60] A. G. Walton, in *Nucleation*, ed. A. C. Zettlemoyer, p. 379, Marcel Dekker, 1969.

[61] A. E. Nielsen, Nucleation in aqueous solution, in *Crystal Growth*, ed. by H. S. Peiser, p. 419-430, Oxford, 1967.

[62] C. M. Pina, U. Becker, P. Risthaus, D. Bosbach, and A. Putnis. Molecular-scale mechanisms of crystal growth in barite. *Nature* **395**, 483-486, 1998.

[63] A. C. Lasaga, Chemical kinetics of water-rock interactions. *J. Geophys. Res.* B6, 4009-4025, 1984.

[64] А. А.Чернов, Слоисто-спиральный рост кристаллов. УФН **73**, вып. 2, с. 277-331, 1961.

[65] W. K. Burton, N. Cabrera, and F. C. Frank, The growth of crystals and the equilibrium structure of their surfaces, *Phil. Trans. Royal Soc. London Ser. A* **243**, 299-358, 1951.

[66] R. A. Berner, Rate control of mineral dissolution under Earth surface conditions, *Amer. J. Sci.* **278**, 1235-1252, 1978.

[67] T. E. Burch, K. L. Nagy, and A. C. Lasaga, Free energy dependence of albite dissolution kinetics at 80°C, pH 8.8. *Chem. Geol.* **105**, 137-162, 1993.

[68] Y. Zhang, D. Walker, and C. E. Lesher. Diffusive crystal dissolution. *Contrib. Mineral. Petrol.* **102**, 492-513, 1989.

[69] W. Horsthemke and R. Lefever, *Noise-Induced Transitions. Theory and Applications in Physics, Chemistry, and Biology*, Springer-Verlag, New York, 1984.

[70] C. W. Gardiner, *Handbook of Stochastic Methods for Physics, Chemistry and the Natural Sciences*, Springer-Verlag, Berlin, 1983.

[71] P. Meakin, *Fractals, Scaling and Growth far from Equilibrium*, Cambridge University Press, 1998.

[72] H. Risken, *The Fokker-Planck Equation: Methods of Solution and Applications*, 2nd ed., edited by H. Haken, Springer-Verlag, Berlin, 1989.

[73] H. Gang, T. Ditzinger, C. Z. Ning, and H. Haken. Stochastic resonance without external periodic force. *Phys. Rev. Lett.* **71**, 6, 807, 1993.

[74] L. Gammaitoni, P. Hängii, P. Jung, and F. Marchesoni, Stochastic Resonance, *Rev. Mod. Phys.* **70**, 223, 1998.

[75] K. Wiesenfeld, Noisy precursors of nonlinear instabilities. *J. Stat. Phys.* **38**, 5/6, 1071-1097, 1985.

[76] A. Neiman, P. I. Saparin, and L. Stone, Coherence resonance at noisy precursors of bifurcations in nonlinear dynamical systems. *Phys. Rev. E* **56**, 1, 270-273, 1997.

[77] A. Longtin, Autonomous stochastic resonance in bursting neurons. *Phys. Rev. E* **55**, 1, 868, 1997.

[78] J. V. Smith and W. L. Brown. *Feldspar Minerals. Vol 1. Crystal Structures, Physical, Chemical, and Microtextural Properties*, 2-nd edition. Springer-Verlag, Berlin, 1988.

[79] L. Klein and D. R. Uhlmann. Crystallization behavior of anorthite. *J. Geophys. Res.* **79**, 4869-4874, 1974.

[80] R. J. Kirkpatrick, G. R. Robinson, J. F. Hays. Kinetics of crystal growth from silicate melts: anorthite and diopside. *J. Geophys. Res.* **81**, 5715-5720, 1976.

[81] R. J. Kirkpatrick, L. Klein, D. R. Uhlmann, and J. F. Hays, Rates and processes of crystal growth in the system anorthite-albite. *J. Geol. Res.* **84**, 3671-3676, 1979.

[82] G. Lofgren. Temperature-induced zoning in synthetic plagioclase feldspar. In the Feldspars, ed. W.S. MacKenzie J. Zussman, 362-375. Manchester Univ. Press, Manchester, 1974.

[83] S. E. Swanson. Relation of nucleation and crystal-growth rate to the development of the granitic textures. *Amer. Mineral.* **62**, 966-978, 1977.

[84] K. Sato, K. Kashima, and I. Sunagawa. Measurements of nucleation rates and real growth rates of plagioclase in a solution of basaltic composition. *J. Jap. Assoc. Mineral. Petrol. and Econ. Geol.* **76**, 294-307, 1981.

[85] A. W. Hofmann, in *Physics of Magmatic Processes*, ed. R. B. Hargraves, Princeton Univ. Press, Princeton, 1980.

[86] Y. Bottinga and D. F. Weill, The viscosity of magmatic silicate liquids: a model for calculation. *Am. J. Sci* **272**, 438-475, 1972.

[87] C. S. Haase, J. Chadam, D. Feinn, P. Ortoleva, Oscillatory zoning in plagioclase feldspar, in *Science* **209**, 272-274, 1980.

[88] C. J. Allègre, A. Provost, C. Jaupart, Oscillatory zoning: a pathological case of crystal growth, *Nature* **294**, 223-228, 1981.

[89] T. H. Pearce, A simple deterministic model of oscillatory zoning in magmatic plagioclase. *Geol. Assoc. Canada Abstracts* **18**, A-81, 1993.

[90] A. Lasaga, Towards a Master Equation in crystal growth, *Am. J. Sci.* **282**, 1264-1288, 1982.

[91] I. L'Heureux and A. D. Fowler, Isothermal constituitive undercooling as a model for oscillatory zoning in plagioclase. *Can. Mineral.* **34**, 1137-1147, 1996.

[92] I. L'Heureux, Oscillatory zoning in plagioclase: Thermal effects, in *Physica A* **238**, 137-146, 1997.

[93] T. Holten, B. Jamtveit, and P. Meakin, Noise and oscillatory zoning of minerals. *Geochim. Cosmochim. Acta.* **64**, 1893-1904, 2000.

[94] S. Katsev, I. L'Heureux, and A. D. Fowler, Mechanism and duration of banding in Mississippi Valley-type sphalerite, *Geophys. Res. Lett.* **28**, 24, 4643-4646, 2001.

[95] S. L. Higman and T. H. Pearce, Spatiotemporal dynamics in oscillatory zoned magmatic plagioclase. *Geophys. Res. Lett.* **20**, 18, 1935, 1993.

[96] P. Calvert and D. Uhlmann, Surface nucleation growth theory for the large and small crystal cases and the significance of transient nucleation. *J. of Crystal Growth* **12**, 291-296, 1972.

[97] Y. Bottinga and D. F. Weill, *Am. J. Sci.* **272**, 438, 1972.

[98] M. Sancho, M. San-Miguel, S. L. Katz, and J. Gunton, Analytical and numerical studies of multiplicative noise. *Phys. Rev. A* **26**, 3, 1589, 1982.

[99] R. Lefever and J. W. Turner, Sensitivity of a Hopf bifurcation to multiplicative colored noise. *Phys. Rev. Lett.* **56**, 16, 1631-1634, 1986.

[100] A. Greiner, W.Strittmatter, and J. Honerkamp, Numerical integration of stochastic differential equations. *J. Stat. Phys.* **51**, 1/2, 95-108, 1988.

[101] L. Fronzoni, R. Mannella, P. V. E. McClintock, and F. Moss, Postponement of Hopf bifurcations by multiplicative colored noise. *Phys. Rev. A* **36**, 2, 834-841, 1987.

[102] A. Tsuchiyama and E. Takahashi, Melting kinetics of a plagioclase feldspar, *Contrib. Mineral. Petrol* **84**, 345-354, 1983.

[103] B. R. Edwards, J. K. Russell, A review and analysis of silicate mineral dissolution experiments in natural silicate melts. *Chem. Geol.* **130**, 233-245, 1996.

[104] C. H. Donaldson, The rates of dissolution of olivine, plagioclase and quartz in a basalt melt. *Mineral. Mag.* **49**, 683, 1985.

[105] M. Prieto, A. Putnis and L. Fernandez-Diaz, Crystallization of solid solutions from aqueous solutions in a porous medium: zoning in $(Ba,Sr)SO_4$. *Geol. Mag.* **130**, 289-299, 1993.

[106] M. Prieto, A. Putnis and L. Fernandez-Diaz, Factors controlling the kinetics of crystallization: supersaturation evolution in a porous medium. Application to barite crystallization. *Geol. Mag.* **127**, 485-495, 1990.

[107] M. Prieto, A. Fernandez-Gonzalez, A. Putnis and L. Fernandez-Diaz, Nucleation, growth, and zoning phenomena in crystallizing $(Ba,Sr)CO_3$, $Ba(SO_4, CrO_4)$, $Ba,Sr)SO_4$, and $(Cd,Ca)CO_3$ solid solutions from aqueous solutions. *Geochim. Et Cosmochim. Acta* **61**, 3383-3397, 1997.

[108] A. Putnis, M. Prieto, and L. Fernandez-Diaz, Fluid supersaturation and crystallization in porous media. *Geol. Mag.* **132**, 1-13, 1995.

[109] A. E. Nielsen, J. M. Toff, Electrolyte crystal growth kinetics, *J. Cryst. Growth* **67**, 278-288, 1984.

[110] A. E. Nielsen, Nucleation and growth of crystals at high supersaturation, *Kristall und Technik* **4**, 1, 17-38, 1969.

[111] I. L'Heureux and B. Jamtveit, A model of oscillatory zoning in $(Ba,Sr)SO_4$ solid solutions grown from aqueous solutions. *Geochim. et Cosmochim. Acta* **66**, 3, 417-429, 2002.

[112] D. Stauffer, Kinetic theory of two-component ("hetero-molecular") nucleation and condensation. *J. Aerosol. Sci.* **7**, 319-333, 1976.

[113] http://www.netlib.org/

[114] B. Chopard, P. Luthi, M. Droz, Reaction-diffusion cellular automata model for the formation of Liesegang patterns. *Phys. Rev. Lett.* **72**, 9, 1384-1387, 1994.

[115] A. Lin, R. Kopelman and P. Argyrakis, Nonclassical kinetics in three dimensions: Simulation of elementary A+B and A+A reactions. *Phys. Rev. E* **53**, 2, 1502-1509, 1996.

[116] R-F. Xiao, J. I. D. Alexander, and F. Rosenberger, Growth morphologies of crystal surfaces. *Phys. Rev. A* **43**, 6, 2977-2992, 1991.

[117] K. A. Jackson, Computer modeling of atomic scale crystal growth processes. *J. Crystal Growth* **198/199**, 1-9, 1999.

[118] G. M. Anderson and R. W. Macqueen, Ore deposit models – 6. Mississippi Valley-type lead-zinc deposits. *Geosci. Can.* **9**, 108-117, 1982.

[119] F. Ghazban, R. H. McNutt, and H. P. Schwarcz, Genesis of sediment-hosted Zn-Pb-Ba deposits in the Irankuh district, Esfahan area, west-central Iran. *Econ Geol.* **89**, 1262-1278, 1994.

[120] H. Etminan and C. Hoffmann, Biomarkers in fluid incusions: A new tool in constraining source regimes and its implications for the genesis of Mississippi Valley – type deposits. *Geology* **17**, 19-22, 1989.

[121] K. Klein and C. S. Hurlbut, *Manual of Mineralogy*, 21st Edition, (Wiley, New York, 1989.

[122] R. E. Liesegang, *Geologische Diffusionen*, Steinkopf, Dresden, Leipzig, 1913.

[123] L. M. Cathles and A. T. Smith, Thermal constraints on the formation of Mississippi Valley-type deposits and their implications for episodic basin dewatering and deposit genesis. *Econ. Geol.* **78**, 983–1002, 1983.

[124] G. Garven, The role of fluid flow in the genesis of the Pine Point Deposit, Western Canada sedimentary basin. *Econ. Geol.* **80**, 307-324, 1985.

[125] A. D. Fowler and M. T. Anderson, Geopressure zones as proximal sources of hydrothermal fluids in sedimentary basins and the origin of Mississippi Valley–type deposits in shale-rich sequences. *Trans. Instn. Min. Metall. (sect. B: Appl. Earth Sci.)* **100**, B14-B18, 1991.

[126] I. L'Heureux and A. D. Fowler, A simple model of flow patterns in overpressured sedimentary basins with heat transport and fracturing. *J. Geophys. Res.* **105**, 23,741-23,752 (2000).

[127] G. S. Plumlee et. al. Chemical reaction path modelling of ore deposition in Mississippi Valley–type Pb-Zn deposits of the Ozark region, U.S. midcontinent. *Econ. Geol.* **89**, 1361-1383, 1994.

[128] S. A. Jackson and F. W. Beales, An aspect of sedimentary basin evolution: the concentration of Mississippi Valley-type ores during the late stages of diagenesis. *Bull. Canadian Petrol. Geol.* **15**, 393-433, 1967.

[129] I. L'Heureux, Origin of banded patterns in natural sphalerite, *Phys. Rev. E* **62**, 3234-3245, 2000.

[130] H. K. Henisch, *Periodic Precipitation*, Pergamon Press, Oxford, 1991.

[131] R. Feeney, S. L. Schmidt, P. Strickholm, J. Chadam, and P. Ortoleva, Periodic precipitation and coarsening waves: Applications of the competitive particle growth model. *J. Chem. Phys.***78**, 1293-1311, 1983.

[132] A. A. Polezhaev and S. C. Müller, Complexity of precipitation patterns: Comparison of simulation with experiment. *Chaos* **4**, 631-636, 1994.

[133] M. Chacron and I. L'Heureux, A new model of periodic precipitation incorporating nucleation, growth and ripening. *Phys. Lett. A* **263**,70-77, 1999.

[134] R. Defay, I. Prigogine, A. Bellemans, and D. H. Everett, *Surface Tension and Adsorption*, Longmans, Green, London, 1966.

[135] F. O. Koenig, On the thermodynamic relation between surface tension and curvature. *J. Chem. Phys.* **18**, 4, 449-459, 1950.

[136] D. U. von Rosenberg, *Methods for the Numerical Solution of Partial Differential Equations*, Elsevier, New York, 1969.

[137] A. E. Boudreau, Crystal aging and the formation of fine-scale igneous layering. *Mineral. and Petrol.* **54**, 55-69, 1995.

[138] R. Sultan and P. Ortoleva, Periodic and aperiodic macroscopic patterning in two precipitate post-nucleation systems. *Physica D* **63**, 202-212, 1993.

[139] R. K. McLiman, H. L. Barnes, and H. Ohmoto, Sphalerite stratigraphy of the Upper Mississippi Valley Zinc-Lead District, Southwestern Wisconsin. *Econ. Geol.* **75**, 351-361, 1980.

[140] G. Sugihara and M. R. May, Nonlinear forecasting as a way of distinguishing chaos from measurment error in time series, *Nature*, **344**, 734-741, 1990.

[141] N. B. Abraham, A.M. Albano, B. Das, G. de Guzman, S. Yong, R. S. Gioggia, G.P. Puccioni, and J. R. Tredicce, Calculating the dimension of attractors from small data sets, *Phys. Lett.*, **114A**, 5, 217-221, 1986.

[142] T. Schreiber and A. Schmitz, A., Surrogate time series, *Physica D*, **142**, 3/4, 346-382, 2000.

[143] B. Dubuc *et al*, Evaluating the fractal dimension of profiles, *Phys. Rev. A*, **39**, 3, 1500, 1989.

[144] T. Holten and B. Jamtveit. Self-affine fractal geometry of agate, *Eur. J. Mineral.* **10**, 149-153, 1998.

[145] M. Cortini and D. Anastasio. Chemical banding in volcanic minerals: a statistical phenomenological approach. *Eur. J. Mineral* **13**, 571-575, 2001.

[146] D. L. Turcotte, *Fractals and Chaos in Geology and Geophysics*, 2nd ed., Cambridge University Press, 1997.

[147] B. S. Singer, M. A. Dungan, and G. D. Layne, Textures and Sr, Ba, Mg, Fe, K, and Ti compositional profiles in volcanic plagioclase: Clues to the dynamics of calc-alkaline magma chambers. *Am. Mineral.* **80**, 776-798, 1995.

[148] T. Schreiber, Interdisciplinary application of nonlinear time series methods. *Physics Reports*, 308, 1-64, 1999.

[149] J. W. Havstad and C. L. Ehlers, Attractor dimension of nonstationary dynamical systems from small data sets. *Phys. Rev. A*, 39, 2,, 1989.

[150] http://geol.queensu.ca/people/pearce/comments.html

[151] http://mineral.galleries.com/minerals/silicate/garnets.htm

[152] T. I. Ivanova, A. G. Shtukenberg, Y. O. Punin, O. V. Frank-Kamenetskaya, P. B. Sokolov. On the complex zonality in grandite garnets and implications. *Min. Mag.* 62(6), 857-868, 1998.

[153] B. Jamtveit. Oscillatory zonation patters in hydrothermal grossular-andradite garnet: Nonlinear dynamics in regions of immiscibility. *Am. Mineral.* 76, 1319-1327, 1991.

[154] N. R. Gadd, Lithofacies of Leda Clay in the Ottawa basin of the Champlain Sea, Geological Survey of Canada, Paper 85-21, 44 pp., 1986.

[155] N. R. Gadd, Lithofacies relationships in a freshwater-marine transition of the Champlain Sea. *in* N. R. Gadd, ed., The Late Quaternary Development of the Champlain Sea Basin: Geological Association of Canada, Special Paper 35, p. 83-90, 1988.

[156] C. G. Rodrigues, Late Quaternary invertebrate faunal associations and chronology of the western Champlain Sea basin. *in* N. R. Gadd, ed., The Late Quaternary Development of the Champlain Sea Basin: Geological Association of Canada, Special Paper 35, p. 155-176, 1988.

[157] J. Persival, J. Aylworth, personal communication, 2000.

[158] B. P. Boudreau, *Diagenetic Models and Their Implementation: Modelling Transport and Reactions in Aquatic Sediments*, Springer, Berlin, 1997.

[159] P. Grassberger and I. Procaccia, Measurement of the strangeness of the strange attractors. *Physica D* 9, 189-208, 1983.

[160] A. Grossman and J. Morlet, Decomposition of Hardy functions into square integrable wavelets of constant shape. *SIAM J. Math. Anal.* 15, 732-736, 1984.

[161] J. S. Langer, Instabilities and pattern formation in crystal growth. *Rev. Mod. Phys.* 52, 1, 1-28, 1980.

[162] K. Popper, *Conjections and Refutations*, London, Routledge & Kegan Paul, 1963.

[163] G. Lofgren, An experimental study of plagioclase crystal morphology: isothermal crystallization. *Amer. J. Sci.* 274, 243-273, 1974.